1996

Microstructural characterisation of nitrogen implanted and plasma nitrided austenitic stainless steel

Xinyang Li
University of Wollongong

Candidate's Certificate

This is to certify that the work presented in this thesis is original and was carried out by the candidate in the laboratories of the Department of Materials Engineering, at the University of Wollongong, Australia, and has not been submitted for a degree to any other unisversity or insitution.

XINYANG LI

ACKNOWLEDGEMENT

I would like to express my deep gratitude to my supervisor, Dr. M. Samandi, for his valuable guidance and constant encouragement throughout the years, and for arranging financial support from time to time.

Also, I would like to acknowledge Dr. G. Collins and Dr. J. Tendys of Australia Nuclear Science and Technology Organisation (ANSTO) for arranging an AINSE scholarship, their advice and encouragement.

I wish to thank Professor D.P. Dunne for helping arranging my University Post Study Award and Department Scholarship, also his advice and encouragement.

Many thanks are due to Dr. D. Wexler for his help in TEM, to Mr. G. Hamilton, Mr. G. Tillman, Mr. A. Scobie, Mr. R. Kinnell, Mr. N. Mackie, Mr. R. De. Jong for their technical assistance, to Mrs. R. Cambareri for her help in official matters. Thanks are also to Mr. M. Blackford of ANSTO for his assistance on TEM.

I am specially grateful to my wife, S. Li and my daughter, C. Li who support me whatever I do and for their love, understanding, and patience.

MICROSTRUCTURAL CHARACTERISATION OF NITROGEN IMPLANTED AND PLASMA NITRIDED AUSTENITIC STAINLESS STEEL

A thesis submitted in fulfilment of the requirements for the award of the degree of

DOCTOR OF PHILOSOPHY

from

The University of Wollongong

by

Xinyang Li, B.E., M.E.

Department of Materials Engineering

August 1996

ABSTRACT

In the present work, the cross-sectional transmission electron microscopy (XTEM), traditional selected area diffraction (SAD), nanobeam electron diffraction (NBD), high resolution electron microscopy (HREM) and glancing angle X-ray diffraction (GAXD) have been used to investigate the surface microstructure of AISI 316 austenitic stainless steel after plasma immersion ion implantation (PI^3) and plasma nitriding.

It has been established that GAXD is incapable of unambiguous characterisation of the microstructure of nitrogen implanted and nitrided austenitic stainless steel. Further, it has been demonstrated that sole reliance on GAXD could, at best, provide a very complicated and confusing picture of the microstructure and, at worst, could lead to totally false and erroneous interpretation. In stark contrast, the combination of XTEM + NBD provides a powerful technique to completely and unequivocally characterise the very fine microstructural features in this system.

Detailed microstructural characterisation by XTEM + NBD has shown that the sequence of the microstructural evolution in austenitic stainless steel after PI^3 and plasma nitriding is primarily controlled by diffusion processes. In other words, the high energy implantation effects in PI^3, i.e. collision cascade and radiation damage, plays only a minor role. However, PI^3 offers the possibility of building up higher nitrogen concentration in the near surface region which could influence the evolution of microstructure.

More specifically, it has been shown, for the first time, that the microstructure of austenitic stainless steel after PI^3 and plasma nitriding treatments is very complex, consisting of several layers of amorphous, or semi-amorphous and nanocrystalline structure with nanocrystalline precipitates such as CrN and α-ferrite. The formation of an amorphous layer in high temperature nitrogen implanted or nitrided austenitic stainless

steel, either as a sole layer or located as a sublayer underneath a nano-crystalline sublayer, seriously challenges the conventional wisdom that the radiation damage is the cause of amorphisation.

It has been argued that the incorporation of high nitrogen concentration into austenitic stainless steel leads to the formation of highly supersaturated austenite which is akin to a supercooled eutectic structure. Given the low diffusivity of substitutional elements, in particular chromium, the re-arrangement of atoms to allow co-precipitation of CrN and α is very difficult. Under this condition, the total energy of the system could only be lowered by amorphisation. Depending on temperature and nitrogen content, some re-arrangement of atoms could take place on a very short scale, thus resulting in the formation of nano-sized CrN and α precipitates.

The precipitation of CrN and α is strongly influenced by the temperature. Above 500°C, CrN and α can directly nucleate from γ. Below this temperature, precipitation of CrN and α requires extensive atomic rearrangement which under restrictive diffusion condition induces the collapse of γ substrate into an "amorphous" phase from which very fine CrN and α precipitates nucleate. Therefore, author suggests that the solid state eutectic reaction provides the driving force for amorphisation in nitrogen implanted austenitic stainless steel. Both Bain and N-W (Nishiyama and Wasermann) relationships have been observed between CrN and α precipitates. The K-S (Kurdjumov and Sachs) relationship has also been observed between CrN and α at low temperature and low nitrogen concentration (e.g. 350°C plasma nitrided sample).

At low nitrogen concentration, Cr_2N, as an eutectoid phase, can precipitate directly from γ to form a nanocrystalline $Cr_2N + \alpha$ layer. The following orientation relationship has been observed between Cr_2N and γ:

$$(011)\gamma \,//\, (\bar{3}211)Cr_2N$$

$$[100]\gamma \,//\, [12\bar{3}2]Cr_2N$$

CONTENTS

CHAPTER 1 INTRODUCTION

Austenitic stainless steels are widely used in aggressive environments where resistance to corrosion is the main consideration. However, their poor tribological properties pose serious problems in certain industrial and prosthetic applications where abrasion resistance is also important (e.g., in the food processing and aerospace industry).

Over the last decade or so, nitrogen ion implantation and plasma nitriding have been successfully used to improve the tribological properties of stainless steels [1-8]. However, this has usually occurred with concurrent loss of corrosion resistance. Recently, it has been demonstrated that, under correct treatment conditions, e.g., treatment temperature between 300-500°C, it is possible to minimise the loss of corrosion resistance or, more significantly, to enhance the corrosion resistance while imparting excellent tribological properties to the material [1-4, 43].

To understand why nitrogen ion implantation and plasma nitriding of austenitic stainless steels results in such an outstanding surface, traditional microstructural characterisation techniques have frequently been used to determine the morphology and crystallographic details of microstructure. Such techniques include x-ray diffraction (XRD), glancing angle x-ray diffraction (GAXD), transmission electron microscopy in conjunction with selected area diffraction (TEM+SAD), scanning electron microscopy (SEM), x-ray photoelectron spectroscopy (XPS), conversion-electron Mössbauer spectroscopy (CEMS), and Rutherford back-scattering spectroscopy (RBS). In spite of the plethora of proposed hypotheses, conflicting results reported by researchers cannot be easily reconciled and the exact nature of the microstructure introduced by nitrogen implantation and plasma nitriding of austenitic stainless steel is still unclear.

A few years ago, Samandi et al [4] initiated on investigation into the standing of the emerging technology of plasma immersion ion implantation (PI^3) in relation to plasma nitriding and conventional nitrogen implantation. Using GAXD to characterise the surface microstructure, Samandi et al [4] suggested that a nitrogen-expanded austenite forms on the samples treated below 500°C. Schematic illustration of the microstructure formed at different temperatures are summarised in Figure 1.

However, the proposed nitrogen-expanded austenite, based on interpretation of GAXD spectra, is inconsistent with the established principles of physical metallurgy. For instance, it is suggested [84] that the maximum solubility of nitrogen in austenite is less than 2.2 at.% (1.0 wt.%), while the detected nitrogen content in the surface of implanted and nitrided 316 stainless steel by Samandi et al [4] was estimated to be greater than 40 at.%. The implausibility of this extremely high level of supersaturation becomes even more apparent when it is realised that accommodation of this level of nitrogen concentration necessitates filling of almost all of octahedral interstices in austenite lattice. This would undoubtedly give rise to an isotropic expansion of the lattice which is contrary to the different shifts in diffraction peaks for different planes shown in the GAXD spectra reported by Samandi et al [4]. Furthermore, given the high concentration of chromium in austenitic stainless steel (18wt.%), and bearing in mind that chromium is a strong nitride former, it is very hard to accept the assertion that no CrN precipitate forms until 500°C.

Another indirect evidence undermining the interpretation by Samandi et al [4] is why the corrosion resistance of the austenitic stainless steel should be enhanced by lattice expansion of austenite. There is no reason why the expansion of lattice, be it isotropic or not, should influence the electrochemical behaviour of alloy. From the foregoing, it is obvious that a closer scrutiny of the microstructure of high temperature nitrogen implanted and nitrided austenitic stainless steel is required before a satisfactory account of the microstructural evolution can be afforded.

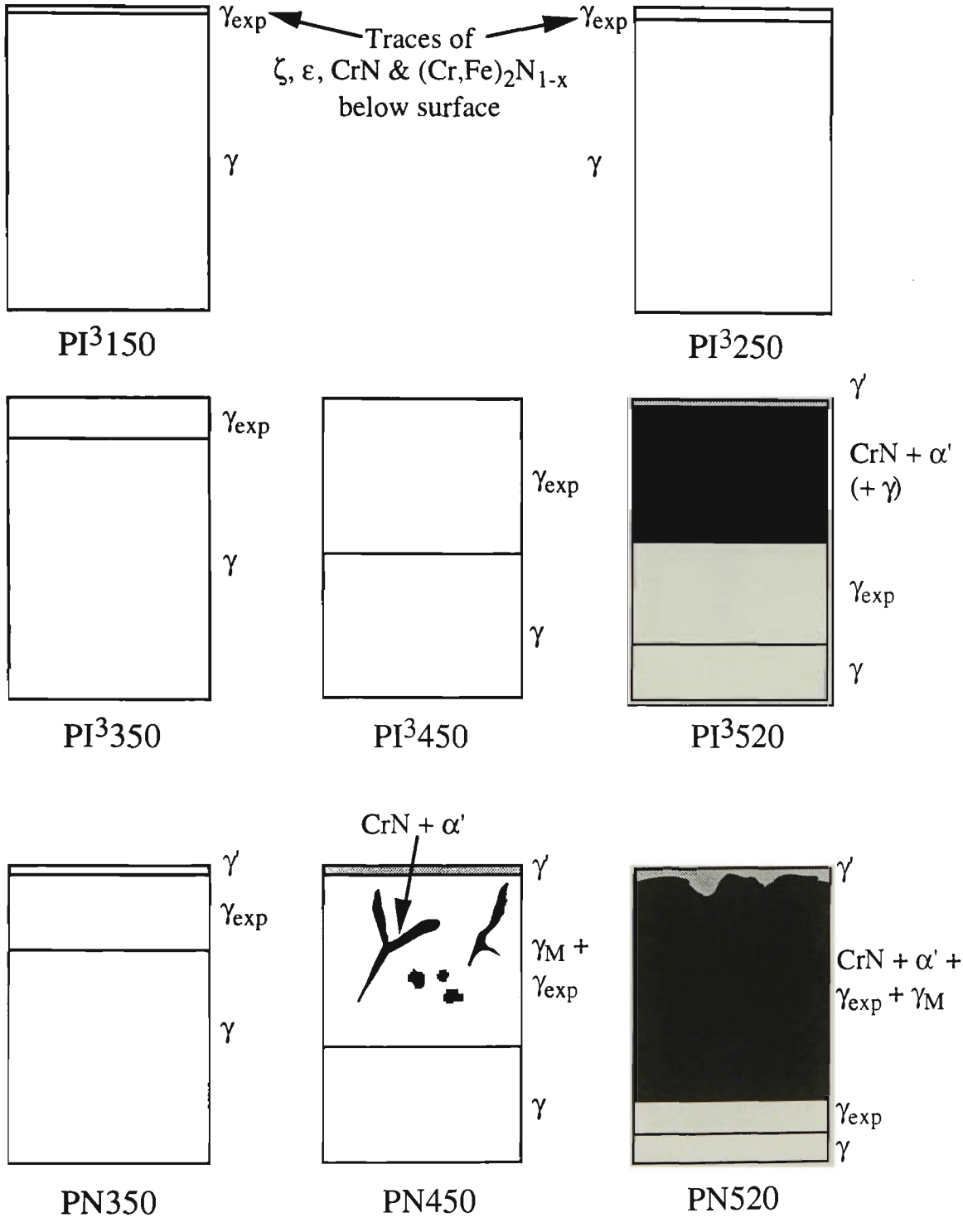

*γ_M: γ-martensite

Figure 1. Schematic description of the microstructure of nitrogen implanted and plasma nitrided 316 stainless steel [43].

PI^3: plasma immersion ion implantation PN: plasma nitriding

The major thrust of this investigation was, therefore, to answer the questions left by Samandi et al [4]. From the literature review of Chapter 2, it is clear that the

microstructural characterisation of the nitrogen implanted and plasma nitrided austenitic stainless steel requires sophisticated analytical techniques capable of resolving features on a nanometre scale, as well as the entire depth of treated surface which could be up to several micrometers thick. Therefore, in the present work, the cross-sectional transmission electron microscopy (XTEM) technique, traditional selected area diffraction (SAD), nanobeam electron diffraction (NBD), and high resolution electron microscopy (HREM) were used to investigate the surface microstructure of nitrogen ion implanted and plasma nitrided AISI 316 austenitic stainless steel. Glancing angle X-ray diffraction (GAXD) were also employed on all plasma nitrided and PI^3 treated samples for comparison.

CHAPTER 2 LITERATURE REVIEW

2.1 Nitriding and Nitrogen Ion Implantation Techniques

2.1.1 Methods of Nitriding

2.1.1.1 Gas Nitriding

Gas nitriding of steels is a ferritic thermochemical treatment which hardens the surface by the formation of iron and alloy nitrides. In the case of stainless steel, gas nitriding is of little value due to the oxide layer on the surface which makes it impossible to enrich the surface with nitrogen . More details on the practice of gas nitriding can be found elsewhere [9-11].

2.1.1.2 Plasma Nitriding

A schematic diagram of a typical plasma nitriding unit is shown in Figure 2. During plasma nitriding the workpiece is placed in a vacuum furnace and biased to a negative potential between 300 and 1000 volts. The vessel is at ground potential and acts as the anode of the electrical circuit. The chamber is evacuated and then refilled with the treatment gas (usually mixed N_2 and H_2 or cracked NH_3) to a working pressure between 0.1-10 Torr. Under this potential difference and low pressure, the gas molecules become excited and ionised to create a 'plasma' or 'glow discharge' [12-21].

The treatment gas is usually a mixture of nitrogen and hydrogen, but pure nitrogen can also be used. The positive ions of the treatment gas are accelerated towards the negatively charged workpiece and absorbed onto the surface. The kinetic energy released upon impact raises the temperature of the workpiece so that a separate heating system is not required. At the surface, typical current densities are in the range 0.5-2 mA/cm^2 (where current density is defined as ion current divided by the cathodically charged surface area) [12-21].

Although potential differences of up to 1000 volts are used, the ion energies are

significantly lower due to the relatively higher pressures employed in the chamber (compare to ion implantation). At such a pressure numerous collisions take place between ionised and neutral species which continuously reduces the ion energy. The majority of the ions possess energies below 50 eV [12-21].

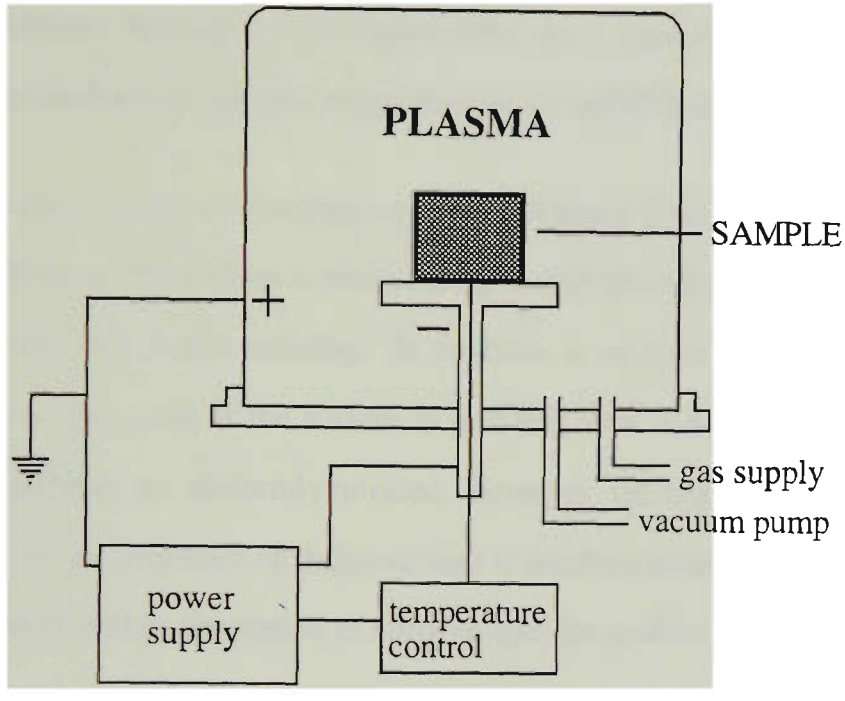

Figure 2. Plasma nitriding apparatus

Treatment times can be up to 48 hours at temperatures between 350 and 600°C depending upon the grade of steel and depth of layer required. The voltage drop between the anode and cathode is almost entirely restricted to a few millimetres in front of the cathode, in a region called the 'cathode fall'. Consequently, the surface treatment is practically independent of the distance between the wall and the workpiece [12-21].

A number of theories have been proposed for the mechanism of nitrogen absorption. Although none of these theories adequately explain the complete process, nevertheless, it is worth mentioning the main elements of the most widely cited one. Edenhofer [12] suggests that sputtering of iron atoms causes nitride formation in the cathode fall after collision with nitrogen, followed by redepositing onto the workpiece.

A study by Hudis [13,14] concluded that a simple bombardment mechanism by NH^+ and/or NH_2^+ molecular ions is responsible for nitriding. Tibbets [16] suggests that bombardment by neutral nitrogen atoms of high energy is the main mechanism. Nevertheless, it was generally observed that the presence of hydrogen in the treatment gas increased the rate of nitriding. Indeed, Hudis [14] found it difficult to produce a nitrided case without hydrogen in the processing gas. Spalvins [17] describes the mechanism as a simultaneous process of gas absorption and ionic bombardment.

Advantages of plasma nitriding over gas nitriding have been widely reported [10,12,13,17]. Most notably, there is greater control over the composition and thickness of compound layer than in gas nitriding. In addition, a separate heating system is not required, nitrogen saturation of the surface is possible even at low temperatures (350-450°C), and all surfaces are uniformly nitrided. However, the fundamental advantage of plasma nitriding in the treatment of stainless steel is the depassivation of the oxide layer by sputtering, which makes absorption of nitrogen into the surface possible.

2.1.2 Ion Implantation

In the process of ion implantation, high energy ions are implanted below the surface of a solid material [22]. Conventional implantation involves the acceleration of a beam of ions across a high voltage potential of 10 - 400 keV; the energetic ions strike the workpiece at the end of a vacuum tube. The workpiece is usually maintained at a low temperature (less than 100°C). This may require an additional cooling facility if the current density of the beam is high. Implantation is carried out in a chamber at very low pressures in the range 10^{-5} to 10^{-7} Torr to prevent scattering of the beam. The high ion energy means that the current density is typically very low, varying from 1 to 40 $\mu A/cm^2$. The main advantages of ion implantation over other established nitriding techniques are that it can be conducted at room temperature. However, it is a 'line of sight' process with very shallow treatment depth. Therefore, its application is restricted to treatment of simple geometries and in tribological systems where high contact stresses are not involved [22-28].

2.1.3 Plasma Immersion Ion Implantation (PI^3)

In recent years, a new non-line-of-sight nitrogen implantation process, known as Plasma Immersion Ion Implantation (PI^3), has emerged [4, 29-30]. PI^3 involves the application of a pulsed high voltage bias to components immersed in a radio frequency (r.f.) plasma [29]. This process offers the possibility of producing surface structures typical of ion implantation, plasma nitriding or a combination of both, depending on the treatment temperature [30].

PI^3 is similar to plasma source ion implantation (PSII) developed by Conrad *et al* [31]. The major distinctions between the two methods being the method of plasma generation, the nature of the cathodic sheath, and the fact that PI^3 is designed to operate at higher temperatures, encouraging more diffusion [29].

A schematic of the PI^3 system is shown in Figure 3. The basic components are the (r.f.) power supply and antenna, the high voltage power supply and pulse circuitry connected to the treatment table and the vacuum pump. The r.f. antenna and treatment table are contained inside a stainless steel vacuum chamber [30]

The chamber is pumped down and then back filled with nitrogen gas to a working pressure of about 1-2 mTorr. When the r.f. power is applied to the antenna, a diffuse plasma fills the chamber. An r.f. plasma is used because its ionisation efficiency is higher than that of a d.c. plasma. This plasma is created independently from the workpiece, unlike the practice of DC plasma nitriding [30].

The workpiece is heated by the current drawn from the plasma when the high voltage pulses are applied. This current depends upon the bias voltage, the plasma density and the surface area of the workpiece. It is usually in the range 1-4 mA/cm^2. Since the plasma surrounds the component, implantation is approximately uniform over all exposed surfaces[30].

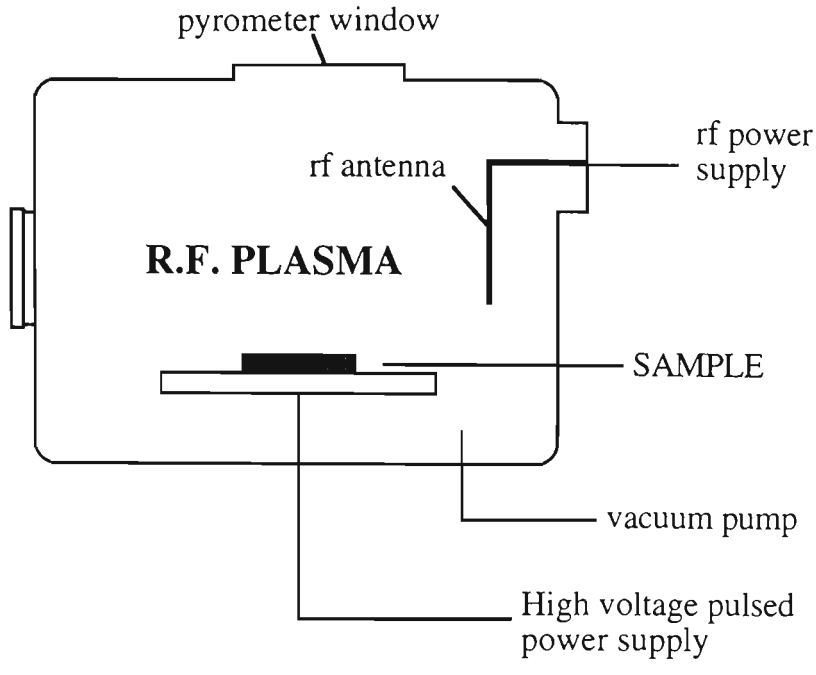

Figure 3. A schematic of the PI^3 system

The high energy ion bombardment causes heating of the sample so that a separate heating device is not required. Precise temperature control is achieved by adjusting the voltage pulse frequency, and monitoring the temperature with an infrared pyrometer. The voltage is pulsed to prevent excessive heating of the components [30].

The major advantage of PI^3 over 'line of sight' ion implantation is that it provides a uniform ion dose over the entire surface of a component [29]. Furthermore, the diffusion of nitrogen beyond the implanted layer has been observed at temperatures greater than 250°C [29]. It is reported that improvements in wear resistance and surface hardness of mild steels at temperatures higher than 250°C were greater than those obtained by ion implantation [29].

In contrast to plasma nitriding, PI^3 can be carried out at lower temperatures, and the treatment gas is generally pure nitrogen [30]. It should be emphasised that the pressures employed in PI^3 are three orders of magnitude lower than those used in plasma nitriding. The ions have a high energy when they strike the surface due to the high voltage pulses and lower pressure [30]. In Table 1, the salient features of plasma nitriding, conventional ion implantation and PI^3 are compared.

Table 1. Nitriding Process Variables

PROCESS	VOLTAGE (kV)	CURRENT DENSITY (mA/cm^2)	PRESSURE (Torr)	TEMP. (°C)	REFERENCES
Plasma nitriding	0.3-1.0	0.5-3.0	0.1-10	350-600	[12,13]
Ion implantation	10-400	0.001-0.03	10^{-5}-10^{-7}	<100	[23-28]
PI^3	40-50 (pulsed)	1-4	10^{-3}	150-500	[30]

2.2. Physical Metallurgy of Stainless Steels

Broadly speaking, stainless steels can be classified to three main classes, namely, ferritic, martensitic and austenitic.

2.2.1 Ferritic Stainless Steels

The characteristics which identify a steel as stainless are imparted by chromium more so than by any other element. Other alloying elements, however, enhance the effect of chromium in many environments and confer many of the special properties such as machinability, weldability, etc. Therefore, the earliest developed, and basic, stainless steels are Fe-Cr stainless steels.

According to the Fe-Cr phase diagram, increasing chromium content decreases the range of temperatures over which austenite exists until, at approximately 12wt.% chromium, ferrite is stable at all temperatures to the solidus. Since all Fe-Cr stainless steels have at least 12wt.% chromium, and generally have a single ferrite phase at all temperatures, Fe-Cr stainless steel is also known as ferritic stainless steel.

The corrosion and oxidation resistance of the ferritic steels are directly related to their chromium content. The higher the chromium content, the better their corrosion and oxidation resistance, primarily owing to the presence of a tenacious protective chromium

oxide layer on the surface.

The ferritic stainless steels are classified by three digits 4xx according to the AISI standard.

2.2.2 Martensitic Stainless Steels

The hardenable martensitic stainless steels are developed from Fe-Cr ferritic stainless steels by adding other austenite-stabilising elements, such as carbon, nitrogen, nickel and manganese, to expand the austenite phase field and permit heat treatment. The composition must be carefully balanced to prevent δ-ferrite formation at the austenitizing temperature to attain the best mechanical properties.

The martensitic stainless steels are also classified as 4xx by AISI standard since fundamentally they are still Fe-Cr stainless steels.

2.2.3 Austenitic Stainless Steel

2.2.3.1 Effect of Nickel on Austenitic Stainless Steels

Addition of nickel to stainless steels can increase their ability to passivate in sulphuric acid, significantly improve corrosion resistance in hydrochloric acid of all concentrations at room temperature, and increase corrosion resistance in aqueous and molten sodium hydroxide. Nickel also improves the toughness, cold formability and resistance of welds to certain corrosive agents.

Progressive additions of nickel displace the δ ferrite zone to higher temperatures and increase the amount of austenite formed at higher temperatures. The stability of the austenite phase is also increased by nickel so that at approximately 8% nickel an austenitic structure persists at room temperature.

2.2.3.2 General Classification

The parents of the austenitic stainless steel class are 302 (0.15wt.% C) and 304

(0.08wt.% C) which have approximately 18wt.% chromium and 8wt.% nickel. Therefore, austenitic stainless steel is commonly known as 18-8 stainless steel. Based on 302 and 304 steels, a series of 3xx austenitic stainless steels have been developed by adjusting the chromium and nickel content or by addition of small amounts of other alloying elements.

The most commonly used austenitic stainless are: (a) the basic 18-8 stainless steels (17-19wt.% Cr, 8-10wt.% Ni), 302 and 304; (b) the higher nickel content 305 (10-13wt.% Ni) to reduce the rate of work hardening and improve deep drawing; (c) the highly corrosion resistant molybdenum-bearing 316 (2-3wt.% Mo) and 317 (3-4wt.% Mo); (d) the stabilised grade 321 (about 0.4% Ti); (e) the extra-low-carbon (0.03wt.% C) grades, 304L and 316L; (e) the oxidation-resistant grades, 308 (19-21wt.% Cr, 10-12wt.% Ni), 309 (22-24wt.% Cr, 12-15wt.% Ni), 310 (24-26wt.% Cr, 19-22wt.% Ni).

The AISI classification of austenitic stainless steels, however, is complicated by an overlapping effect. For example, the chemistry permitted by AISI specifications may allow the low chemistry end of one grade to extend into the high chemistry end of another. Thus, one could buy 304 and 305 of identical composition. Inspite of compositional differences, all austenitic stainless steels still show the same microstructure consisting of a single austenite phase, and the same trend of microstructural evolution under mechanical treatment, heat treatment or chemical treatment.

2.2.3.3 Microstructure

Normally the microstructure of austenitic stainless steels show only austenite. Since carbon content limits are generally lower than 0.15wt.% in these grades, solution annealing will usually dissolve all or most of the carbides present after hot rolling. Rapid quenching from the solution-annealing temperature, typically 1010°C to 1065°C, will retain the carbon in solution, producing a strain-free, carbide-free austenitic microstructure.

It should be pointed out that the austenite in these grades is not stable, but metastable. Martensite can be formed, particularly in the leaner grades, by cooling specimens to very low temperatures, or by extensive plastic deformation. Non-magnetic, hexagonal close-packed (hcp) ε-martensite and magnetic, body-centred cubic (bcc) α'-martensite have been observed [35].

The most widely observed carbide in austenitic stainless steels is $M_{23}C_6$ (M=Fe, Cr, Ni) which occurs as a result of heating the solution-annealed austenitic stainless steels to 500 to 900°C. The fastest rate of $M_{23}C_6$ precipitation takes place from 650 to 900°C. Although the amount of $M_{23}C_6$ precipitates is very small, their precipitation at grain boundaries produces intergranular corrosion. The precipitation of $M_{23}C_6$ can be countered by reducing carbon content or adding strong carbide formers.

Nitrogen solubility in commercial 3xx series austenitic stainless steels made at atmospheric pressure is less than 0.4% (wt). By melting commercial austenitic stainless steels under 4.2 MPa, the nitrogen concentration can be increased to 0.6 wt.% to 0.8 wt.% [68,69]. Even at such a high concentration, all nitrogen in these alloys remains as an interstitials and no second-phase nitrides are observed [68,69]. However, in a cast austenitic stainless steel, an inter dendritic nitride, thought to be M_6N (M=Cr, Mo, Fe, Nb), has been observed between the austenite dendrites[70]. Cr_2N and γ'-Fe_4N have also been identified in cast austenitic stainless steels [70].

2.3 Review of Relevant Phase Diagrams

Reliable information on phase diagrams of the Fe-Cr-Ni-N system is a pre-requisite for a complete elucidation of the microstructure of nitrogen implanted and nitrided austenitic stainless steels. Unfortunately, relevant information on phase diagrams is so far only available for Fe-N binary system, plus limited information from Cr-N and Ni-N systems. For Fe-Cr-N ternary systems there is some information, and for higher-order systems the information is very fragmentary.

2.3.1 Fe-N Binary System

Figure 4 shows the Fe-N binary phase diagram [71].

Three metastable compounds, Fe_8N (or $Fe_{16}N_2$), Fe_4N and Fe_2N (or $Fe_{2-3}N$), form in the Fe-N system. The maximum solubility of nitrogen in α-Fe is 0.4 at.% at 590°C. The lattice parameter of nitrogen saturated α-Fe is almost identical to that of pure α-Fe.

The γ phase is fcc and isomorphous with the γ phase (austenite) in the Fe-C system.

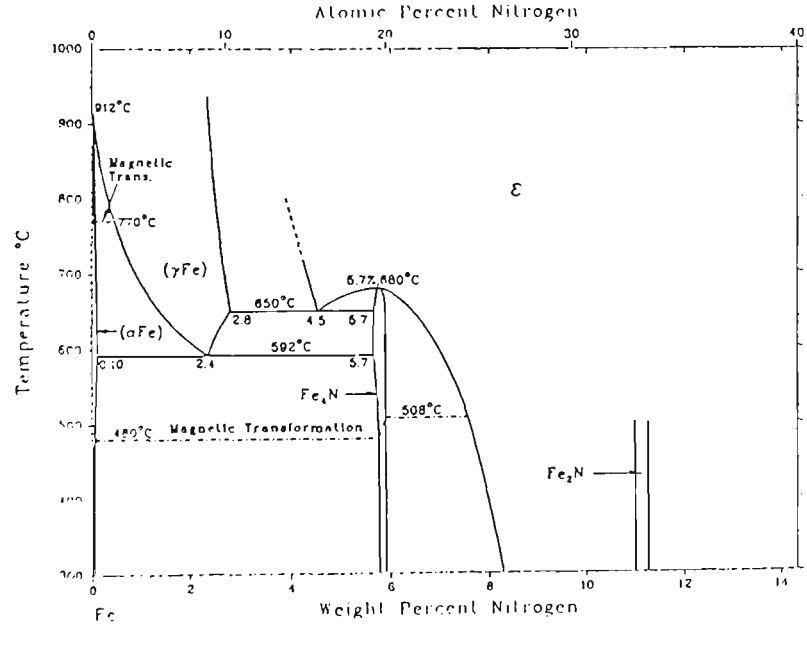

Figure 4 Fe-N phase diagram [71].

The Fe_4N (or γ') phase is not a simple stoichiometric compound with an ordered fcc structure, but exists over a narrow range of compositions, which for example, lie between 19.60 at.% and 19.95 at.% nitrogen at 500°C [72,73].

Investigations by Jack [74] of the ε-Fe_2N (or ε-$Fe_{2-3}N$) and ζ-Fe_2N phase confirmed that both phases show an ordered arrangement of nitrogen atoms, hcp and

orthorhombic, respectively. In the ζ-Fe_2N structure the iron-atoms retain the same relative position as in ε-$Fe_{2-3}N$, however, because the nitrogen atoms are more closely packed in one direction in ζ-Fe_2N, the iron atom lattice is anisotropically distorted. Details of the explanation for the transition between ε-$Fe_{2-3}N$ and ζ-Fe_2N have been proposed by Jack [74].

The $Fe_{16}N_2$ phase is unstable with respect to iron solutions and Fe_4N. It is considered as an ordered α-Fe solution or a transition phase between the α-Fe solution and Fe_4N, existing only below 160°C [75].

2.3.2 Cr-N Binary System

It is surprising that an universally accepted Cr-N phase diagram has not yet been produced. Based on the fragmentary data of the Cr-N system, it is known that: (a) the solubility of nitrogen in Cr is very limited [76]; (b) there exist two intermediate phases, Cr_2N and CrN [76].

Some researchers have reported that Cr_2N has a hcp structure [76,77]. However, other reports show that the true unit cell of Cr_2N is three times larger than that of the simple hcp structure [78-80], with the lattice parameters a = 4.759-4.805Å, c = 4.438-4.479Å, and c/a = 0.933-0.932 in its homogeneity range from 27.6-33.3 at.% N (9.3-11.9 wt.% N) [79-80].

CrN has been shown to have the fcc NaCl type structure with a = 4.140Å. The homogeneity range of CrN is not clear.

2.3.3 Other Binary Alloy-Nitrogen Systems

2.3.3.1 Ni-N Binary System

Only very limited information about Ni-N system is available. An unstable Ni_3N has been reported [81]. The transformation from Ni to Ni_3N follows the change of a cubic to a hexagonal stacking sequence with ordered nitrogen atoms. The crystal

structure of Ni_3N is isomorphous with ε-$Fe_{2-3}N$.

2.3.3.2 Mo-N System

The Mo_2N is the only nitride which exists in Mo-N system when the concentration of nitrogen is lower than 40-50 at.% N and the temperature is below 700°C [82]. Mo_2N has an fcc structure with a = 4.163Å.

2.3.4 Ternary and higher order phase diagrams

2.3.4.1 Fe-Cr-N System

The only information about Fe-Cr-N system is the thermodynamic approach by Frisk and Hillert [83]. However, this thermodynamic approach only gives the high temperature region above 1200 K (927°C) and has a fixed Cr content of 25 wt.%. According to the thermodynamic approach, α+ε-nitride exist at nitrogen content below 1.8 wt.%, γ+ε exist at medium nitrogen content (about 2 wt.%), and γ+CrN exist at the high nitrogen content (above 4.3 wt.%). No Cr_2N is predicted by this thermodynamic approach. Since the temperature for nitriding and ion implantation is lower than 873 K (600°C), this thermodynamic approach has little use for nitriding and ion implantation.

2.3.4.2 Fe-Cr-Ni-N System

One recent work reported the investigation of the high nitrogen concentration 304 and 316 austenitic stainless steels made by hot-isostatic-pressure furnace [84]. This showed that: (a) no nitride precipitates were observed when the nitrogen concentration was below 1wt.%; (b) when the nitrogen content was higher than about 1 wt.%, both eutectic CrN and eutectoid Cr_2N were observed; (c) only CrN was observed when nitrogen content was above about 2 wt.%; (d) above 2 wt.% nitrogen, the steel exhibited the presence of both fcc and bcc phases, and the percentage of the bcc increased with increasing total nitrogen concentration.

2.4 Review of Microstructures of Nitrogen Implanted and Plasma Nitrided Austenitic Stainless Steels

2.4.1 Nitrogen Ion Implanted Austenitic Stainless steels

The most important findings of some of papers published in recent years on microstructural characterisation of nitrogen implanted austenitic stainless steels are summarised in chronological order in Table 2. The most important implantation parameters, i.e. ion energy, dose and temperature are included, where known, in addition to the substrate material and specific characterisation technique. Finally, the major constituents of the microstructure, as ascertained by authors, are highlighted.

Table 2. Summary of microstructural characterisation of the nitrogen implanted austenitic stainless steels

Material being implanted	Ion Energy (keV)	Temp. (°C)	Dose x10^{17} ions/cm^2	Major Microstructural Constituents	Characteri-sation Technique	Year of publ.
304	40	?	0.1-10	CrN type nitrides	XPS	1980[32]
304 316	40	room	0.6-1.2	CrN in nm size coherent with γ	TEM SAD	1981[26]
304	40	?	2	α' martensite formed on the surface due to polishing prior to implantation was transformed to γ at outer most layer, γ stabilised by N with iron nitrides precipitation were formed in subsurface region.	TEM SAD GAXD	1982[33]
Fe-17Cr-13Ni	40	?	up to 2	suggested CrN	RBS	1982[34]

Fe-17Cr-13Ni	25-165	room	0.025-1.5	Cr_2N (no CrN) or probably $Fe_2N+\alpha'$	TEM SAD	1985[36]
304	40	25	1	α', ε and ζ nitrides, high dislocation γ	TEM SAD	1986[37]
			2	α', ε and ζ nitrides		
			6	γ, α' and ζ nitrides		
304	40	room	0.1-0.5	ε-martensite	TEM SAD	1987[38]
			>1	hexagonal and orthorhombic nitrides		
			2	oriented nitrides, small amount of α'		
			>2	highly defective structure, can't discern individual phase		
			1	broadened γ peaks, small amount of α'	GAXD	
			2	hex. and orth. nitrides(ζ-Fe_2N, $Cr_2(C,N)$, $(Cr,Fe)_2N_{1-x}$), with small amount of α'		
			6	ε-Fe_2N, and small amount of α'		
304	40	?	2	polishing introduced α' martensite transformed to γ by nitrogen implantation at outer most layer, γ stabilised by N with iron nitrides precipitation were formed in subsurface region.	TEM SAD	1988[39]
304	25	?	?	Fe_2N	XRD XPS	1988[40]

321	100	room 200 350	<1	} 100% γ	CEMS XRD	1989[41]
		room 200 350	4	$(Fe,Cr)_2N$ $(Fe,Cr)_{2+x}N$ Cr_2N and CrN with α underneath		
Fe-13Cr-15Ni	1100	~200	0.23	SAD did not discern the presence of any second phase because of the complex overlapping of the diffused diffract rings	XTEM SAD	1989[42]
316 (PI^3 treated)	45	150	3	γ_{exp}, with traces of ζ, and ε–nitrides, CrN, $(Cr,Fe)_2N_{1-x}$	GAXD SEM	1991[43]
		250	9	same as 150°C implanted sample		
		350	10	highly supersaturated and expanded γ_{exp}		
		450	12	same as 350°C implanted sample		
		520	14	Thick CrN+α'+γ with γ_{exp}underneath		
304	60	400 500 600	0.5-2	} γ_N only	XRD CEMS	1991[44]
		400		ε-nitride		
		500	100	CrN+α		
		600		CrN+α		
304	60	Low	<4	ε-nitride	XRD CMES	1991[45]
		≥400	4-10	γ_N		
		≥500	100	CrN		

304	33 130 200	150 370 500	3.5	ε-nitride only { mainly distorted α and γ_{exp}, with traces of ε-nitride, CrN and Cr_2N	GAXD	1991[46]
304	60	210±50 380±50 510±50	4 4 100	ε-nitride γ_N CrN+α	CEMS XRD SEM	1992[47]
316	?	<300	0.5-2.5 5	spinel type CrN+Fe_3O_4 at outer most layer with ε-M and α'-M underneath which progressively replaced by Fe,Cr nitrides $(Cr,Fe)_2N_{1-x}$, Cr_2N and ε-M	GAXD TEM	1992[48]
Fe-13Cr-15Ni	550	ambient	0.23	SAD did not show any second phase precipitation in the implanted layer	XTEM SAD	1992[49]
302	130	300	2.5	α'+Cr_2N+ε(Fe_2N-Fe_3N)+γ_{exp} (mechanically polished sample) Cr_2N+γ_{exp}+γ (chemically polished sample)	GAXD	1993[50]
316 (PI^3 treated)	45	150 250 350 450 520	3 9 10 12 14	} modified layer was expanded γ Thick CrN+α' layer	GAXD	1993[4]

304	60 30 2 1	400	*Ion beam (mA/cm^2) 0.1 0.25 1.5 2.5	γ_N for all conditions, lower ion energy and higher ion current corresponding to thicker implanted layer and more expansion of γ_N	CEMS XRD	1994[51]
304	45-90	room	1 2 3	} Cr_2N and Fe_4N, some CrN in Cr rich region	XPS	1994[52]

XPS: X-ray photoelectron spectroscopy

TEM: Transmission electron microscopy

XTEM: Cross-sectional transmission electron microscopy

SAD: Selected area diffraction

GAXD: Glancing angle x-ray diffraction

XRD: X-ray diffraction

RBS: Rutherford back-scattering

SEM: Scanning electron microscopy

CMES: Conversion-electron Mössbauer spectroscopy

The most striking feature of Table 2 is that different microstructures have been reported for materials which were implanted under seemingly similar conditions. For example, Vardiman et al [33] reported that nitrogen implantation would stabilise γ and cause polishing introduced α' to transform to γ, while Aggarwal et al [50] did not observe the α' to γ transformation in their study. More intriguingly, even the same sample, when characterised with different techniques (TEM, GAXD, CEMS), revealed different microstructural constituents [38,44].

Another interesting point in Table 2 is that almost all of the possible and conceivable nitrides and other phases in nitrogen implanted austenitic stainless steel, such as CrN, Cr_2N, γ'-Fe_4N, ε and ζ nitrides, $Cr_2(C,N)$, $(Cr,Fe)_2N_{1-x}$, expanded austenite γ_{exp}, pure austenite γ, N-martensite α', ε-martensite, have been reported to exist separately, or in different combinations.

Studies of ion implantation at elevated temperatures have been reported since the late 80's. From these studies, it has been shown that the implantation temperature plays a very important role in determining the surface microstructure. Summing up the results shown in Table 2, it can be inferred that, although still complicated, the surface microstructure by implantation at elevated temperature showed less complexity than those implanted at room temperature.

For implantation carried out below 250°C, four papers reported the existence of the ε-nitride in the surface, either as the sole constituent [45-47] or one of the minor precipitated nitrides with nitrogen saturated γ_{exp} [43]. However, a number of alternative surface microstructures, such as 100% γ at a dose of less than $1x10^{17}$ ions/cm^2, or mainly $(Fe.Cr)_{2+x}N$ at a dose of $4x10^{17}$ions/cm^2 [41], combination of γ_{exp}+ζ+ε-nitride+CrN+$(Cr,Fe)_2N_{1-x}$ [43], were also reported for nitrogen implantation at below 250°C for austenitic stainless steel.

A number of papers reported nitrogen expanded austenite γ_{exp} or γ_N as the only phase in 300°C-500°C nitrogen implanted austenitic stainless steels [43-45, 47, 51]. Some other papers reported that γ_{exp} or γ_N co-existed with other nitrides or phases, such as CrN+Cr_2N, ε-nitride+α' or distorted α [46,50]. However, different surface microstructures without γ_{exp} or γ_N were also reported. For instance, Leutenecker et al [41] studied the 321 austenitic stainless steel nitrogen implanted at 350°C and found only γ existed in the implantation modified surface layer if the dose was less than $1x10^{17}$ions/cm^2; while Cr_2N, CrN and α present in the $4x10^{17}$ions/cm^2 implanted sample. Although Williamson et al [44] only reported the presence of γ_N in the implantation modified surface layer on 304 stainless steel (≤0.5-$2x10^{17}$ions/cm^2), a single ε-nitride surface layer, resulting from $1x10^{19}$ions/cm^2 implantation, was also reported in the same paper. An unusual structure, reported by Rieu et al [48] after the implantation of 316 stainless steel, exhibited spinel type CrN+Fe_3O_4 at the outer-most surface, with ε-martensite and α'-martensite underneath, when the dose was between 0.5-$2x10^{17}$ions/cm^2; while $(Cr,Fe)_2N_{1-x}$, Cr_2N and ε-martensite were detected if the

dose was $5x10^{17}$ions/cm^2.

Only a few papers reported nitrogen ion implantation at above 500°C on austenitic stainless steels [43-45, 47]. CrN was the only nitride reported in these implanted layers. Wei et al [45] reported that CrN existed in the implantation modified surface, while other papers reported that CrN co-existed with α [44,47] or α' and γ_{exp} [43]. Willainmson et al [44] also reported that when implantation was carried out at low doses (0.5-$2.0x10^{17}$ions/cm^2), even at the temperature above 500°C, only γ_N could be detected in the implantation modified surface layer.

Besides temperature, ion dose is considered to be another important factor to affect the ion implantation of materials, especially in semiconductors. However, some researchers asserted that ion dose did not have an effect on the implanted layer [32,35,36,52] even when the dose varied from 0.1-$10x10^{17}$ions/cm^2 [32,35]. Some researchers believed that different doses would result in different surface microstructures, but unfortunately in these cases implantation temperatures were also varied thus concealing the true influence of different doses [43,45,47]. Recently, Williamson et al [51] suggested the dose rate, instead of total dose, may play a more important role in ion implantation of austenitic stainless steels. 304 stainless steel was used for implantation at a fixed temperature of 400°C, with different ion energy and dose rate combination (refer to Table 2). The thickness of the implanted layer correlated to ion dose rate (ion beam current) but did not relate to ion energy. Low ion energy with high dose rate corresponded to a thick implantation modified surface layer, while high ion energy with low dose rate corresponded to a thin implantation modified layer. Therefore, this suggests that the so called radiation enhanced nitrogen diffusion is not true.

It should be emphasised that only two papers in Table 2 reported XTEM studies on nitrogen implanted austenitic stainless steels [42,49]. Although the XTEM images showed a very dark layer, approximately 0.5 μm at the outer most surface layer, the authors reported that the SAD did not discern the presence of any second phase. The outer-most dark sublayer was then considered to have originated from massive radiation

damage.

2.4.2. Nitrided Austenitic Stainless Steels

Table 3 summarises the most important findings of some of the recently published works on microstructural characterisation of the nitrided austenitic stainless steels.

Table 3. Summary of the microstructural characterisation of the nitrided austenitic stainless steels

Material being nitrided	Nitriding Tech.	Nitriding Atmosphere	Time (hr)	Temp. (°C)	Major Microstructural Constituents	Characteri-sation Technique	Year of publ.
304	plasma	$30N_2$:$70H_2$	5	500	outer layer very fine expanded CrN sublayer CrN	XRD TEM SAD	1982[53]
		$50N_2$:$50H_2$	0.5-5	550	outer layer CrN+γ' sublayer very fine lamellar CrN+γ		
		$30N_2$:$70H_2$	?	600	outer layer fine expanded CrN sublayer lamellar CrN+γ		
316	gas	NH_3	24	600	outer layer 3μm ε-Fe_2N_{1-x} 2nd layer 35μm γ'-$(Fe,Ni)_4N$+CrN 3rd layer 60μm γ+γ'-Fe_4N+CrN 4th layer 70μm γ+CrN+α+Cr_2N 5th layer 5μm deformed γ	XRD	1983[54]
					lamellar N pearlite CrN+γ close to interface Cr_2N+α interface deformed γ	TEM	

316	gas	NH_3	24	600	outer layer very thin ε nitride white layer CrN+γ'-$(Fe,Ni)_4N$ dark layer CrN+γ'-Fe_4N diffusion layer CrN precipitates in γ small amount of α at interface	XRD TEM SAD	1983[55]
304	gas	NH_3	10-15	520	no segregation of Cr, Fe, Ni	SEM	1985[56]
316L	gas	NH_3	24	600	surface ε-$(Fe,Cr)_2N_{1-x}$ white layer fine CrN in γ' matrix dark diffusion layer γ'+CrN precip. in γ matrix inner diffusion layer lamellar CrN+γ heavily deformed interface layer	XRD TEM SAD	1985[57]
316	plasma	?	24	570	surface 20-40μm γ+γ' (with traces CrN and ε nitride?) 2nd 70-90μm lamellar CrN+α or CrN+γ, small amount tetr. α interface 3-4μm γ_{exp}	TEM SAD XRD	1985[2]
18Cr-8Ni stainless steel	gas	any $1N_2:100H_2$ $1N_2:9H_2$ $4N_2:1H_2$ $1N_2:100H_2$ $1N_2:9H_2$ $4N_2:1H_2$	1-8	400 500 600	"S" phase } CrN, α and γ CrN, γ' } CrN, α and γ CrN and γ'	XRD	1986[21]

304	plasma	$1N_2:10H_2$	50	510	$\gamma_{exp}+\alpha+CrN+\gamma'_{exp}$	XRD SEM	1986[58]
304	plasma	$1N_2:10H_2$	50	510	N and Cr co-precipitates into 1-2μm islands, may be CrN	XRD SEM	1987[59]
	gas	NH_3	10-15	520	Fine CrN precipitates (<0.1μm)		
316	plasma	$4N_2:1H_2$	24	350	outer layer γ'_{exp} or γ_{exp} underneath $\gamma'+\varepsilon$ nitride	XRD TEM SAD	1988[60]
304	plasma	N_2	0.89	280	γ'+small amount ε nitride,	XRD	1988[61]
			0.33	480	evidence of Cr nitride was detected		
			0.2	570	but may be mixed with γ' matrix		
			0.17	625			
316	plasma	$5N_2:95H_2$	10-64	450	"S" phase	Optical SEM XRD	1988[1]
			10-64	500	"S" phase+γ', "S" decrease with time increase		
			10	550-650	} $\gamma'+\gamma+CrN$		
			10	700	$\gamma+CrN$		
				750-850	} $\gamma'+\gamma+\gamma_{exp}+CrN$		
		NH_3		500	"S" phase		
				550-650	} $\gamma+CrN$		
				700-800	} $\gamma+\alpha+CrN$		
				850	$\gamma+\gamma_{exp}+CrN+Cr_2N$		
					* all CrN and γ showed lamellar structure.		

304 316	plasma	$4N_2:1H_2$	1 6 24	350±5	γ_{exp}+ε-nitride+ε-M γ_{exp}+ε-nitride+undetermined phase γ_{exp}+ε-nitride+undetermined fcc phase	XRD TEM	1989[18]
316	plasma	$5N_2:95H_2$ NH_3		<500 >550 850	"S" phase with little γ' γ' at surface with CrN+γ underneath Cr_2N formed with α, plus γ+γ_{exp}+CrN	Optical SEM XRD	1990[62]
316	plasma	$25N_2:75H_2$	5	350 450 520	thin γ' surface with γ_{exp} underneath thin γ' surface with γ_{exp} + bct γ_M underneath, some fine CrN+α' thin γ' surface, the underneath is CrN+α+γ_{exp}+γ_M	GAXD	1991[43]
310	plasma	$12N_2:88H_2$ $20N_2:80H_2$	120 60	350 350	Total nitrided layer is 3-4μm γ_N N<22at.% Total nitrided layer is 4-5μm 2μm thick CrN+γ_N at surface the rest of the underneath is γ_N N>22at.%	XRD TEM SAD	1991[19]
304	plasma	$40N_2:60Ar$	1	400-450	γ+"B" phase (close to γ' or γ_{exp})	XRD TEM SAD	1993[63]

TEM: Transmission electron microscopy

SAD: Selected area diffraction

GAXD: Glancing angle x-ray diffraction

XRD: X-ray diffraction

SEM: Scanning electron microscopy

Optical: Optical microscopy

Similar to the case of nitrogen implantation, the microstructure of nitrided stainless steels has been interpreted differently by different researchers. However, summing up the results presented in Table 3, it is obvious that nitriding temperature and time play a very important role during nitriding.

For example, CrN is widely reported to exist in high temperature (>500°C) nitrided austenitic stainless steels. Some researchers reported that CrN was the only nitride in the nitrided layer, either as the sole phase [53] or the sole precipitates [59]. However, in most cases, CrN was reported to co-exist with other nitrides and phases, to form a two phase layer (or sublayer) with either γ [1,54,55,57,62], γ' [21,53-55,57] or α [40]. Alternatively, it could form a complex layer (or sublayer) with $\gamma+\gamma'$[1,54], $\gamma+\alpha$ [21], $\gamma+\alpha+Cr_2N$ [54], $\gamma_{exp}+\gamma'_{exp}+\alpha$ [58], or $\alpha+\gamma_{exp}+\gamma_M$ [43]. Some papers reported a thin compound layer of ε-nitride [54,55,57], or a thin γ' [43,62] compound layer, or a thin $\gamma+\gamma'$ [2]) layer at the outer most surface. Others reported a thin transition layer of deformed γ [54,57] or γ_{exp} [2] between the nitrided layer and the substrate.

A lamellar structure, or so called "nitrogen pearlite", has been observed with TEM in the high temperature nitrided layer [2,53-55, 57]. Urao et al [53] established with XRD and TEM+SAD that this lamellar structure was composed of CrN and γ. Billon and Hendry [54,55,57] suggested that the structure consists of either two phases, CrN and γ, or three phases, CrN, γ and γ'. Zhang and Bell proposed that the structure was composed of either CrN+γ or CrN+α in which CrN was the dominant phase [2].

It is interesting to note that, similar to the nitrogen implanted austenitic stainless steels, the same nitrided surface has been characterised differently by using different surface characterisation techniques. Using careful grinding to reveal the heterogeneity of the nitrided surface, Billon and Hendry [54] reported that the microstructural characterisation by XRD and TEM yielded different results. XRD results suggested a layered structure with a 3 μm thick ε-nitride at the outer-most surface, followed by a 35 μm thick γ'+CrN, a 60 μm thick $\gamma+\gamma'$+CrN, then a 70 μm thick γ+CrN+α+Cr_2N and

finally a 5 μm thick deformed γ at the interface with the core. In contrast, TEM revealed CrN+γ at the outer-most surface, followed by CrN+α and a thin deformed γ between the nitrided layer and the substrate.

Generally speaking, when nitriding is carried out at below 500°C, the nitrided surface shows a more complicated structure than those treated at above 500°C. Some researchers suggested that the low temperature nitrided surface comprised of γ_{exp} or γ'_{exp}, with or without small amounts of ε-nitride, ε-martensite and CrN+α [18,43,60]. Saker and Leroy et al [19] suggested that the nitrogen concentration in the nitrided surface layer controlled the surface microstructure. If nitrogen concentration was less than 22at.%, the nitrided surface layer would be a single γ_N. With nitrogen concentration above 22at.%, the nitrided surface layer was composed of a thin CrN+γ_N sublayer at the outer-most surface and a sublayer consisting solely of γ_N underneath.

However, other researchers were not so sure about the surface microstructure of the low temperature nitrided austenitic stainless steel. El-Hosarry et al [61] reported that nitrided layer composed of γ' and a small amount of ε-nitride, but they also suggested that the nitrided layer might be composed of Cr nitride mixed with γ'. D'haen et al [63] reported a nitrided layer composed of γ and an uncharacterised phase, which they named the "B" phase, with a suggested structure similar to γ' or γ_{exp} [63]. Confused by the x-ray diffraction results of their 400°C and 500°C nitrided sample, Ichii et al suggested a new f.c.c. M_4N (M=Fe, Cr, Ni...) phase, named "S" phase, in the nitrided layer [21]. This "S" phase was then reported again by Dearnley et al [1,62]. Hannula et al reported that an undetermined phase existed with γ_{exp}+ε-nitride after nitriding had been carried out for a long time at 350°C [18,60].

2.5 Comments on Interpretation of Microstructure of Nitrided and Nitrogen Implanted Austenitic Stainless Steels

It is abundantly evident from the summaries presented in Tables 2 and 3 that the voluminous literature dealing with the microstructure of nitrogen implanted and nitrided

austenitic stainless steels is littered by conflicting and opposing interpretations. In this author's opinion, the lack of unanimity amongst researchers regarding the exact nature of microstructural modification brought about by implantation and nitriding can be traced back to three problems. Firstly, the characterisation techniques employed in the majority of the reported works appear to be inadequate or inappropriate for the task undertaken, or at best only capable of providing limited information on certain features (e.g. XPS would only provide chemical information about the first few atomic layers of a surface). Secondly, the implantation and nitriding parameters such as ion energy, dose, temperature and time vary over a large range. Indeed, some researchers have shown scant regards for the importance of these parameters in influencing the microstructure and have not mentioned these treatment parameters in their work. Finally, the lack of consensus amongst researchers is probably originated or at least compounded by the lack of reliable information about the pertinent phase diagrams in a multi-component system. These three aspects are more critically reviewed in the following sections.

2.5.1 Surface Characterisation Techniques

2.5.1.1 XRD and GAXD Surface Characterisation

Limited lateral resolution (about 10 mm) and the depth (or spatial) resolution (about 30 μm) of the X-ray diffraction technique renders it incapable of discerning individual phases in a very fine multi-phase, multi-layer systems. This problem is especially acute when the phases in the system are present in small volume fraction (<5%) and have their diffraction peaks close to each other, i.e., similar crystal structure and interplanar spacing. When using XRD to characterise the very thin ion implanted layer, the substrate may contribute significantly to the diffraction spectra so as to make the interpretation of the diffraction results even more complicated. Although the latter problem can be overcome by using glancing angle configuration (GAXD), this in turn creates problems of its own, owing to low signal to noise ratio, broadening and skewing of peaks. Bearing in mind these problems, the presence of extremely fine microstructural features and high level of residual stresses in the nitrided and implanted surface, which

result in broadening and shifting of diffraction peaks as well, makes the interpretation of GAXD spectra very difficult, if not impossible. In fact, from the XRD and GAXD spectra of the nitrogen ion implanted and nitrided austenitic stainless steels which have been published in recent years [18,19,21,38,40,41,43,44,46,47,50,51,53,57,60,63], almost all of them showed very broadened and shifted diffraction peaks. Thus, it is very difficult to match any standard diffraction peaks of the nitrides or other phases to those spectra. Given the inadequacy of XRD and GAXD in unequivocal determination of microstructure, it is difficult to concur with those researchers who suggested, solely on the basis of XRD, that the nitrogen expanded austenite, γ_{exp} or γ_N, would be the main constituent phase for the nitrogen implanted or low temperature nitrided austenitic stainless steels[19,44-47,53,63]. Also, very little credence can be given to the work of some other researchers who created their own phases, dubbed as "S" phase [1,21,62] or "B" phase [63] to identify the possible new phases based on the abnormal XRD spectra.

It is interesting to mention that a number of researchers only reported their interpretation of the microstructure as characterised by XRD or GAXD, without providing the original XRD patterns [1,36,48,54,55,58,59,62]. One paper [2], in particular, shows the XRD pattern taken from the interface which showed only γ peaks, but no XRD patterns of the rest of nitrided layer. Another paper only presents schematic XRD patterns instead of the originals [61], but still elaborates on the exact nature of the microstructure throughout the modified layer.

More encouragingly, a few recently published papers report a more careful scrutiny of the abnormal XRD patterns of the nitrided and nitrogen implanted stainless steels before formulating their interpretations. A notable example is the work reported by Saker et al [19] who studied the surface micorstructure of a plasma nitrided 310 stainless steel at 350°C. They differentiated the peaks on XRD spectra into two groups of γ_N with different expanded lattices. One group showed normal shifting of the γ peaks, i.e. all the austenite peaks shifted to lower diffraction angles, suggesting uniform expansion of austenite lattice by nitrogen while another group showed the (200) peak shifted more than

(111) peak, indicating an anisotropic expansion of austenite lattice.

D'haen et al [63] studied the 400-450°C plasma nitrided 304 stainless steel samples and found two sets of diffraction peaks, thus corroborating the findings reported by Saker et al [19]. However, instead of naming both of these sets as γ_N , they designated γ for the normally shifted peaks, and "B" phase for the abnormally shifted and strongly broadened peaks. Further, D'haen et al asserted that the (220) peak of the "B" phase is shifted less than all the other "B" phase peaks. Besides the peak shifting, the relative intensity of the diffraction peaks of "B" phase is completely out of proportion with the peaks of the γ phase. For example, the relative intensity of the (220) peak of the "B" phase is abnormally low in comparison to the strong (111) and (200) peaks. Therefore, the author suggested that the (111) "B" peak may represent a mixture of the $(Cr,Fe)_2N$ or Cr_2N with "B".

Abnormal XRD pattern has also been obtained by Willaimson et al [44] who investigated the microstructure of nitrogen implanted 304 stainless steel at 400°C. Their XRD pattern showed that the intensities of both $(111)\gamma_N$ peak and $(200)\gamma_N$ peaks increase with decreasing ion energy, but the intensity increase of the $(200)\gamma_N$ peak was found to be abnormally greater than that of the $(111)\gamma_N$ peak. Besides, the shift associated with the $(200)\gamma_N$ peak is more than the $(111)\gamma_N$, $(220)\gamma_N$ and $(300)\gamma_N$ peaks. The author calculated the possible nitrogen content in γ_N based on the shifting of the peaks. The calculation shows 28at.% N for the $(111)\gamma_N$ peak and 40at.% N for that of the $(200)\gamma_N$ peak. The calculated stress along the $<200>\gamma_N$ direction, again calculated according to the peak shift, is unrealistically high at 12 GPa. However, their hardness results indicates a more believable stress level at about 2 GPa in the $<200>\gamma_N$ direction, thus questioning the validity of calculated 40at.% N for the $(200)\gamma_N$. This also undermines the main conclusion of the authors who stated that γ_N is the only phase presented after implantation at 400°C for a range of doses, and reinforces the fact that the microstructure is far more complicated than those suggested by cursory interpretation of XRD spectra.

Appreciating the complexity of the microstructure of nitrogen implanted 316 stainless steel [48], Rieu et al used GAXD, TEM and SAD for characterisation. Unfortunately, the authors concluded that the TEM and SAD failed to illuminate the situation and, therefore, no results were included in their paper, and their discussion was based entirely on XRD spectra. However, they emphasised the shortcomings of XRD in elucidating the complex microstructure because of the close proximity of the diffraction peaks for the large number of Fe, Cr and Ni nitrides. Nevertheless, the authors proposed that the 300°C nitrogen implanted 316 steel surface had a spinel type CrN and Fe_3O_4 layer at the outer-most surface, and ε-martensite and α'-martensite underneath. The ε-martensite and α'-martensite sublayer was replaced by Fe and Cr nitrides $(Cr,Fe)_2N_{1-x}$ and Cr_2N) and ε-martensite after high dose implantation, at the same temperature.

2.5.1.2 TEM and SAD Surface Characterisation on Nitrogen Implanted Austenitic Stainless Steels

Unfortunately, some researchers who used TEM and SAD to study the microstructure of nitrogen implanted austenitic stainless steel, merely reported the conclusions drawn from the SAD results, without showing the corresponding SAD patterns [38,49] (refer to Table 2). On the SAD patterns reported in other published works, diffuse rings [33] or mixed diffuse rings superimposed with complex diffraction spots [36] are discernible. In spite of these observations, the indexing of diffraction patterns and characterisation of microstructure proved to be inconclusive. Although not conceded by the authors, it is believed that the origin of uncertainties associated with SAD patterns can be explained by reference to the very fine nanocrystalline structure, the similarity of crystal structures of the phases involved and the closeness of the interplanar spacings of the possible nitrides and other phases, see Table 4. Thus, it is very difficult to obtain a clear picture of the surface by using only SAD technique, which analyses a large area of the order of μm^2 compared to the nanometre scale structure of the implantation modified surface. Another problem associated with SAD has been highlighted by Lee et al [42] who studied nitrogen implanted Fe-13Cr-15Ni austenitic

stainless steel, and realised that SAD did not discern the presence of any second phases due to the complex overlapping strain contrast from the highly defective structure presumably caused by radiation damage or lattice distortion induced by expansion or precipitation of different phases. Rieu et al [48] also used TEM and SAD without success to study nitrogen implanted 316 stainless steel.

Amongst all the researchers who used SAD, only two groups have managed to confidently index the diffraction patterns of nitrogen implanted 304 and 316 stainless steels. Baron et al [26] identified γ with an overlapped CrN ring pattern, Whereas Fayeulle and Treheux [37] identified γ with overlapped ε, ζ and α' patterns. It is interesting to note that in both works, although conducted at different laboratories, the same stainless steel was used for implantation, and the implantation parameters, i.e. temperature, ion energy and ion dose were almost identical, yet the microstructures as reported by these two groups are very different. This discrepancy could possibly be attributed to the inadequacies of SAD to uniquely and conclusively identify different phases in this system, as mentioned earlier.

Table 4. The d-spacing of the strongest diffraction atomic planes of γ, α phase and some nitrides [information from ASTM cards]

α {110}	γ {111}	ε–$Fe_{2-3}N$ {101}	CrN {200}	ζ-Fe_2N {021}{211}	Cr_2N {111}	$(Cr,Fe)_2N$ {111}	ε–$Fe_{2-3}N$ {002}	γ' {111}
2.027Å	2.067Å	2.062Å	2.070Å	2.110Å	2.117Å	2.114Å	2.186Å	2.191Å

2.5.1.3 TEM and SAD Results of the Nitrided Austenitic Stainless Steels

A number of publications have provided TEM micrographs of a lamellar structure, or "nitrogen pearlite" structure for high temperature (>500°C) nitrided austenitic stainless steels [2,53-55,57]. However, the exact composition of this lamellar structure has not yet been fully and unambiguously determined. Urao et al [53] suggested this lamellar structure to be composed of CrN and γ. Billon and Hendry [54,55,57] on the other hand reported it to be composed of either a two phase mixture, CrN and γ, or three phases, CrN, γ and γ'. Zhang and Bell [2] expounded that the lamellar structure

comprised CrN and γ or CrN and α, both with CrN as the predominant constituent. Again, the different description of the lamellar structure may have been caused by the difficulty in interpreting the complicated SAD patterns. Compared to the size of the lamellar structure which forms colonies of less than 100 nm, the selected area for diffraction may still be too large to identify the individual colony, so that overlapped complex diffraction patterns are obtained. In fact, the SAD patterns in these papers showed not only complicated patterns, but diffuse rings superimposed on the pattern as well.

As a result of the much finer microstructure of the low temperature (<500°C) nitrided surface, a far more complicated SAD pattern would be generally expected. Saker et al [19] obtained a very diffuse ring pattern on a 310 stainless steel sample plasma nitrided at 350°C and were unable to index the pattern. On the other hand, through their studies of plasma nitrided 316 stainless steel at 350°C, Hannula et al [18,60] identified overlapping γ and ε-nitride rings in SAD patterns, while their XRD result showed very broadened and shifted peaks of an unknown phase which they thought was γ_{exp}. Careful examination of the results reported by Hannula et al establishes that one of the SAD patterns was taken from the surface which had only been nitrided for 15 minutes. Another SAD pattern was taken from the 24 hour nitrided surface which had a thicker surface layer, and the authors admitted that was not representative of all the nitrided samples. Another problem with this work is that the one side plan-view TEM sample was slightly pre-thinned by sputtering on the nitrided side. The pre-thinning depth was not mentioned by the author. Thus, making it impossible to correlate the findings to the exact point on the nitrided surface. On the same work in which D'Haen et al [63] named "B" phase based on their XRD results, they also identified overlapping γ'-Fe_4N and $(Cr,Fe)_2N_{1-x}$ on the SAD pattern but the authors doubted the reliability of their SAD result.

2.5.1.4 Surface Characterisation by XPS

XPS (X-ray photoelectron spectroscopy) uses X-ray photons of certain energy to

hit a sample, exciting shell electrons of the elements. By measuring the energy of the excited electrons, the binding energy of the electrons of the specific element will be obtained which can be used for elemental concentration analysis. The formation of compounds will cause the energy of the shell electrons to shift. This will therefore give information on the chemical state of the elements of the compound. However, according to Barr [64], there are two major problems or uncertainties in the use of XPS to study the chemical state, namely, the techniques employed to determine chemistry, and quantification. Interestingly, these features seem to have been treated with reasonable success in individual laboratories, but universally accepted procedures, particularly for detecting binding energy shifts indicative of changes in chemistry, do not yet exist. The primary reasons for the lack of consensus in these areas would seem to be the inability to fix the binding energy zero (charge shifting problem) and the inhomogeneity that characterises many compounds.

Among the three papers [32,40,52] in Tables 2 and 3 which used XPS for analysing the surface, only Singer and Murday [32] used XPS to determine the chemical state of different elements in the nitrogen implanted surface, while the other two used XPS for surface concentration analysis. Although Singer and Murday mentioned their XPS results, they did not give any XPS spectra, showing only their Auger electron spectroscopy (AES) spectra in the paper.

Although the depth resolution of XPS can reach 0.5-3 nm, the lateral resolution of XPS is about 150 μm [65]. Because of the poor lateral resolution, XPS is not suited for analysing chemical states on complex structures consisting of multiple nanocrystalline phases, irrespective of the above mentioned problems.

2.5.1.5 Surface Characterisation by Mössbauer Spectroscopy

The Mössbauer effect (also known as nuclear gamma resonance) is the recoilless transition of a radioactive source from an excited nuclear level to its nuclear ground state, and the subsequent recoilless absorption of the emitted γ-photon by an absorber

containing the same isotope. Mössbauer spectroscopy couples this effect with the Doppler effect to provide a sensitive tool for the analysis of energy shifts and splitting of the nuclear levels involved. In the most common transmission geometry, a standard (single transition) radioactive source is driven in repeated motion relative to a rigidly mounted specimen of the absorber material which is to be studied. When the Doppler - shifted γ-ray energy matches that of an absorber transition, resonant absorption takes place and a reduced count rate is registered at a γ-ray detector positioned behind the absorber. The Mössbauer spectrum is the accumulated record of count rate versus relative speed. The differences between speeds at which resonant absorption occurs correspond to differences between respective absorber transition energies. It is common, therefore, to express energy differences in terms of velocity units. The Mössbauer effect is widely used for (a) the qualitative and quantitative identification of various alloy phases and (b) the measurement of the specific properties of the phases.

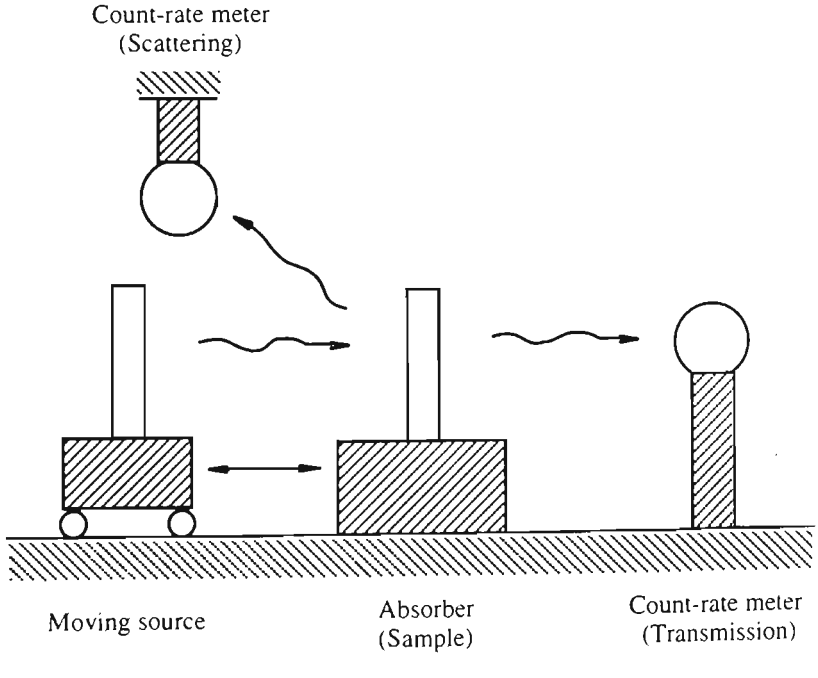

Figure 5. The arrangement of major components of Mössbauer spectroscopy

Although most measurements are made with transmission geometry, the scattering technique has very interesting applications. Scattering is particularly useful for surface analysis or very thick samples. The arrangement of the Mössbauer spectroscopy with both transmission and scattering geometries is shown in Figure 5.

In many Mössbauer isotopes the gamma radiation is internally converted into an x-ray and conversion electron, therefore, three means of detecting the Mössbauer effect are then used for scattering method: (a). the normal scattered Mössbauer radiation, (b). the conversion x-ray, (c). the conversion electron, which is known as conversion electron Mössbauer spectroscopy (CEMS).

CEMS provides information from a thin layer on the surface of a metal. The depth of the layer is limited by the range of conversion electrons within the metal. For iron-rich alloys, the depth being probed is of the order of 30 nm [113]. The very shallow detected depth of CEMS makes it an ideal technique for surface analysis. However, the lateral resolution of CEMS is very poor, of the order of 1 cm^2. The poor lateral resolution of CEMS also makes the technique unsuitable for analysis of very fine complex structure introduced by ion implantation.

Since Mössbauer spectroscopy detects the hyperfine magnetic field around the core of an atom, it may not be very good for the analysis of poly-phase complex systems. Gonser [66] reported studies of the precipitation in a Cu-Fe system. It was found that an analysis in terms of three components (Fe in solution, γ-Fe precipitates, and small atomic clusters) is rather difficult because of insufficient resolution and statistical uncertainties. The same paper also reported the study of Fe-C alloys, which showed that the Mössbauer effect can distinguish various simultaneously present phases, and within these phases, various atomic environments. However, the study also showed that it is often very difficult to unravel the spectra because of the variety of substitutional and interstitial impurities and the presence of the different simultaneously present phases: martensite, austenite, cementite, ε-phase and others.

Among the five papers [41,44,45,47,51] in Table 2 which reported using CEMS to characterise the nitrogen implanted surface, two of them [45,47] did not show their Mössbauer spectra. Leutenecker et al utilised CEMS to study nitrogen implanted AISI 321 stainless steel and reported [41] that it was impossible to differentiate between ε-martensite and austenite with CEMS since it supplies practically the same single line.

CEMS could also not differentiate nitrides on the ($4x10^{17}$ ions/cm^2) implanted sample, which the authors suppose to have mixed nitrides of Fe_2N and $(Cr,Fe)_2N$. In their CEMS and XRD studies of the nitrogen ion implanted 304 stainless steel, Willainmson et al [44] reported that the CEMS data from some of the 500°C implanted samples and all of the 600°C implanted samples showed weak evidence of the γ_N resonance, even though the XRD showed that it was clearly present. In addition, slight decomposition of the γ-(Fe, Cr, Ni) austenite is often observed by CEMS but not detected by XRD.

The recent CEMS studies of a nitrogen ion implanted AISI 304 stainless steel by Williamson et al [51] revealed an expanded γ_N single phase implantation modified surface layer, and a dramatic change in the magnetic nature of the γ_N phase with increase of the nitrogen content from a predominantly paramagnetic phase $\gamma_N(P)$ to a predominantly magnetic phase $\gamma_N(M)$. However, the magnetic resonance shown in the paper is very broad and can be matched with a distribution of magnetic hyperfine fields with an average value of about 16 Tesla, while the f.c.c. stainless steel and f.c.c. Fe become anti-ferromagnetic at low temperature, and the internal fields are typically as low as of the order of 2 Tesla. Based on their results, they suggested that the γ_N phase was analogous to the f.c.c. ordered phase γ'-Fe_4N, even though it was not ordered, which has a much expanded f.c.c. lattice compared with γ-Fe, and is ferromagnetic at room temperature.

2.5.1.6 Surface Characterisation by RBS

When a flux of high energy charged projectiles impinges on a material, a very few of the incident particles undergo "billiard ball" type collisions with the target nuclei. This occurs to the projectile ions which pass close enough to a target nucleus for wide angle elastic scattering due to coulombic electrostatic repulsion. In this scattering mode both energy and momentum are conserved and the impinging particle rebounds with an energy characteristic of the mass of the target atom. The energy of the scattered projectile, E, is always less than its original incoming energy, E_0, and is given by $E=KE_0$, where K is the kinematic factor of the collision obtained from the classical conservation laws of

energy and momentum, and is a function of the mass of the projectile M_P, the mass of the target atom, M_T, and the scattering angle of the projectile, Θ_S. Therefore, RBS can be used to discriminate between the different elements making up a target, e.g., the sample to be analysed.

Generally, RBS can do three things: (a) it identifies the masses of the constituent elements making up the target; (b) it determines the amounts of each element in the target; (c) it associates a depth scale with each element in a thin target. Typically RBS can be used to analyse materials up to a few microns depth from the surface. After this the depth resolution degrades due to energy straggling in the incoming projectile beam.

RBS provides a further possibility for atom location studies because for monocrystalline material, the penetration of the ion beam, and hence the backscattered signal, is very sensitive to the orientation of the incoming beam to the crystal lattice. The positions of impurity atoms within a host crystal lattice can be determined with a precision of a few hundredths of a nanometre unit.

I.V. Mitchell described the working conditions, advantages and disadvantages of RBS [67]. The lateral resolution of RBS is about 0.5 mm, which is too large to analyse the surface of the nitrogen ion implanted austenitic stainless steel. Besides, an inherent ambiguity exists in the interpretation of the spectra, particularly for complex targets, because the energy axis is simultaneously a mass scale. So, for example, a light element at the surface can be confused with a heavier mass element residing beneath the surface.

Whitton et al [34] studied the nitrogen implantation modified surface structure of AISI 321 (Fe-17Cr-13Ni) austenitic stainless steel with RBS. To eliminate the orientation effect of the poly-crystalline structure on the accuracy of the RBS analysis, a single crystal sample was used for this study. The result showed that implantation introduced lattice disorder in the steel. The disorder level increased in an approximately linear fashion with implant dose, up to a dose of $10^{16}/cm^2$, and saturated at a dose of $\sim 2x10^{17}N^+/cm^2$. The implanted nitrogen was found to sit in the octahedral interstitial

site. In any case, because of the lattice disorder, it was impossible to determine whether Cr atoms in the implanted steel were displaced from lattice sites by a Cr-N interaction. Therefore, the exact picture of the surface structure still could not be drawn out. However, the author proposed that the RBS results supported the suggestion of CrN forming in the implanted layer. It should be pointed out that the paper missed one important fact, that after implantation, the implanted surface layer of the single crystal sample may no longer be a single crystal, which may introduce extra uncertainty to the RBS analysis.

2.5.1.7 Summary of Surface Characterisation Techniques

Table 5 summarises the microstructural characterisation techniques mentioned in this Chapter. From the information given in Table 5, it is obvious that none of these techniques has adequate spatial resolution to characterise the complex layered nano-crystalline structure of nitrogen implanted and plasma nitrided austenitic stainless steels. As discussed previously, the information from the hyperfine structure such as chemical state of atoms, can be very confusing if there are more than two phases present and there is no standard spectrum available. Therefore, the application of CEMS, XPS and RBS in surface characterisation of nitrogen implanted and plasma nitrided austenitic stainless steels provides limited information which is insufficient to fully describe the microstructure.

2.5.2 TEM Sample Preparation

The conflicting TEM results of the nitrogen implanted and nitrided austenitic stainless steels may also be a result of sample preparation. A number of papers [18,19,38,48,53,60,63] in Tables 2 and 3 reported using plan-view TEM to study the nitrogen ion implanted and nitrided austenitic stainless steel. The plan-view TEM was realised by thinning the sample only from the untreated side until the samples were thin enough for electron transparency. Therefore, the plan-view TEM showed only the outer-most surface of the treated sample. However, in most cases, the ion implanted or

nitrided surface layer was not homogeneous throughout the whole treated layer, so that the plan-view TEM can not give any information below approximately 2000Å (maximum thickness for electron transparency) of the outer most surface.

Table 5 Summary of surface characterisation techniques mentioned in Chapter 2

	XRD	GAXD	SAD	RBS	XPS	CEMS
Crystal Structure	Yes *Difficult for multi-phase system*	Yes *Difficult for multi-phase system*	Yes *Multi-phase system 'OK' but only for μm scale structures*	No	No	No
Hyper Fine Structure	No	No	No	location of the impurity atoms *Very difficult for multi-phase system*	Chemical State *Very difficult for multi-phase system* *uncertainty from inability to fix the binding energy zero*	Chemical State *Very difficult for multi-phase system*
Depth Resolution	~100 μm	Better than XRD	-	20-30 nm	0.5-3 nm	30 nm
Lateral Resolution (diameter)	~10 mm	~10 mm	~500 nm	~0.5 mm	~2 mm	~1 cm

Some researchers have tried using Ar^+ bombardment [26,33,39] or electrochemical thinning [37] to pre-thin TEM samples to a certain depth from the ion implanted side. Then, the sample is thinned from the untreated side to show the heterogeneity of the implanted layer. The problem is that it is very difficult to control the pre-thinning precisely, especially with the very thin implanted layer (usually less than a few μm totally). Besides, this technique can not give a continuous image of the

heterogeneity of the whole implanted layer, and may miss some very important information such as interface or transition zone, etc.

Some researchers tried using careful grinding at the treated side of the sample to different depths, then thinned from the untreated side to prepare the plan-view TEM sample [2,54,55,57]. To ensure an accurate pre-thinning thickness, the ground side had to be kept untouched at the thinning stages. It is well known that mechanical polishing will certainly introduce deformation on the surface. If the deformation is severe it could induce phase transformation. In fact, an extremely thin plastic deformation induced martensitic layer has been detected by some researchers [33,39] on the surface of austenitic stainless steel subjected to mechanical polishing. Therefore, it is very possible that the grinding will introduce artefacts into the TEM sample, resulting in wrong information on the nitrided surface layer. Besides the deformation problem, similar to the Ar^+ bombardment and the electrochemical pre-thinning, the accuracy of the pre-thinning by grinding is very difficult to control.

2.5.3 Temperature Effect on Ion Implantation

It is now generally accepted that the temperature of ion implantation plays a very important role in determining the surface microstructure for metals. Unfortunately, some of the early works shown in Table 2 [32,33,35,39,40] did not pay any attention to temperature monitoring at all. In these papers, no mention of the implantation temperature was made. It is perhaps not too surprising that the microstructure of the implantation modified surface reported in these early works is also the most confused one.

Even though for those papers in Table 2 which reported the implantation temperature, careful study shows that most of the researchers did not seriously consider the importance of the accuracy of monitoring and controlling the implantation temperature. Among all the papers which reported the implantation temperature, only two of them [50,51] mentioned how the temperature was monitored. In fact, only D.L.

Williamson et al [51] mentioned carefully monitoring the implantation temperature using a thermocouple attached within 1-2 mm of the surface being implanted. S. Aggarwal et al [50] mentioned using a thermocouple to monitor the temperature but did not disclose where the thermocouple was located.

Neglecting the implantation temperature by researchers can be further proved by the reported temperature error range of ±50°C [44,45,47] or ±25°C [13], showing very poor temperature monitoring. For papers where the ion implantation was carried out at room temperature [26,36,38,52] or ambient temperature [49], most papers reported using very small and thin samples for ion implantation (3 mm in diameter and 0.2 mm thick discs [26,38]; 10x10 mm^2 and 0.5 mm thick sheet [52]; 0.76 mm thick strip [49]). Under high energy ion bombardment, it is a real problem to keep the temperature of samples of such a small size constant, even if the sample is cooled by a water circulation device [38,52].

2.5.4 The Limited Information for Cr-Fe-Ni-N System

As it is mentioned in §1.4, for Fe-Cr-Ni-N alloy system, only Fe-N binary system has a generally accepted phase diagram. Interestingly, quite a lot of discussions on the surface microstructure of nitrogen implanted or nitrided austenitic stainless steels have been confined to the limited information mainly from the Fe-N binary system. It is obviously inadequate to refer complicated multi-phase systems to Fe-N binary diagram.

CHAPTER 3 EXPERIMENTAL

3.1 Material

A 25 mm diameter bar of AISI 316 stainless steel supplied by ASSAB Steel was used. Chemical analysis by spark emission spectroscopy indicated that the steel was within AISI specification for 316 grade (Table 6). Several discs approximately 3 mm in thickness were cut from the bar. One surface of each sample was abraded to a 600 grit finish, using standard metallographic techniques. Plasma nitrided samples were treated in the abraded condition. PI^3 samples were polished to a 1 μm diamond finish prior to treatment.

Table 6. Chemical composition of untreated AISI 316

C	Cr	Ni	Mo	Mn	Si	Ti	Cu	Other	Fe
0.043	16.40	10.56	2.34	1.18	0.48	0.012	0.24	0.27	Bal

3.2 Treatment Conditions

3.2.1 PI^3 Treatments

PI^3 treatment was conducted in the developmental system at Australia Nuclear Science and Technology Organisation (Ansto). The important parameters affecting the process, such as the target temperature, the time for which the target is at the temperature and the implanted nitrogen dose, were controlled during the treatment. The temperature was monitored continuously so that the input power can be adjusted. No auxiliary heating was used. The duty cycle of the high voltage pulses was used to control heating due to ion bombardment. The nitrogen dose was calculated from the total number of pulses, the pulse length and the average number of ions per pulse, which is calculated from the implantation current.

To begin the process, the rf power supply is turned on and the electron source filament is pulsed for several seconds to ignite the plasma. After several minutes of discharge cleaning, the high voltage (HV) pulses commence and the temperature is allowed to ramp to the desired value. When the required dose is achieved, the process controller turns off the HV and rf power. The nitrogen flow is adjusted to atmospheric pressure to cool the target more quickly.

To identify the effect of the temperature of the PI^3 treatment on microstructure of the modified layer, samples were treated at different temperatures with fixed ion dose. Since the samples were actually heated by the high voltage pulses during the implantation, to get high temperature, high frequency pulses had to be employed to achieve a high enough energy density to heat the sample up. Since the total ion dose increases linearly with the total pulses, in order to maintain a constant ion dose for samples treated at different temperatures, the treatment time has to be adjusted.

Table 7. PI^3 treated sample identification and treatment details

Sample ID	Voltage (keV)	Temperat. (°C)	Time (minute)	ion current (mA/cm^2)	Frequency (100 μs pulse) (Hz)	Nitrogen dose ($x10^{17}$ ions/cm^2)	Dose rate ($x10^{15}$ ions/cm^2·min)
PI150	40	150±5	430	3.1	4	2	0.47
PI250	40	250±5	250	3.2	27	8	3.2
PI350	40	350±5	130	3.3	47	8	6.2
PI450	40	450±10	70	2.7	122	8	11.4
PI520	40	520±30	45	2.9	156	8	17.8

The details of the treatment conditions are given in Table 7. It should be noted that the 150°C treatment of the first group received a reduced nitrogen dose of

$2x10^{17}$ions/cm^2 at the temperature, due to the low pulse frequency required to maintain this temperature. After treatment, the samples were allowed to cool in the PI^3 chamber.

3.2.2 Plasma Nitriding Treatments

Plasma nitriding was conducted using a 40 kW Klöckner Ionon unit. The treatment conditions and sample identification are listed in Table 8. The treatment temperatures of 350°C, 450°C and 520°C were selected. The temperature of nitriding was measured by a K-type Ni-Cr/Cr-Al thermocouple set in a small hole of the dummy sample. The error of the temperature measurement was estimated approximately ±15°C. After nitriding, the samples were cooled with nitrogen gas in the treatment chamber.

Table 8. Plasma nitrided sample identification and treatment details

Sample ID	Treatment Temperature (°C)	Time at Temperature (min.)	Atmosphere (vol%) # H_2	N_2
PN350	350±15	300	75	25
PN450	450±15	300	75	25
PN520	520±15	300	75	25

chamber pressure = 300 Pa, heating rate = 500°C/hour

3.3 Glancing Angle X-ray Diffraction

Conventional powder diffractometers are unsuitable for studying thin films because the depth of x-ray penetration usually exceeds the film thickness. By placing a sample at a glancing angle of typically less than 2°, the effective length of the beam in the surface is dramatically increased [86]. Consequently, the effective penetration depth of x-rays is reduced with decreasing glancing angles to the critical angle of total reflection (~0.4° in Fe [87]). As an example, it is reported that Cu $K\alpha$ radiation, with a glancing angle of 1°, has a maximum penetration of about 70 nm in pure iron [87]. However, the penetration depth is not uniform, but follows a probability type of relationship [88].

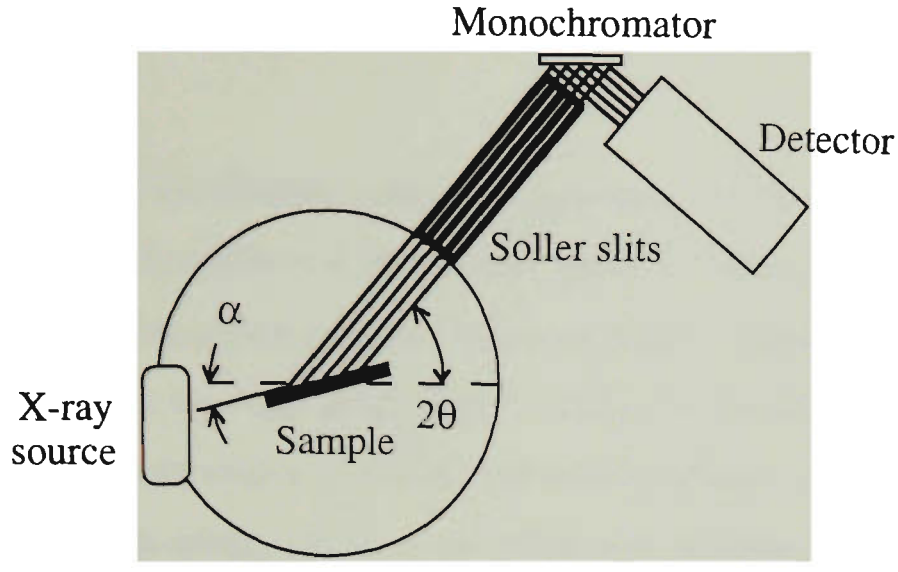

Figure 6. Schematic of the glancing angle attachment used for GAXD [86]

Glancing angle x-ray diffraction is achieved by fitting a glancing angle attachment to a conventional Bragg-Brentano parafocusing x-ray powder diffractometer, which converts it to a parallel beam non-focusing diffractometer [86]. This attachment consists of a series of long soller slits with their plates perpendicular to the diffraction plane, as shown in Figure 6. Thus, each set of plates define the same 2θ position. The large number of plates and their finite width cause significant intensity loss in the diffraction peaks. The width of the profile at full width half-maximum (FWHM) is given by [86]:

$$\text{FWHM} = \tan^{-1}(S/L)$$

where S is the separation of the soller slits, and L is the collimator length. Thus, increasing the length and/or decreasing the spacing of the soller slits causes the peaks to narrow, but reduces the peak intensity. The soller slit divergence used in this investigation was 0.1°.

The size of the 2θ-scanning step also limits the resolution of the results [88]. One of the main problems with the use of glancing-angle x-ray diffraction at very low angles of incidence (e.g., <1°) is that background noise intensity is of similar magnitude to the

diffracted x-rays. This necessitates slow 2θ scanning speeds, so that the total testing time can be quite long (up to several days), in order to improve the signal to noise intensity ratio.

Broadening of the diffraction peaks tends to occur at large Bragg angles because the diffracted x-rays do not focus at the receiving slit [85]. Additionally, the effective length of the beam in the surface is reduced with increasing 2θ. Therefore, the detection of diffraction peaks at very high Bragg angles is difficult. The diffraction peaks can broaden if the film on the sample is very thin and polycrystalline, and this effect cannot be avoided. False peak splitting can also occur at high glancing angles, particularly when a low divergent slit is used [86]. This anomaly is identified by matching the spacing of the split peaks with the divergent angle.

A Siemens D500 θ-2θ diffractometer was used for glancing angle x-ray diffraction (GAXD). The incident radiation was Co K_α (λ = 178.9 pm), and a range of incidence angles α between 0.5° and 10° was used to evaluate the distribution of phases with depth. Bragg angles (2θ) of between 30° and 130° were examined with a 2θ scan step of 0.1° and a dwell time of 6.5 s between each step. Errors in peak location were determined from the full width at half maximum (FWHM).

3.4 Cross-sectional Transmission Electron Microscopy

3.4.1 Sample preparation

3.4.1.1 Disc Preparation

The method used for the disc preparation is given in Figure 7, and it is essentially a simplification of the approach taken by Alani *et al* [89]. The PI^3 treated AISI 316 stainless steel, with the modified surface carefully protected, was sectioned into slabs of 2 mm wide and 1 mm thick. These slabs were subsequently sandwiched using G-1 epoxy from Gatan, with the treated surfaces facing each other. G-1 epoxy was recommended by Gatan for this purpose based on its claimed high temperature stability.

The specimen sandwich was then cast into a brass tube of 3 mm outer diameter, using E-SOLDER 3021 silver epoxy supplied by ACME Division of the Allied Products Corporation.

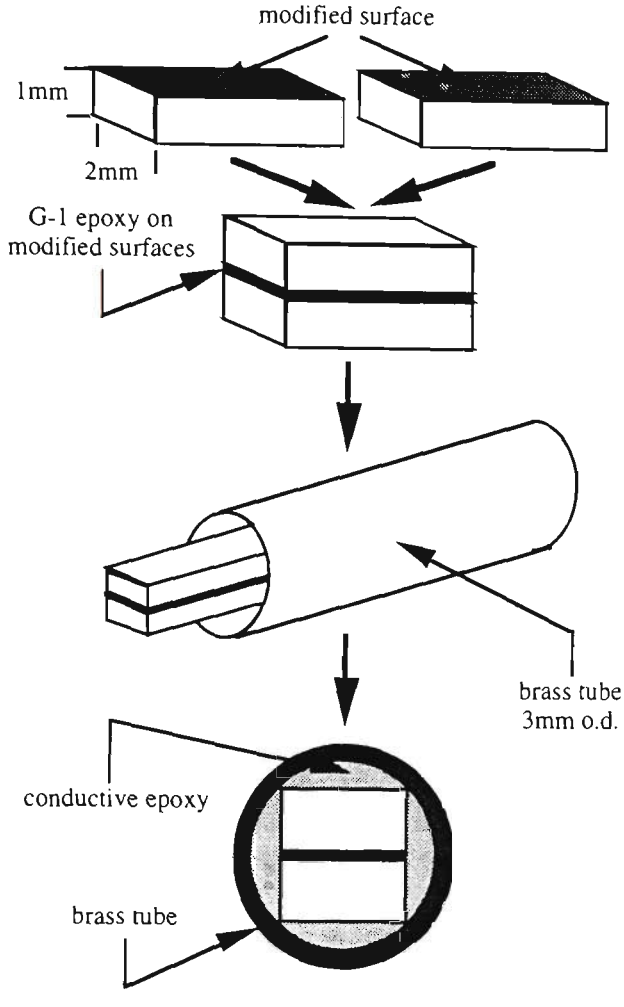

Figure 7. Schematic description of the main steps in preparing a TEM cross-sectional sample

Discs of 400-500 μm thickness were sectioned from the tube assembly using a LECO VC-50 thin section slitting wheel. The discs were subsequently ground on both sides with 600 SiC paper to less than 100 μm. The direction of cutting and grinding was perpendicular to the epoxy-bonded joint to minimise loss of the epoxy.

3.4.1.2 Pre-ion Beam Thinning

The pre-ion beam thinning technique involved the use of a TENUPOL-2 jet polisher. The sample was ground to a thickness of 100 μm prior to jet polishing. Jet polishing was carried out at 30 V, 200 mA with a 5% perchloric acid and 95% acetic

acid solution. The solution temperature was kept at 5-10°C during polishing. Polishing was stopped when perforation of the sample had just occurred. The perforation typically appeared at the place slightly away from the epoxy-line of the sample. The profile of the polished sample is shown in Figure 8.

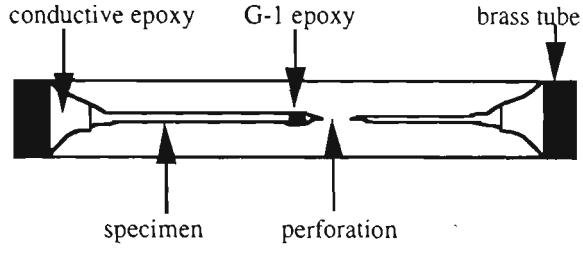

Figure 8. Profile of XTEM sample after jet polishing

3.4.1.3 Ion Beam Thinning

Ion-beam thinning was conducted on a multi-function EDWARDS IBT Auto Model 306 Coater. High purity argon was used for the ion source. The voltage for ion beam thinning was 5 kV and the gun current was about 0.5 mA/per gun. A nickel mask was used to shield the ion beam so that thinning occurred from a direction approximately normal to the interface, as shown in Figure 9. The main function of the mask was to protect the modified layer and to get a uniformly thinned area.

The thinning of the sample was first conducted with the ion-beam inclined at an angle of 15° to the plane of the disc. The small hole on the sample produced by jet polishing would slowly enlarge during ion-beam bombardment. When the hole approached the epoxy line, the angle was decreased to 10° and thinning continued until the hole reached the epoxy line. This area of the modified layer was sufficiently thin for TEM examination. The thinning was continued for a further 1 hour with the incident angle of the ion-beam reduced to 8-9°, and the mask removed. This had the effect of removing ditches caused by masked ion-beam thinning, and also removed most of the

epoxy at the interface near the edge of the hole. The total ion beam thinning process took about 20 to 30 hours.

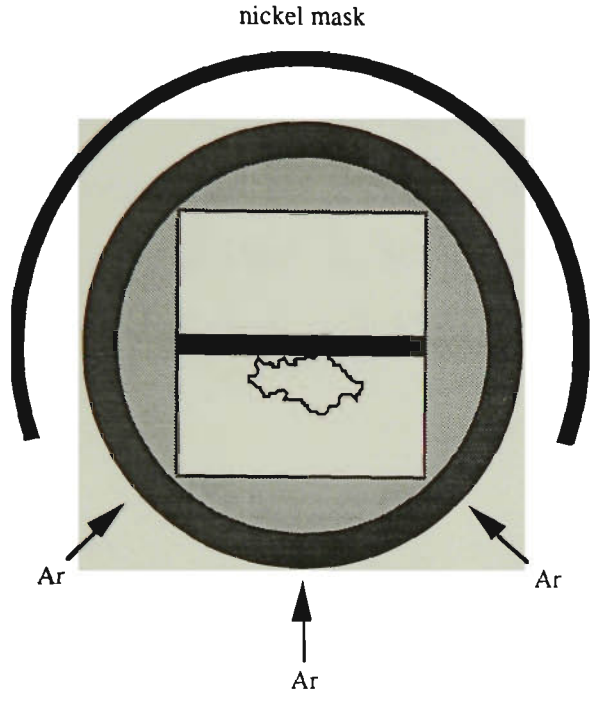

Figure 9 Ion-beam thinning with nickel mask

3.4.2 Transmission Electron Microscopy (TEM)

A Jeol-2000FX microscope operated at 200 kV was used for the characterisation of all PI^3 treated and plasma nitrided cross-sectional samples.

3.4.2.1 SAD and NBD

The ray diagrams for selected area diffraction (SAD) and nano-beam diffraction (NBD) are given in Figure 10.

The selected area diffraction (SAD) is realised by inserting a field limiting aperture in the image plane of the objective lens (Figure 10a.). Suppose the selected area is between A' and B', tracing the rays back to the specimen plane shows that the diffraction pattern obtained is only from the area between A and B of the specimen. However, the

diffracted beams pass through the lower objective lens inclined at an angle 2θ (2θ = Bragg angle) from the optic axis and are subject to spherical aberration because of electrons passing through the outer portion of a lens being focused more strongly than those electrons passing closer to the optic axis. Therefore, the diffracted beam that would be focused on a flat focal plane by a perfect lens is brought to focus on a spherical surface. The practical result of this phenomenon is that the image formed by the main beam and the diffracted beam do not coincide in the image plane and this lack of coincidence increases as 2θ increases. Thus, the diffraction spots in the SAD pattern are not formed from the same area of the specimen as the main beam. The extent of the error is described by the equation

$$x = C_s(2\theta)^3$$

where x is the distance on the image between the centres of the origin of the main beam and the diffracted beam, C_s is a constant. An additional error, resulting from defocussing the objective lens from the optimum value, increases x by an amount $2D\theta$, where D is the amount of defocus. In practice, this error is less serious than that from spherical aberration. Because of these errors, the regions forming the main and diffracted beams do not even overlap if the diameter of the selected area at the specimen plane is less than 500 nm. Thus, SAD is not suitable for analysing area smaller than 500 nm in diameter.

The ray diagram of nano-beam electron diffraction (NBD) is given in Figure 10b. The smallest condenser aperture (20 μm) is used to get the smallest convergence angle of the beam. The two condenser lenses and the upper objective lens act as a triple condenser system to produce a highly convergent probe that illuminates only a small portion of the sample. The diffraction pattern itself is formed in the same objective focal plane as SAD . Since the diffraction pattern can arise from the illuminated area alone, the spherical aberration effect resulting from a field limiting aperture that selects only a portion of the illuminated area does not interfere, and the minimum diameter that can be examined is limited only by the spot size of the probe and scattering effects dependent on sample thickness. In the present study, the measured probe size for NBD is less than 10 nm. To

minimise the exposure time to get good quality negatives, and to minimise the electron beam damage on sample, the 15 cm camera length (for tungsten filament) or 28 cm camera length (for LaB_6 filament) was selected for photographing NBD patterns.

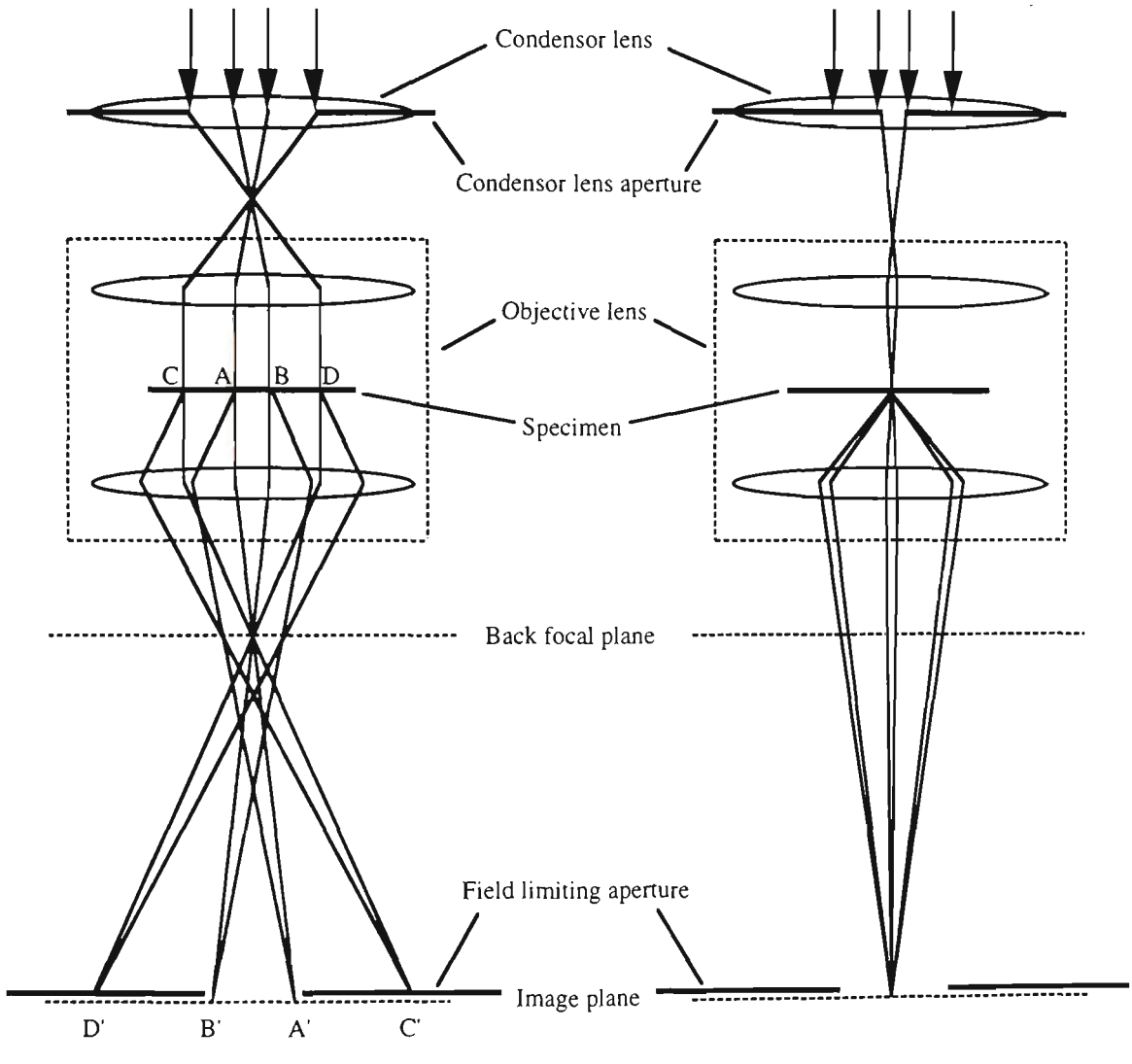

a. SAD ray diagram b. NBD ray diagram

Figure 10. Ray diagrams of SAD and NBD techniques

3.4.2.2 High resolution electron microscopy (HREM)

Generally, TEM images are formed by using either the undeviated beam alone (bright-field image) or a single diffracted beam alone (dark-field image). However, if two or more than two coherent beams (e.g. the undeviated beam and one or more diffracted beams) reach the image, the image intensity shows a periodic variation, with a

periodicity equal to the spacing between the planes of atoms or molecules giving rise to the diffracted beam. The fringes of this periodic array are perpendicular to the corresponding reciprocal lattice vector, so that geometrically the fringes represent the projection of these planes of atoms or molecules on the image plane. The technique using coherent beams to get lattice image is called high resolution electron microscopy (HREM).

It should be pointed out that the positions and visibility of the fringes depends upon the thickness and exact orientation of the specimen. (a) With thickness variation of the crystal, the position of the fringes shifts laterally. The shift is one fringe spacing for each change in specimen thickness of one effective extinction distance. Thus the fringes do not necessarily coincide with the projection of the lattice planes. (b) The spacing of the fringes decreases slightly as the crystal is rotated off the exact Bragg setting. The spacing therefore decreases away from the centre of an extinction contour.

3.4.2.3 Indexing of diffraction patterns

A diffraction simulation and analysis software package for the Macintosh computer, written by Schlienger et al, was used to assist indexing diffraction patterns. By inputting the lattice parameter of crystals and diffraction conditions into computer, the diffraction patterns can be exactly simulated. The simulation of overlapped patterns is also very helpful in checking the indexed orientation relationship between the phases, since at some zone axes, there is only a single overlapped pattern that can be obtained for a specific orientation relationship.

CHAPTER 4 RESULTS

4.1 Glancing Angle X-ray Diffraction (GAXD)

Selected glancing angle X-ray diffraction patterns for PI^3 treated and plasma nitrided samples are shown in Figures 11 and 12, respectively. For all of the traces, only γ peaks can be unequivocally identified, while all other peaks are either too difficult to match accurately to any specific phases, or too complicated to index. Except for the PI^3520 sample, peaks shifted to lower 2θ compared to the austenite peaks in all other spectra, especially for 350-450°C treated samples. Similar shifts of the peaks have been reported by other researchers on nitrogen implanted or nitrided austenitic stainless steels, which is attributed to nitrogen "expanded austenite γ_{exp}" [18,43,46,50,60]. The details of these patterns are described in the text below.

4.1.1 PI^3 Treated Samples

Both PI^3150 and PI^3250 have very strong austenite peaks in their diffraction patterns at a glancing angle of α=1°. PI^3250 shows some evidence of $\gamma(111)$ peak broadening and a shoulder at 2θ (50°). No α peaks were present on the 150°C or 250°C diffraction traces.

PI^3350 has the same number of distinct "expanded austenite" peaks (Figure 11c). The diffraction pattern for PI^3450 is dominated by "expanded austenite" peaks. The peaks correspondent to austenite are not observed except a small $\gamma(111)$ peaks. The PI^3520 diffraction trace is dominated by CrN and α peaks. One of the peaks which roughly matches $\gamma'(111)$ indicates that γ' might exist in modified layer. Traces of austenite are also detected for PI^3520 at glancing angle α=5°.

4.1.2 Plasma Nitrided Samples

PN350 shows clear "expanded austenite" peaks, but with smaller 2θ-shift than PI^3350. The unshifted austenite peaks are also quite strong at α=5°, indicating that the

nitrided layer is shallow so that the austenite substrate contributes to the diffraction.

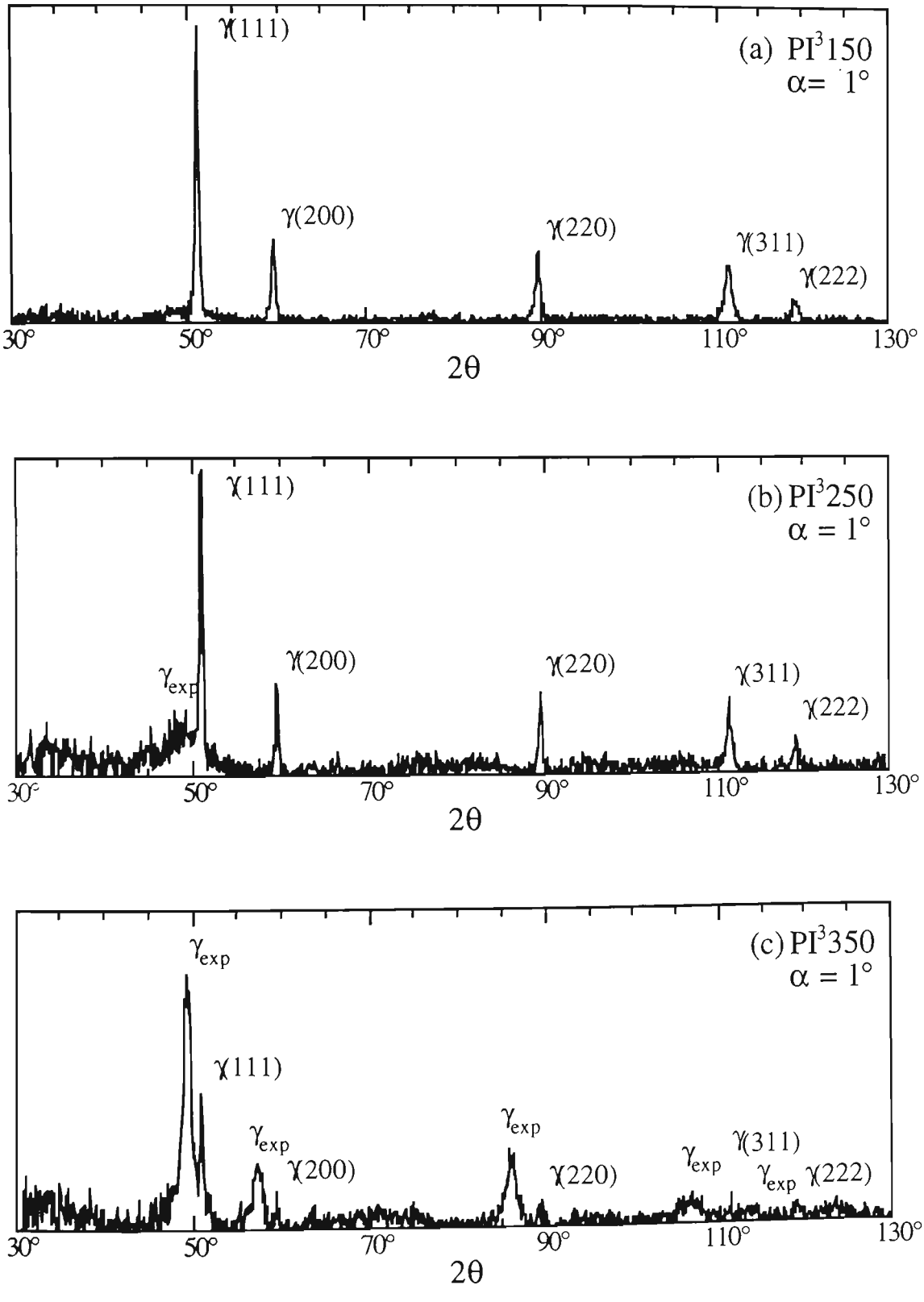

Figure 11 Glancing angle x-ray diffraction traces for PI^3 samples treated at (a) $PI^3$150; (b) $PI^3$250; (c) $PI^3$350;

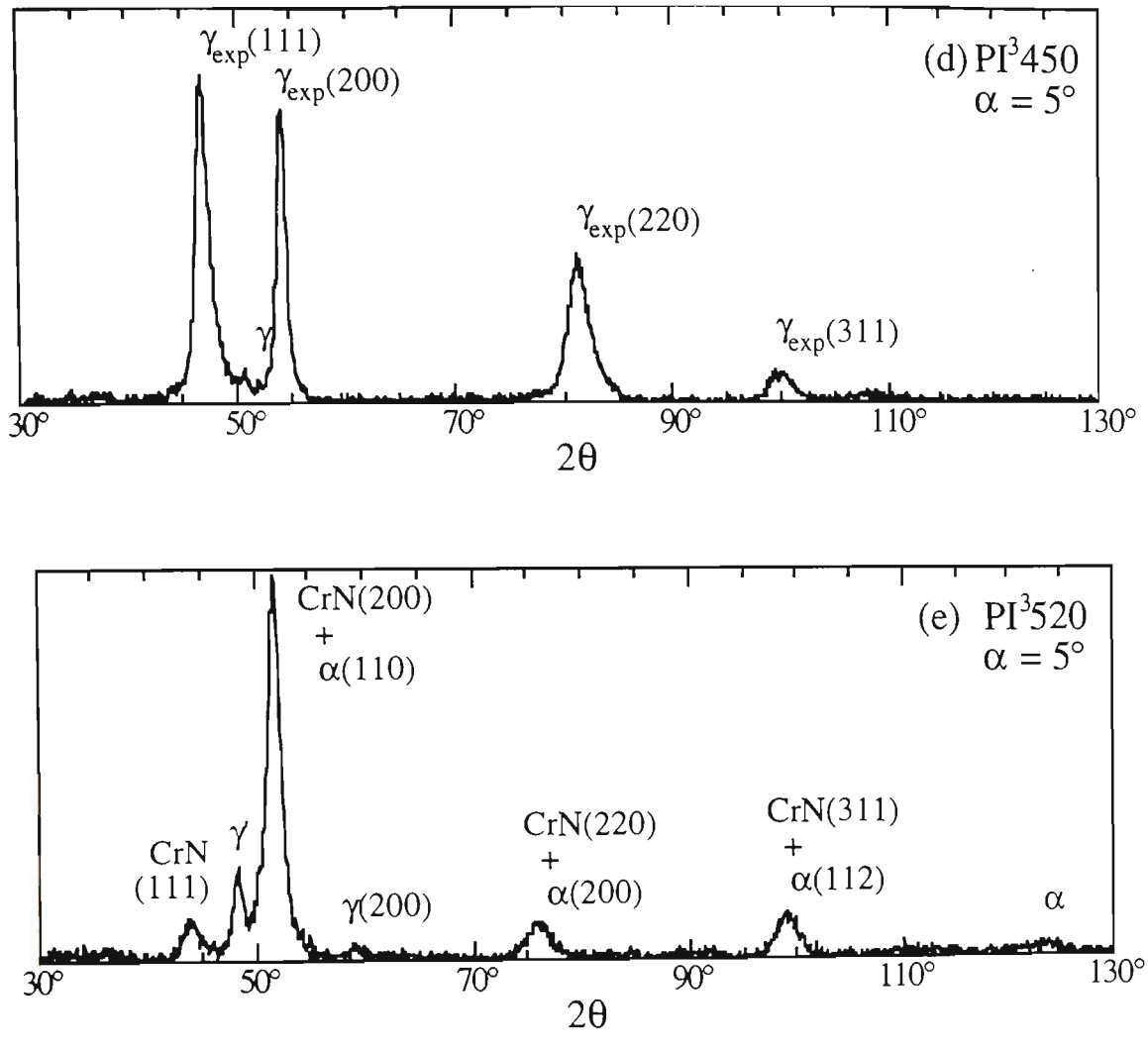

Figure 11(cont.) Glancing angle x-ray diffraction traces for PI^3 samples treated at (d) PI^{3}450; and (e) PI^{3}520

γ_{exp}: expanded austenite

Accurate interpretation of the diffraction patterns for the PN450 is very complicated due to the peak overlaps. However, "expanded austenite", CrN, α and γ' can be roughly identified, though some other phases, such as ε-nitride, Cr_2N, ζ-nitride may also fit in the overlapped peaks. "Expanded austenite" is most evident for α=5°, rather than 1°, indicating that it was distributed some depth below the surface. The 2θ location of the "expanded austenite" peaks is similar to those experienced for PN350. Peaks corresponding to CrN and α-ferrite were present at all glancing angles. There was also a peak at 53.6°, which did not match any documented phases.

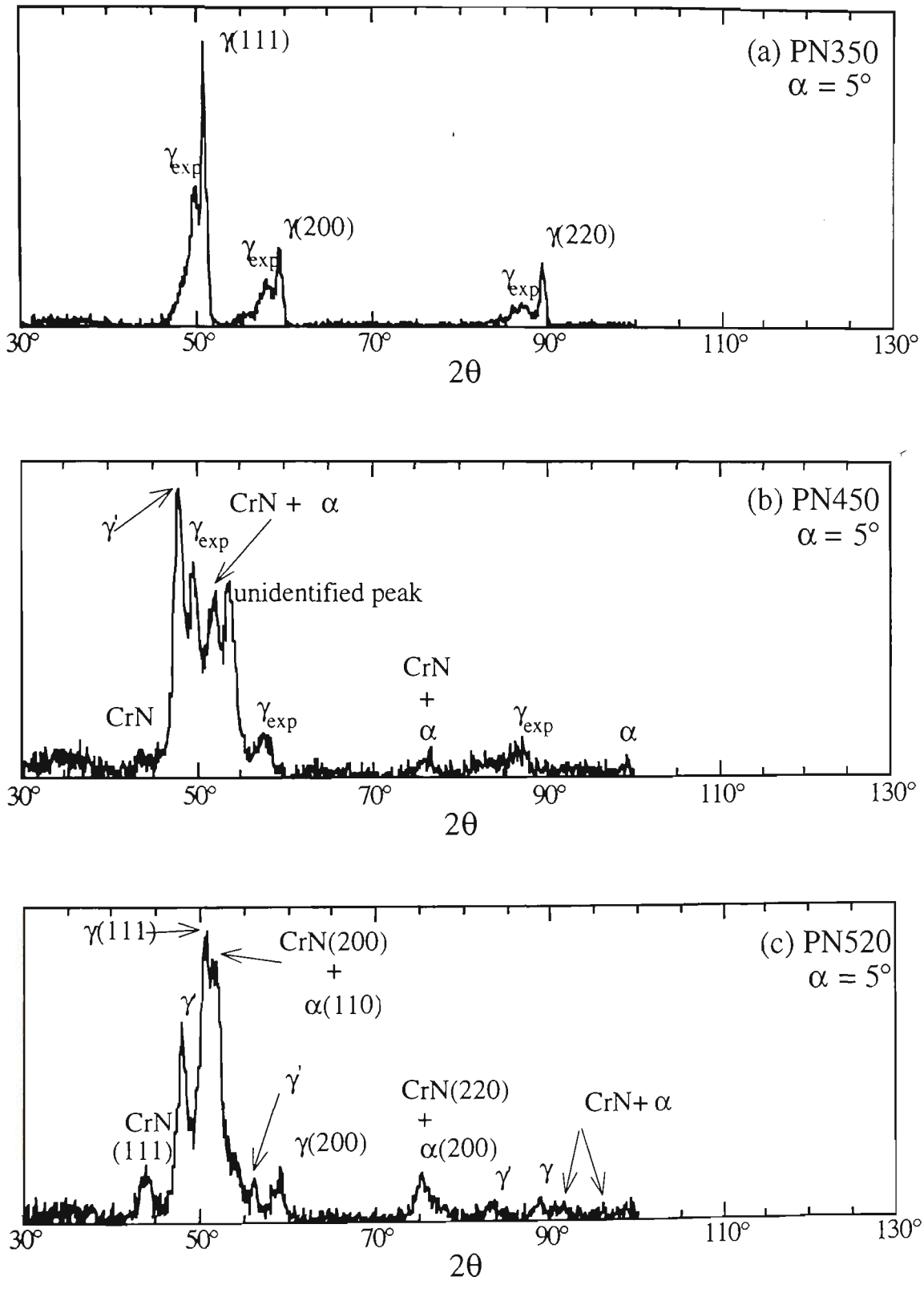

Figure 12 Glancing angle x-ray diffraction traces for plasma nitrided samples, treated at (a) 350°C; (b) 450°C; (c) 520°C

Similar to PN450, PN520 also shows quite complicated peaks. The possible phases are γ', γ, CrN and α.

4.2 XTEM Characterisation

The characterisation of nitrogen implanted and plasma nitrided samples by using XTEM and NBD shows very different results to the GAXD. Besides the nanocrystalline structure, a thick amorphous layer, which has never been reported before, was observed in the PI^3 treated and plasma nitrided samples up to 450°C. In the following sections the micrographs and diffraction patterns obtained by XTEM and NBD techniques are presented.

4.2.1 Definition of Amorphous Structure

Before proceeding further, it is neccessary to clarify the terminology used in this section to describe different microstructures. The detailed structure of amorphous phases is a topic which has been debated for some time. However, short range and middle range order in amorphous metals has been widely reported in recent years [90, 96-101]. Ke proposed that the size of the ordered cluster determines the degree of amorphisation [90], that is, smaller clusters correspond to a higher degree of amorphisation. Since the extent of amorphisation is a relative concept, in this thesis, the amorphous structure is defined by NBD patterns. A microstructrue which shows only diffuse ring NBD patterns, or mainly ring patterns with a few dim spots is defined as amorphous. If the ring pattern is mixed with clear diffraction spots, the pattern corresponds to the semi-amorphous structure. NBD patterns without, or with only dim rings correspond to a crystalline structure.

4.2.2 TEM Characterisation of the As-received 316 Stainless Steel

A TEM micrograph of the as recieved 316 stainless steel is shown in Figure 13. This specimen was prepared using a standard electopolishing technique. The microstructure of the untreated 316 stainless steel shows the common features of austenitic stainless steels after solution annealing, i.e. single austenite grain with low dislocation density and some stacking faults.

To ensure that preparation techniques did not introduce any artefact into the structure, a cross-sectional sample of the as-received 316 stainless steel was also prepared and studied by TEM (Figure 14). The microstructure shown in Figure 14 shows a slightly higher dislocation density than that of Figure 13. A very thin (≈ 50nm) deformed layer can be seen at the top surface, presumably caused by mechanical grinding.

4.2.3 XTEM Characterisation of the PI^3 Treated Samples

4.2.3.1 PI^3 treated at 150°C

The implantation modified layer is amorphous and approximately 0.9-1 μm thick (Figure 15). A very sharp interface is observed between the modified layer and the substrate (Figure 16). Closer examination of the implantation modified layer (Figure 17) reveals that the amorphous structure is actually clustered. The cluster size is about 4-6 nm. Figures 18a and 18b show the corresponding SAD and NBD patterns of the amorphous layer.

The substrate under the implantation modified layer is so stressed that a heavily stressed zone is formed, which is up to 4 μm in thickness. NBD patterns taken from the heavily stressed zone show that it is composed of α-ferrite, ε-martensite and γ. Though there is no quantitative information about these three phases, NBD results show that ε-martensite is most likely detected at the low stress area away from the interface, and γ and α are dominant phases at the near interface area. The observed orientation relationships between the γ and α phases are consistent with Nishyama-Wassermann (N-W) and Kurdjumov-Sachs (K-S) relationships (Figures 19 and 20). The detected orientation relationship between the γ and ε-martensite is $(2\bar{2}0)\gamma//(\bar{1}01\bar{2})\varepsilon$-martensite, $[001]\gamma//[10\bar{1}0]\varepsilon$-martensite (Figure 21). The {111} twin is also observed in the γ phase in the heavily stressed zone (Figure 22).

4.2.3.2 PI^3 treated at 250 °C

The total thickness of the implantation modified layer at 250°C is about 4.5 μm, and is composed of 3 sublayers (Figure 23).

The top nanocrystalline sublayer I is about 0.9 μm thick, composed mainly of CrN and α-ferrite precipitates, with traces of ε-nitride (Figure 24). The precipitates are grouped in colonies smaller than 20 nm in size. The NBD pattern of the nanocrystalline sublayer I shows that both N-W and Bain relationships exist between CrN and α precipitates (Figure 25). The NBD failed to pick up ε-nitride, indicating that the volume of ε-nitride may be too small to be detected by NBD.

The second sublayer is semi-amorphous and about 2 μm thick, showing stripe-like modulation with a strip spacing between 4-6 nm dotted with some tiny CrN and α crystals (Figure 26). The corresponding NBD pattern clearly reveals the semi-amorphous nature of the microstructure judging by spots which are super-imposed on a diffuse ring pattern.

The third sublayer is amorphous, and about 1.5 μm thick (Figure 27). The amorphous structure shows a mottled appearance with sharper contrast which is similar to clustered structure of the 150°C implanted sample. The size of the clusters is about 4-7 nm. The truly amorphous character of the microstructure is ascertained from both the mottled contrast in the BF image and the absence of any diffraction spots in the diffuse ring pattern of NBD. The HREM (high resolution electron microscopy) image of the amorphous sublayer III shows that short-range order exists in the amorphous structure (Figure 28).

Close to the sublayer III/substrate interface (i.e. within 100 nm of it), the contrast of the cluster gradually fades and the structure is seen to be reverting to the semi-amorphous state (Figure 29). The NBD pattern (Figure 30) taken in this thin semi-amorphous region shows that tiny (Cr,Fe)N (identified by superlattice spots) and α

crystals exist in this area. Among the diffraction spots, [111] (Cr,Fe)N spots are readily discernible.

A sharp interface is observed between the third sublayer and the γ substrate, as is shown in Figure 31. There is a stress affected zone about 250 nm thick in the substrate, located just below the interface (Figure 31b). Although the dislocation density was similar to the unstressed substrate, the NBD pattern taken from the stress affected zone shows slightly expanded γ and α precipitates. The N-W relationship is observed between the slightly expanded γ and α (Figure 32).

Cr_2N precipitates are also detected by NBD at the interface together with slightly expanded γ (Figure 33). The orientation relationship between the Cr_2N and γ was determined to be: $(011)\gamma//(\bar{3}211)Cr_2N$, $[100]\gamma//[12\bar{3}2]Cr_2N$.

The HREM image of the interface (Figure 34) shows that some of the crystalline structure of the γ substrate crosses over the interface into the sublayer III for a short distance before it disappears into the amorphous state.

4.2.3.3 PI^3 treatment at 350 °C

The total thickness of the modified layer in the specimen PI^3 treated at 350°C is about 2.3 μm (Figure 35). Similar to the sample treated at 250°C, a three sublayer structure is found in this sample. The first sublayer is nanocrystalline about 0.9-1 μm thick. However, in this instance, the second sublayer is amorphous, about 0.9 μm thick. Following sublayer II is a 0.5-0.6 μm thick semi-amorphous sublayer III.

Figures 36a and b show the details of the nanocrystalline sublayer I. The tiny precipitates are grouped in colonies less than 20 nm in size. The colonies may appear as stripes or clusters in TEM image according to the orientation of the parent austenite grains. Figure 37 shows the HREM image of the nanocrystalline sublayer I.

The SAD pattern of the nanocrystalline sublayer I (Figure 38) shows that besides CrN and α precipitates, traces of ε-$Fe_{2-3}N$ also exist in nanocrystalline sublayer I. NBD

patterns of the sublayer I (Figures 39a and b) show that the orientation relationship between CrN and α phases obeys both the Bain and N-W relationships. Similar to the PI[3]250°C sample, the amount of ε-$Fe_{2-3}N$ in the nanocrystalline sublayer is too little to be detected by NBD.

Figure 36 also shows the gradual transition from the nano-crystalline sublayer to the amorphous sublayer II. The amorphous structure shows clusters of 4-7 nm in size, though the contrast of the clusters is not as sharp as that in the 250°C treated sample. The HREM image of the amorphous sublayer II is given in Figure 40, showing a short range order structure in the clusters. The NBD pattern of the amorphous sublayer II is shown in Figure 41.

Figure 42 shows the details of the third semi-amorphous sublayer and the interface between this sublayer and the substrate. Some dark spots of less than 10 nm in size are observed in the third sublayer. NBD results reveal these dark spots are tiny (Cr,Fe)N, α and small amount of Cr_2N crystals (Figures 43-44). These crystals start to form at the interface, and gradually disappear into amorphous towards the amorphous sublayer (notice that the [001]α and the $[\bar{1}\bar{1}1]$(Cr,Fe)N diffraction shown in Figure 43 is still visible in Figure 44 even though with different intensity or orientation). The γ substrate shows about 3% volume expansion at the interface, measured by comparing two NBD patterns of the same zone axis, one is taken at the interface and another is taken at the original γ substrate under exactly the same diffraction conditions. The expansion of the γ substrate decreases to zero only 30-50 nm away from the interface. γ'-Fe_4N may also exist at the interface as a transition phase (Figure 44). The HREM image of the third sublayer is given in Figure 45.

Towards the substrate (within 100 nm of the interface), the contrast of the clusters in the third semi-amorphous sublayer gradually fades. A sharp interface is observed between the modified layer and the substrate. The NBD pattern of the substrate

below the interface (Figure 46) does not show any difference from that of normal untreated austenite. The HREM image of the interface (Figure 47) shows clearly the evolution of the semi-amorphous structure from the substrate. In contrast to the sample treated at 250°C, there is no observable stress effected zone in the substrate below the interface. The lack of stress effected zone may come from less nitrogen concentration in the semi-amorphous sublayer, comparing to the amorphous sublayer above the interface of the sample treated at 250°C.

The series of NBD patterns (Figures 43-44) taken at the interface and the sublayer III show clearly how the crystalline austenite substrate is expanded, distorted and gradually collapsed into the amorphous structure. At the interface, the γ austenite is expanded about 3%, and Cr_2N (may be γ' as well), (Cr,Fe)N and α phase start to precipitate (Figure 44), together with the collapse of the parent γ into semiamorphous structure. From interface to amorphous sublayer II, the nitrogen concentration gradually increases, and the semiamorphous structure with tiny unstable (Cr,Fe)N, Cr_2N and α-ferrite gradually transforms to an amorphous structure.

Another important fact revealed by this series of NBD patterns for sublayer III is that the diffraction of some of the precipitates in Figures 43-44, such as $[001]\alpha$ and $[\bar{1}\bar{1}1]$(Cr,Fe)N, is kept almost unchanged. This is a further proof that the amorphous structure is evolved from the same parent austenite grain.

It should be noted that the thickness of the 350°C implantation modified layer is lower than the 250°C implantation modified layer probably because of the shorter treatment time. This result indicates that the thickness of the implantation modified layer is actually controlled by the diffusion of nitrogen, and shorter treatment times may result in thinner implantation modified layers, even at a higher treatment temperature. Another possibility of the lower thickness of the 350°C treated layer is that the thickness is not uniform with the XTEM micrographs taken from a very small area which may just happened to be located at the thinnest area.

4.2.3.4 PI^3 treatment at 450 °C

The sample PI^3treated at 450°C shows a 3 μm thick modified layer, which has a sharp interface with the γ substrate (Figure 48). Details of the modified layer is given in Figure 49a, showing an amorphous structure with a cluster size of 4-7 nm. The NBD pattern of the amorphous layer is given in Figure 49b.

Towards the interface, the contrast of the cluster structure gradually fades, as is shown in Figure 50. The NBD pattern (Figure 51) taken at the near interface area (about 100 nm away from the interface) of the amorphous layer shows semiamorphous features which contains some very tiny (Cr,Fe)N and α crystals. Figure 52 shows the SAD pattern taken at the interface, which exhibits an overlapped (Cr,Fe)N ring pattern, and expanded γ and α spots. By comparing diffraction pattern of the interface to the diffraction pattern of the untreated γ substrate (both were taken at the exactly same diffraction condition), the expanded γ shows about 3% expansion. The Bain relationship is observed between the γ and α phases.

The substrate immediately below the modified layer shows a very high dislocation density. The thickness of this high dislocation zone is about 1.5-2μm. The expansion of γ decreases from 3% at the interface to zero at the end of the high dislocation zone. Figure 53 shows the interface between the high dislocation zone and the normal γ austenite. The NBD pattern of the normal γ austenite under the high dislocation zone is shown in Figure 54. Comparing the NBD pattern in Figure 54 to the SAD pattern in Figure 52, it can be seen that the high dislocation zone has the same orientation as the unexpanded γ austenite below it.

4.2.3.5 PI^3 treated at 520 °C

The sample treated at 520°C comprises two sublayers, a 0.4-0.5 μm thick sublayer I and a 7.5-8.5 μm thick sublayer II. The total thickness of the modified layer

is thus about 8-9 μm (Figure 55). Although the time of treatment is the shortest, the thickness of the modified layer for $PI^3$520°C sample is the deepest amongst the PI^3 treated samples.

The first sublayer is nano-crystalline, characterised by very fine randomly dispersed precipitates ranging from a few nm to about 50 nm (Figure 56a). The NBD pattern shows that the first sublayer comprises mainly CrN and α phases, together with a small amount of ε nitride, Cr_2N and $CrMoN_x$ (Figure 56b).

Sublayer II is made up from colonies displaying a lamellar structure (Figure 57), which is formed by a cellular precipitation so that it possesses a pearlite-type appearance. With the aid of NBD, the phases present are identified to be CrN and α. Both Bain and N-W relationships are observed between CrN and α phases (Figures 58 and 59).

At the near surface region of sublayer II, a small amount of ε nitride phase is observed between the CrN and α colonies, having the appearance of small islands (Figure 60). The NBD pattern of one of these ε nitride islands is given in Figure 61.

Unlike all other samples, the modified layer of the 520°C treated sample does not show a flat interface with the substrate (Figure 62a). The rugged interface shows that the growth of the modified layer into the substrate is actually achieved by means of the growth of the individual pearlite-like CrN and α colonies into the γ substrate. A few tiny Cr_2N and $CrMoN_x$ crystals, of about 10-20 nm in size, are found to exist at the node area between the CrN and α colonies near the interface (Figures 62b and 62c).

The NBD pattern taken at the substrate just away from the interface shows [001]γ diffraction and faint {220}CrN ring patterns (Figure 63). This result indicates that the CrN may precipitate from the γ substrate prior to the precipitation of the α phase. The very weak {100}fcc superlattice shows that γ', as a transition phase between the γ and the CrN, may exist at the interface as well.

4.2.4 XTEM Characterisation of the Plasma Nitrided Samples

4.2.4.1 Plasma nitrided at 350°C

The nitrided layer is nanocrystalline, about 6 μm thick (Figure 64). Figure 65a shows a typical nanocrystalline structure which keeps the same through the whole nitrided layer. The size of precipitates is generally less than 30 nm. Due to the very fine size, and the complicated composition of the nitrided layer, a SAD pattern taken from this layer gives very little information about the microstructure of the nitrided layer (Figure 65b).

However, the study of the nitrided layer by NBD shows that the nitrided layer is composed mainly of very fine γ and Cr_2N precipitates, together with some α precipitates.

Figure 66 shows one of the Cr_2N precipitates (the dark area in the centre of the image shown in Figure 66a) and the corresponding NBD pattern (Figure 66b). The superlattice spots shown in the NBD pattern indicate that the Fe atoms may take some of the positions of the Cr atoms to form $(Cr,Fe)_2N$.

The orientation relationship between the Cr_2N and γ is revealed by NBD as: $(001)\gamma//(\bar{3}211)Cr_2N$, $[100]\gamma//[12\bar{3}2]Cr_2N$ (Figure 67). The NBD study of the nanocrystalline nitrided layer also reaveals that the N-W relationship exists between the γ and α (Figure 68). Figure 68 also shows a twin structure in γ precipitate.

Traces of CrN precipitates were detected at the near surface area of the nitrided layer, as is shown in Figure 69. The K-S relationship is observed between the α and CrN precipitates.

A 70-80 nm thick transition zone, similar in appearance to the nanocrystalline nitrided layer, is observed between the nitrided layer and the substrate (Figure 70). The NBD patterns taken from this transition zone failed to show any structural difference from the nitrided layer.

The first layer of γ grains under the nitrided layer shows a higher dislocation density than unaffected γ grains beneath this (Figure 71). The detail of the grain boundaries between the high dislocation density γ grains and the underneath normal γ grains is shown in Figure 72. At the nitrided layer/substrate interface, the γ shows about a 5-6% expansion but this quickly decreases to about 3% within a few tens of nanometres from interface, and then gradually decreases to zero at the grain boundary, between the first layer of γ grains and the underneath normal γ grains.

Some α phase and ε-martensite are detected in the high dislocation γ at the near interface area (Figures 73 and 74). The NBD pattern in Figure 74 shows the N-W relationship between the γ and α phases.

4.2.4.2 Plasma nitrided at 450°C

The entire 450°C nitrided layer is about 10-11 μm thick, divided into two sublayers. The first sublayer is nano-crystalline and about 10 μm thick. The size of the precipitates gradually decreases from about 10 nm at the surface of the nitrided layer to 2-3 nm at the near substrate area. The second sublayer is amorphous, about 0.6-0.7 μm thick. Figure 75 gives the cross-sectional TEM image of the whole implanted layer.

Figure 76a shows the details of the nanocrystalline sublayer I. The SAD pattern of the sublayer I is given in Figure 76b. It is obvious that the SAD is not powerful enough to discern the very tiny precipitates in the first nanocrystalline sublayer.

The NBD study of the nanocrystalline sublayer I reveals that the precipitates in sublayer I comprise very fine γ, CrN and α phases (Figure 77). A twin structure is observed in the γ precipitates (Figure 77a). Both N-W and Bain relationships are observed between the CrN and α precipitates (Figure 77b). It should be noticed that the proportion of the γ precipitates is slightly decreased in the near surface area, compare to the proportion of the γ precipitates in the near amorphous sublayer II area.

Although the low magnification image (Figure 75) shows that there is a sharp interface between the nanocrystalline sublayer I and the amorphous sublayer II, a higher magnification image (Figure 78) shows that a gradual transition occurs from the nanocrystalline sublayer I to the amorphous sublayer II. Figure 79 gives the NBD pattern of the amorphous sublayer II.

Figure 80 shows the HREM image of the interface between amorphous sublayer II and the substrate. The amorphous structure gradually changes to semi-amorphous towards the interface. Sublayer II has a quite sharp interface with the substrate. It is obvious from the HREM image that the amorphous sublayer II originates from the substrate, since some of the crystalline structure of the substrate crosses over the interface into the amorphous sublayer II.

The α phase is detected by NBD in γ substrate in the area just away from the interface (Figure 81). The superlattice spots in Figure 81 also suggest that γ'-Fe_4N, as a transition phase, may also exist at the interface area. By comparing the NBD pattern in Figure 81 to the NBD pattern of the untreated austenite, it can be infered that the γ phase in the near interface area expanded by about 3%. However, the expanded γ does not extend very far into the substrate, since the SAD pattern (the size of the selected area for diffraction is about 500 nm in diameter) taken from the substrate a short distance from the interface shows only normal unexpanded γ (Figure 82).

4.2.4.3 Plasma nitrided at 520°C

The thickness of the nitrided layer at 520°C is about 40 μm. The pearlite-like CrN and α lamellar precipitates, similar to that in the 520°C PI^3 treated sample, are the dominant phases throughout the nitrided layer. Figure 83 shows the typical structure of this nitrided layer.

NBD study of the precipitates show that a Bain relationship exists in most of the CrN and α lamellar precipitates (Figure 84). However, the N-W relationship is also observed between the CrN and α (Figure 85).

Small amounts of islands-like residual γ are observed at the node area between the CrN and α lamellar colonies (dark island-like area at the middle of Figure 83, the size is about 30-50 nm). The NBD pattern taken at the γ islands shows overlapped γ, CrN and α diffractions (Figure 86). The γ phase has the same orientation as that of CrN. The N-W relationship is observed between the fcc phases (γ and CrN) and bcc α.

Traces of ε-nitride are detected and it is co-existing with γ in the γ islands at the near surface area. Figure 87a shows one such γ+ε island near the surface. The corresponding NBD pattern of the γ+ε island is given in Figure 87b.

Similar to the 520°C implantation modified sample, a sharp and rugged interface is observed between the nitrided layer and the substrate (Figure 88a). However, no hexagonal phases such as Cr_2N and $CrMoN_x$ are observed to exist between the CrN and α colonies in the near interaface area of the modified layer. The NBD pattern taken at the interface shows overlapped γ, CrN and α diffraction (Figure 88b). The superlattice spots indicate that a small amount of γ', as a transition phase between the γ and CrN, may exist at the interface. No γ expansion is detected by NBD.

4.2.5 Summary of the XTEM and NBD Characterisation of PI^3 Treated and Plasma Nitrided 316 Stainless Steel

From the previous results, it is shown that XTEM plus NBD are very powerful techniques for characterisation of thin layers with very fine and complex structures like PI^3 treated and plasma nitrided 316 stainless steels. However, because of such an abundance of information, it is not easy to draw a clear picture of the surface microstructure. To make the picture clearer, it is helpful to summarise the information obtained. Figures 89 and 90 give schematic descriptions of the surface layers from all PI^3 treated and plasma nitrided 316 stainless steel samples, based on XTEM and NBD characterisation.

It should be noted that the γ'-Fe_4N is not included in the schematic description in Figures 89 and 90, although γ'-Fe_4N is detected at the interface of some nitrogen

implanted and plasma nitrided samples. In fact, the existence of fcc γ'-Fe_4N is normally judged by the presence of superlattice spots and measured lattice parameters from NBD patterns. However, (Cr,Fe)N and expanded γ at the interface, both with fcc structure, also give superlattice spots as γ'-Fe_4N does. Besides, the lattice parameters of both (Cr,Fe)N and expanded γ are quite close to those of γ'-Fe_4N. Considering both (Cr,Fe)N and expanded γ have distorted lattices and the possible error from the NBD pattern measurements, whether γ'-Fe_4N really exists at the interface is still not clear. Even if the γ'-Fe_4N does occur at the interface, it exists only as an unstable transition phase at the interface since it has never been detected in any layer or sublayer.

Fig.13 TEM BF micrograph of the as-received 316 stainless steel, prepared by electropolishing, showing γ austenite with low dislocation density and some stacking faults.

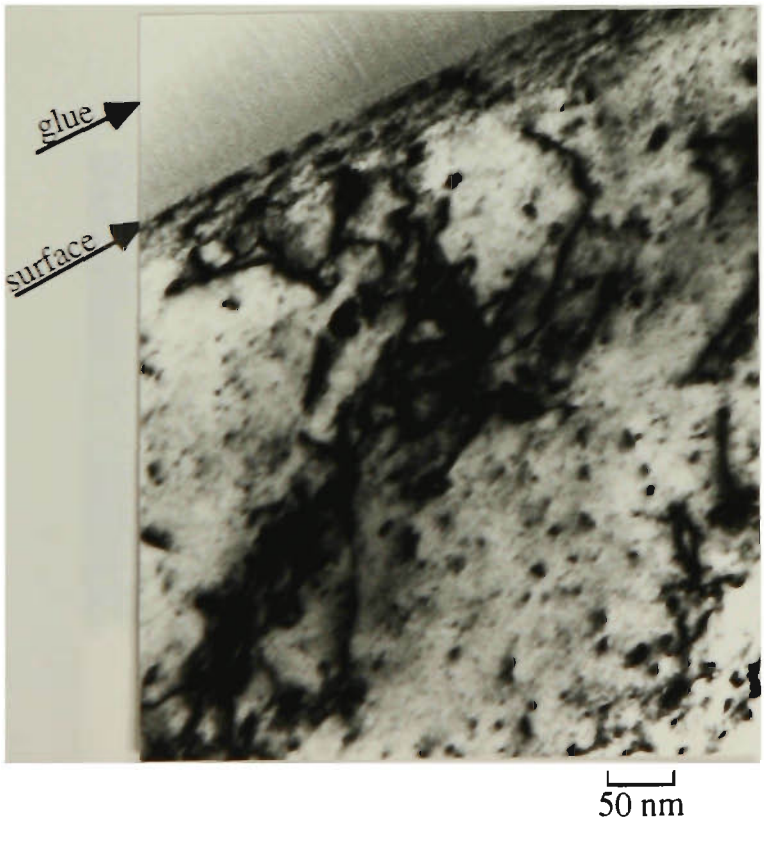

Fig.14 Cross-sectional TEM micrograph of the as-received 316 stainless steel. An approximately 50 nm thick deformed layer can be seen at the top surface.

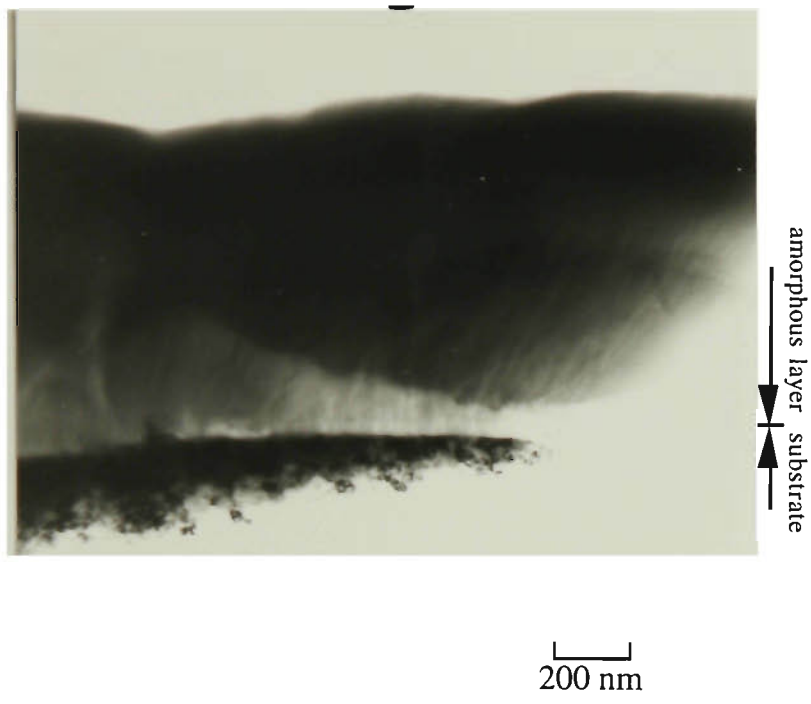

Fig.15 TEM micrograph of the sample PI^3 treated at 150 °C. The implantation modified layer is amorphous, about 0.9-1 μm thick. There is a heavily stressed zone up to 4 μm thick in the substrate (below the interface) which comprises γ-austenite, α-ferite and ε-martensite.

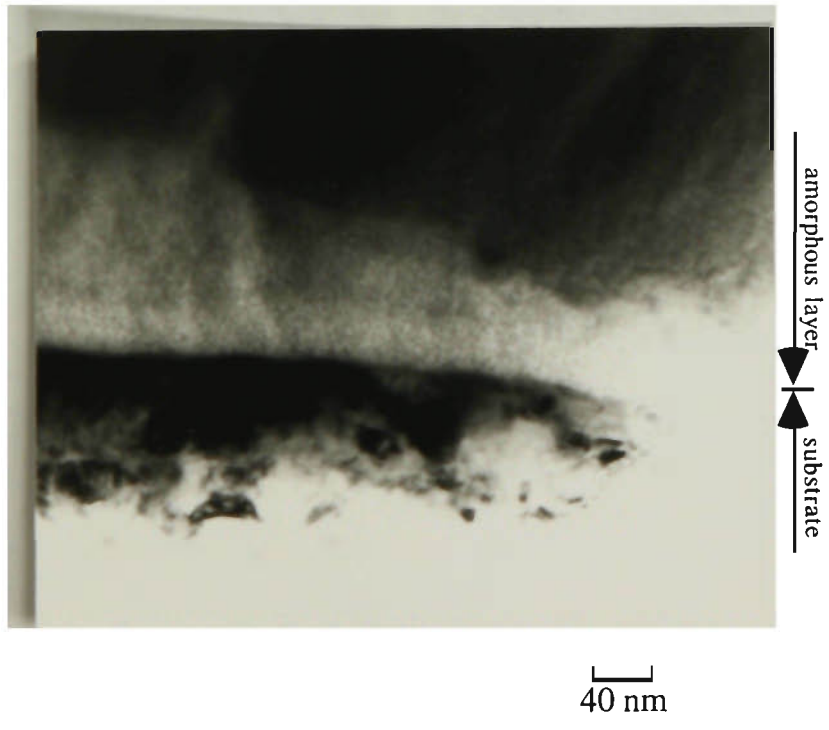

Fig.16 The interface between the amorphous layer and the heavily stressed substrate. PI^3 treated at 150 °C, $2x10^{17}$ ions/cm^2, 430 minutes.

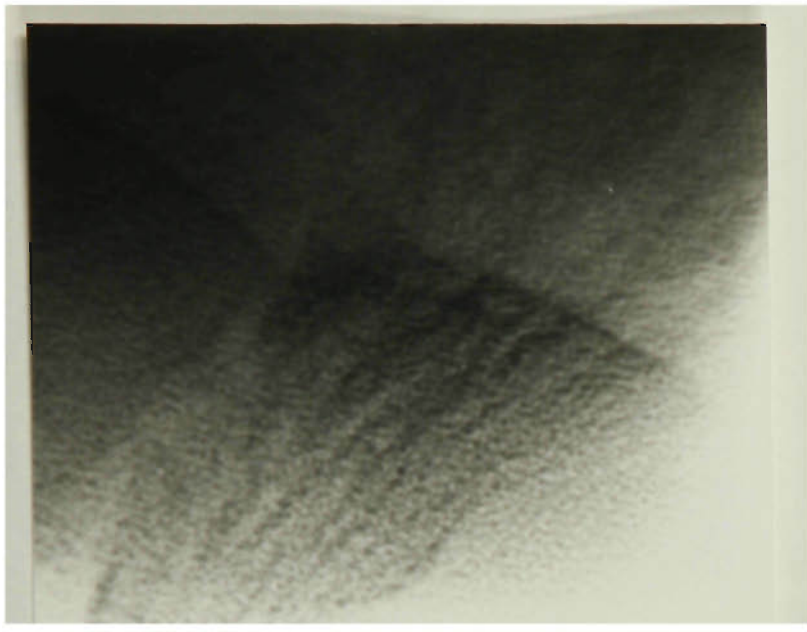

Fig.17 Details of the amorphous layer showing clustered structure. The size of the clusters is about 4-6 nm.

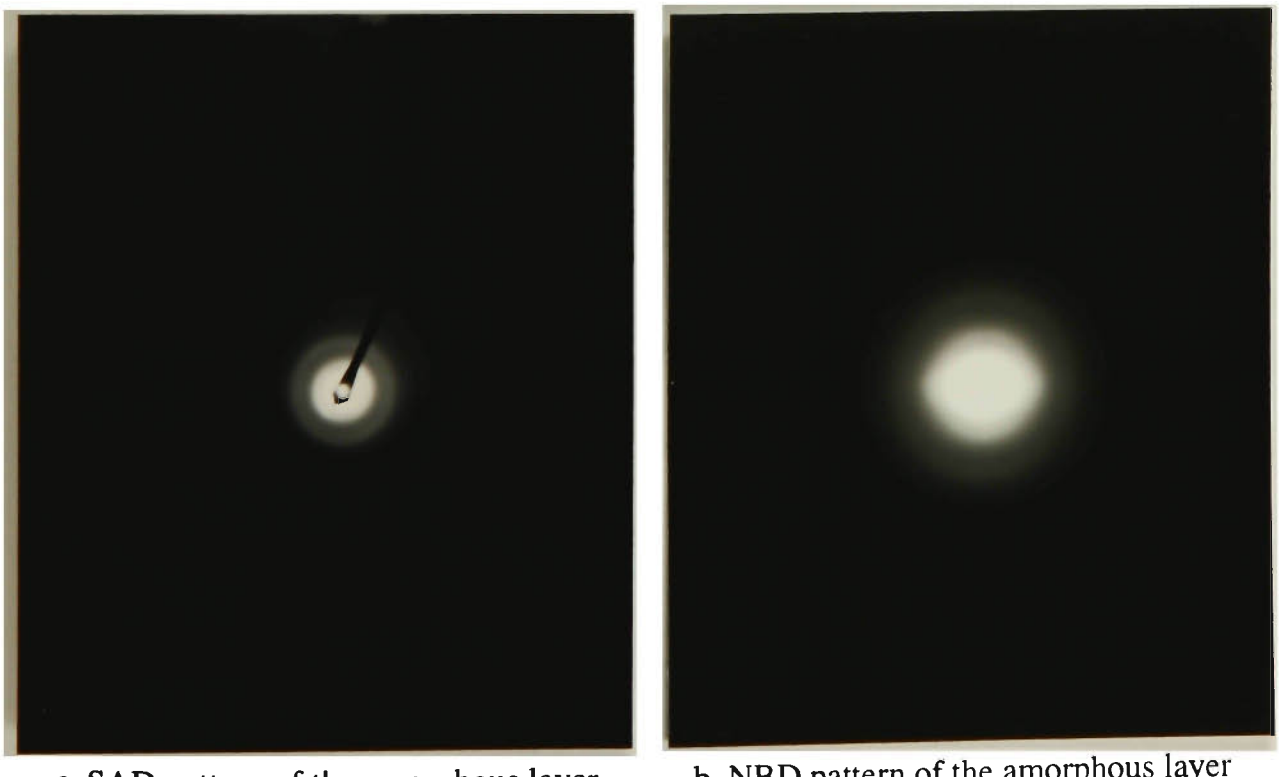

a. SAD pattern of the amorphous layer b. NBD pattern of the amorphous layer

Fig.18 SAD and NBD patterns of the amorphous layer shown in Figure 14.

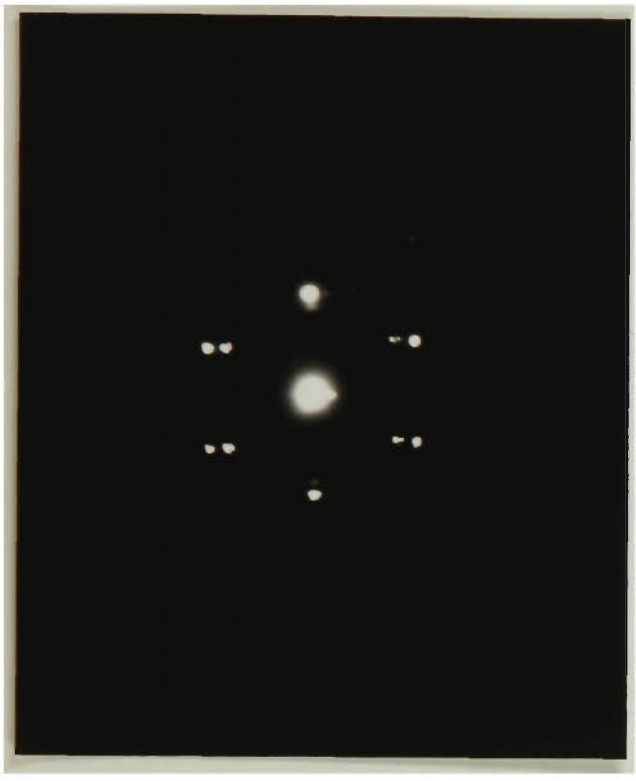

Fig.19 NBD pattern of the heavily stressed substrate, showing N-W relation between [411]γ and α, plus [111]γ. PI[3] treated at 150 °C.

Fig.20 NBD pattern of the heavily stressed substrate, [10$\bar{1}$]γ with α, K-S relation. PI[3] treated at 150 °C.

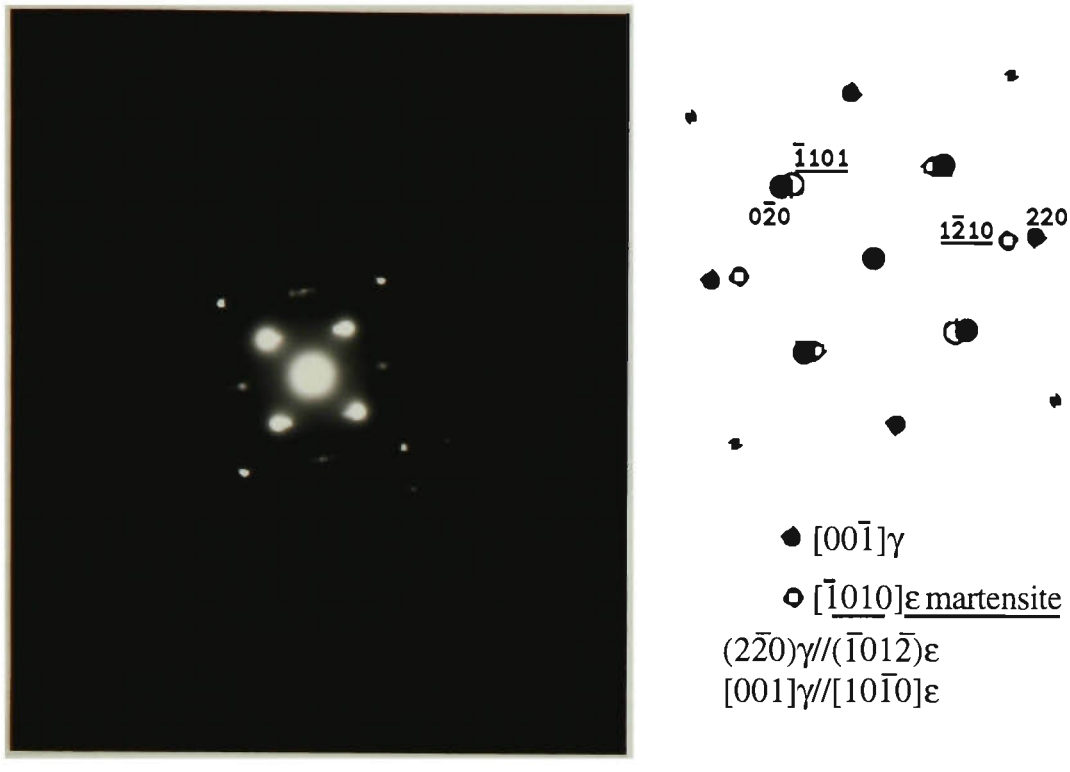

Fig.21 NBD pattern of the heavily stressed substrate, $[00\bar{1}]\gamma$ with ε-martensite. PI[3] treated at 150 °C.

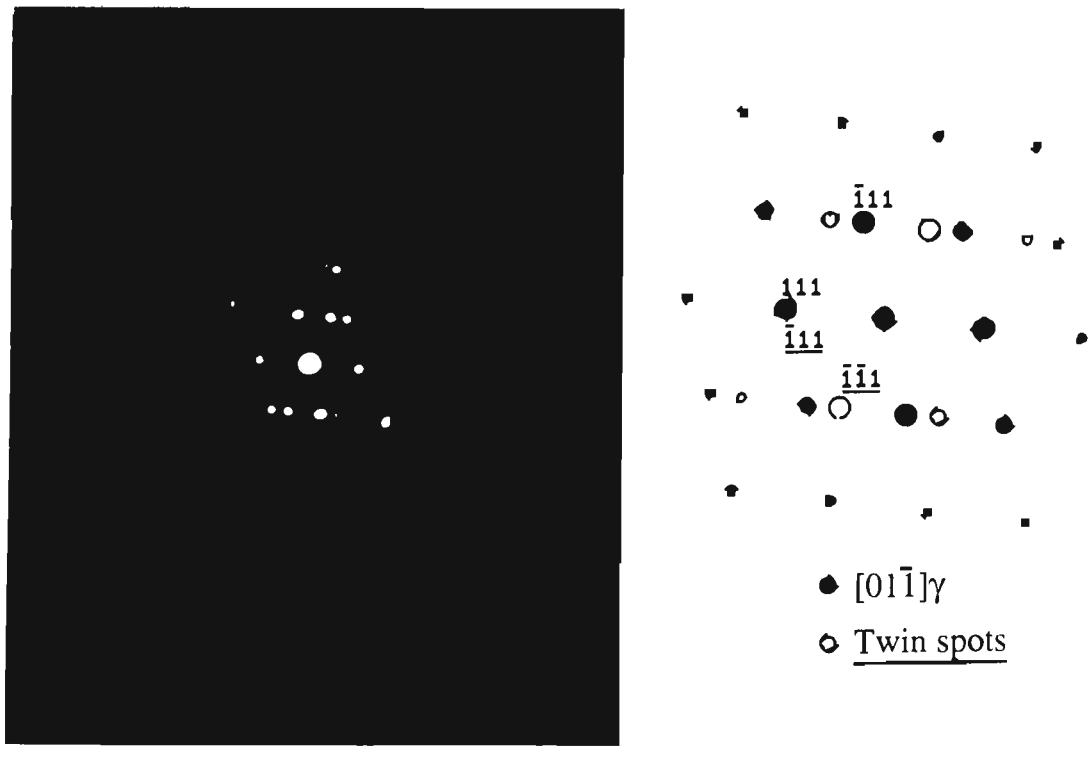

Fig.22 NBD pattern of the twin structure in heavily stressed substrate, $[01\bar{1}]\gamma$, <012> twin. PI[3] treated at 150 °C.

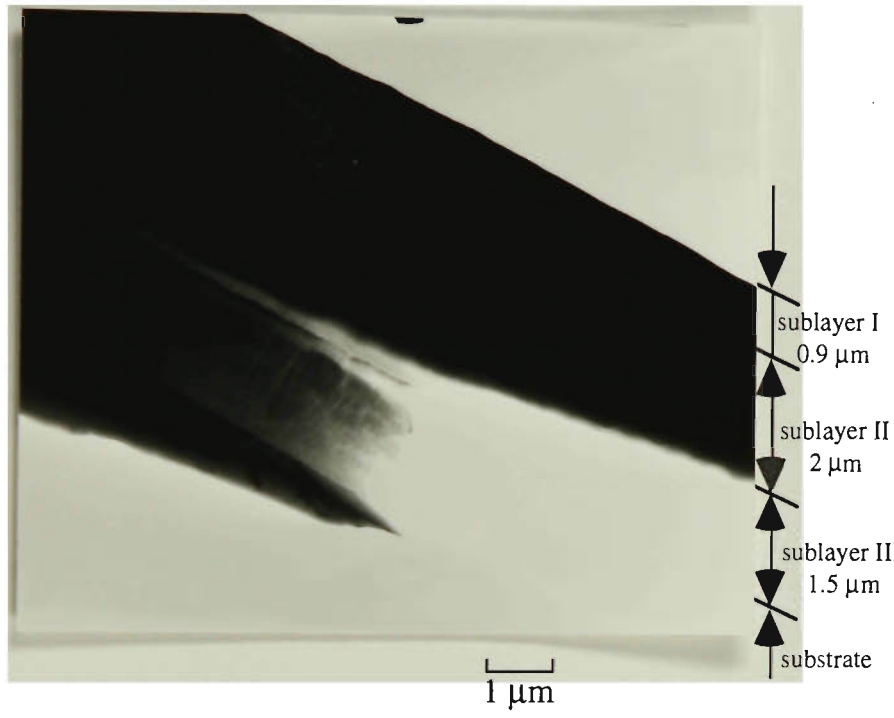

Fig.23 TEM micrograph of the specimen PI[3] treated at 250°C. The total thickness of the modified layer is about 4.5 μm, divided into 3 sublayers. The first nano-crystalline sublayer is about 0.9 μm thick, composed mainly of CrN and α-ferrite, with traces of ε-nitride. The second semi-amorphous sublayer is about 2 μm thick dotted with some very tiny CrN and α precipitates. The third sublayer is amorphous, about 1.5 μm thick. Close to the interface (about 100 nm), the amorphous beomes semi-amorphous again. Very fine (Cr,Fe)N and α crystals are detected in this thin semi-amorphous transition region. Small amount of Cr_2N(Cr,Fe)$_2$N (or (Cr,Fe)$_2$N) precipitates are found at the interface, with austenite substrate.

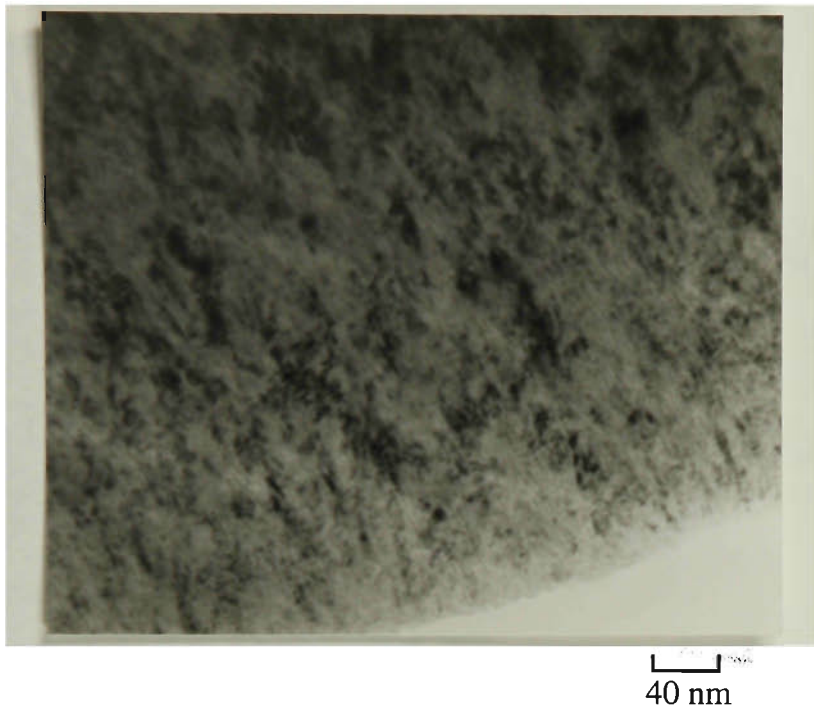

a. Nanocryastalline structure of sublayer I, consisting of tiny CrN and α precipitates grouped in extremely small colonies less than 20 nm in size.

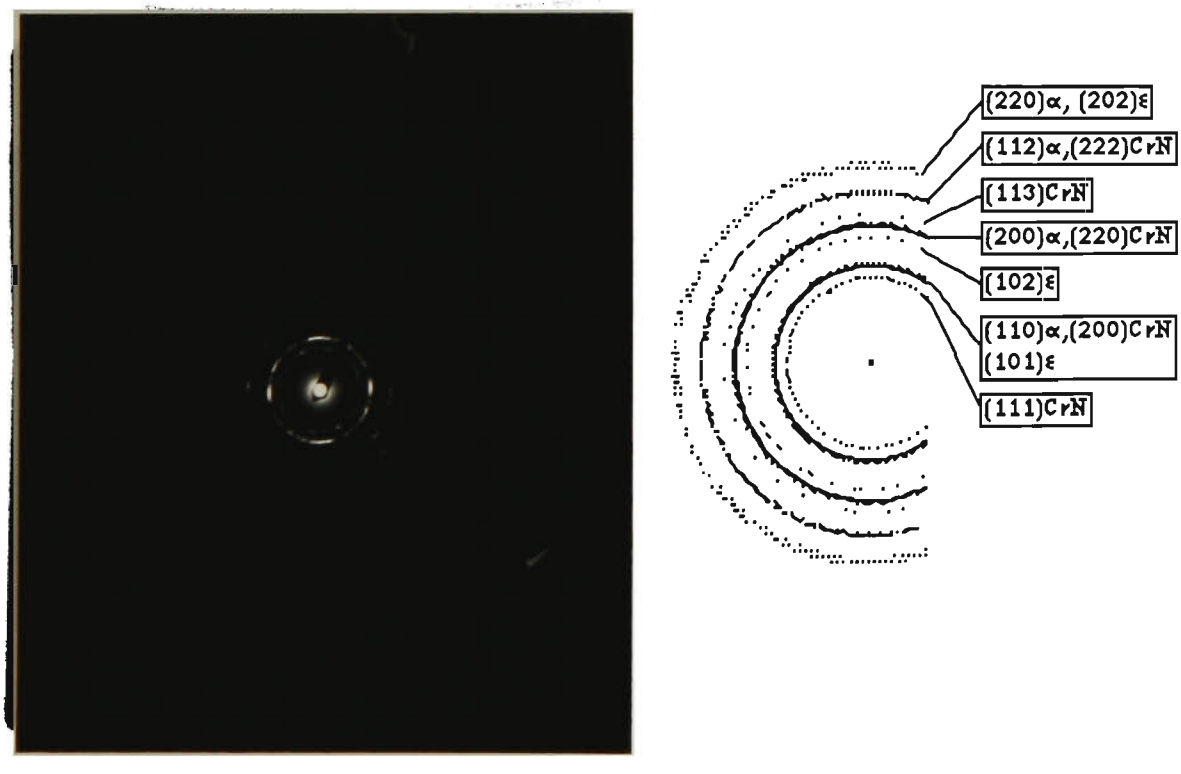

b. SAD pattern of the nano-crystalline sublayer I, showing diffraction rings attributed to CrN, α and traces of ε-nitride.

Fig.24 Details of the nanocrystalline sublayer I and correponding SAD pattern. PI[3] treated at 250°C.

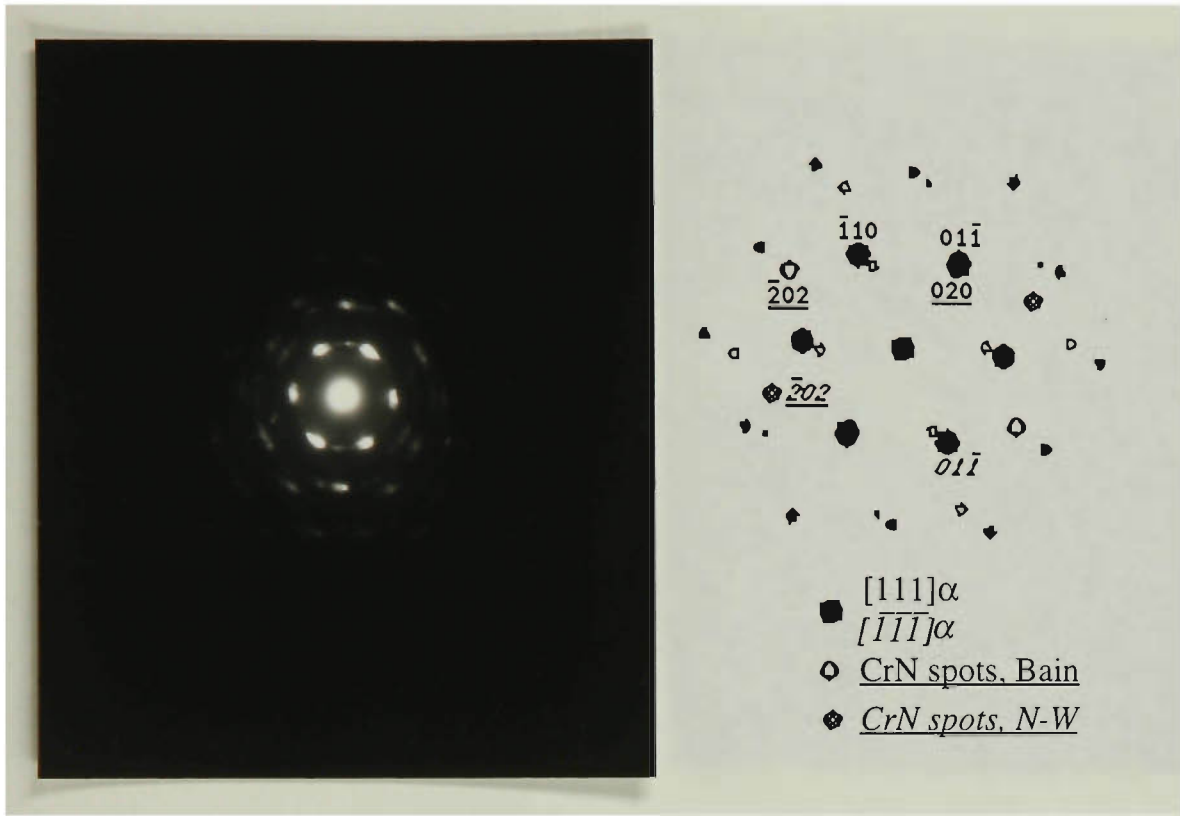

Fig.25 NBD pattern of the nanocrystalline sublayer I. Both Bain and N-W relation are observed between CrN and α precipitates. PI^3 treated at 250°C.

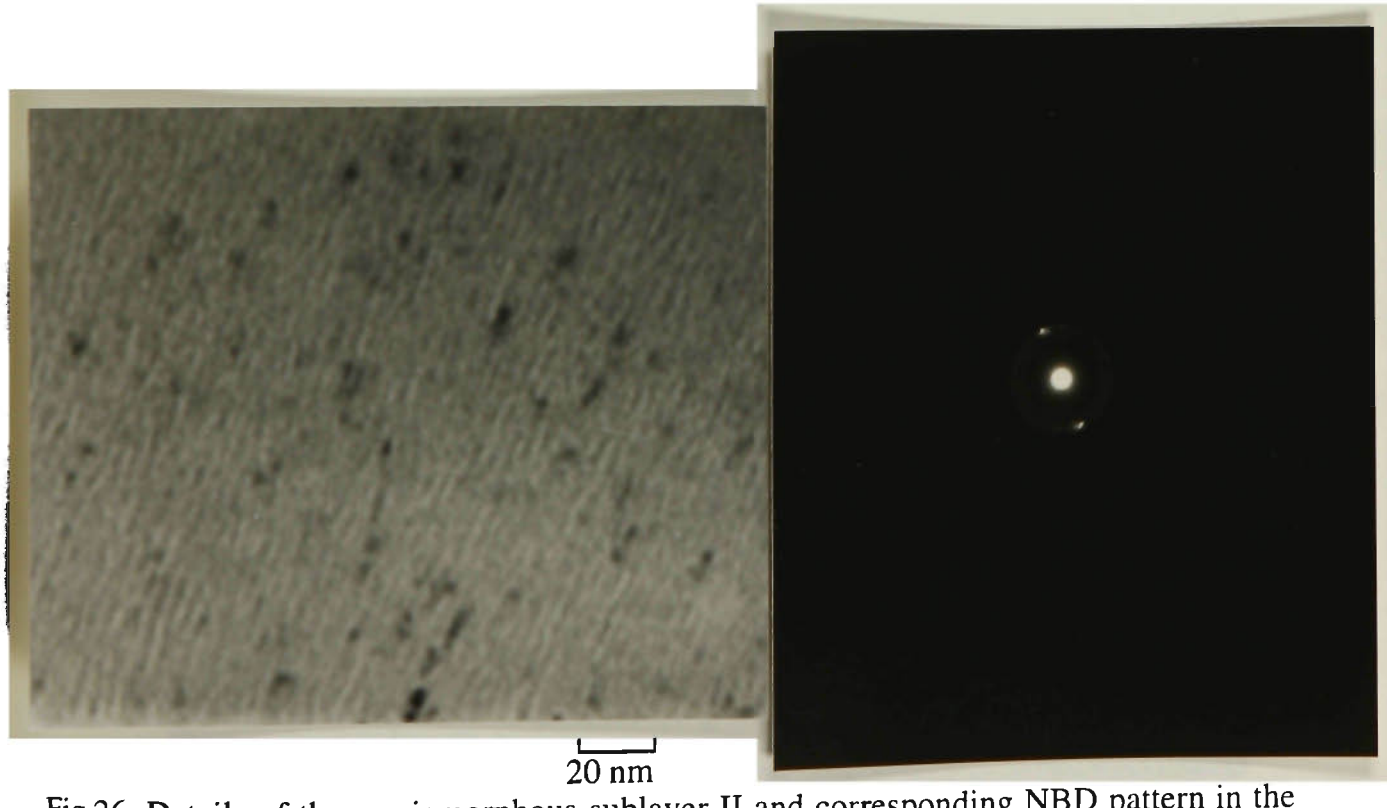

Fig.26 Details of the semiamorphous sublayer II and corresponding NBD pattern in the specimen PI^3 treated at 250°C. The black spots in the BF image are tiny CrN and α precipitates interposed between the stripe-like features. The NBD pattern clearly revealed the semi-amorphous nature judging by spots superimposed on a diffuse ring.

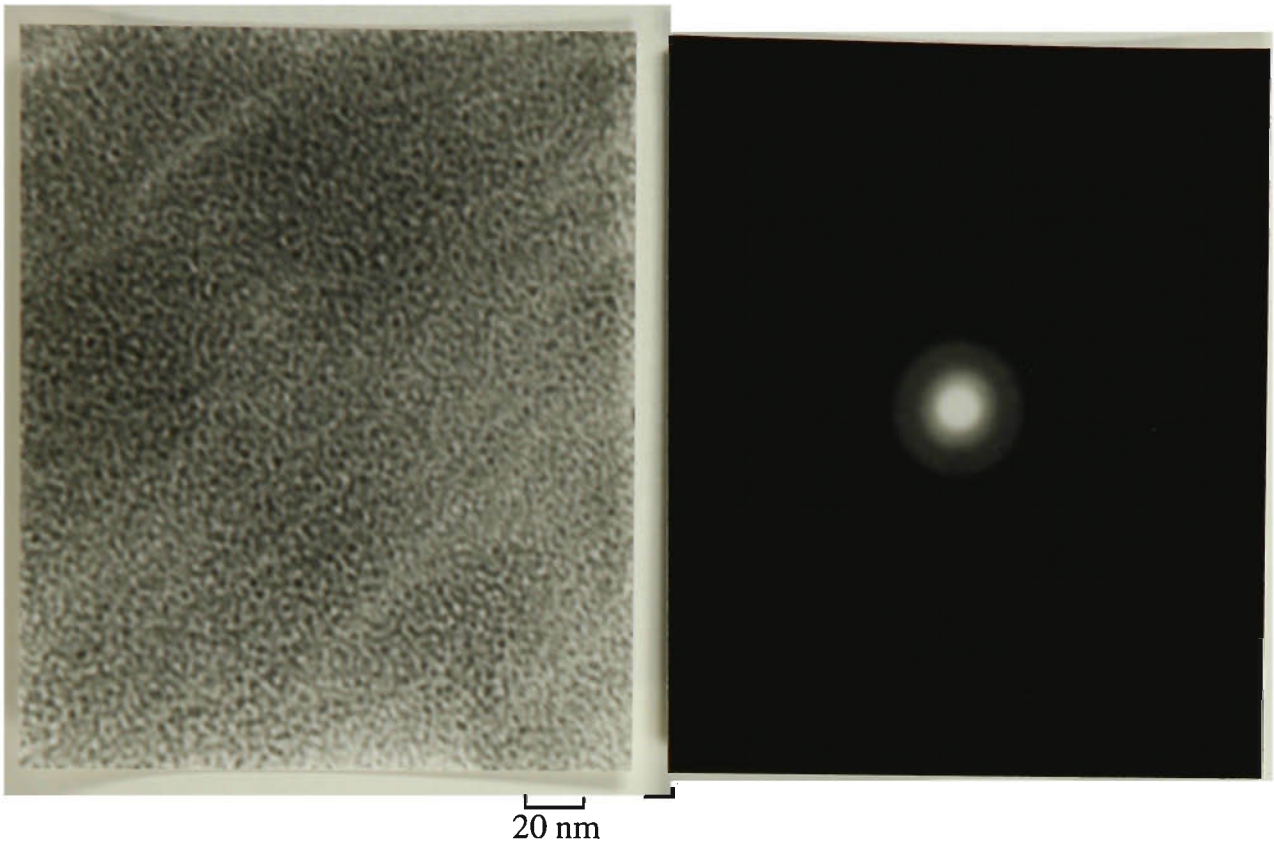

Fig.27 Details of the amorphous sublayer III and corresponding NBD pattern in specimen PI^3 treated at 250°C.

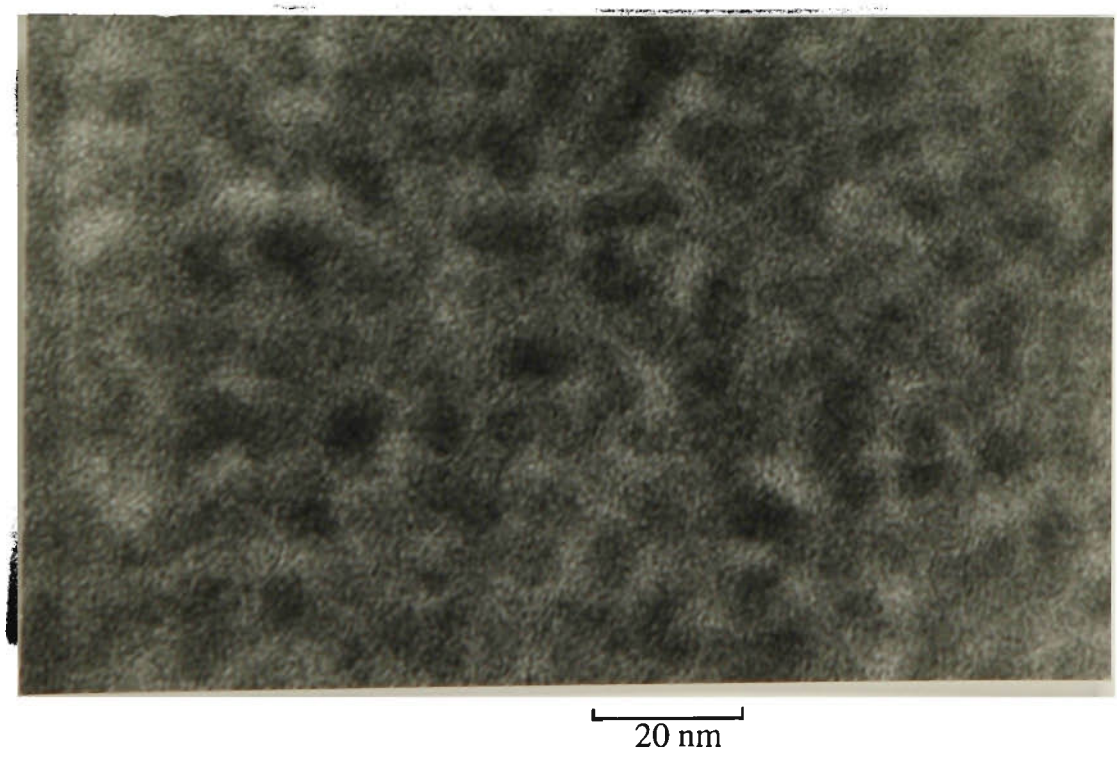

Fig.28 HREM image of the amorphous sublayer III. Short range order can be seen within the clusters. PI^3 treated at 250°C.

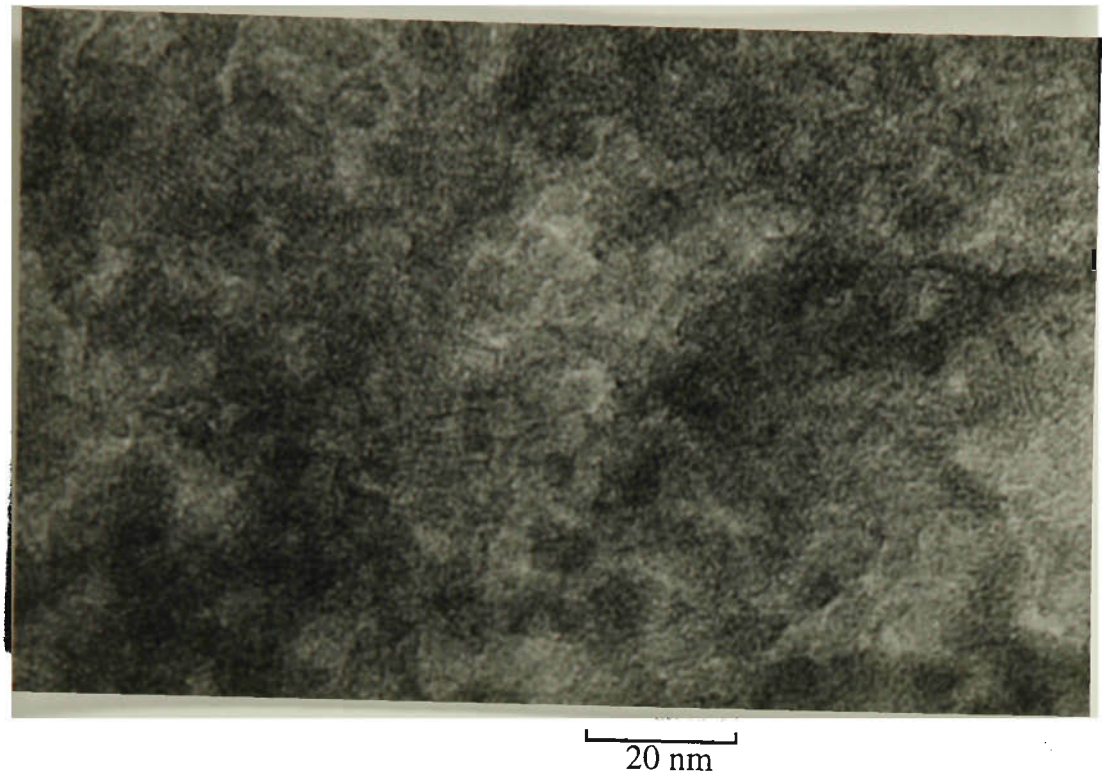

Fig.29 HREM image of the very thin semi-amorphous transition region near the interface in amorphous sublayer III. PI[3] treated at 250°C.

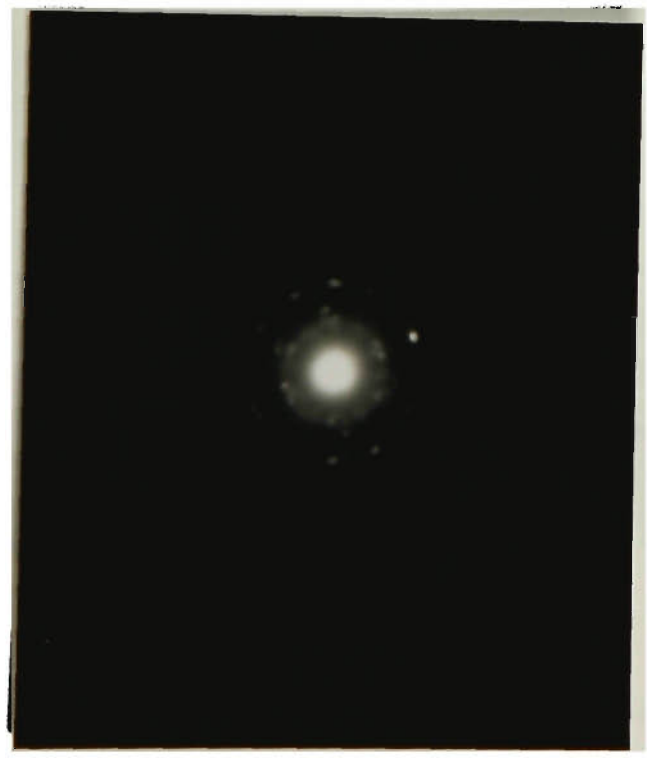

Fig.30 NBD pattern of the very thin semi-amorphous transition region near the interface in amorphous sublayer III, showing rings and dim spots of both (Cr,Fe)N (identified by superlattice spots) and α. Among the diffraction spots, [111](Cr,Fe)N diffraction spots can be discerned. PI[3] treated at 250°C.

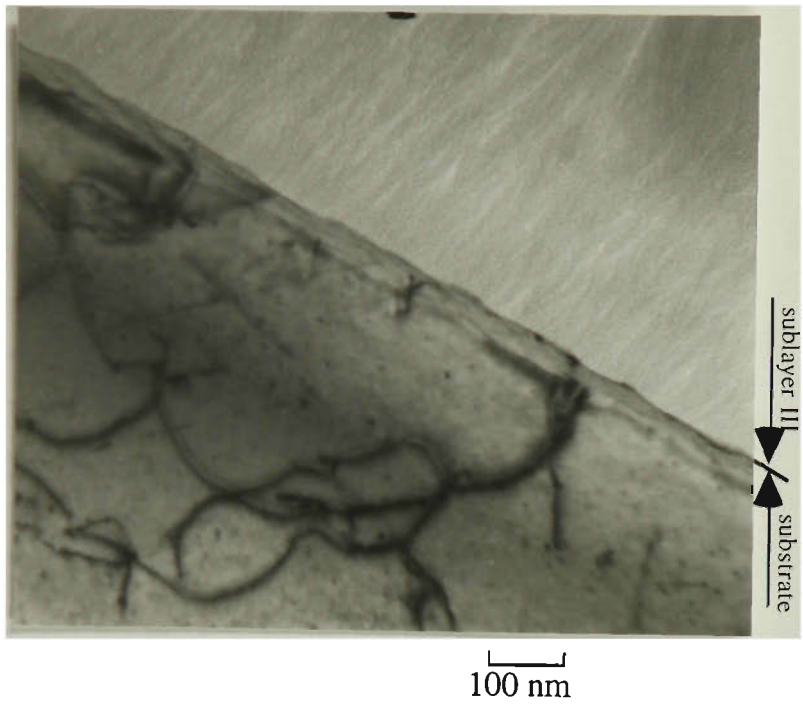

a. Interface between the amorphous sublayer III and the substrate.

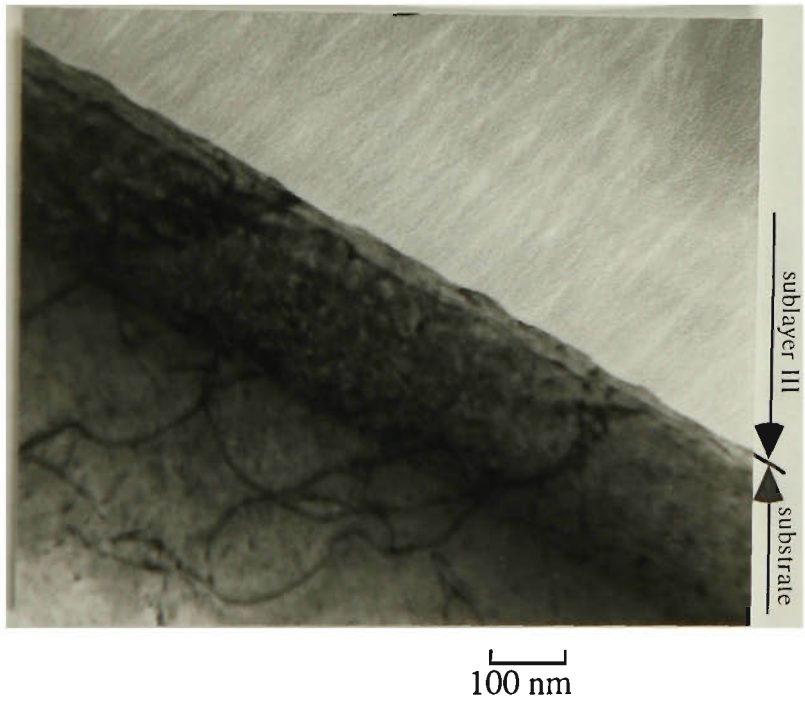

b. Interface between the amorphous sublayer III and the substrate, the specimen was slightly tilted compared to the one shown in (a) to show the stress affected region in the substrate.

Fig.31 Interface between the amorphous sublayer III and the substrate. A 250 nm thick stress effected region in substrate can be observed below the interface. PI^3 treated at 250°C.

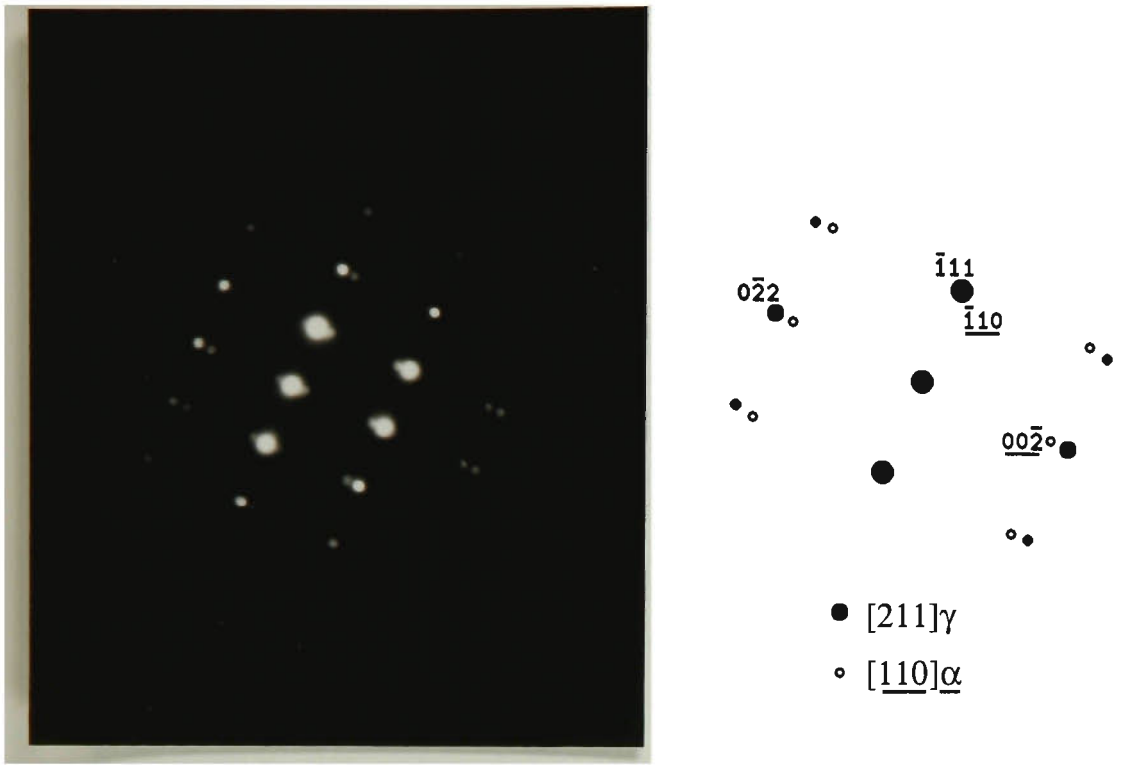

Fig.32 NBD pattern of the substrate just below the inerface, showing slightly expanded γ with α phase. N-W relation between [211]γ with [110]α. PI[3] treated at 250°C.

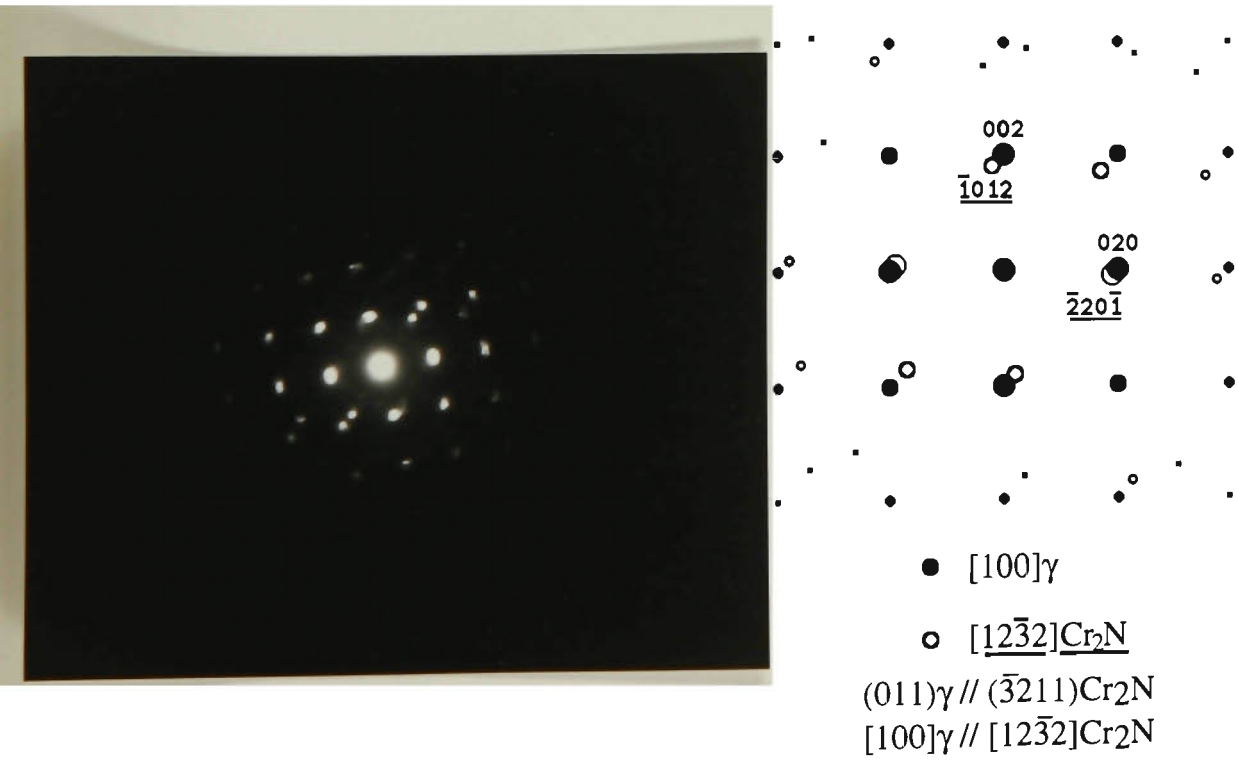

Fig.33 NBD pattern taken at the interface, showing Cr_2N precipitated at the interface from γ. The orientation relationship between the γ and Cr_2N is: (011)γ // ($\bar{3}$211)Cr_2N, [100]γ // [12$\bar{3}$2]Cr_2N. PI[3] treated at 250°C.

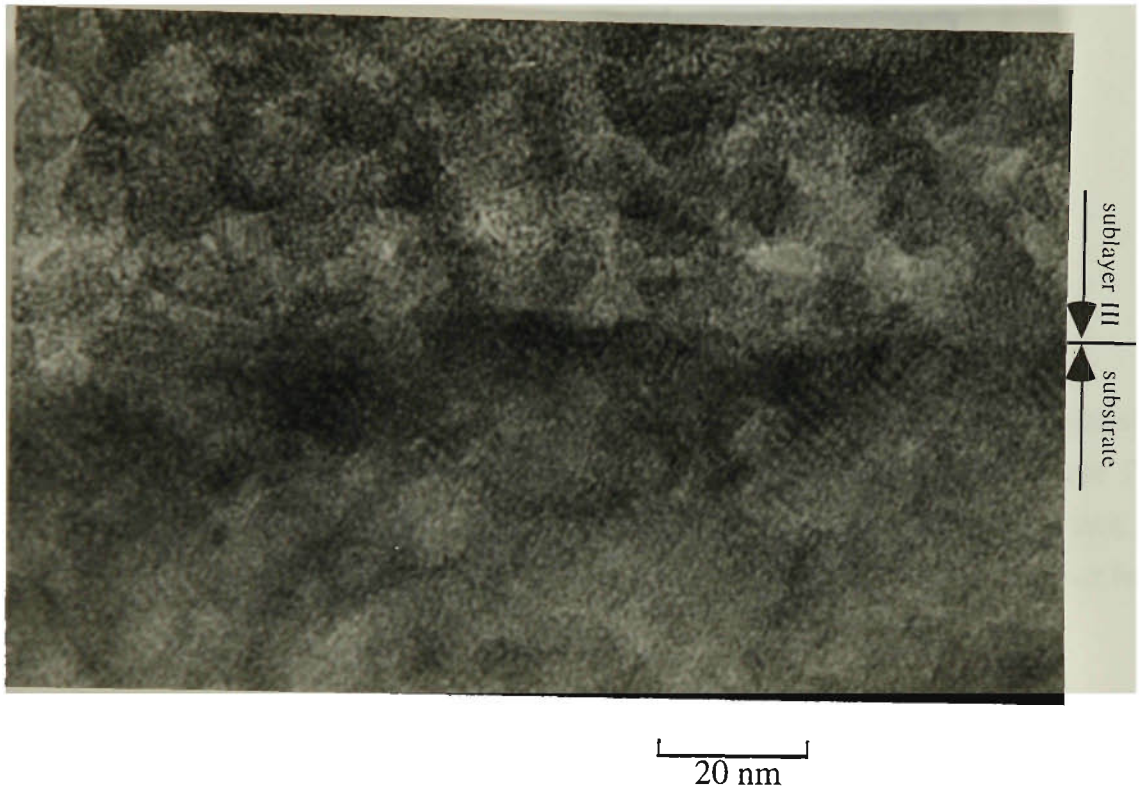

Fig.34 HREM image of the interface between amorphous sublayer III and the substrate. Notice that some crystalline structure of the substrate crosses over at the interface into the amorphous sublayer III. PI^3 treated at 250°C.

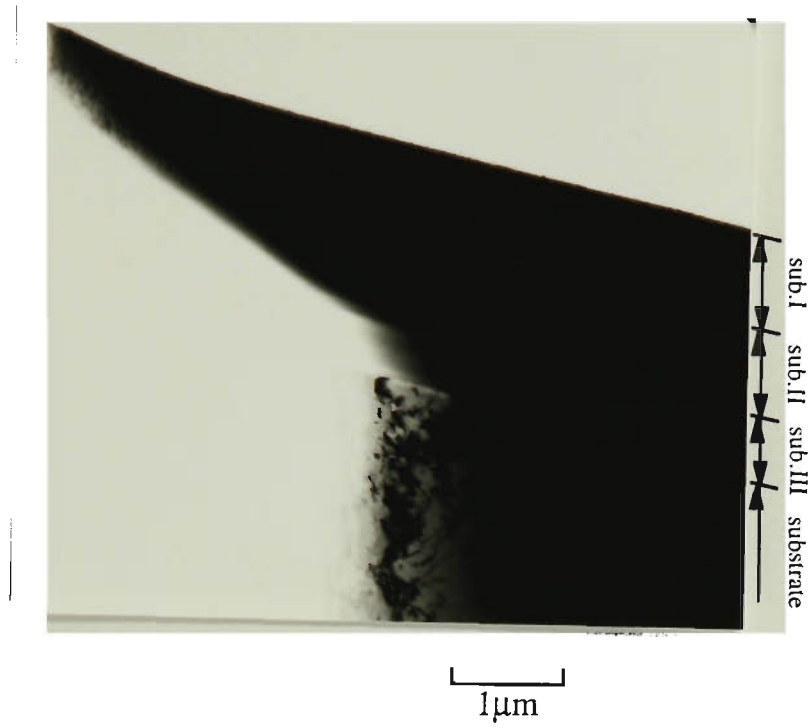

Fig.35 The XTEM image of the entire implantation modified layer in specimen PI^3 treated at 350°C. The modified layer is about 2.3 μm thick, and can be divided into 3 sublayers. The first sublayer is nano-crystalline and about 0.9-1 μm thick, followed by an amorphous sublayer about 0.9 μm thick. The third sublayer is semi-amorphous, about 0.5-0.6 μm thick.

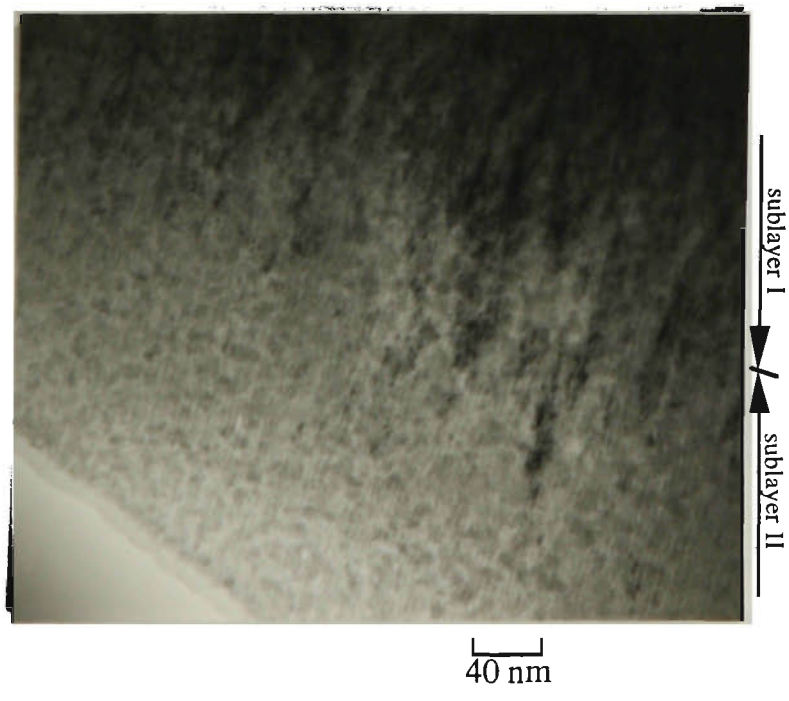

a. Transition of the nanocrystlline sublayer I to the amorphous sublayer II.

Fig.36 Details of the nanocrystalline sublayer I and the amorphous sublayer II in the specimen PI^3 treated at 350°C.

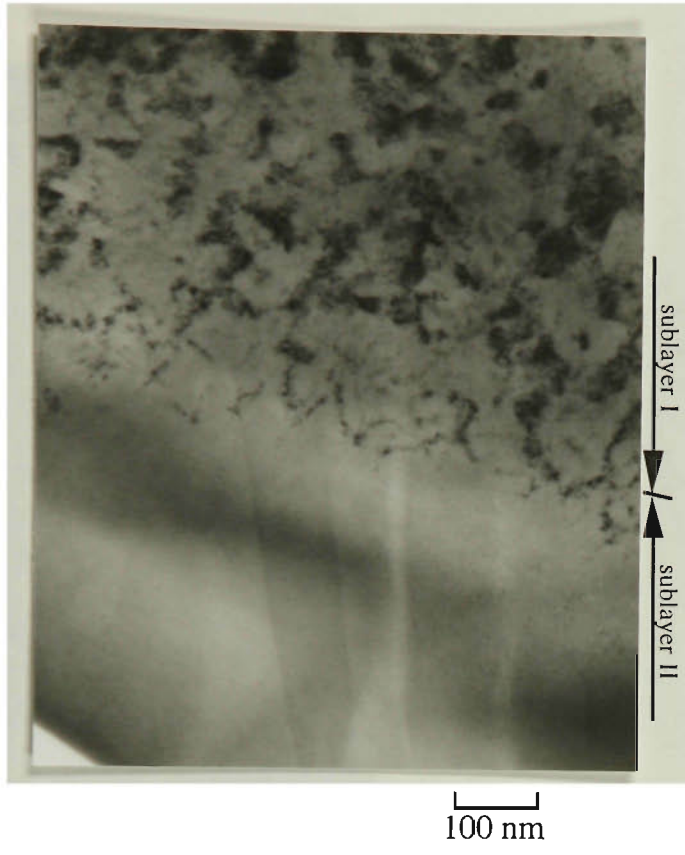

b. Same as (a) but evolved from a differently oriented austenite grain.

Fig.36(**cont.**) Details of the nanocrystalline sublayer I and the amorphous sublayer II. PI^3 treated at 350°C.

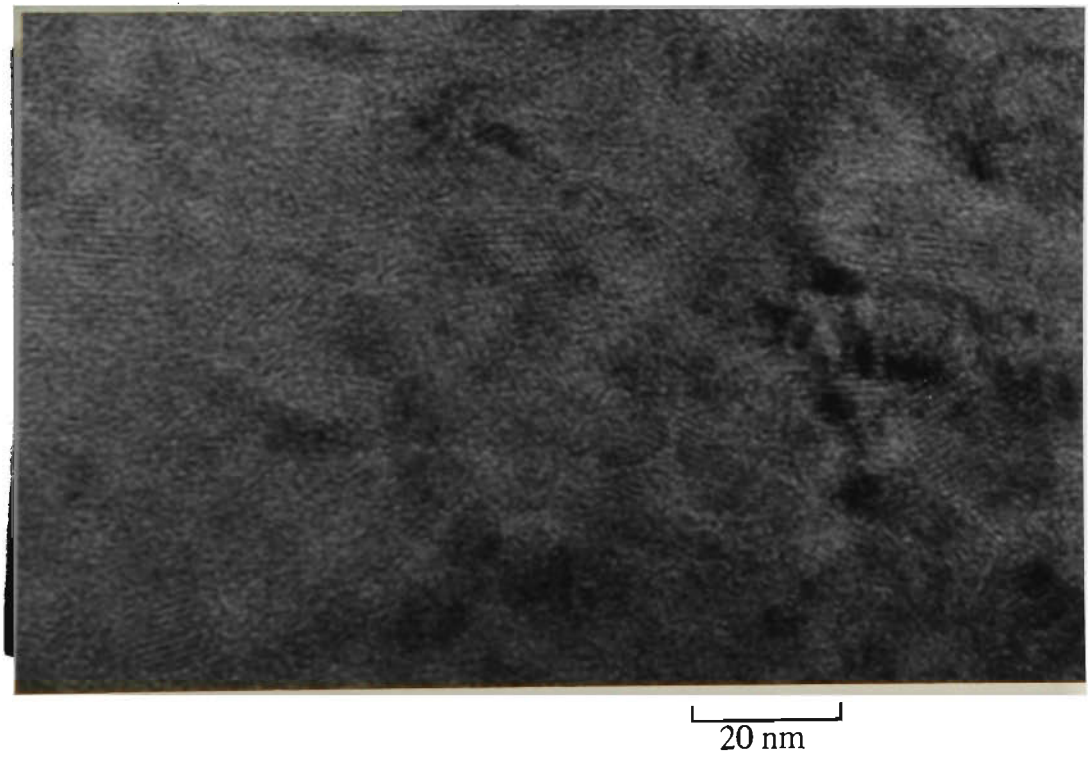

Fig.37 HREM image of the nanocrystalline sublayer I. PI^3 treated at 350°C.

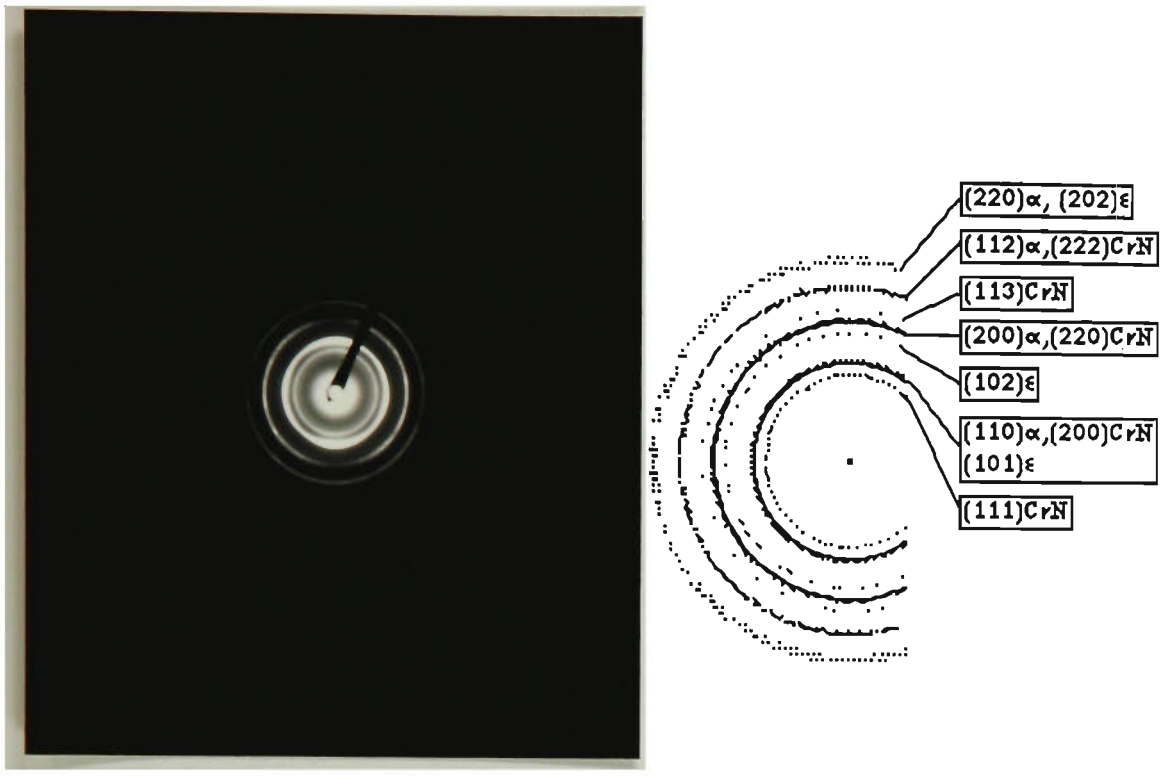

Fig.38 SAD pattern of the nanocrystalline sublayer I, showing CrN and α as the main phases in the nanocrystalline sublayer I, together with traces of ε nitride. PI[3] treated at 350°C.

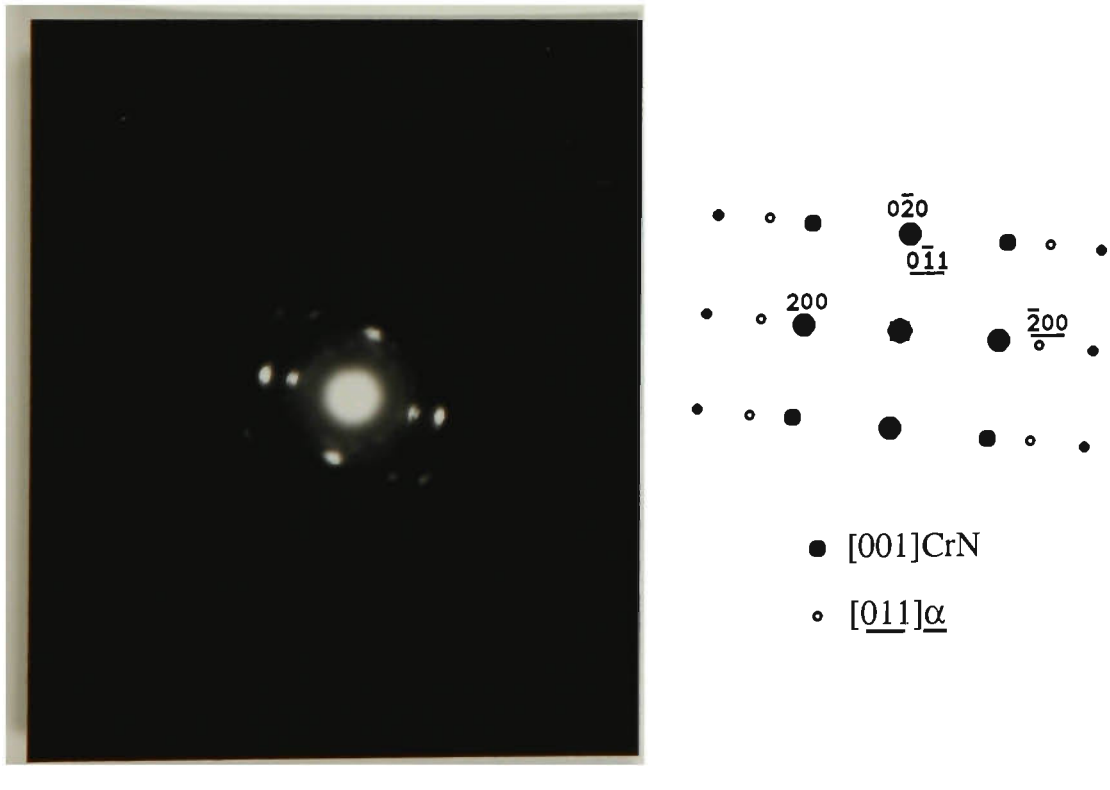

a. NBD pattern of the precipitates in sublayer I. [001]CrN with α, Bain relation.

Fig.39 NBD patterns of the nanocrystalline sublayer I, showing (a) Bain and (b) N-W relations between CrN and α phases. PI[3] treated at 350°C.

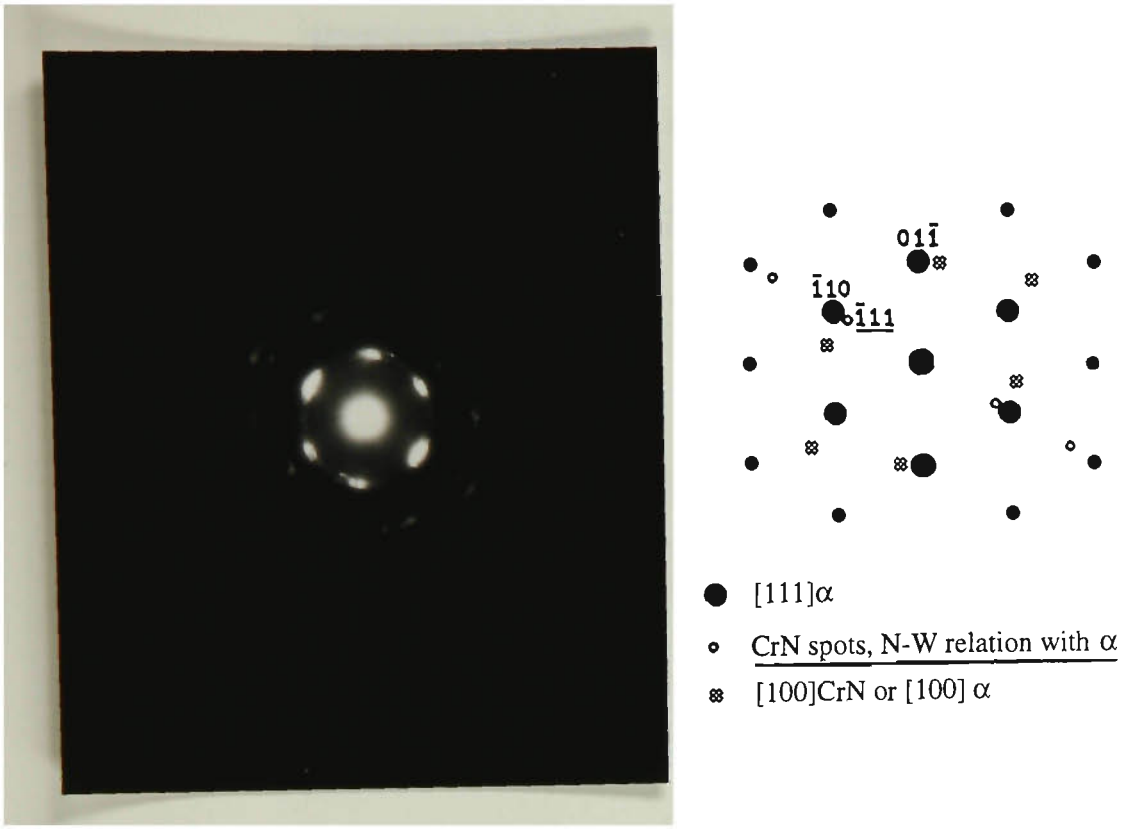

b. NBD pattern of the precipitates in sublayer I. [111]α with CrN, N-W relation.

Fig.39(cont.) NBD patterns of the nanocrystalline sublayer I, showing (a) Bain and (b) N-W relations between CrN and α phases. PI^3 treated at 350°C.

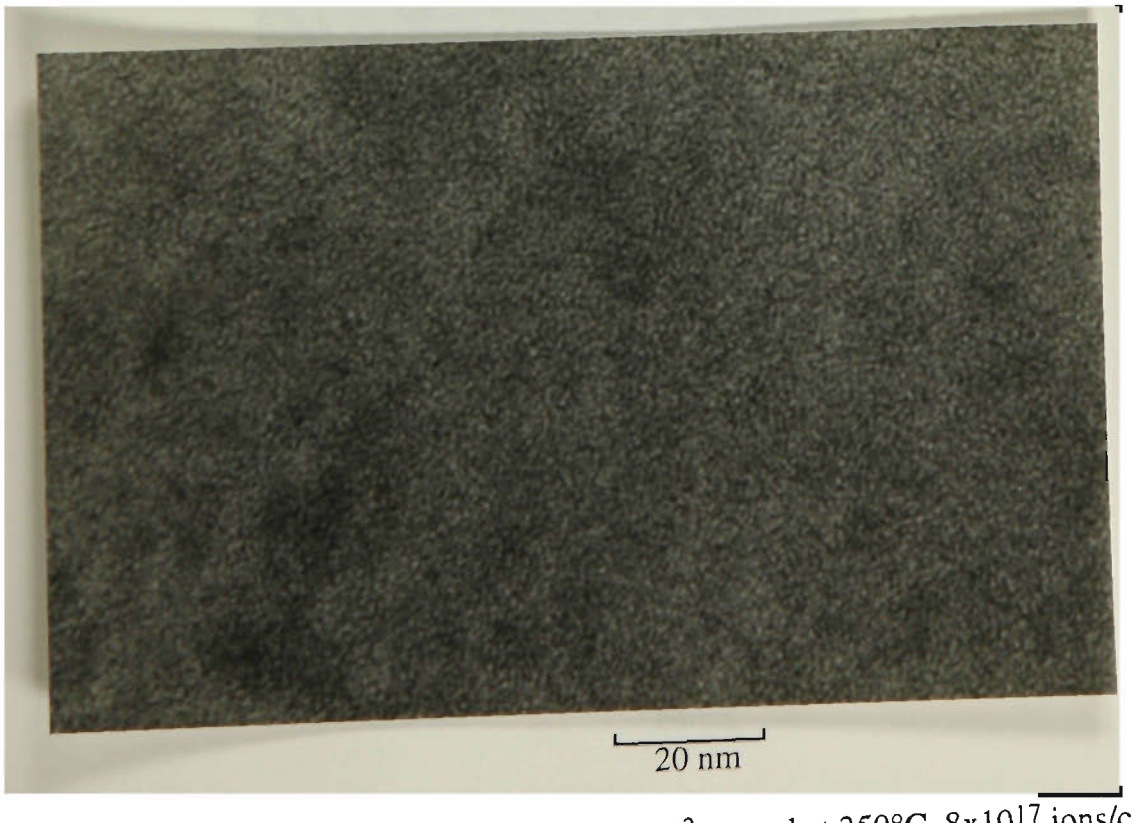

Fig.40 HREM image of the amorphous sublayer II. PI^3 treated at 350°C, $8x10^{17}$ ions/cm^2, 130 minutes.

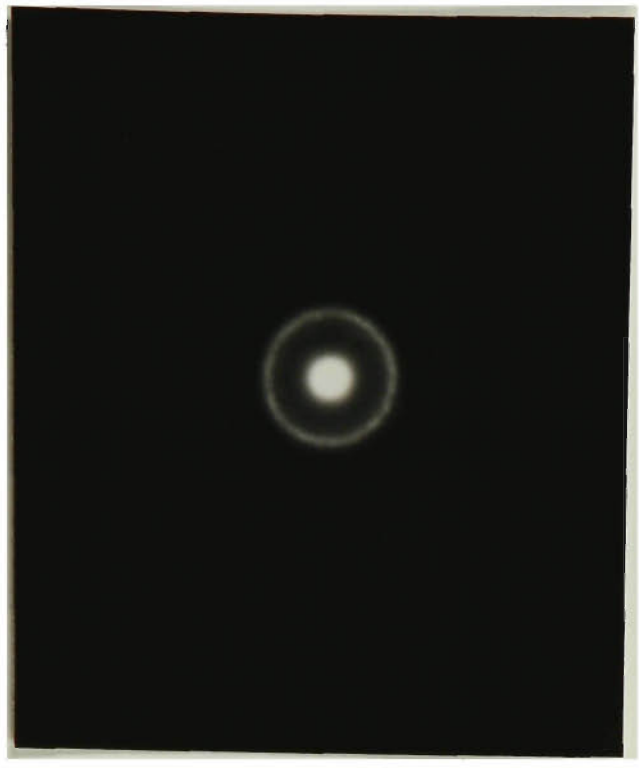

Fig.41 NBD pattern of the amorphous sublayer II. PI^3 treated at 350°C.

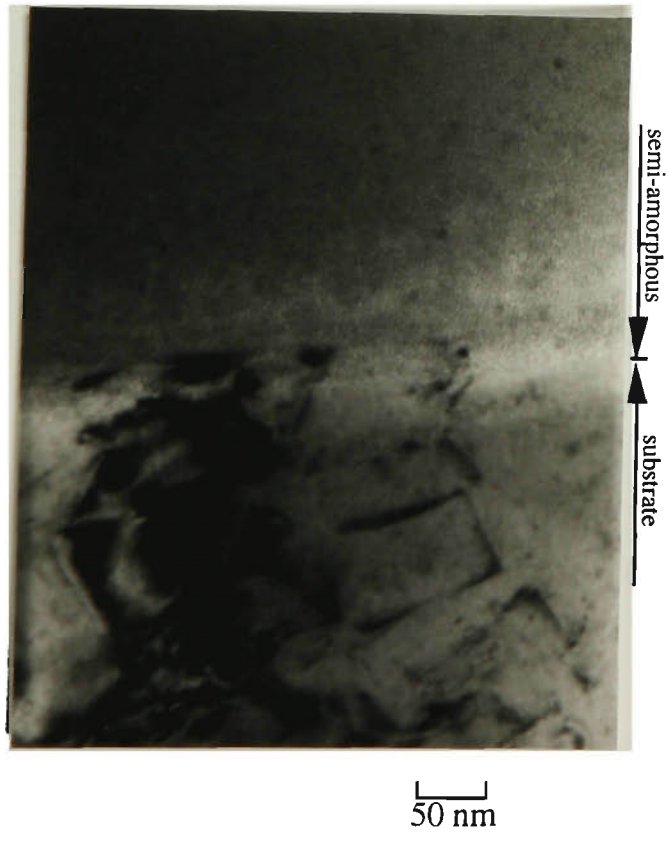

Fig.42 Interface between the semiamorphous sublayer III and the substrate. PI^3 treated at 350°C.

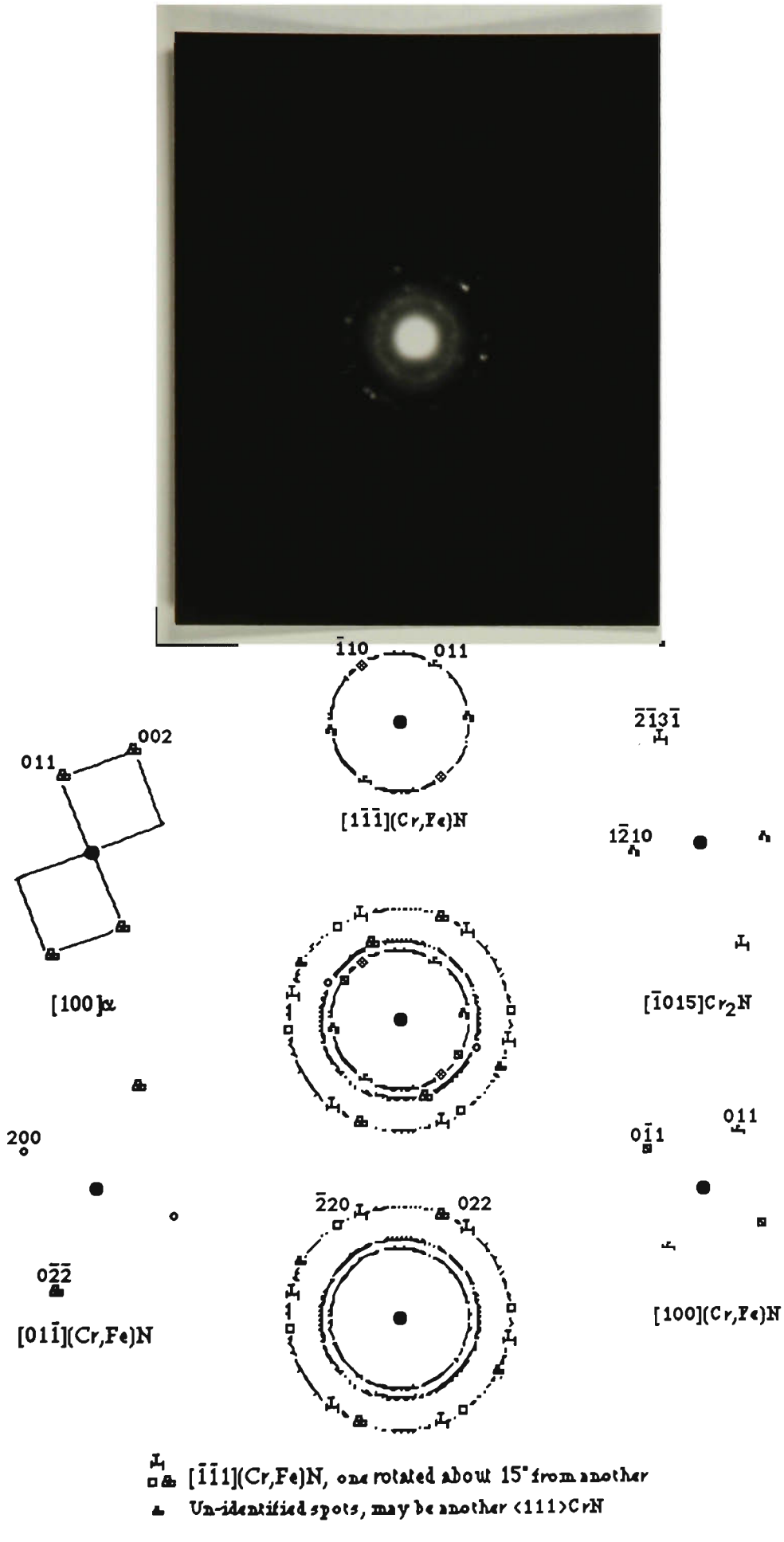

Fig.43 NBD pattern of the top region (near sublayer II) of the semi-amorphous sublayer III. The crystalline structures are mainly (Cr,Fe)N and α, with small amount of Cr_2N phase. PI[3] treated at 350°C.

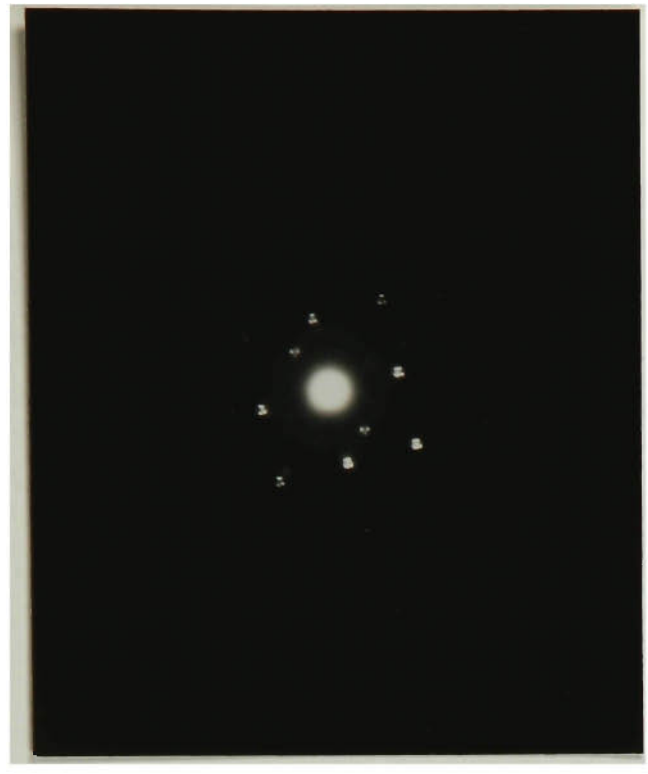

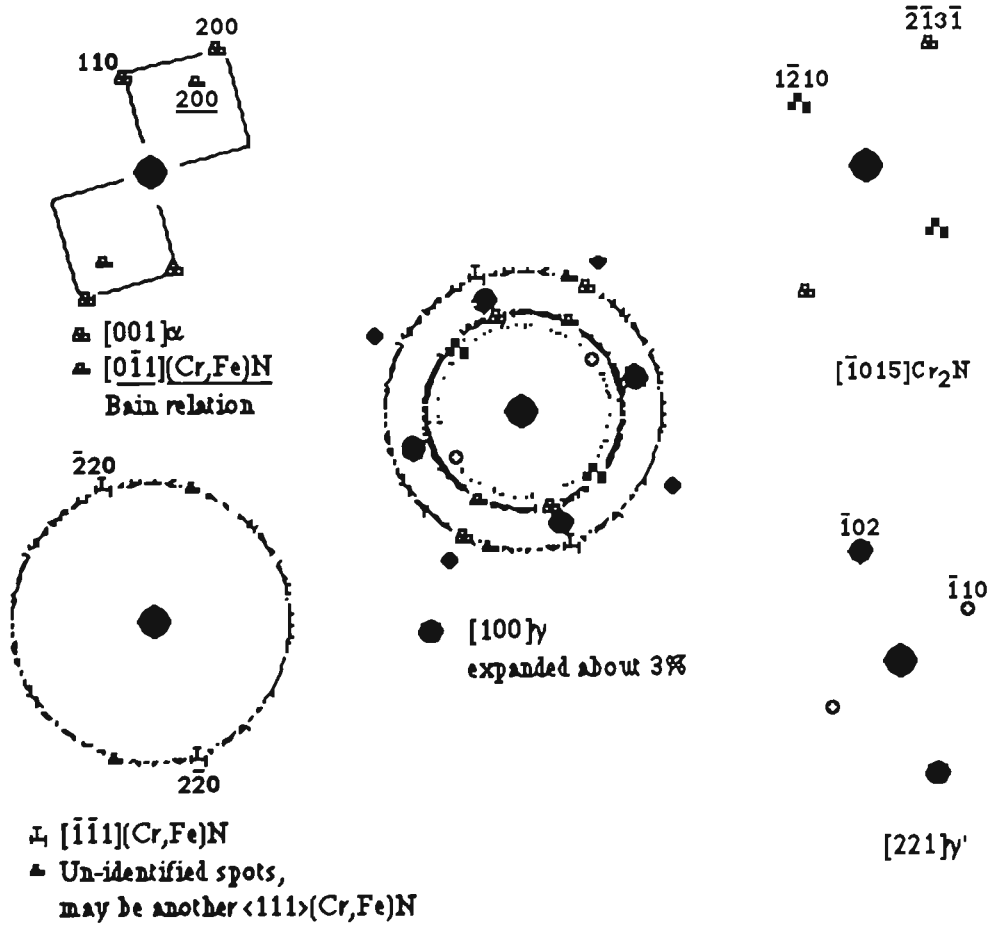

Fig.44 NBD pattern taken at the interface, showing that (Cr,Fe)N and α, as well as Cr_2N have just started to form. Small amount of γ' was also detected. The γ phase shows about 3% expansion at the interface. The expansion decreases to zero only 30-50 nm away from the interface. Notice that the [001]α and the [$\bar{1}\bar{1}$1](Cr,Fe)N diffraction shown in Fig.43 is still visible even though with different intensity or slightly rotated. PI[3] treated at 350°C.

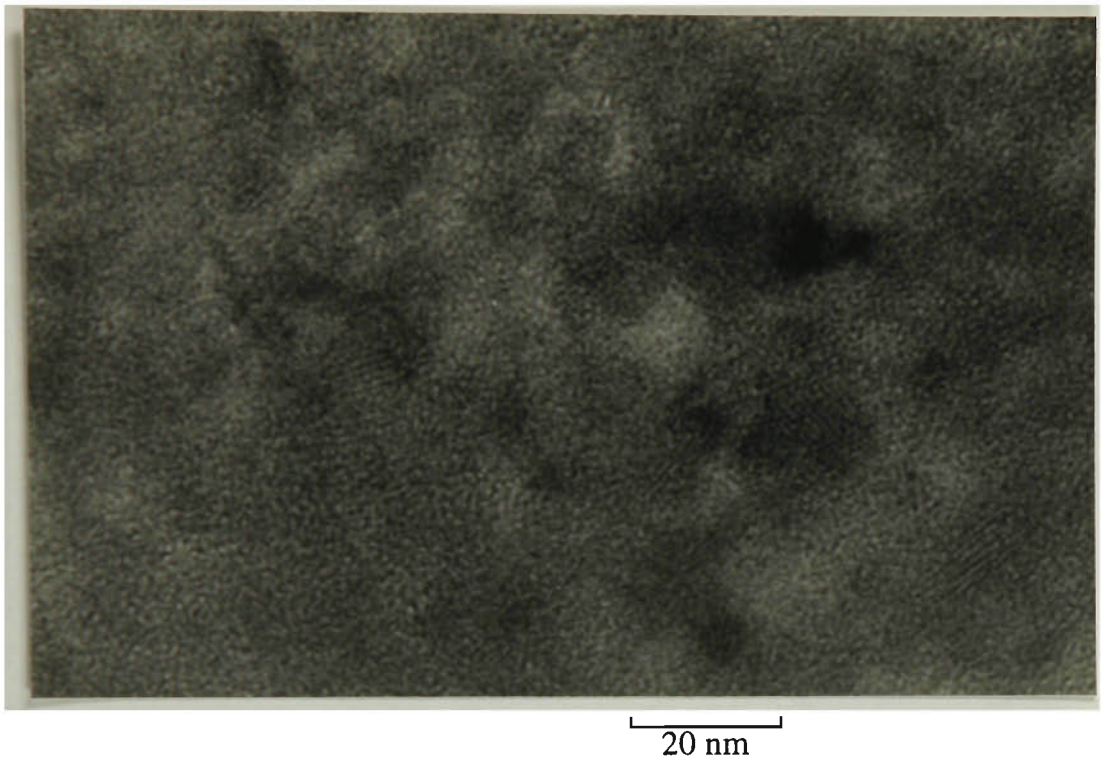

Fig.45 HREM image of the semi-amorphous sublayer III. PI^3 treated at 350°C.

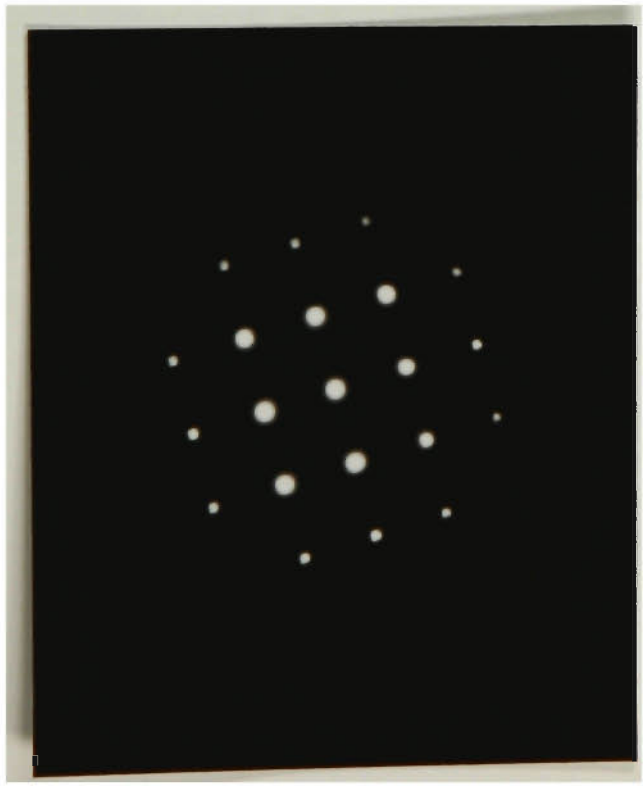

Fig.46 NBD pattern of the substrate. PI^3 treated at 350°C.

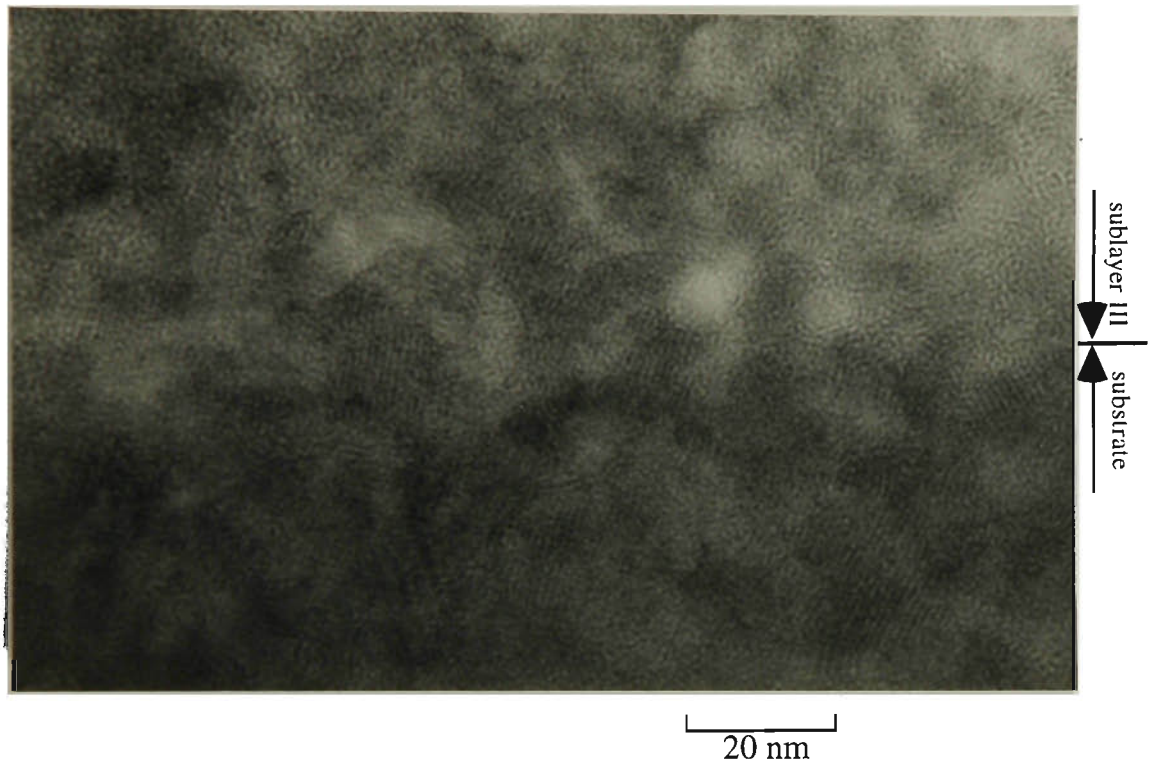

Fig.47 HREM image of the interface between semiamorphous sublayer III and the substrate. Notice that some of the crystalline structure of the substrate crosses over at the interface into the semiamorphous sublayer III. PI^3 treated at 350°C.

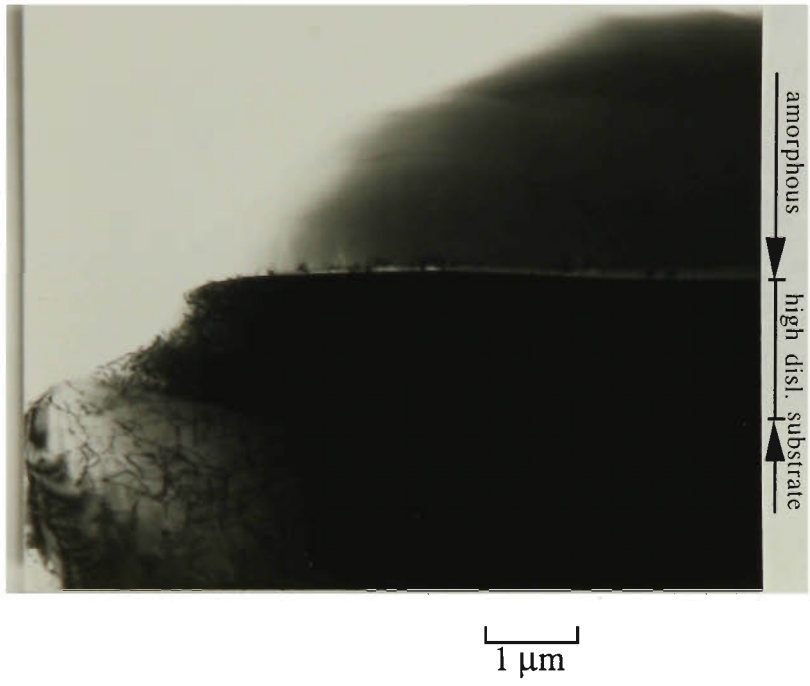

Fig.48 XTEM micrograph of the specimen PI^3 treated at 450°C. The whole of modified layer (about 3 μm thick) is amorphous, except for a very thin semiamorphous transition region, within 100 nm from the interface. A 1.5-2 μm thick high dislocation density region is observed between the amorphous layer and the unexpanded substrate. By comparing the SAD patterns, the γ phase of the high dislocation zone shows about 3% expansion.

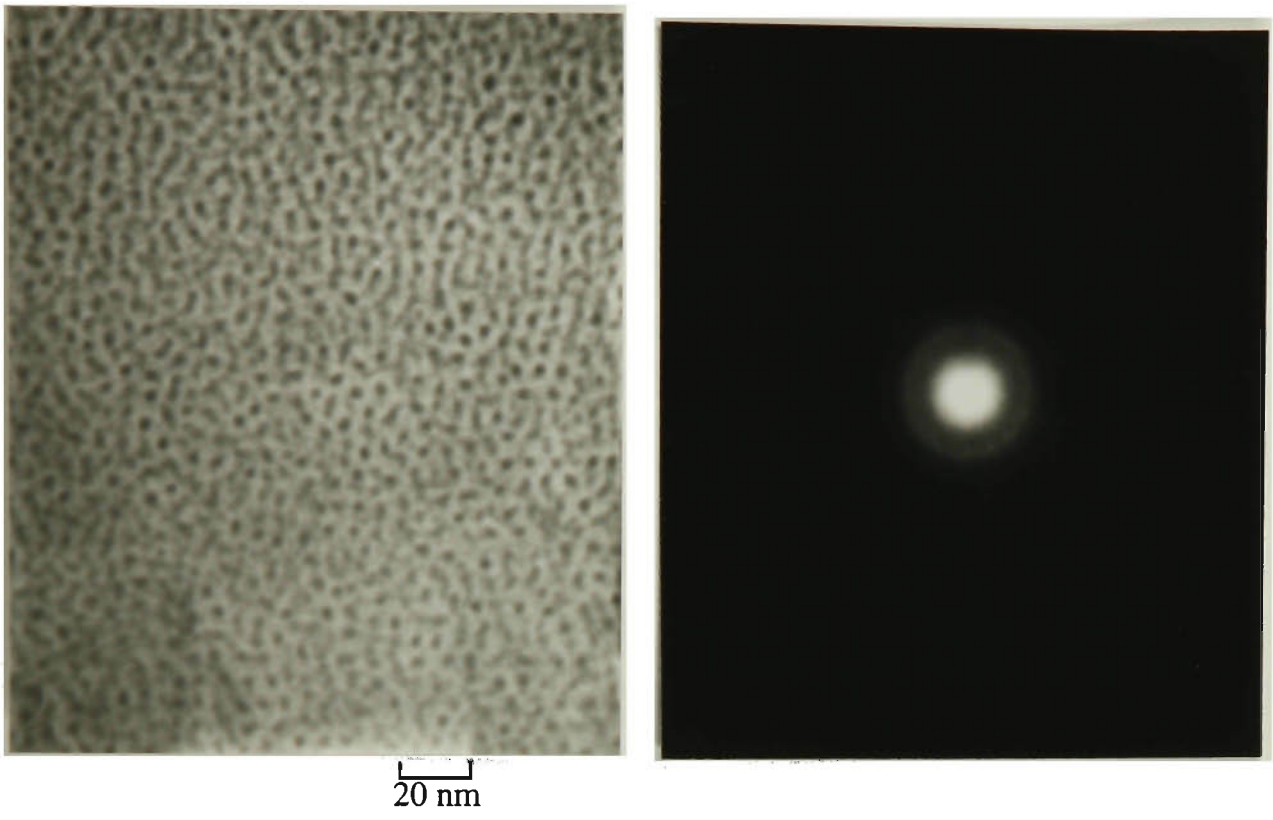

a. Details of the amorphous layer

b. NBD pattern of the amorphous structure

Fig.49 Details of the amorphous layer. PI^3 treated at 450°C. The amorphous layer shows clustered structure with the clusters in sizes of 4-6 nm.

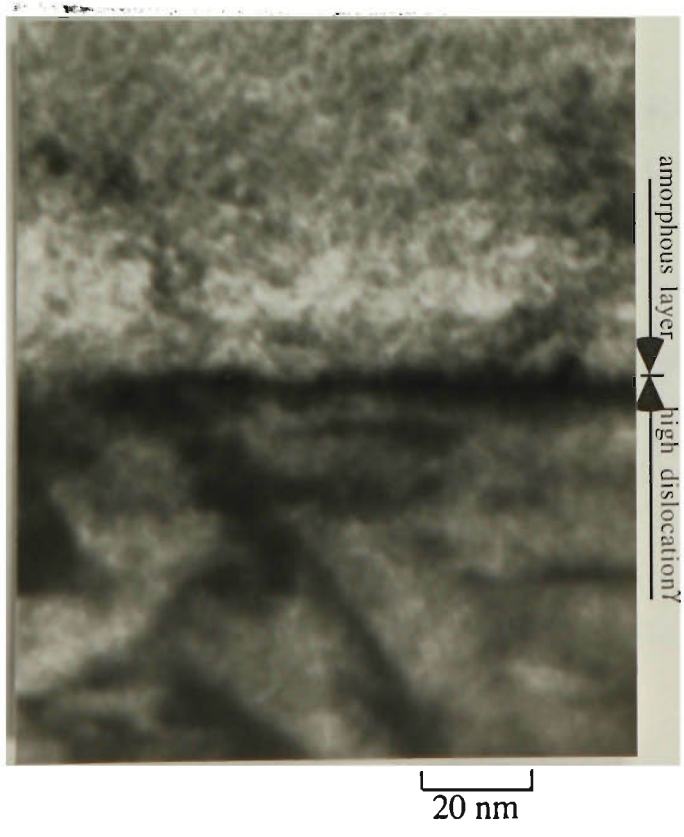

Fig.50 Interface between the amorphous layer and the high dislocation density γ region. PI^3 treated at 450°C, $8x10^{17}$ions/cm^2, 70 minutes.

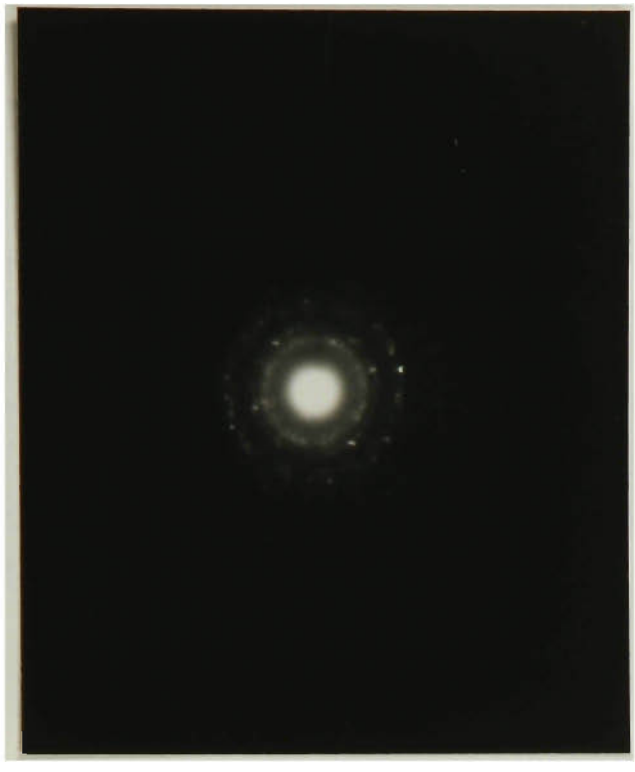

Fig.51 NBD pattern taken at the thin semiamorphous transition region in the amorphous layer. PI[3] treated at 450°C.

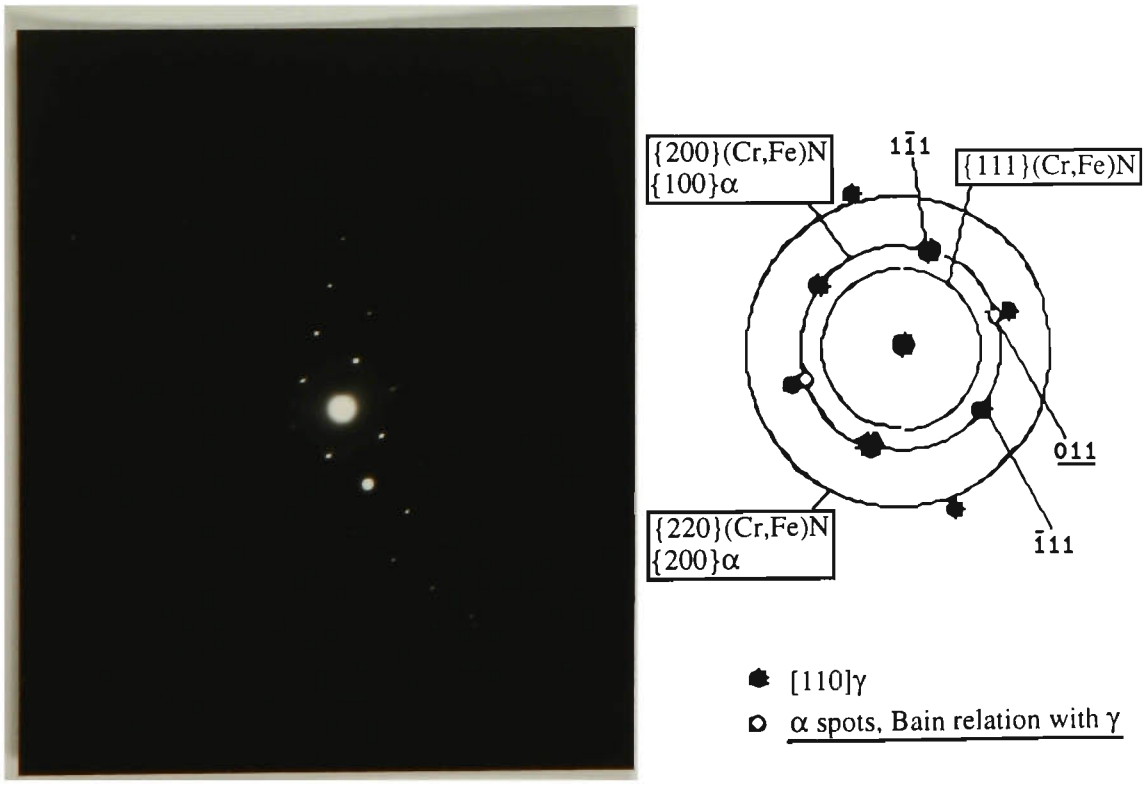

Fig.52 SAD pattern of the interface between the amorphous layer and the high dislocation density zone of the substrate. The pattern shows (Cr,Fe)N and α ring pattern plus $[110]\gamma_{exp}$ and α diffraction spots. Bain relation exists between the γ_{exp} and α. The γ_{exp} expanded about 3%. PI[3] treated at 450°C.

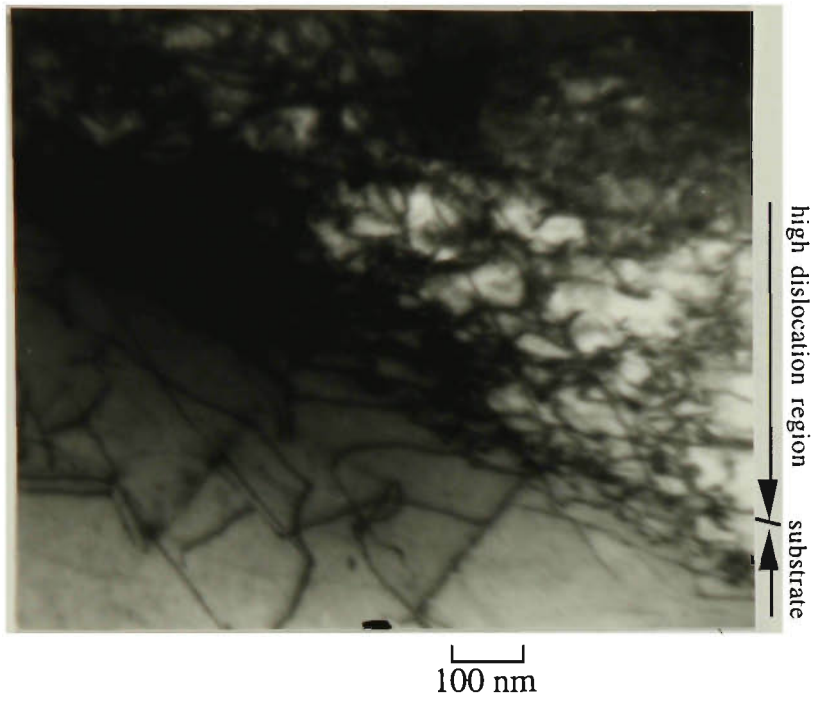

Fig.53 Interface between the high dislocation density region and the unexpanded γ austenite. PI^3 treated at 450°C.

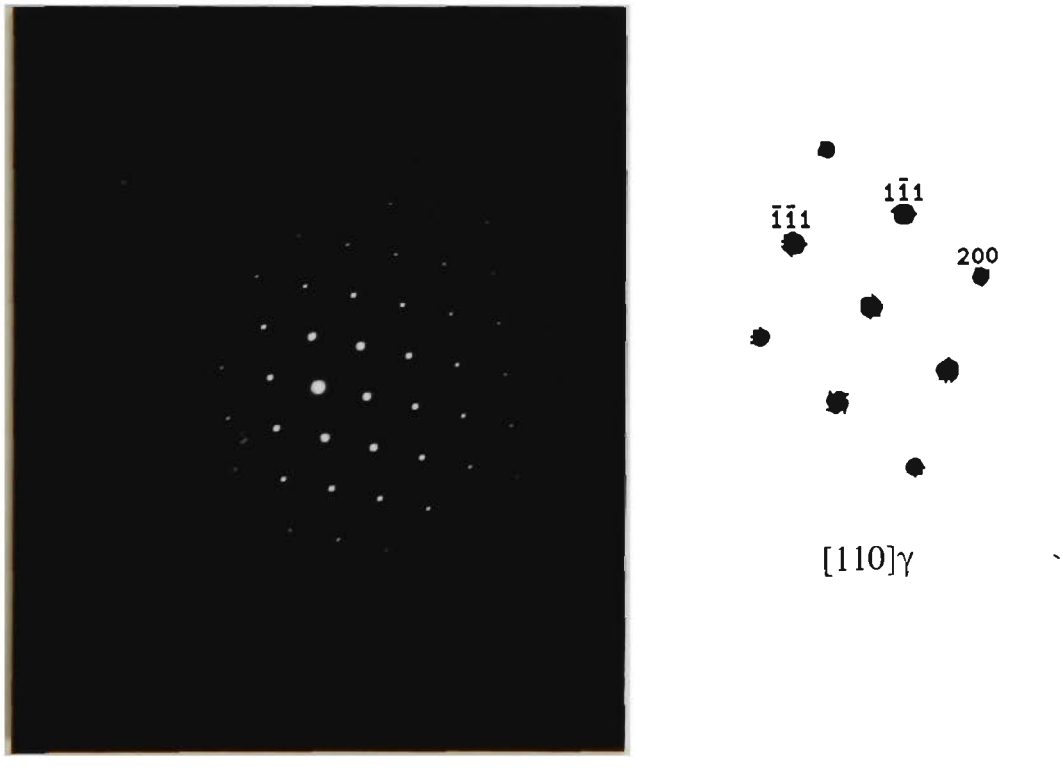

Fig.54 NBD pattern of the unexpanded γ substrate under the high dislocation region. Notice the orientaion of the γ diffraction pattern is the same as that shown in Fig.52. No more γ expansion is detected. PI^3 treated at 450°C.

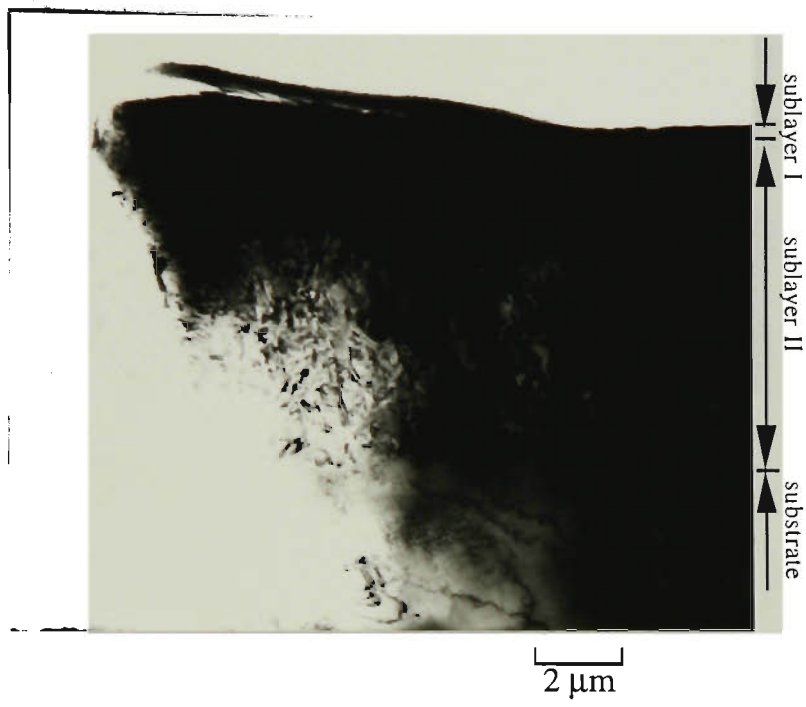

Fig.55 The whole modified layer of the specimen, PI^3 treated at 520°C. The modified layer is about 8-9 μm thick, divided into two sublayers. Sublayer I is nano-crystalline, about 0.4-0.5 μm thick, characterised by the very fine randomly dispersed CrN and α precipitates of less than 30 nm in size. Small amount of ε-nitride, Cr_2N and $CrMoN_x$ are also detected in this region. Sublayer II is composed of pearlite-type lamellar CrN and α.

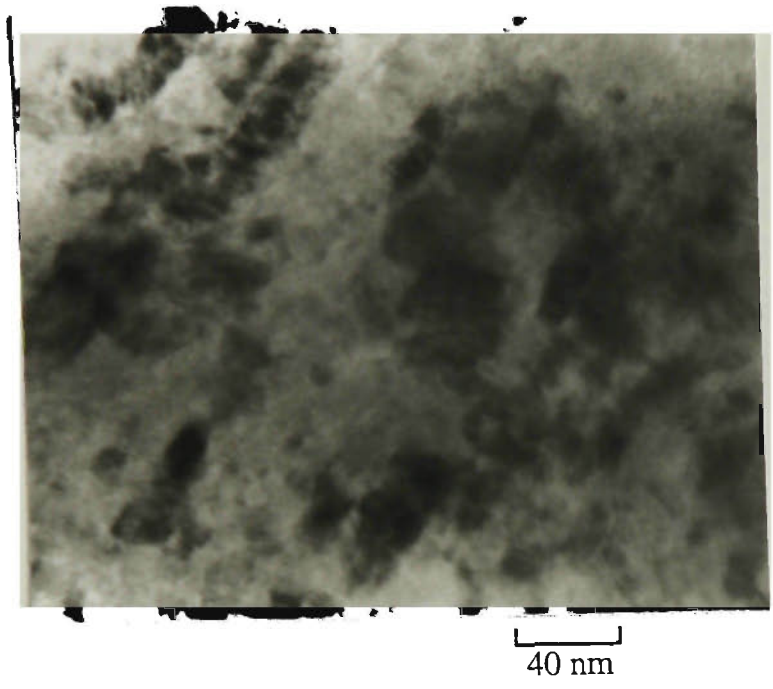

a. BF image of the Sublayer I

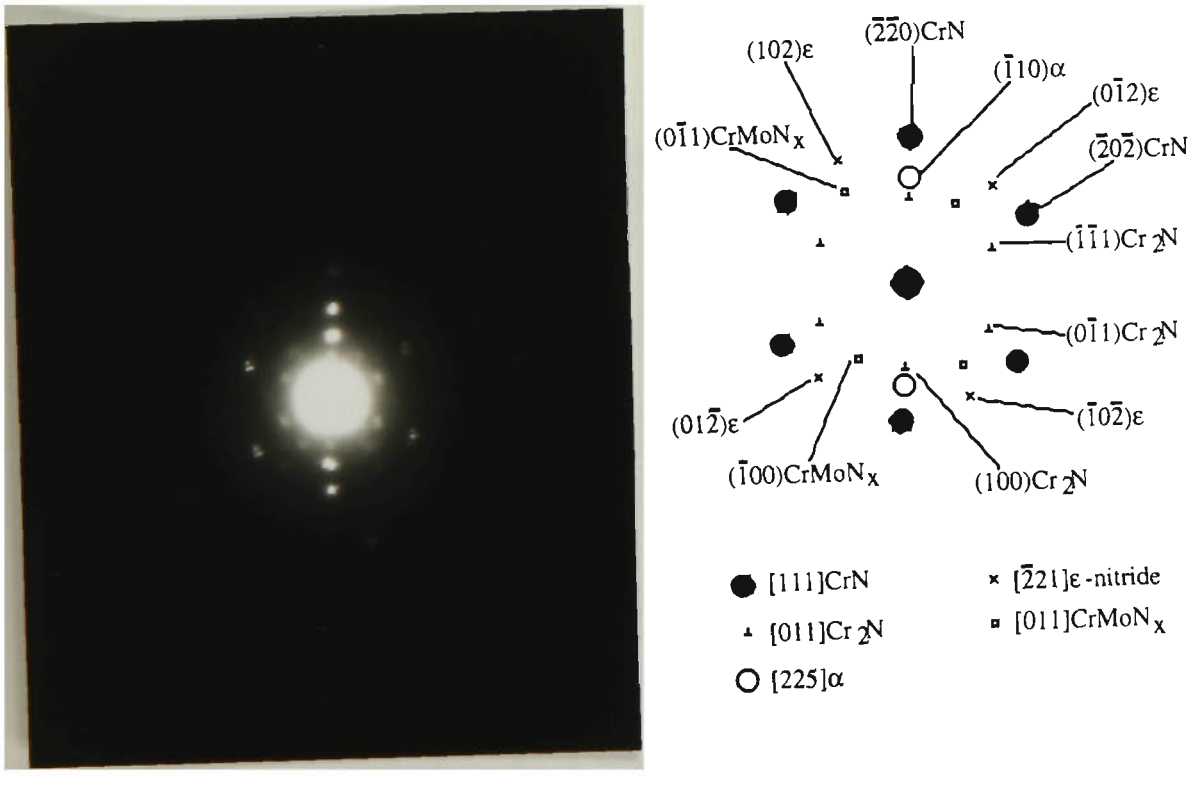

b. NBD pattern of the sublayer I

Fig.56 Details of the sublayer I, PI[3] treated at 520°C. BF image shows nanocrystalline CrN and α precipitates grouped in less than 30 nm size colonies. Small amount of ε-nitride, Cr_2N and $CrMoN_x$ are also detected in this region.

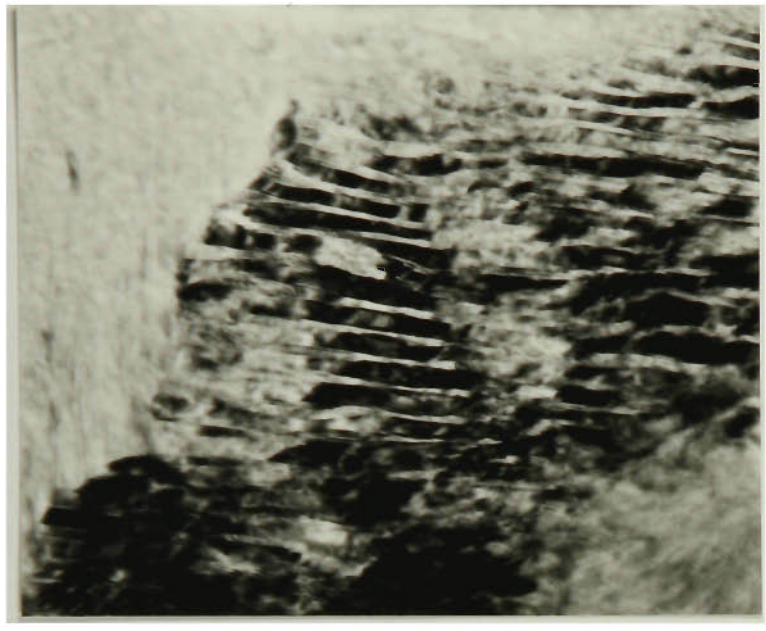

Fig.57 Details of the typical pearlite-like lamellar structure of CrN and α precipitates. PI[3] treated at 520°C.

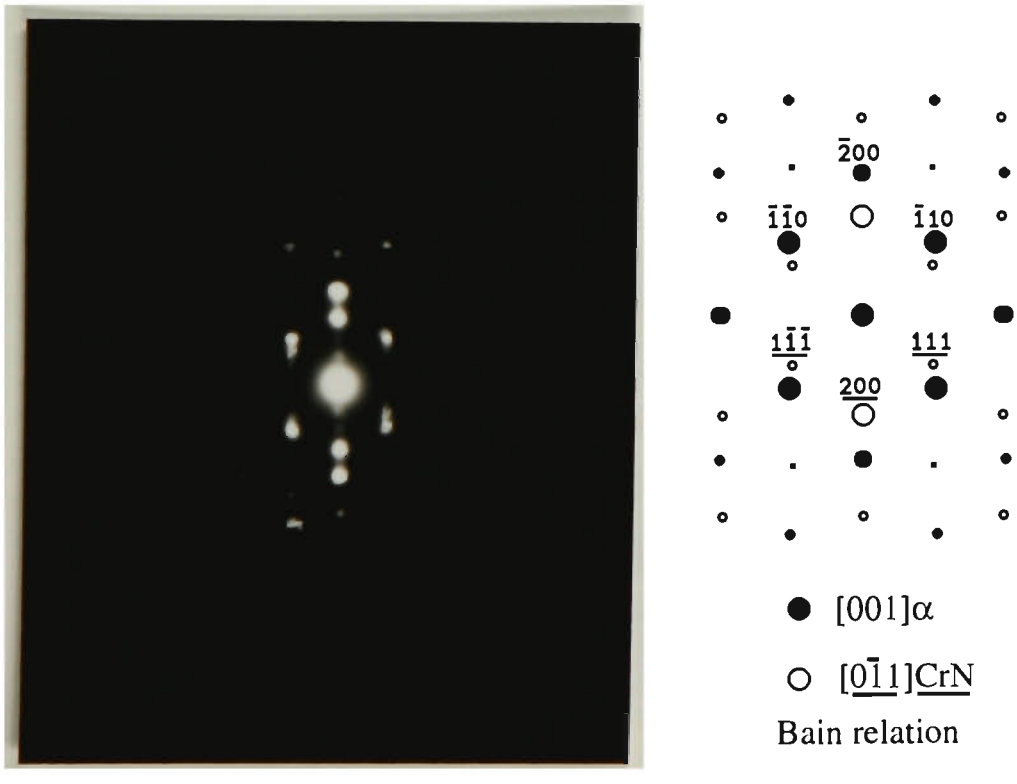

Fig.58 NBD pattern of the parallel lamellar structure shown in Fig.55, [001]α with [0$\bar{1}$1]CrN, Bain relation. PI[3] treated at 520°C.

Fig.59 Another NBD pattern of the lamellar CrN and α precipitates. [111]α with CrN, N-W relation. PI[3] treated at 520°C.

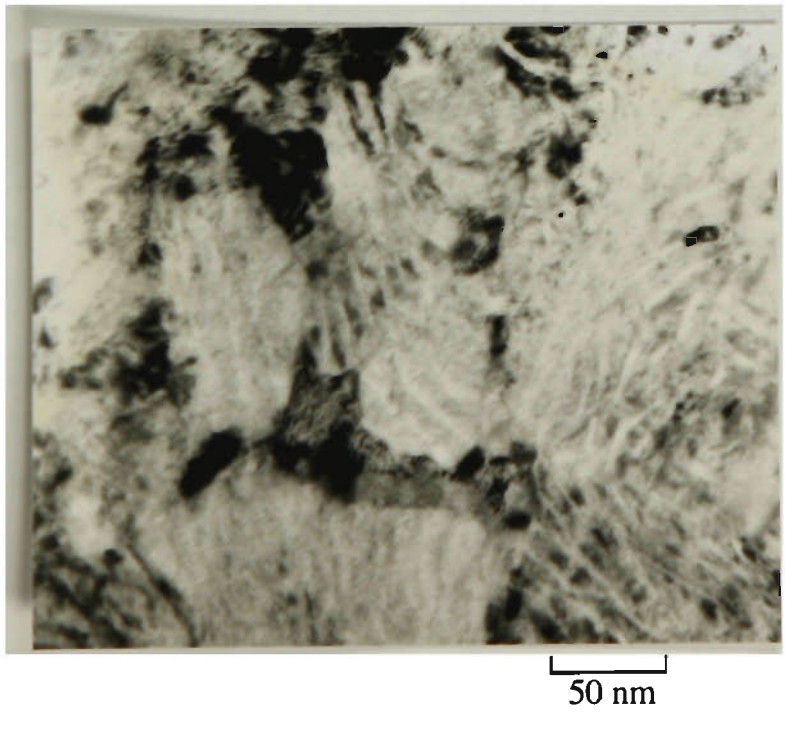

Fig.60 Small amount of ε nitrides are observed between the colonies of the lamellar CrN and α (dark islands-like area at the centre of the image with Moiré fringes) at the near surface area of the sublayer II. PI[3] treated at 520°C.

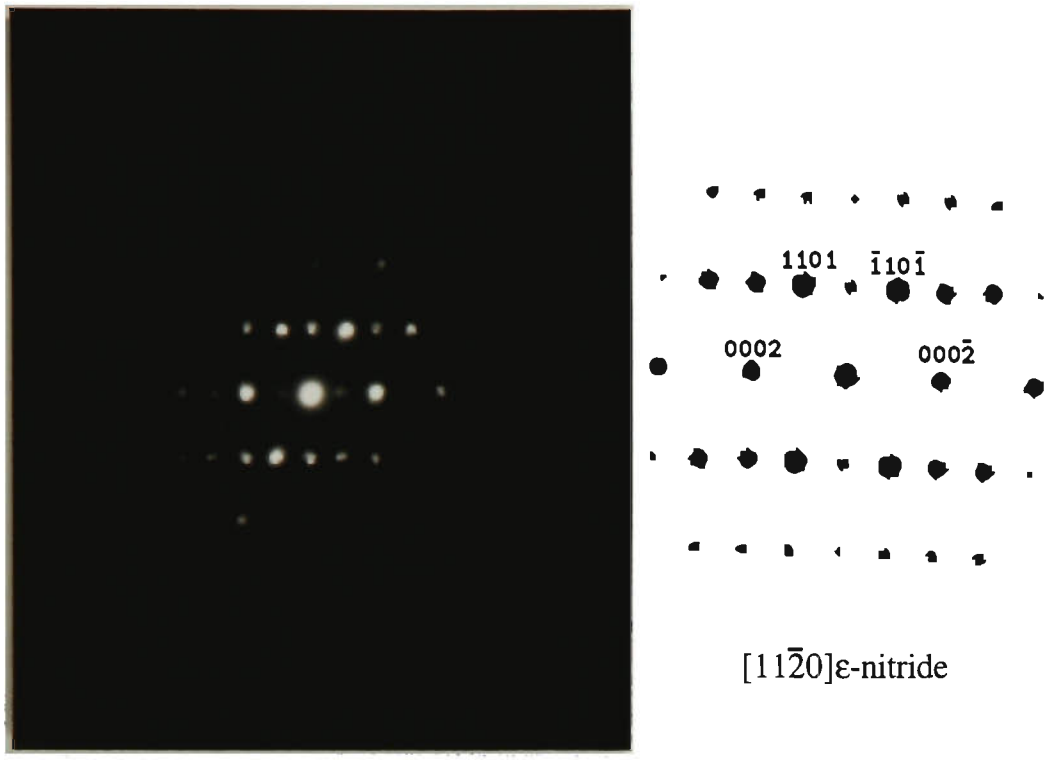

Fig.61 The NBD pattern of the ε nitride shown in Fig.58. PI[3] treated at 520°C.

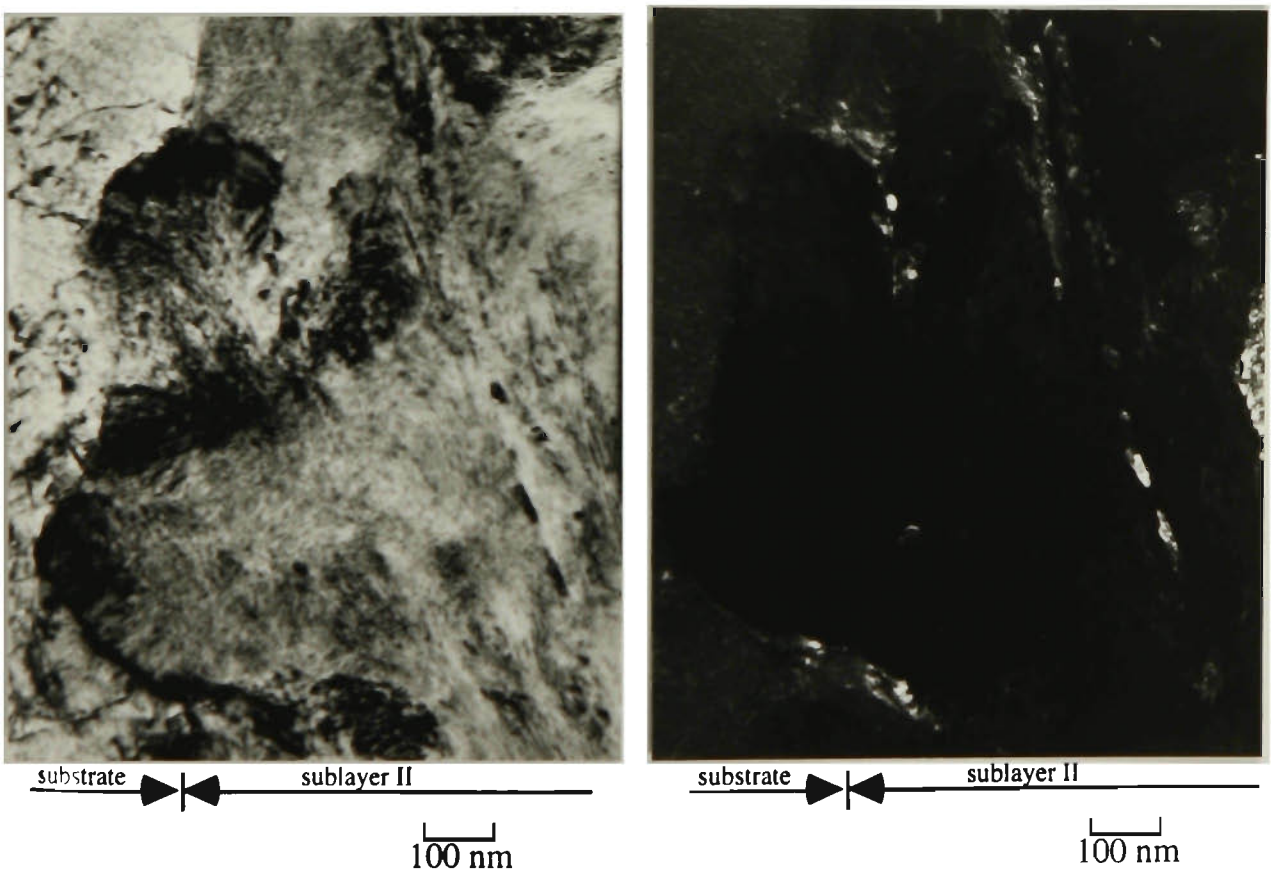

a. BF image of the interface between the sublayer II and the substrate.

b. DF image of the same area as (a), using $(\bar{2}110)CrMoN_x$ to form the image.

Fig.62 Details of the interface between the sublayer II and the substrate. Small amount of tiny $CrMoN_x$ and Cr_2N precipitates can be seen at the boundaries between the CrN and α colonies. PI[3] treated at 520°C.

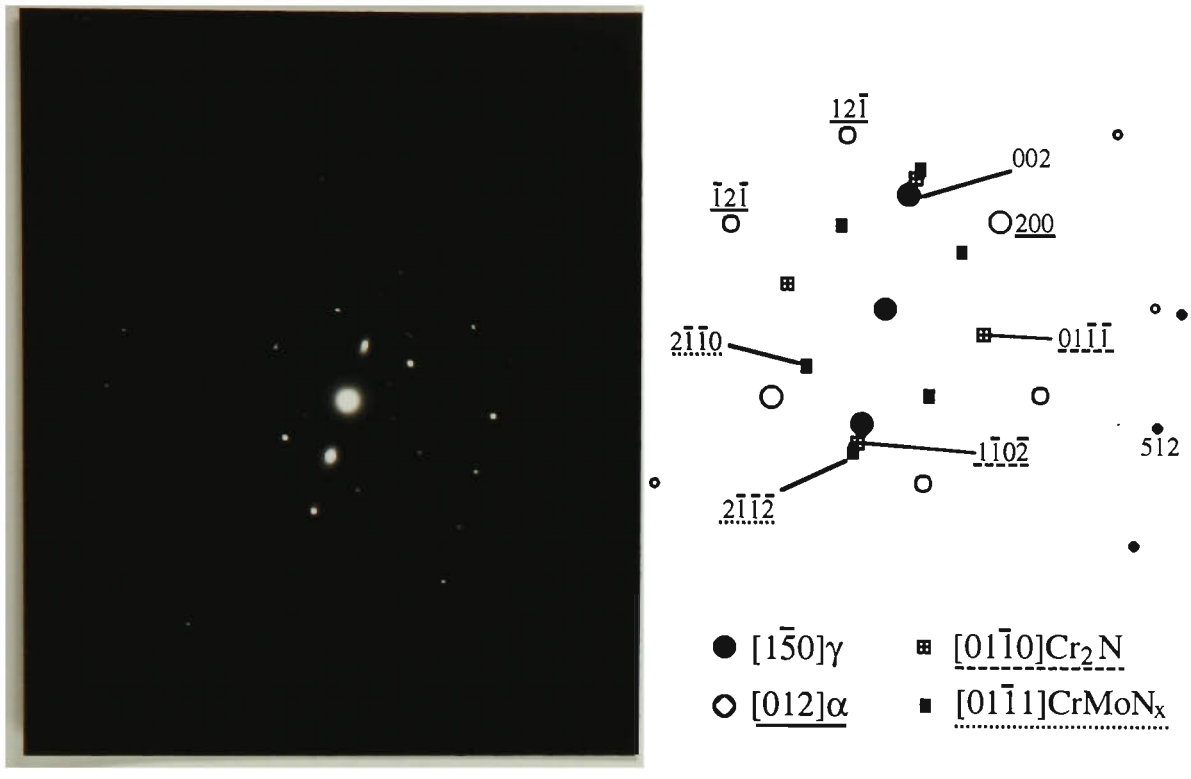

c. SAD pattern taken from the interface area shown in (a)

Fig.62**(cont.)** Details of the interface between the sublayer II and the substrate. Small amount of tiny $CrMoN_x$ and Cr_2N precipitates can be seen at the boundaries between the CrN and α colonies. PI[3] treated at 520°C.

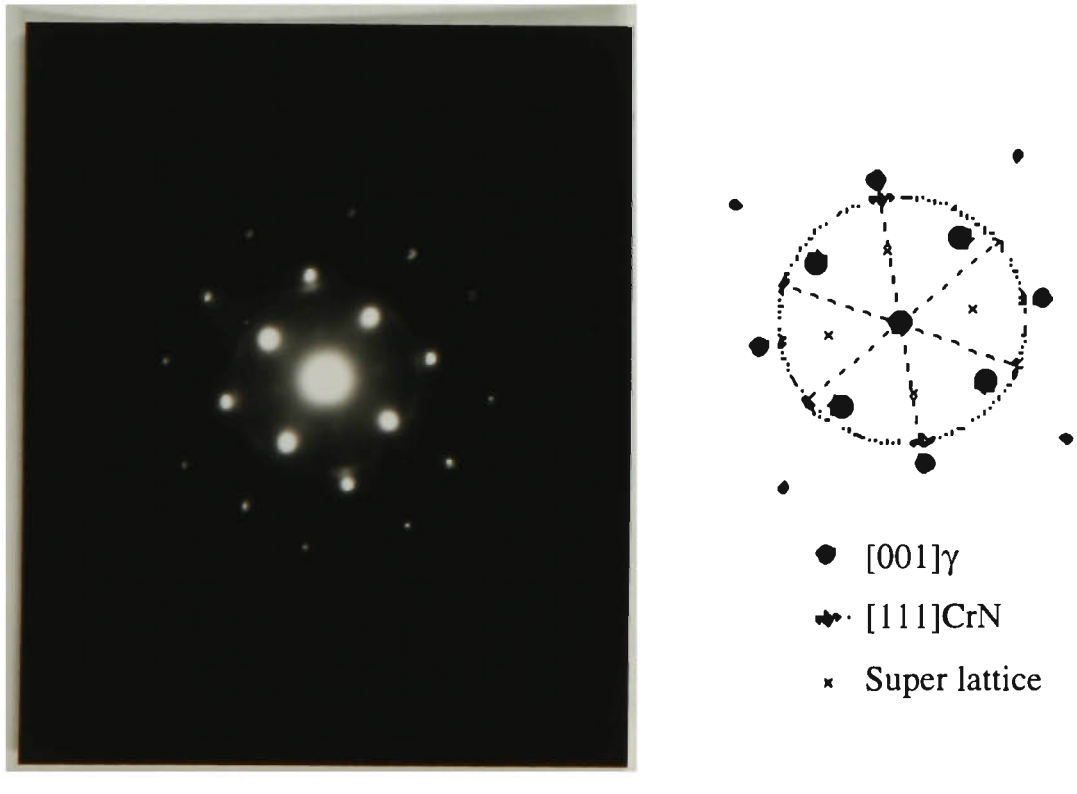

Fig.63 NBD pattern of the substrate just in front of the interface, showing CrN starting to precipitate from the γ. {100}fcc superlattice shows that γ', as a transition phase between the γ and CrN, may exist at the interface as well. PI[3] treated at 520°C.

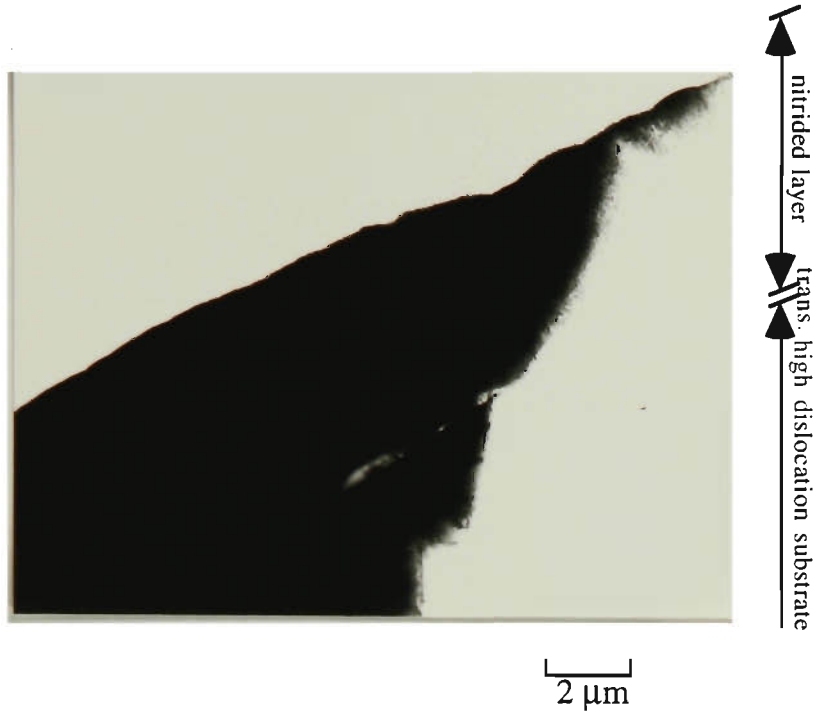

Fig.64 The entire depth of plasma nitrided layer, treated at 350°C, 5 hours. The nitrided layer is nanocrystalline, about 6 µm thick. A 70-80 nm thick transition zone is observed between the nitrided layer and the substrate. The first γ grains (about 7-8 µm thick) under the nitrided layer shows expansion and higher dislocation density.

a. Typical nanocrystalline structure of the nitrided layer

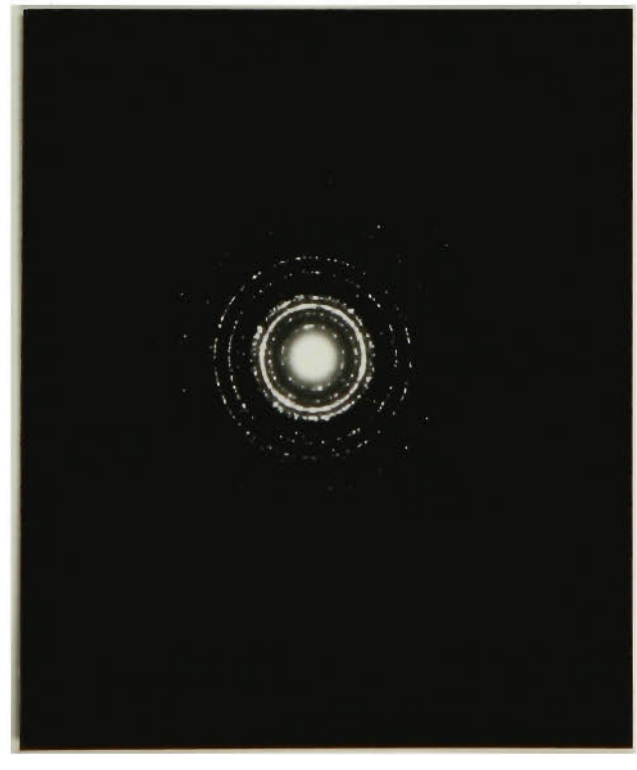

b. SAD pattern of the nanocrystalline structure

Fig.65 Tipical nanocrystalline structure of the nitrided layer, 350°C nitrided, 5 hours. The size of the precipitates is generally less than 30 nm. The SAD pattern of the nanocrystalline structure is too complicated to discern individual precipitates.

a. Typical Cr_2N or $(Cr,Fe)_2N$ precipitate (dark area at the centre of the image).

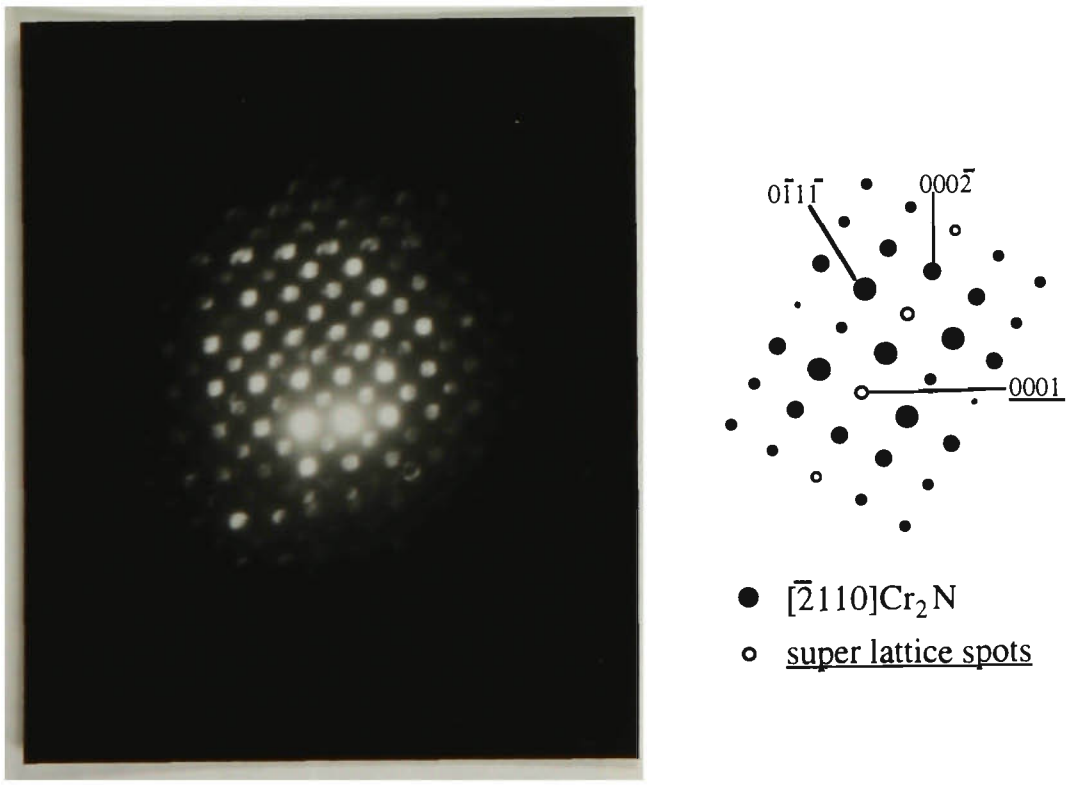

b. NBD pattern of the Cr_2N precipitate shown in (a). The superlattice spots indicate that the Fe atom may take Cr atom positions to form $(Cr,Fe)_2N$.

Fig.66 Typical Cr_2N precipitate and its corresponding NBD patterns. The Fe atom may take the position of the Cr atom to form $(Cr,Fe)_2N$. 350°C nitrided, 5 hours.

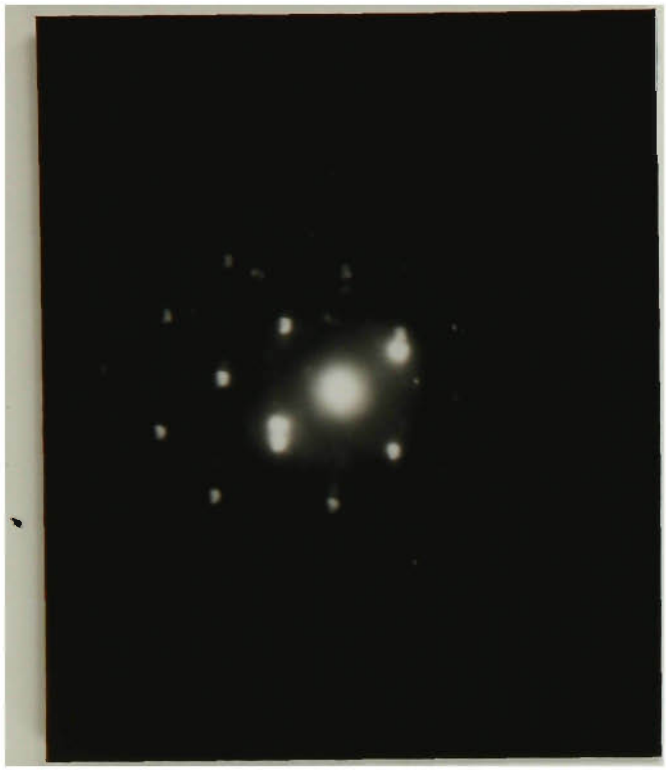

Fig.67 NBD pattern shows the orientation relationship between the γ and Cr_2N precipitates in nitrided layer. 350°C nitrided, 5 hours.

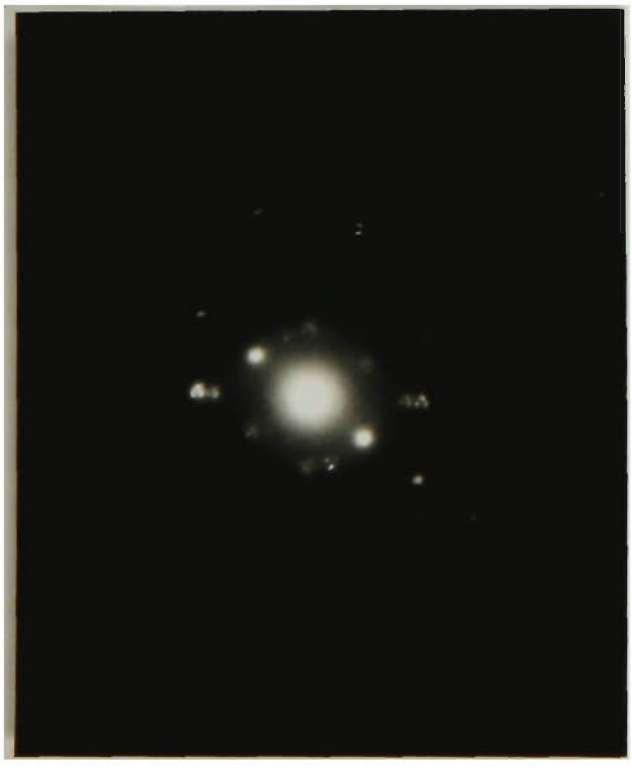

Fig.68 NBD pattern of the nitrided layer, showing the N-W orientation relationship between the γ and α precipitates, as well as twin structure of γ. 350°C nitrided, 5 hours.

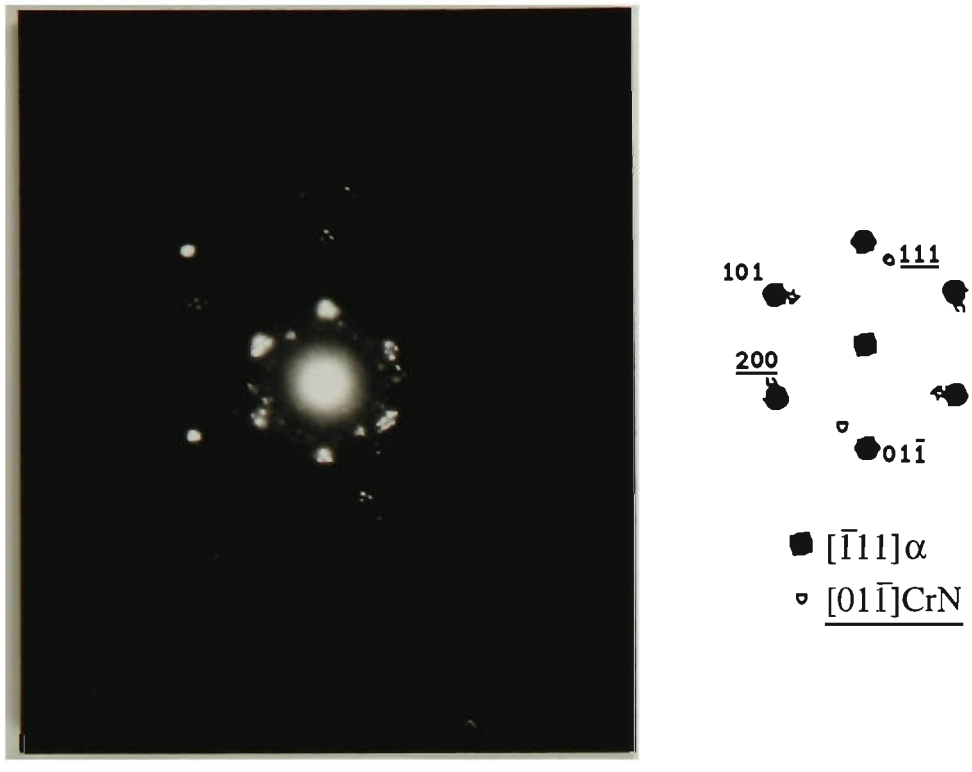

Fig.69 One of the NBD pattern taken at the near surface region of the nitrided layer, showing that traces of CrN exist at the near surface region. K-S relation between α and CrN. 350°C nitrided, 5 hours.

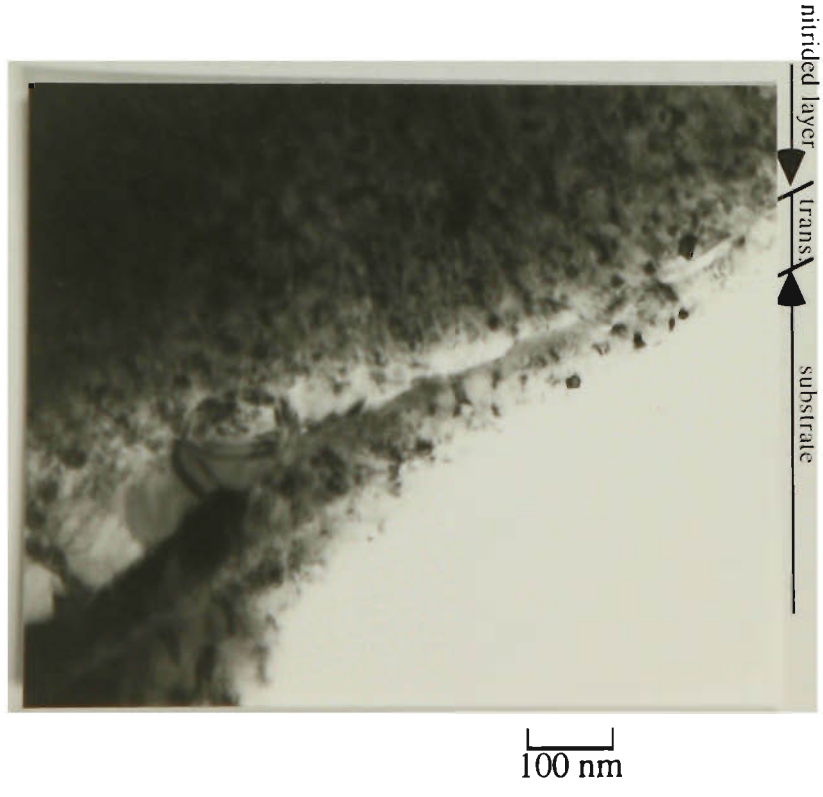

Fig.70 The thin transition layer between the nitrided layer and the substrate. However, NBD study of this transition layer doesn't show any structural difference from the nitrided layer. 350°C nitrided for 5 hours.

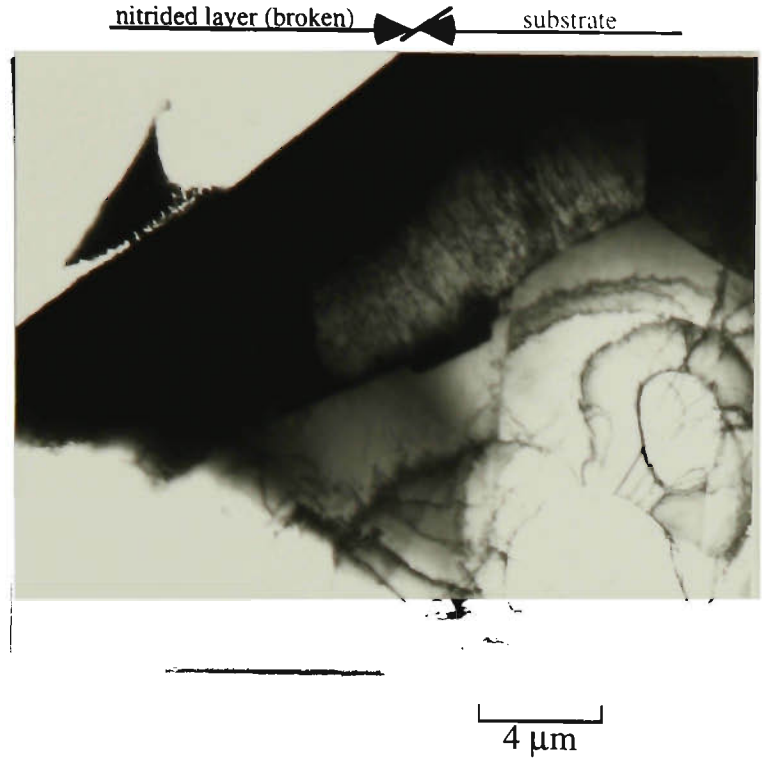

Fig.71 The first layer of the γ grains under the nitrided layer shows higher dislocation density than the normal unexpanded austenite grains. 350°C nitrided for 5 hours.

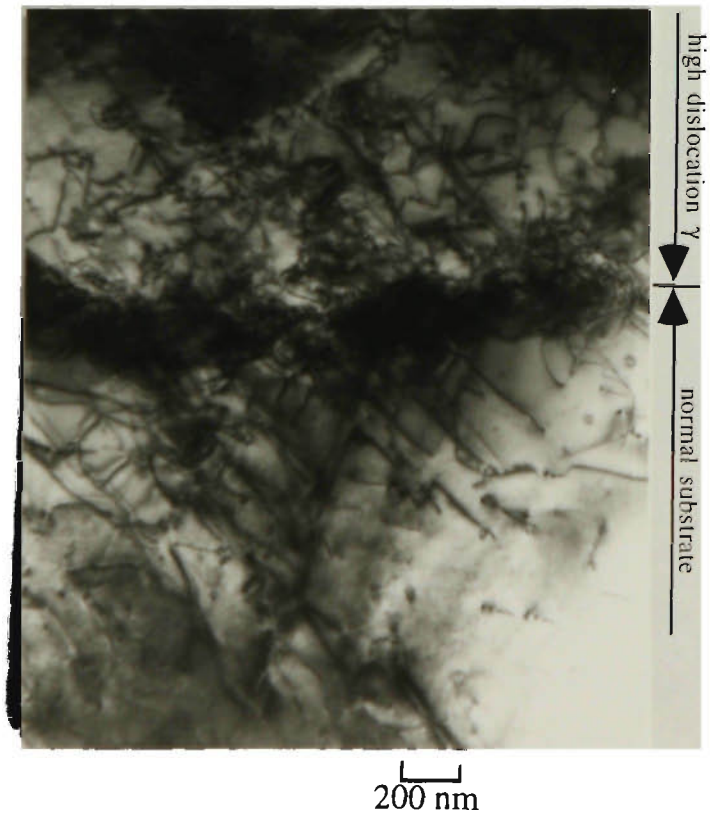

Fig.72 Detail of the boundary between the first layer of high dislocation γ grains and the normal γ grains underneath. 350°C nitrided for 5 hours.

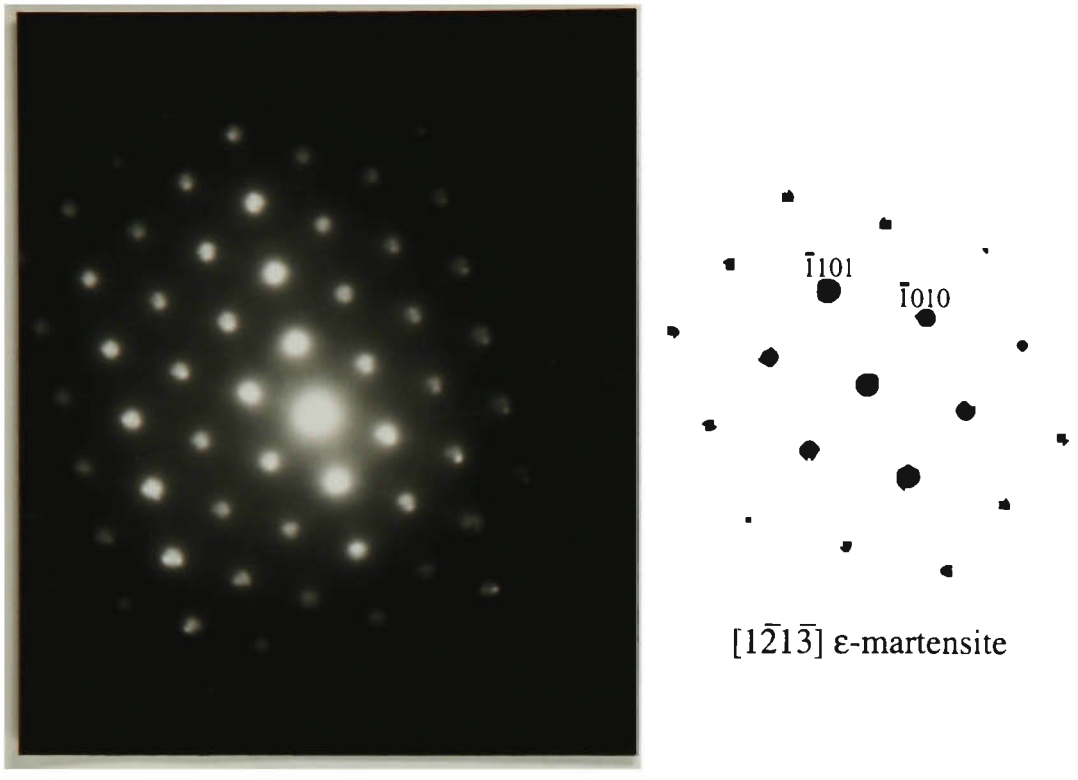

Fig.73 NBD pattern of the ε-martensite, detected in the high dislocation substrate at the area just off the interface. 350°C nitrided for 5 hours.

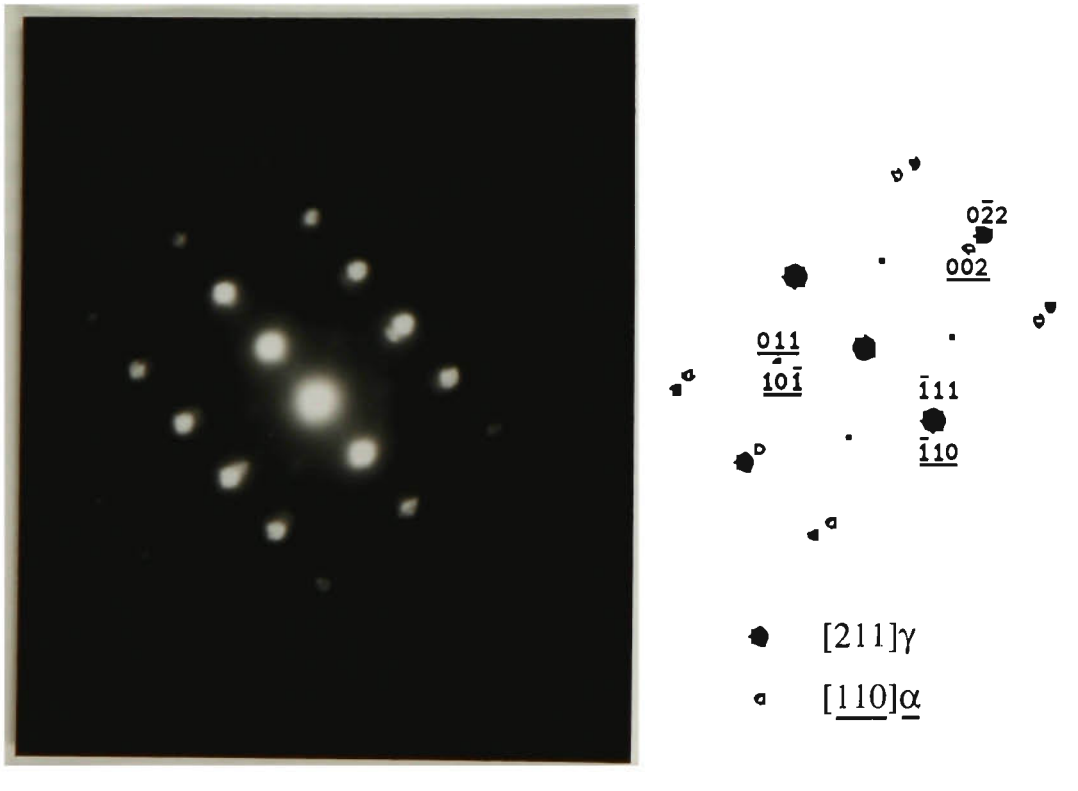

Fig.74 NBD pattern taken in the high dislocation substrate just in front of interface, showing α-ferrite together with expanded γ-austenite. N-W relation is observed between γ and α The expansion of γ is about 5-6% but quickly drops to about 3%, then gradually decreases to zero towards the end of the high dislocation zone. The very weak {110}α spots (off Bragg setting) indicates that the α precipitates are very small.

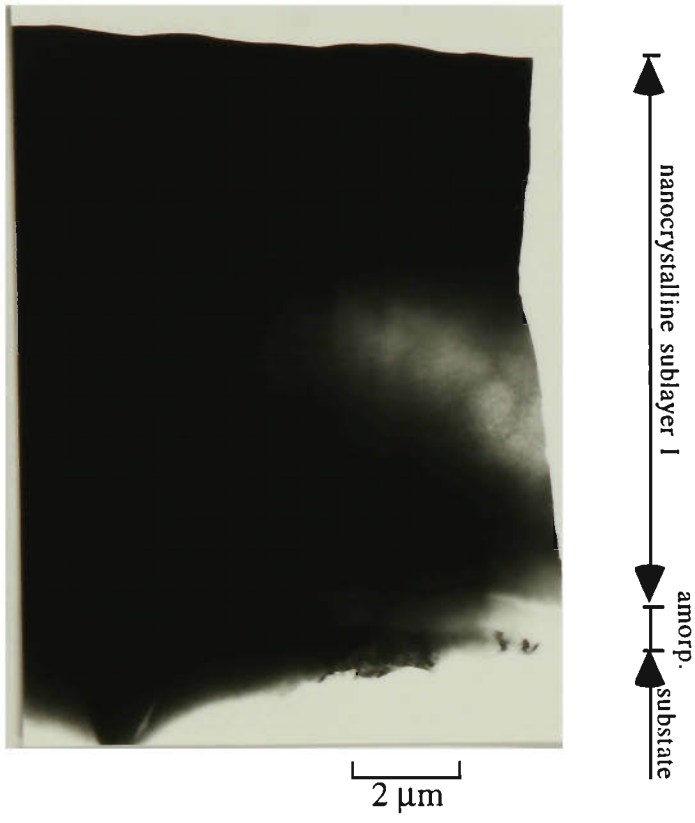

Fig.75 The plasma nitrided layer, treated at 450°C, 5 hours. The whole nitrided layer is about 10-11 μm thick, divided into two sublayers. The first sublayer is nano-crystalline and about 10 μm thick. Very fine γ, CrN and α phases are found in the first sublayer. The second sublayer is amorphous and about 0.6-0.7 μm thick. Very thin semi-amorphous transition zone (less than 100 nm) is found between sublayer I and sublayer II, as well as beween sublayer II and the substrate. The γ substrate shows about 3% expansion at the near interface area. The expanded γ region is only a few hundred nm thick.

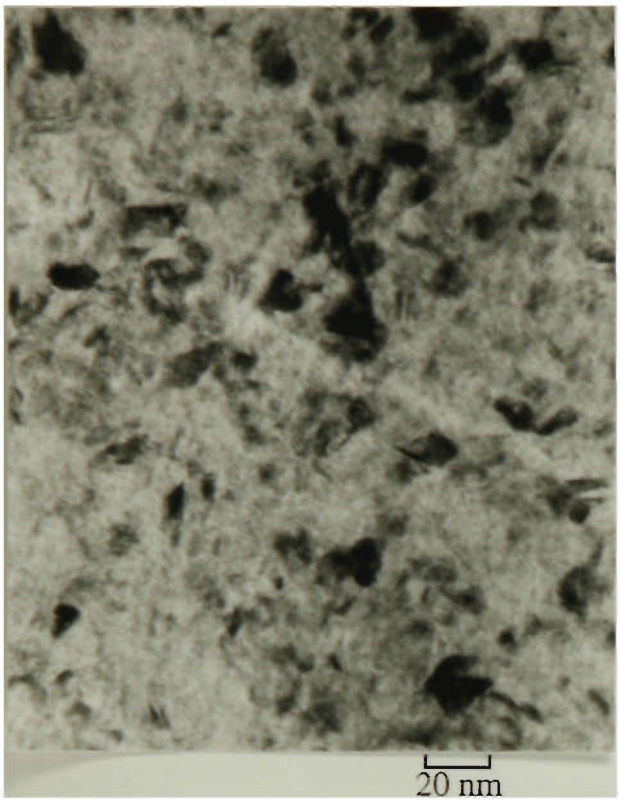

a. The details of the nano-crystalline structure of the first sublayer

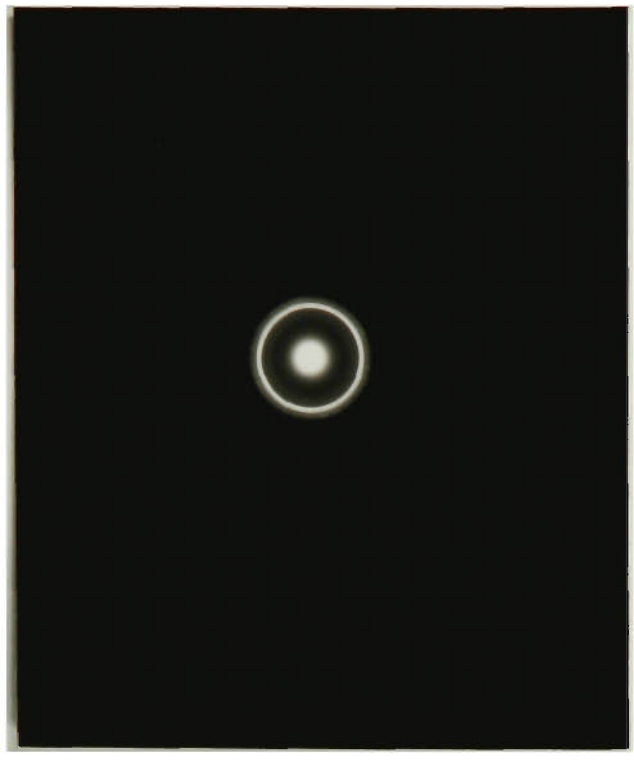

b. SAD pattern of the nanocrystalline structurte of the first sublayer

Fig.76 Details of the nanocrystalline sublayer I. The size of the precipitates is less than 10 nm. The SAD pattern of the nanocrystalline structure is too complicated to discern the precipitates. 450 nitrided, 5 hours.

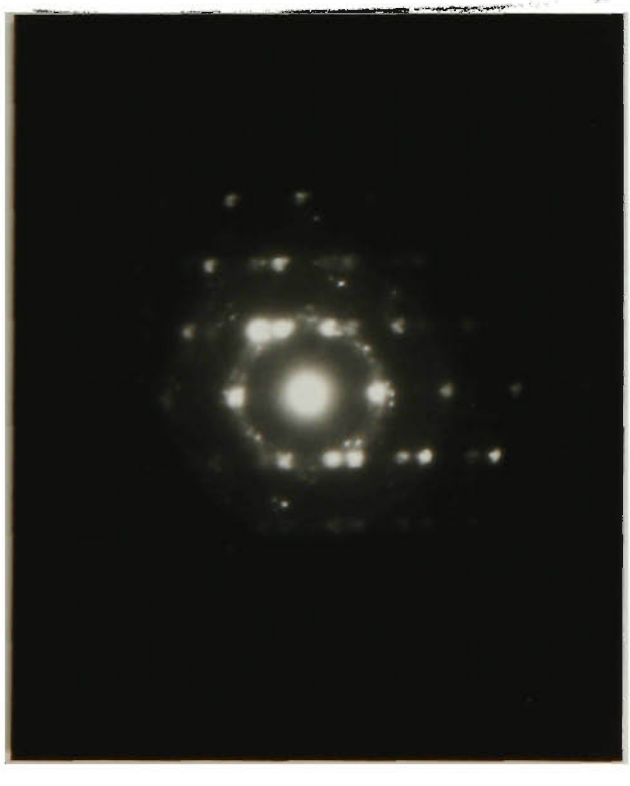

Fig.77a NBD pattern of the γ precipitate in nanocrystalline sublayer I, showing twin structure in γ precipitate. 450°C nitrided, 5 hours.

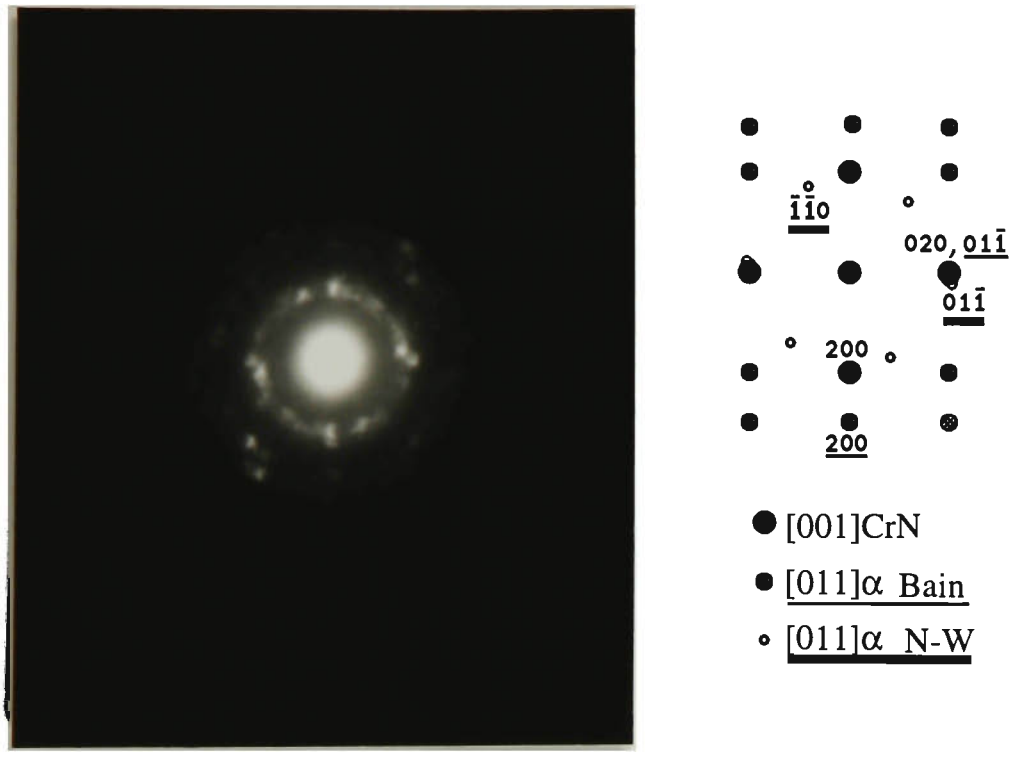

Fig.77b NBD pattern of the CrN and α precipitates of nanocrystalline sublayer I, both Bain and N-W are observed between the CrN and α. 450°C nitrided, 5 hours.

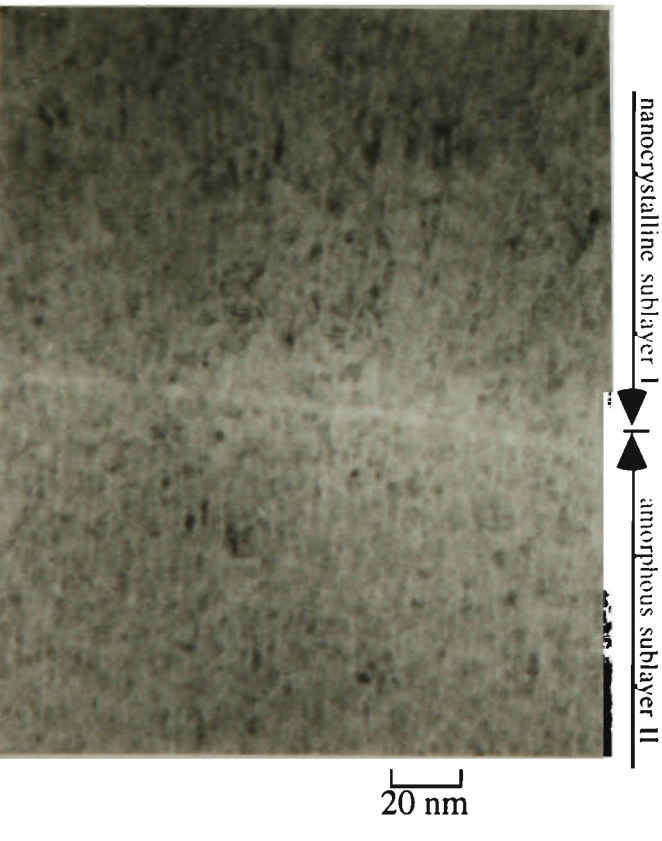

Fig.78 Transition from nanocrystalline sublayer I to amorphous sublayer II. 450 nitrided, 5 hours.

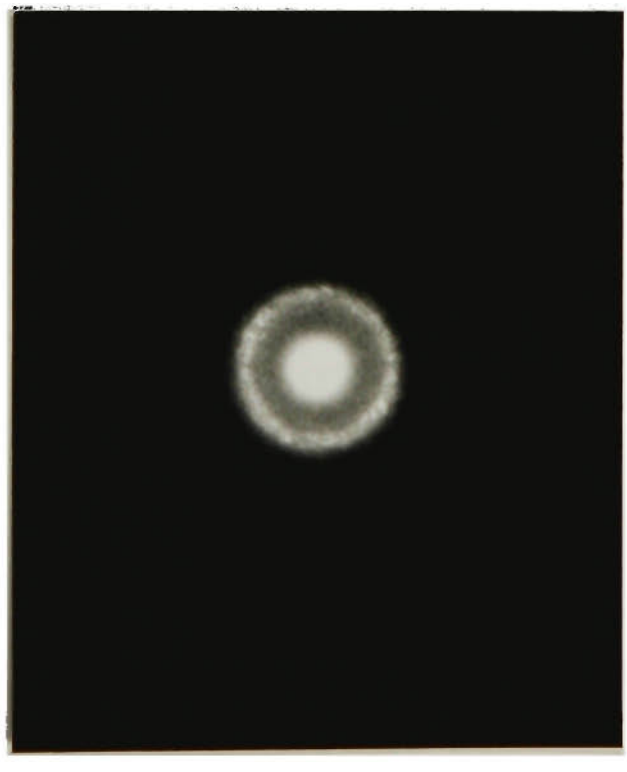

Fig.79 NBD pattern of the amorphous sublayer II. 450°C nitrided, 5 hours.

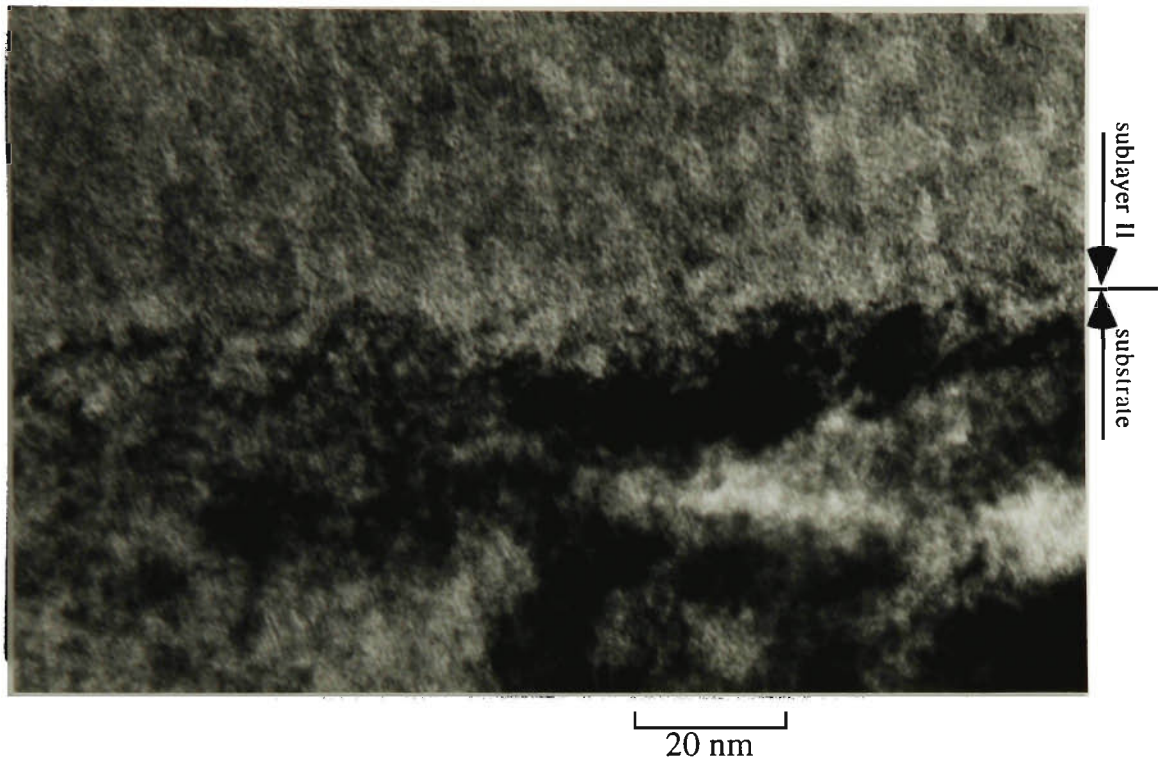

Fig.80 HREM image of the interface between the sublayer II and the substrate. 450°C nitrided, 5 hours. Notice some crystalline structure crosses over at the interface from substrate into amorphous sublayer II.

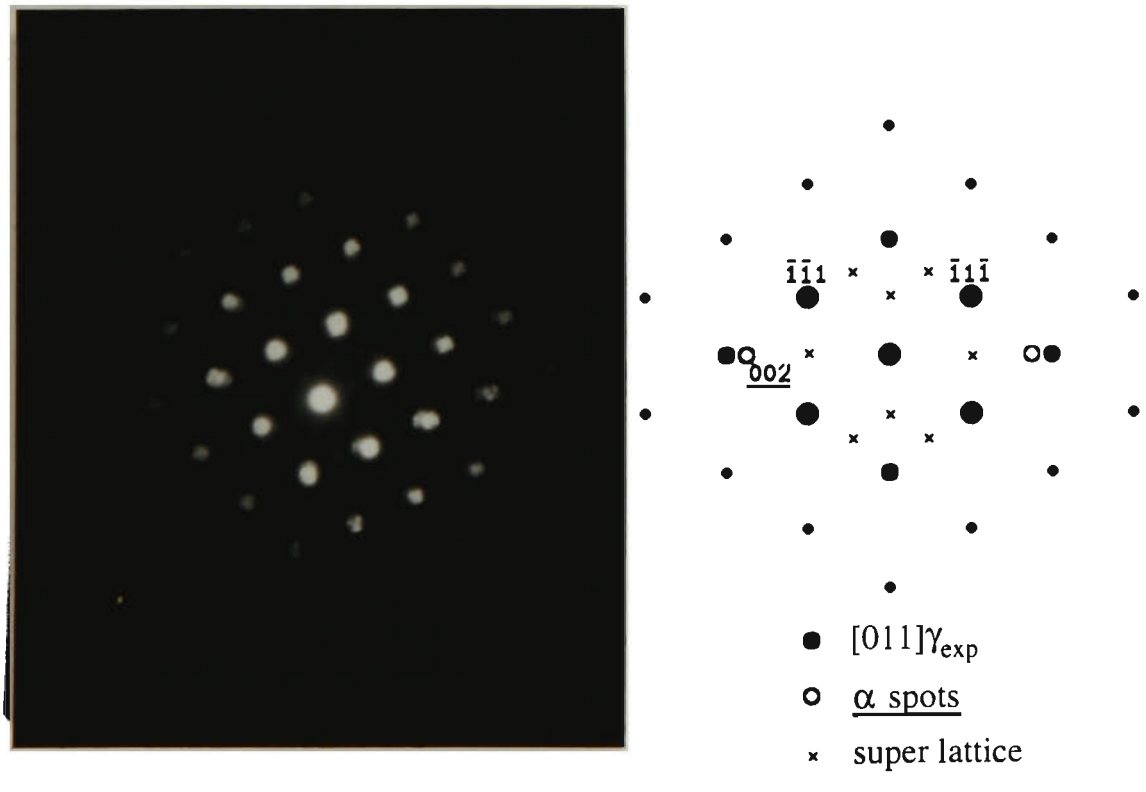

Fig.81 NBD patterns of the substrate just below the interface, showing γ_{exp} and some α. The expansion of γ_{exp} is about 3%. The presence of superlattice spots suggest that the γ' phase may also exist at the interface.

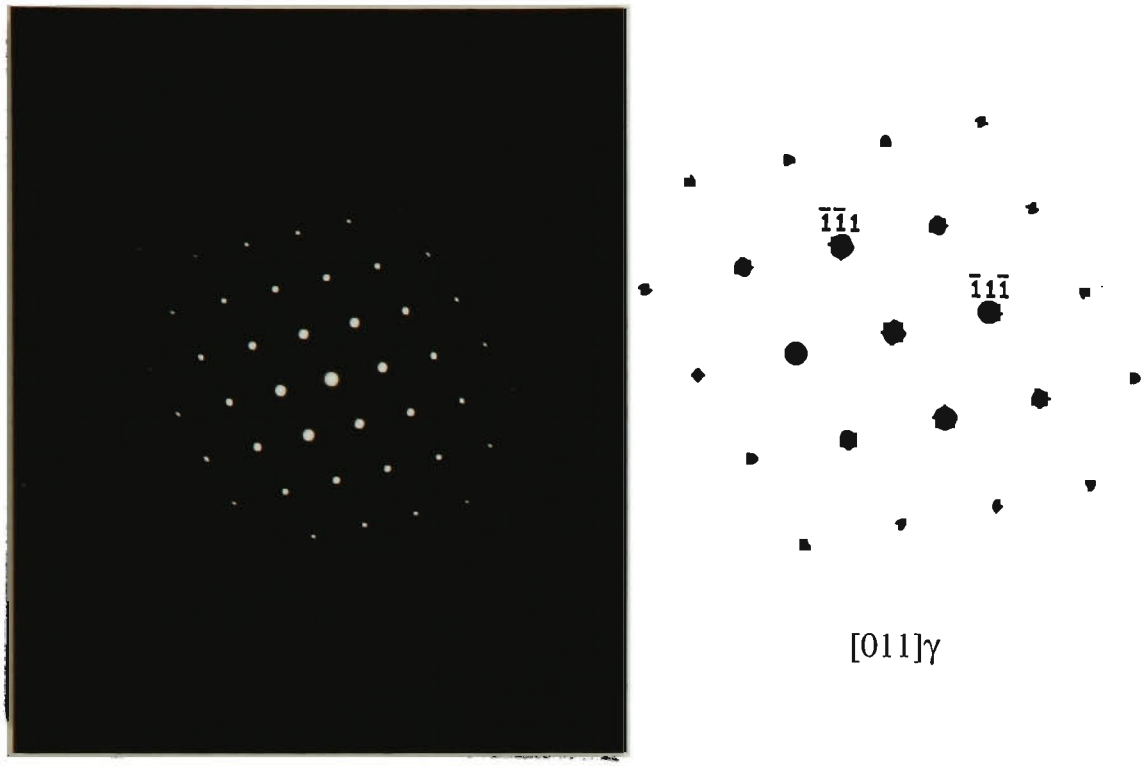

Fig.82 SAD of the substrate taken slightly off the interface. The SAD pattern shows only normal unexpanded γ diffraction. 450°C nitrided, 5 hours.

Fig.83 Typical structure of the nitrided layer, 520°C nitrided, 5 hours. A small amount of island-like retained austenite can be observed between the lamellar CrN and α colonies (dark area in the middle of the image).

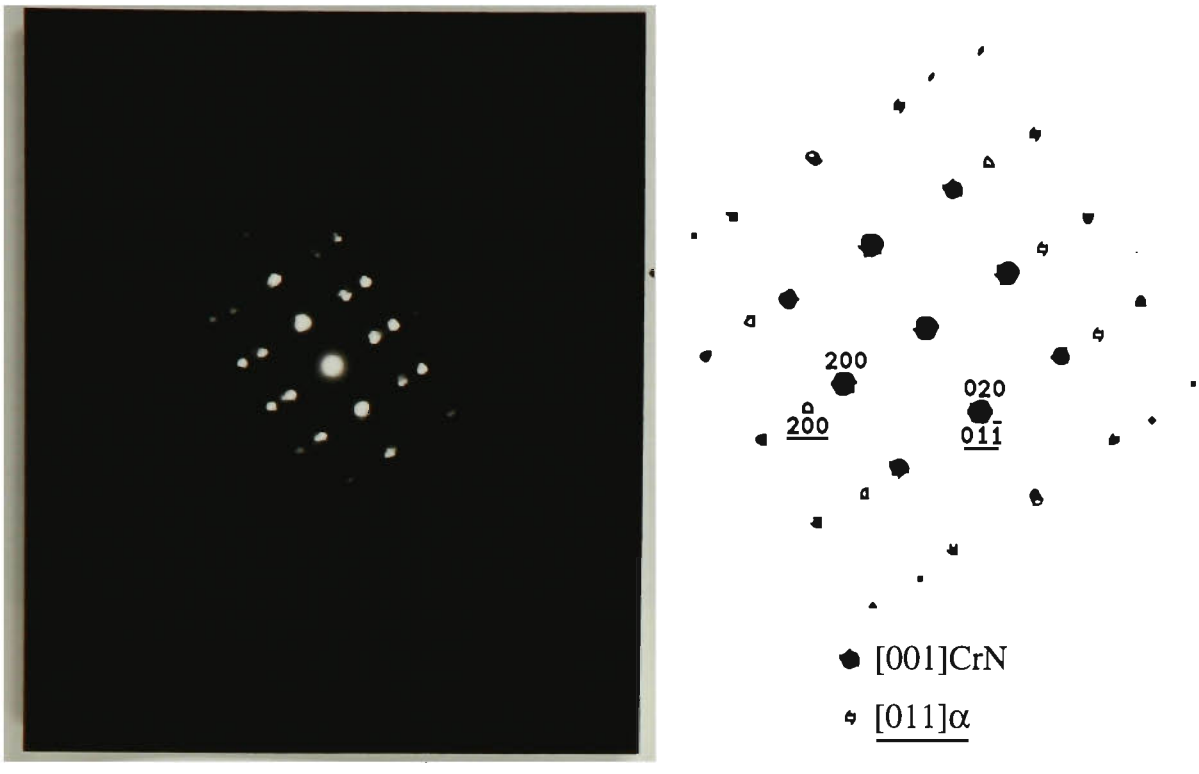

Fig.84 NBD pattern of the lamellar CrN and α precipitates. Bain ralation between the two phases. 520°C nitrided, 5 hours.

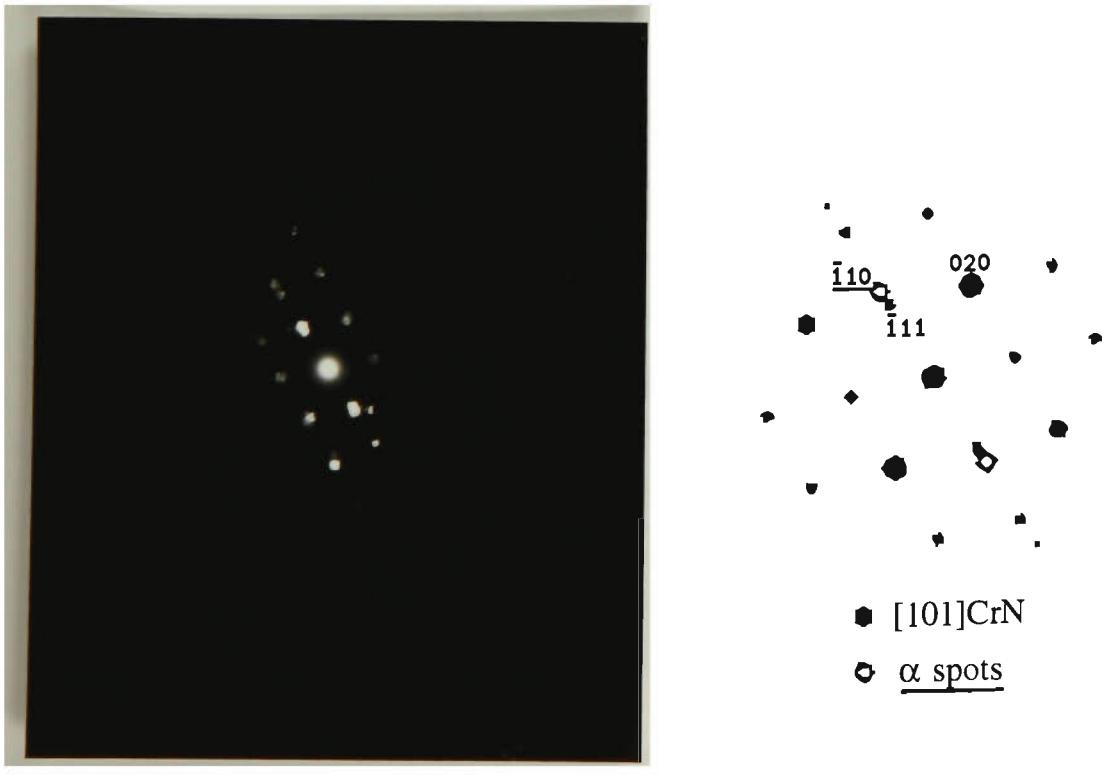

Fig.85 NBD pattern of the lamellar CrN and α precipitates. N-W relation between the two phases. 520°C nitrided, 5 hours.

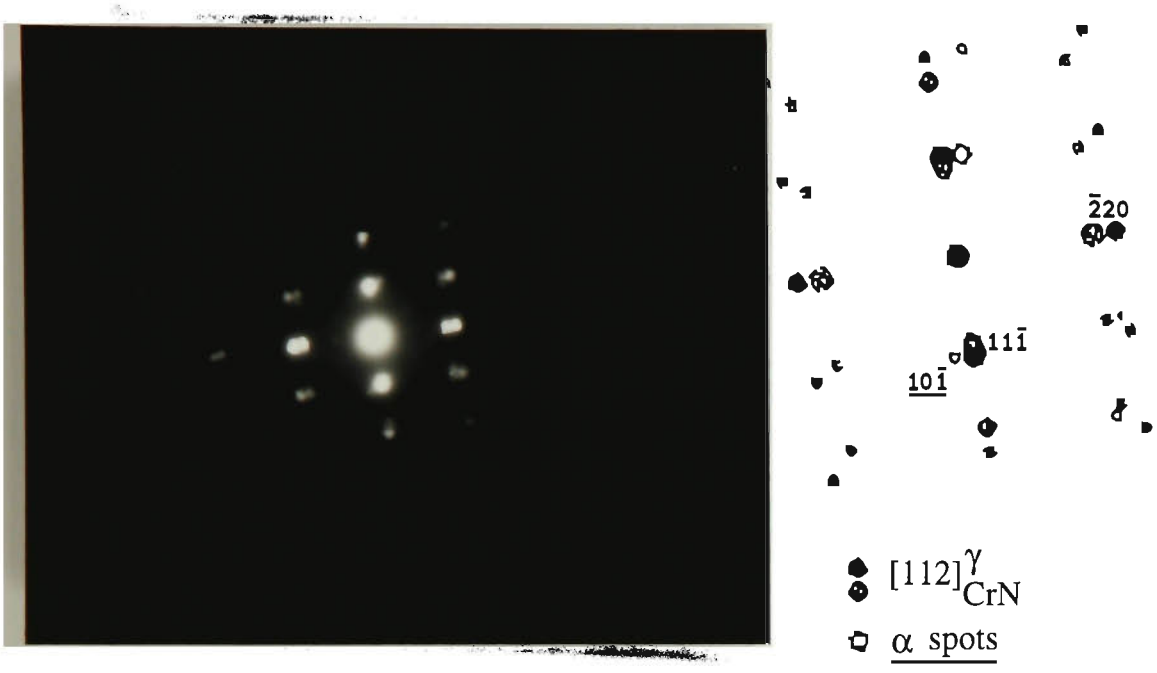

Fig.86 NBD pattern of the γ islands with surrounding lamellar CrN and α, both γ and CrN are fcc and have the same orientation, N-W relation between fcc γ (or CrN) and α . 520°C nitrided, 5 hours.

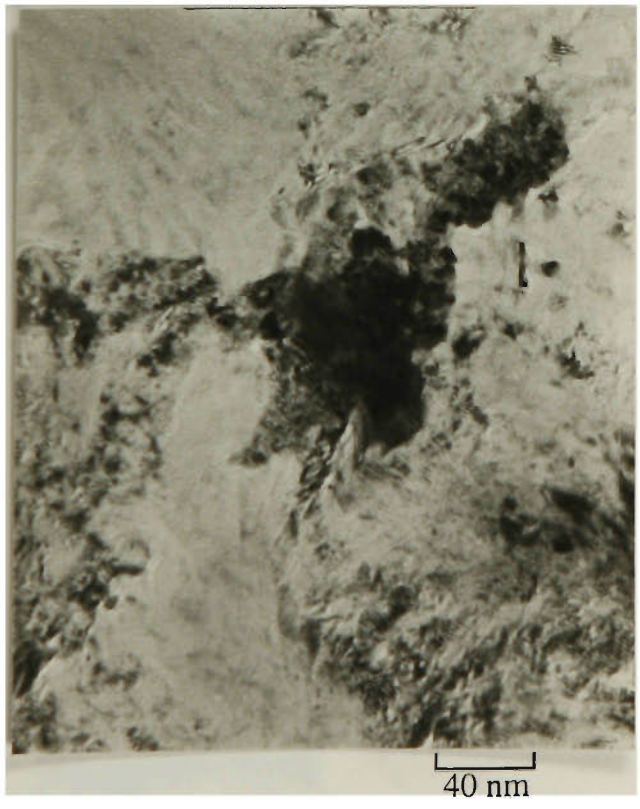

Fig.87a One of the γ islands between CrN and α colonies (dark area in the middle of the image) at the near surface region of the nitrided layer. ε-nitride is detected to co-exist with γ in the island.

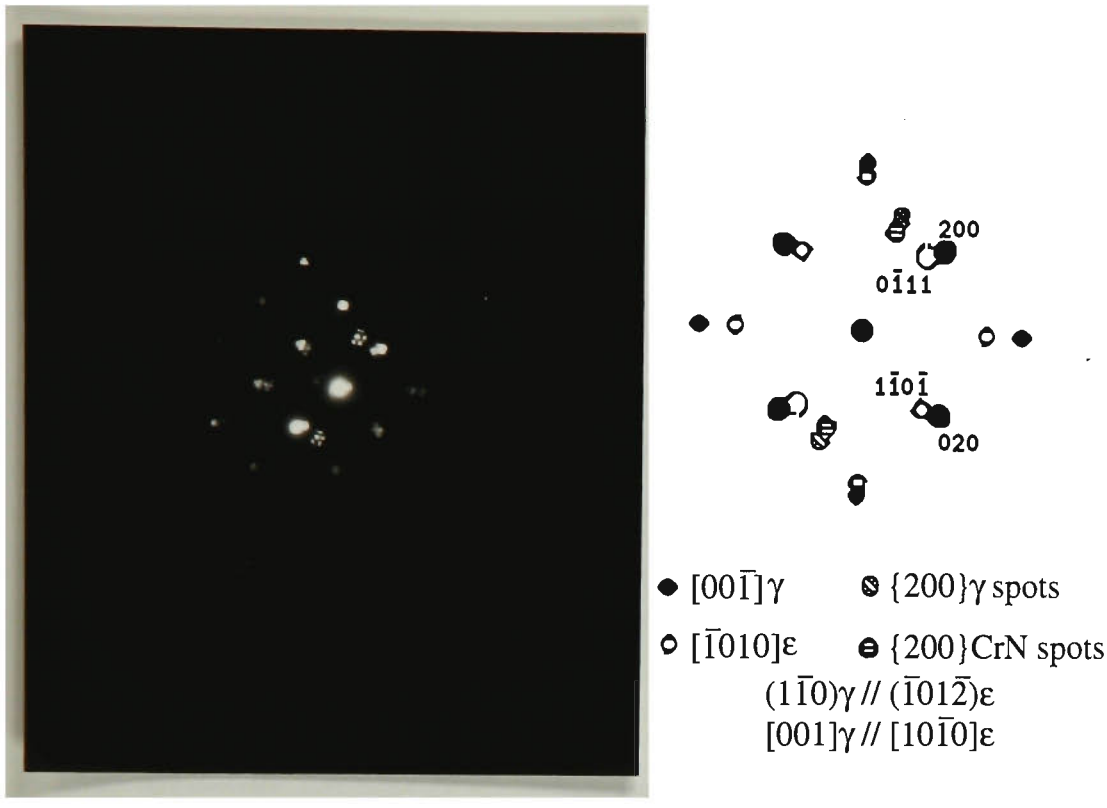

Fig.87b NBD pattern of the γ island shown in Fig.85a. ε-nitride is detected in the island. The orientation relationship between the γ and ε-nitride follows: (1$\bar{1}$0)γ // ($\bar{1}$01$\bar{2}$)ε, [001]γ // [10$\bar{1}$0]ε. 520°C nitrided, 5 hours.

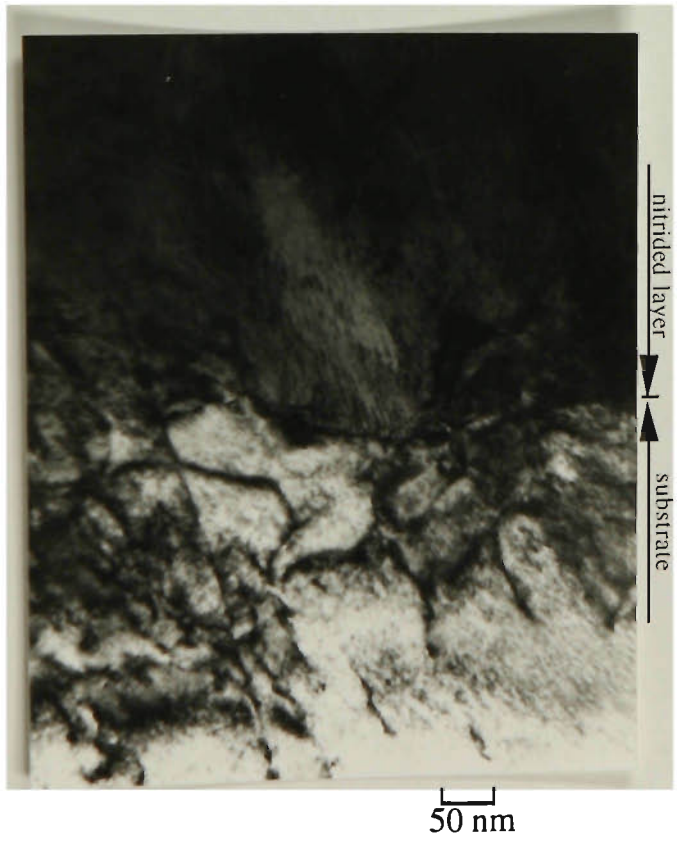

Fig.88a The interface between the nitrided layer and the substrate. 520°C nitrided, 5 hours.

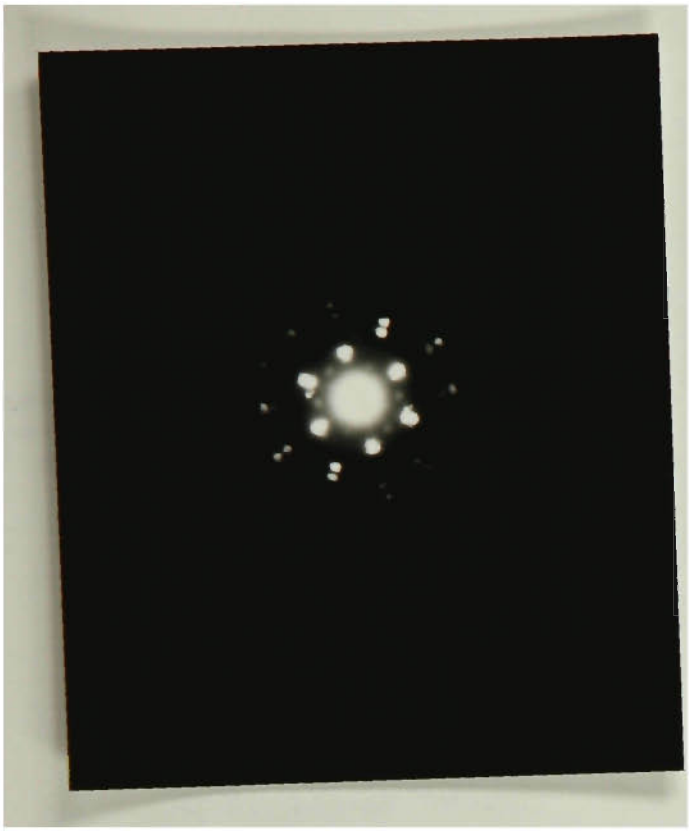

Fig.88b NBD pattern taken at the interface, showing γ, CrN and traces of α. N-W relation is observed between the fcc γ (or CrN) and α. The dim superlattice spots indicate that γ', as a transition phase between the γ and CrN, may exist as well.

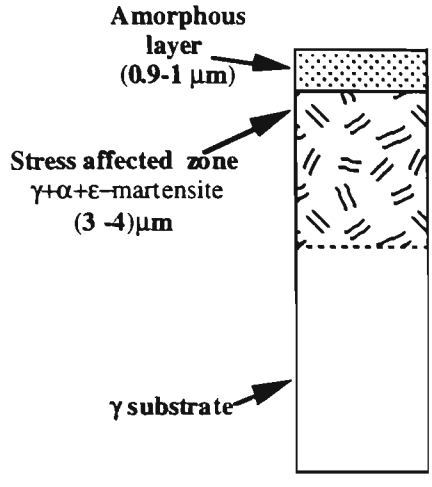

a. PI³ treated at 150°C
$2x10^{17}$ atoms/cm², 430 min.

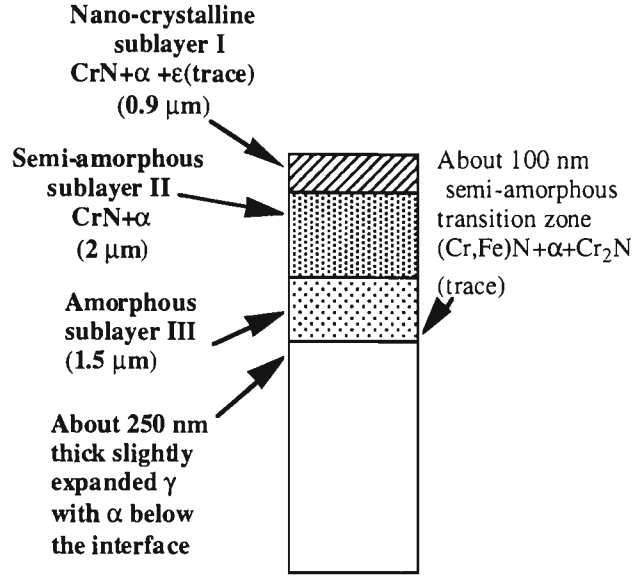

b. PI³ treated at 250°C
$8x10^{17}$ atoms/cm², 250 min.

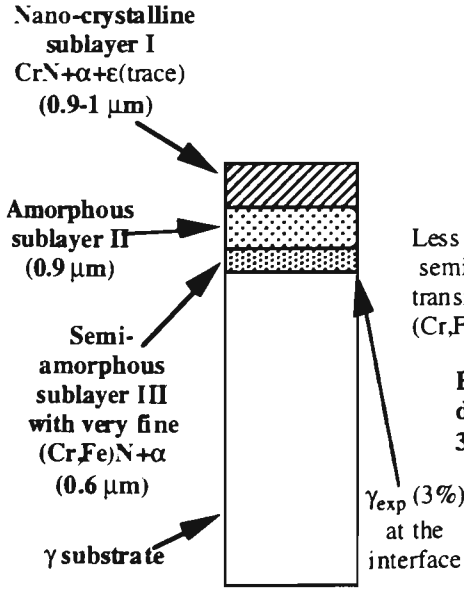

c.PI³ treated at 350°C
$8x10^{17}$ atoms/cm², 130 min.

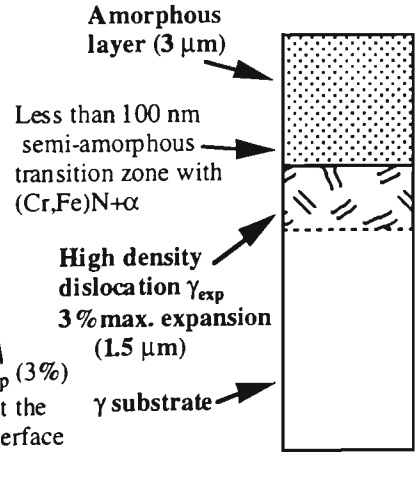

d. PI³ treated at 450°C
$8x10^{17}$ atoms/cm², 70 min.

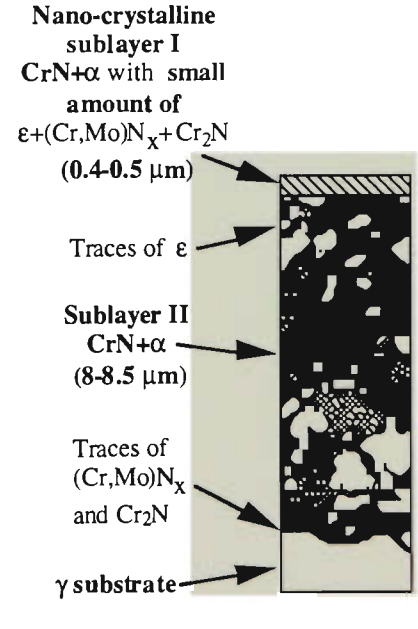

e. PI³ treated at 520°C
$8x10^{17}$ atoms/cm², 40 min.

Figure 89 Schematic illustration of the PI³ treated 316 stainless steel samples

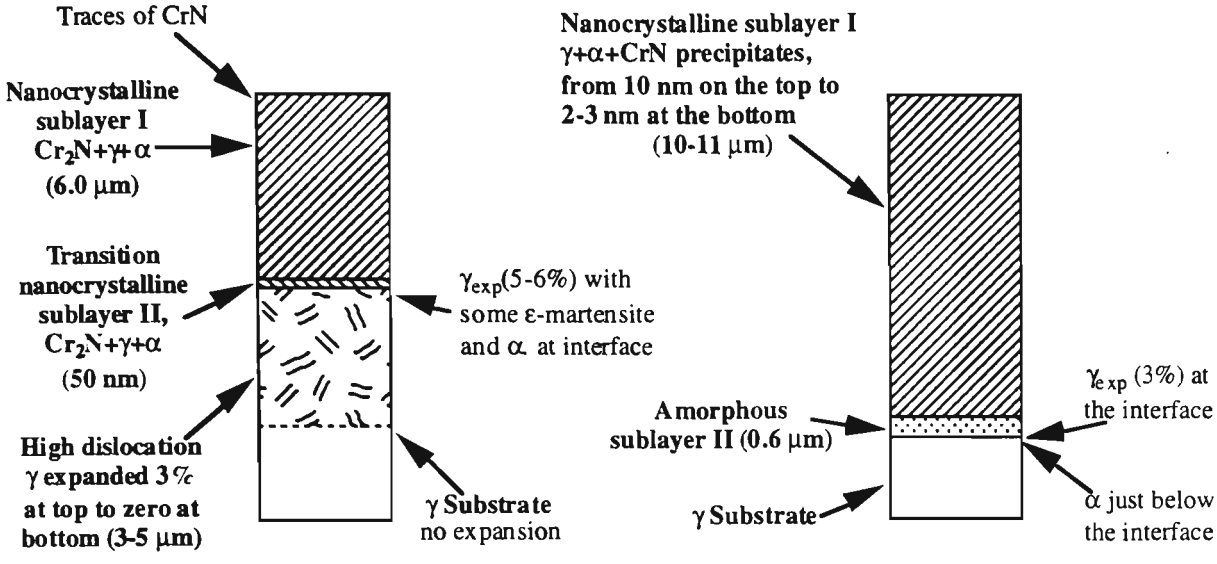

a. 350°C Plasma nitrided, 300 min.

b. 450°C Plasma nitrided, 300 min.

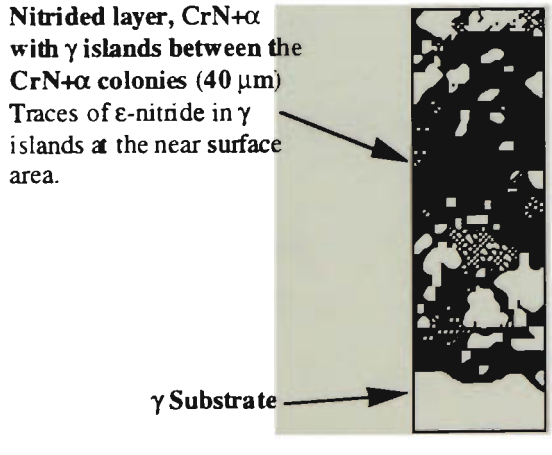

c. 520°C Plasma nitrided, 300 min.

Figure 90 Schematic illustration of the plasma nitrided 316 stainless steel samples

CHAPTER 5 DISCUSSION

5.1 XTEM + NBD and GAXD CHARACTERISATION

As discussed in Chapter 2, due to the limitations of the lateral (about 10 mm) and the depth resolutions (about 30 μm) of the x-ray diffraction technique, it is very difficult to discern individual phases in a very fine multi-phase system, especially when the phases in the system have their diffraction peaks close to each other. When using XRD to characterise a very shallow ion implanted layer, the substrate may contribute to the diffraction, rendering the interpretation of the diffraction results even more complicated. Although the depth resolution can obviously be improved, in the GAXD configuration, the lateral resolution is still too poor to discern conclusively the constituents of a fine multi-phase system. Therefore, microstructural characterisation of nitrogen ion implanted or nitrided surfaces by XRD or GAXD is not straightforward and can easily lead to an erroneous interpretation.

5.1.1 Comparison of GAXD and XTEM+NBD Results

5.1.1.1 PI^3 Treated Samples

a). 150°C PI^3 treatment

According to XTEM+NBD, the PI^3 specimen at 150°C consisted of a 1 μm thick amorphous layer on the surface, with a underlying 3-4 μm thick heavily stressed austenite substrate containing traces of α and ε-martensite. In stark contrast, the GAXD pattern of the same sample showed only sharp un-shifted γ peaks. The only evidence to suggest an amorphous structure in the GAXD pattern is the presence of a small hump just to the left of the strongest peak, (111)γ, which has resulted in a slight broadening (See Figure 11a). The fact that there is no evidence of α and ε-martensite in the GAXD

spectrum indicates the inability or insensitivity of GAXD to identify minor phases that are present only in small amounts.

Undoubtedly, the sharp un-shifted γ peaks shown in the GAXD pattern originated from the γ substrate. This serves to illustrate that the X-rays, even for 1° glancing angle, penetrated more than 1 μm and produced strong signals from the substrate. It is worth mentioning that according to conventional wisdom, the maximum depth of X-ray penetration in Fe, at such an angle must be around 70 nm (0.07 μm) [43]. Both the GAXD and NBD patterns show that it is unlikely that significant nitrogen is dissolved in the stress affected γ.

b). 250°C PI^3 treatment

The GAXD pattern of the sample PI^3 treated at 250°C also shows sharp γ peaks. There is a broadened peak beside (111)γ (the strongest peak) which was labelled as γ_{exp}, consistent with previous work [4]. Bearing in mind that XTEM + NBD unambiguously demonstrated the presence of nanocrystalline CrN and α, in addition to semi-amorphous and amorphous structures within the modified layer, it is possible that this conveniently labelled γ_{exp} peak is in fact a manifestation of several mixed peaks originating from the complex phases of this modified layer.

Another interesting feature on the GAXD pattern is the slight hump between 70° and 80° where the (220)CrN and (200)α peaks should be located (Figure 11b). This hump is probably a true feature, reflecting the nanocrystalline nature of CrN and the presence of α precipitates, but it is too weak, compared to the γ and γ_{exp} peaks, to be indexed.

Since the thickness of the nanocrystalline sublayer from XTEM is about 0.9 μm, the minor nature of the hump in the GAXD pattern, if it does indeed stem from CrN and

α precipitates, indicates that glancing angle x-rays penetrated well beyond the thickness of the nanocrystalline layer. In fact, the strong and sharp γ peaks in the GAXD pattern suggest the glancing angle x-rays may have even penetrated through the entire modified layer into the γ substrate, i.e. more than 4.5 μm.

c). 350°C PI^3 treatment

It is interesting to note that the GAXD pattern of the sample PI^3 treated at 350°C (Figure 11c) shows quite strong peaks which are conveniently ascribed to expanded γ, even though the total thickness of the modified layer is thinner than the $PI^3$250°C treated sample. Since no expanded γ was revealed by XTEM+NBD, and the relative intensities of the "γ_{exp}" peaks are also different from the γ peaks, the "expanded γ" peaks are believed to have originated from the semi-amorphous sublayer III which inherits some of the structural features of the γ substrate, as shown in Figures 43-44, together with mixed information from other constituents of the modified layer.

Similar to the GAXD pattern of the 250°C PI^3 treated sample, there is a slight hump between 70° ~ 80° which corresponds to overlapped (220)CrN and (200)α diffraction peaks. The slight hump and the sharp γ peaks of the GAXD pattern again indicate that the penetration of glancing angle x-rays is deeper than the total thickness ($\approx$2.3μm) of the modified layer.

It should be pointed out that the presence of a series of peaks which are shifted to lower diffraction angles compared to austenite peaks might, at first glance, be consistent with the presence of an expanded austenite lattice. However, closer examination reveals that different planes are expanded to different degrees and the amount of expansion is more than that can be accommodated by crystalline structure. This point is discussed further in section 5.1.2.

d). 450°C PI^3 treatment

It appears that the "γ_{exp}" peaks shown in the GAXD pattern for the 450°C PI^3 treated sample match the expanded γ region under the amorphous modified layer, revealed by XTEM and NBD. However, the NBD and SAD patterns of the expanded γ region show that the maximum lattice expansion is only about 3%, while the calculated expansion from the GAXD pattern is as high as 8%. Furthermore, the "γ_{exp}" peaks exhibit different relative intensities to those of austenite, such as an abnormally strong $\{200\}\gamma_{exp}$ peak. It is possible that the clusters in the 3 μm thick amorphous layer, and the very thin semi-amorphous transition zone in the amorphous layer have caused the formation of the so called "γ_{exp}" diffraction peaks, resulting in "γ_{exp}" peaks with an abnormal relative intensity which differs from the relative intensities of the real γ_{exp} diffraction peaks.

The weak $(111)\gamma$ peak at about 50° may arise from the γ substrate below the expanded γ.

e). 520°C PI^3 treatment

The GAXD pattern of the PI^3 sample at 520°C matches quite well with the XTEM+NBD results, showing CrN and α as the dominant phases.

However, the small amount of Cr_2N and $CrMoN_x$ at the interface, as well as ε-nitride, Cr_2N and $CrMoN_x$ in the nanocrystalline sublayer are not revealed by the GAXD pattern, even though XTEM and NBD show their existence clearly.

Another interesting point on the GAXD pattern is the peak at around 48° which is marked as $(111)\gamma'$. No trace of γ' was found by XTEM and NBD. In the light of findings from XTEM+NBD which show that a small amount of ε-nitride was found between the CrN+α colonies as well as in the thin nanocrystalline sublayer at the sample surface, it is proposed that this peak is quite likely due to ε-nitride. In fact, the interplanar spacing of the strongest diffraction planes for γ' and ε-nitride, e.g. $(111)\gamma'$

and (002)ε-nitride, are very close ($d_{(111)\gamma}$=2.191Å, $d_{(002)\varepsilon}$=2.186Å, only 0.005Å different). Therefore, it is very difficult to separate these two peaks on the GAXD pattern.

The GAXD pattern for this sample also indicated a peak at 58° which was attributed to (200)γ. Bearing in mind that the strongest peak for γ, i.e. (111)γ, appears to be absent and all other peaks for γ are also missing, it is likely that the 58° peak originates from other constituents in the microstructure.

5.1.1.2 Plasma Nitrided Samples

a). 350°C nitriding treatment

The GAXD pattern of the 350°C plasma nitrided sample fails to show the existence of Cr_2N, γ and α nanocrystalline precipitates in the nitrided layer while their existence is unequivocally revealed by XTEM + NBD. Instead, the GAXD pattern shows a group of quite sharp γ peaks and a group of peaks which are conveniently marked as expanded γ. Although the XTEM + NBD study does prove that there is an expanded γ underneath the 6 μm thick nanocrystalline layer, the "γ_{exp}" peaks are again quite possibly due to the overlapped peaks from nanocrystalline precipitates, owing to the close proximity of the interplanar spacings for different phases (See Table 4 in Chapter 2).

In addition to the contribution from the γ phase in the nanocrystalline layer, the very strong γ peaks in the GAXD pattern indicate that the normal austenite from the substrate may also contribute to the γ diffraction.

b). 450°C nitriding treatment

The GAXD pattern of the 450°C nitrided sample shows very complicated peaks around 50°. There is a strong peak which is labelled as γ', although XTEM and NBD did not reveal the existence of γ' in the nitrided layer. There is another strong peak at the

right hand side of the CrN + α peak which did not match any possible phase in the nitrided layer, and is labelled as "unidentified".

The XTEM establishes that the 450°C nitrided sample has the smallest precipitates among all of PI^3 treated and plasma nitrided samples, ranging from 2 to 10 nm in size, with a large number of defects, such as twins and stacking faults. Therefore, the γ' peak, and the "unidentified" peaks may have originated from the defects and the nanocrystalline precipitates.

Ignoring the γ' and the unidentified peaks , the GAXD pattern of the 450°C plasma nitrided sample shows more or less the same phases revealed by XTEM and NBD. However, the indicated presence of expanded γ phase may not be associated with the γ precipitates since the NBD results do not show expansion of the nanocrystalline γ in the nitrided layer. Instead it may be due to the very thin expanded γ region at the interface.

c). 520°C nitriding treatment

Apart from the γ' peaks and the quite strong γ peak, the GAXD pattern of the 520°C plasma nitrided sample matches quite well with the XTEM and NBD results.

The reason that no γ' phase was detected by XTEM and NBD may be explained by its crystal structure. The stacking sequence of close packed {111} planes in a fcc crystal is -ABCABC-(Figure 91a). Suppose there is a extended dislocation on a C plane which comprises two partial dislocations (Figure 91b), a stacking fault will exist between the two partial dislocations with a stacking sequence of -ABABC-. Since the -ABABAB- sequence is the stacking sequence of the close packed planes of a hcp crystal, the overlap of more than one stacking fault will form a hcp structure. Therefore, the hcp ε-nitride can be considered as heavily stacking faulted γ' with dissolved nitrogen atoms orderly occupying the interstitial sites. In their TEM study on γ'-Fe_4N precipitation in the iron-nitrogen system, Dahmen et al also pointed out that the ε-nitride may be considered as a polytype of the γ'-Fe_4N with a stacking fault on every other {111}γ' plane [114].

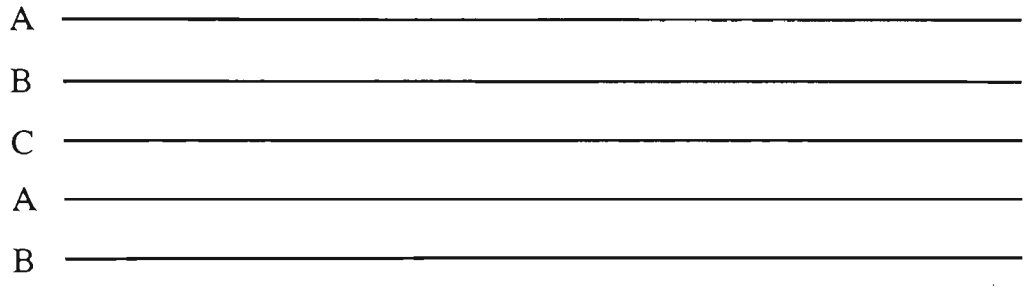

a. The stacking sequence of close packed planes in f.c.c. crystal

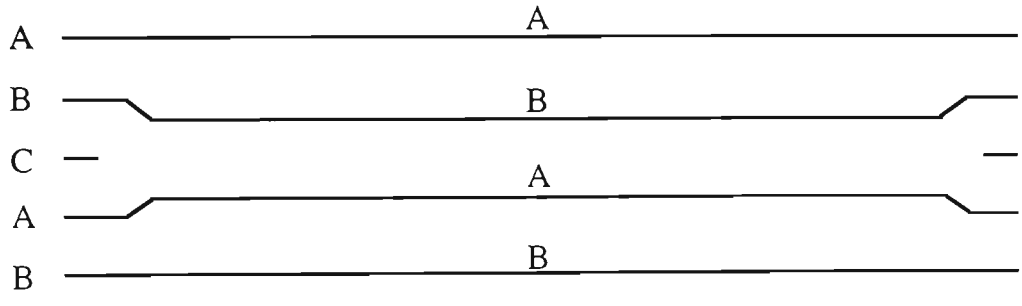

b. The stacking fault caused by two partial dislocations on plane "C"

Figure 91. The stacking sequence of a stacking fault on close packed planes in f.c.c. crystal

From the previous description, it can be seen that the close packed planes in γ'-Fe_4N, i.e. {111}γ', are equivalent to {200}ε, the close packed planes of ε-nitride. In X-ray diffraction patterns, both {111}γ' and {200}ε correspond to the strongest diffraction peaks at almost the same Bragg angle. Therefore, it is quite possible that the "γ'-Fe_4N" diffraction pattern for GAXD diffraction is actually from the ε-nitride, especially in very fine nanocrystalline structure where it is very hard to draw a clear line between the heavily stacking faulted γ'-Fe_4N and ε-nitride.

The labelled γ peaks may not be correctly attributed, since the XTEM image shows that γ exists only as small islands between the lamellar CrN + α colonies which can not lead to strong peaks. Besides, the nitrided layer is thick enough to prevent the substrate contributing to the diffraction. In fact, the interplanar spacing for (111)γ, which is the strongest diffraction plane, is 2.067Å, while the corresponding value for the (200)CrN plane is 2.070Å, i.e. only 0.003Å different. It is, therefore, not inconceivable

that under the stressed condition such as those prevailing in the nitrided layer, the CrN lattice may be slightly distorted, therefore slightly shifting the CrN diffraction peak to give a fake "γ" peak.

5.1.2 Factors Affecting GAXD

The above comparison between GAXD and XTEM+NBD, clearly highlights the inability of GAXD to unambiguously characterise the fine microstructural features of nitrogen implanted and nitrided austenitic stainless steel. It is obvious that GAXD at best provides a very complicated and confusing picture of the microstructure and at worst could lead to totally false and erroneous interpretation. Thus, the sole reliance on GAXD for complete microstructural characterisation, as attempted by a number of researchers, is unjustified. The shortcomings of GAXD in determining the microstructure of implanted and nitrided stainless steel stem from some intrinsic limitations of the techniques which are exacerbated by some peculiar microstructural features in this system. In the following sections these intrinsic and extrinsic limitations are briefly discussed.

5.1.2.1 Penetration of X-ray and Depth Resolution of GAXD

It is reported that GAXD has excellent depth resolution, for example, 70 nm in pure Fe for Cu Kα at a glancing angle of 1° [87]. However, the present results seriously question the depth resolution of GAXD.

For example, the GAXD pattern of the 150°C PI^3 treated sample shows very sharp γ peaks, even at 1° glancing angle, while a 1μm thick implantation modified amorphous layer was detected by XTEM. The only hint on the GAXD pattern which may suggest the presence of an amorphous structure is the unusually broadened (111)γ peak.

Even though the total thickness of the modified layer is about 4.5 μm for the PI^3 sample at 250°C, very strong, sharp γ peaks, which most likely originated from the substrate, are evident on the GAXD pattern.

Similarly, sharp γ peaks can also be observed in the GAXD pattern of the 350°C PI^3 treated sample.

More interestingly, the 6 μm thick 350°C plasma nitrided layer, plus 3-5 μm expanded γ underneath the nitrided layer, fail to prevent the x-rays penetrating to the normal substrate at the 5° glancing angle. This can be proved by the strong and sharp γ peaks of the GAXD pattern which are much stronger than those originating from any γ precipitates in nitrided layer.

All the above mentioned evidence points to the fact that the penetration of the glancing angle x-ray is far deeper than has been reported previously. Thus, when applying GAXD to thin surface layers, the resultant spectrum could contain information from a depth of several μm. It is, therefore, advisable to pay extra attention in interpreting the information. It is concluded that GAXD is not suitable for characterisation of thin surface layers, especially when the modified layer is a complicated multi-phase system.

5.1.2.2 Proximity of the Atomic Plane Spacings of Different Phases

The effect of the similarity of the crystal structure and interplanar spacing of several nitrides on diffraction pattern has already been discussed in Chapter 2, and the d spacings of the strongest diffracting planes of some of the nitrides has also been given in Table 4. From Table 4, it can be seen that the d spacings of the strongest diffraction planes for α, γ, ε-nitride, γ' and CrN are very close to each other. For instance, the d spacings of the strongest diffraction planes of γ' and ε-nitride have only 0.005Å difference between them. Thus, under the GAXD condition, especially with regard to its poor lateral and depth resolutions, it is not too surprising that a complicated GAXD pattern with overlapped, broadened diffraction peaks, was obtained.

5.1.2.3 *Crystal Size Effect*

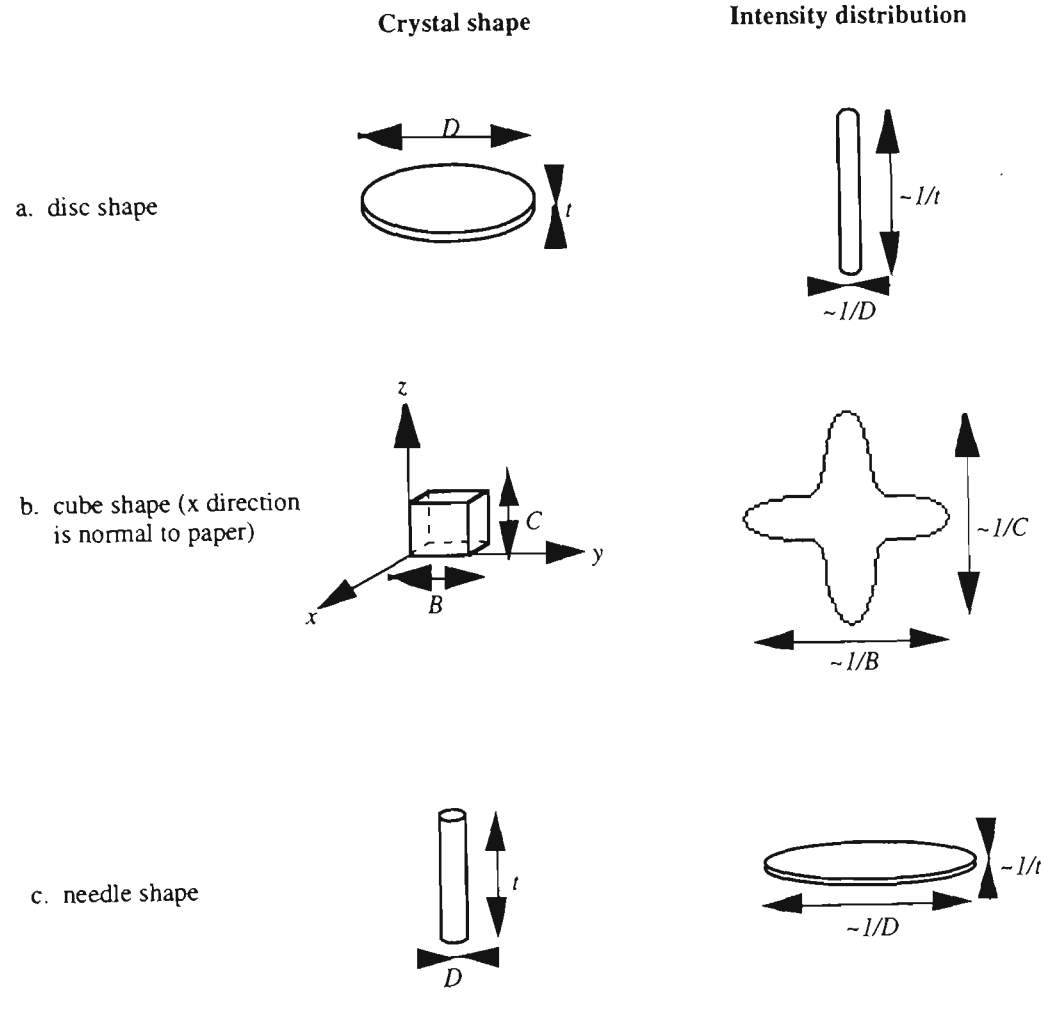

Figure 92 Schematic description of the intensity distribution around reciprocal lattice points for various crystal shapes

It is well known that the shape of the reciprocal lattice point can be strongly affected by the size and shape of the crystallites when the crystal is very small [115]. For example, the reciprocal lattice points for a thin, plate-like crystallite are elongated along the direction normal to the plate, resulting in reciprocal lattice spikes (Figure 92a). The length of these spikes is inversely proportional to the thickness of the plate, until the thickness reaches the extinction distance, when the minimum possible spike length occurs.

The reciprocal lattice points for a polyhedral crystal are extended in all directions perpendicular to the bounding facets of the crystal, i.e. a finite number of spikes pass through each reciprocal lattice point (Figure 92b). Again, the length of these spikes is also approximately inversely proportional to the size of the crystallites. The relative intensities of the various spikes from a particular polyhedral crystal can be approximately considered as proportional to the areas of the corresponding facet.

For needle shaped crystallites, all reciprocal lattice spikes will lie in a plane perpendicular to the needle axis (Figure 92c). If the cross-section of the needle has no well-defined crystallographic shape, the system of spikes is replaced by a disc perpendicular to the needle axis. The diameter of these discs is inversely proportional to the needle diameter.

When these elongated or broadened reciprocal lattice points intersect the sphere of reflection, the GAXD pattern of the small crystallites will show broadened peaks. More specifically, if the sample for GAXD analysis contains a multitude of nanocrystalline phases with similar crystal structures or interplanar spacings, such as in the case of austenitic stainless steel samples which are PI^3 treated or plasma nitrided below 500°C, the overlapping of these broadened diffraction peaks will make interpretation of the GAXD pattern very difficult.

5.1.2.4 Lattice Imperfection

Lattice defects could have an effect on diffraction patterns because of the elastic strain fields associated with them. However, for point and line defects such as vacancies and dislocations the strain fields are so highly localised that the proportion of highly strained materials is too low to give rise to any observable effects.

Planar defects on the other hand can appreciably affect the diffraction peaks, especially if their density is very high. Single stacking faults, or sequences of

overlapping stacking faults lead to streaks or spikes through the reciprocal lattice points. Hence, the influence of planar defects on GAXD closely follows size effects, e.g., significant broadening of diffraction peaks.

5.1.2.5 Twinning

The basic crystallography of twinning is the formation of a region with a new and specific orientation with respect to the matrix. Twins can form on several different planes (e.g. the four {111} planes of the f.c.c. austenitic structure), so that the diffraction peak from the matrix, plus its various twins, is a composite one reflecting several related orientations. In some cases, extra peaks arising from the twins will be observed, and in some other cases the twins will cause splitting of the matrix diffraction peak [115]. If there is a large density of twins in the sample to be analysed with GAXD, the extra peaks and the splitting of the peaks will undoubtedly lead to more complication of the pattern.

5.1.2.6 Double Diffraction

It is well known that under certain geometrically favourable condition, it is possible for diffracted beams originating in one component to be re-diffracted by a second component of the same crystalline structure, resulting in occurrence of double diffraction. Double diffraction can give rise to anomalous extra peaks in addition to the normal diffraction peaks. Therefore, if one is not careful, unjustified conclusions as to the origin of certain extra peaks can easily be drawn.

Much more prominent double diffraction effects take place when a specimen contains more than one crystalline component, such as regions of different orientations within a single material or the co-existence of two or more phases. Furthermore, if the multi-phase specimen has a nanocrystalline structure such as that in low temperature PI[3] treated and nitrided 316 stainless steel, the diffracted beam from one crystal will have ample opportunity to be re-diffracted, resulting in very strong double diffraction peaks, and hence a very complicated GAXD pattern.

5.1.2.7 Elastic Strain Effects

Reciprocal lattice points can be broadened or elongated as a result of elastic strain in the crystal, in the same way as size effects give broadened diffraction peaks. The elastic strain of the lattice can also result in shifting of the diffraction peaks because of the change of d spacing under the strain. For example, compressive stress in a particular direction leads to shortening of the interplanar spacing which, in turn, results in shifting of the diffraction peak to a lower Bragg angle. In the case of a single phase sample, the elastic strain can be calculated by the degree of broadening and shifting of the diffraction peaks. However, for multi-phase samples, the elastic strain may cause overlapping of the diffraction peaks of the different phases, adding more uncertainty to the GAXD analysis.

5.1.3 The Real Value of Information Provided by GAXD

In most cases, the effects of the factors mentioned in the previous section are not obvious in GAXD. For example, if the surface to be analysed has a simple structure and is thick enough to avoid mixed information from the substrate, or it contains phases with very different crystal structure with their own distinctive diffraction peaks, the problem with overlapping will not be as restrictive. Also if the size of the crystallites is not small enough to affect the diffraction, and the number of imperfections and twins is also too small to be detected by GAXD.

However, in PI^3 treated or plasma nitrided 316 stainless steel, especially when treated at 500°C or lower, the modified layer will possess all these factors, such as highly strained, multiphase nanocrystalline structure, in addition to semi-amorphous and amorphous structure. The problem is compounded by the presence of a large number of micro-twins and imperfections. The overall affects of all these complications is a diffraction spectrum which conveys little true information regarding the exact nature of the microstructure.

Summing up the previous discussion, it is now quite clear that the information afforded by GAXD patterns is actually a very complex mixture of peaks from real phases of both modified layer and substrate, plus extra abnormal peaks, due to peak broadening and overlapping.

5.1.4 So Called "Expanded γ", "S" Phase and "B" Phase

As discussed in Chapter 2, the "expanded γ" or "γ_{exp}" has been widely reported in nitrogen implanted or nitrided austenitic stainless steels, characterised by XRD or GAXD [18,19,43,44,45,46,47,48,60]. Other researchers, however, have recognised some problems with this characterisation, such as the unbelievably high strain calculated from the expansion of γ [44], as well as the abnormal shifting and strange relative intensity of the diffraction peaks. For these reasons, they have suggested uncharacterised phases such as "S" phase [62] or "B" phase [63], instead of expanded austenite "γ_{exp}".

Based on their study of austenitic stainless steels melted under high nitrogen pressure, Rawers et al. [84] reported that when nitrogen concentration reached about 1wt.% (about 2.2 at.%), several nitrides would start to precipitate, and the interstitial nitrogen would decrease. In 304 stainless steel, when nitrogen concentration reached 2.01 wt.% (about 4.4 at.%), only eutectic CrN was observed. According to their study, the maximum nitrogen concentration in solution in γ is about 1 wt.% (2.2 at.%) under equilibrium condition.

It is now accepted that thermodynamical criteria are still valid even under the non-equilibrium conditions encountered in ion implantation [91]. So, it is reasonable to assume that the maximum nitrogen dissolved in γ should not be far from 1 wt.% (2.2 at.%) for PI^3 treated and nitrided austenitic stainless steel. Bearing in mind that most of the "expanded γ" is reported at temperatures between 300 - 500°C at which nitrogen atoms should have sufficient mobility for precipitation, it is very difficult to imagine that at such temperatures, the γ phase of the austenitic stainless steel, which is a complex system with a high concentration of very strong nitride former (Cr), would proportionally

expand with an increase of nitrogen concentration, without nitride precipitation or phase transformation.

Based on the present XTEM + NBD study of the PI^3 treated and plasma nitrided 316 stainless steel, expanded γ does exist. However, the maximum expansion most likely occurs in the 300-500°C temperature range, and is limited to about 3%, otherwise amorphisation or precipitation will take place. No expansion of γ was detected where precipitates were present. From the previous discussion, it is reasonable to conclude that unless the nitrogen concentration is very low, whenever the precipitates can be detected or the calculated expansion of the γ is over ~3%, the "expanded γ" detected by XRD or GAXD does not represent a real γ_{exp} phase, but rather a false "expanded γ" which is due to a complex mixture of information from the precipitates and substrate. The so called "S" and "B" phases can also be explained in this way.

5.1.5 Advantages of XTEM + NBD Compared to GAXD

Compared to GAXD, the XTEM + NBD method offers a unique means for direct observation of the microstructural variation through the depth of surface modified layers. It also enables the measurement of the total layer depth directly from a single TEM specimen. Since NBD analyses an extremely small area of a few nanometres in size, the factors which strongly affect the GAXD can be decreased to a minimum. Therefore, unambiguous information from a single nano-precipitate, or from two nano-precipitates, with their crystallographic relation can be obtained by NBD. Consequently the XTEM + NBD method is far more powerful than GAXD and is ideally suited for microstructural characterisation of surface engineered materials, especially nitrogen implanted or nitrided austenitic stainless steel.

5.2 NBD and SAD

Compared to NBD, SAD has a much poorer lateral resolution (500 nm), especially for probing nanocrystalline structures. Since electron diffraction follows Bragg's Law, all the factors which adversely affect the GAXD characterisation, except

for the depth resolution, can equally reduce the effectiveness of SAD characterisation. Figure 65b shows a typical complicated SAD pattern from the 350°C plasma nitrided layer. The NBD pattern of the same specimen, Figure 66b, enables identification of nano-precipitates, which is impossible from SAD.

However, SAD can detect a much thinner and smaller area than GAXD. For example, SAD can limit the area to be detected on a XTEM sample to strictly within a single sublayer, without mixing information from all the other sublayers and substrate, as GAXD does. So, the complications due to the similarity of crystal structures and interplanar spacings, imperfections and so on, are not as serious as they are in GAXD. In some cases, SAD patterns can be used as an auxiliary method for XTEM + NBD characterisation.

5.3 Microstructural Evolution of Nitrogen Implanted and Nitrided Austenitic Stainless Steel

Since the results obtained from XTEM and NBD characterisation give a much clearer picture of the surface microstructure of the PI^3 treated and plasma nitrided samples than that obtained from GAXD and SAD, the discussion on the microstructural evolution of the 316 stainless steel samples will mainly be based on the XTEM and NBD results.

To better understand the evolution of the microstructure of the PI^3 treated and plasma nitrided 316 stainless steel, some pertinent facts should be noted. First, based on the fact that the thickness of the PI^3 treated layer is far beyond the range of implanted nitrogen, it is obvious that the diffusion of nitrogen plays a crucial role in the evolution of the microstructure of the PI^3 treated layer. Likewise, the plasma nitriding can also be treated as a purely diffusion process. Secondly, the mobility of the nitrogen in γ-austenite is much lower (less than one thousandth) than that of nitrogen in α-ferrite. A third factor is the solubility of nitrogen in α-ferrite, which is only about one tenth of the solubility of the nitrogen in γ-austenite [92].

5.3.1 PI^3 Treated Samples

5.3.1.1 Microstructural evolution at 150°C PI^3 treatment

Owing to the sluggish mobility of nitrogen at 150°C, a very high nitrogen concentration will easily be built up at the surface during implantation, i.e. the nitrogen atoms are implanted into the surface faster than they can diffuse out. This extra high nitrogen concentration at the surface will cause so much stress on the crystalline structure of the γ substrate that a martensitic transformation is activated. NBD patterns show that the products of this martensitic transformation are ε-martensite and α ferrite. Though these two phases are too fine to be quantitatively identified by the TEM image, NBD results show that ε-martensite is mostly detected in the lower stress area away from the interface. Therefore, the products of the stress induced martensite transformation may be controlled by the stress rate in the γ substrate. The observed orientation relationship between austenite and ε-martensite is $(2\bar{2}0)\gamma//(\bar{1}01\bar{2})\varepsilon$, $[001]\gamma//[10\bar{1}0]\varepsilon$. The orientation relationship between γ and the stress triggered α is consistent with both K-S (Kurdjumov and Sachs) and N-W (Nishiyama and Wasermann) relationships.

Since the solubility of nitrogen in α is very low, nitride precipitation is required to accommodate the extra nitrogen atoms. However, due to the different affinities of the alloying elements for nitrogen atoms in the steel (such as Cr, Ni and Fe), the nitride precipitates require rearrangement of the metal atoms within γ, or even between the γ and α phases.

At 150°C, the mobility of metal atoms is too low to allow the rearrangement of substitutional atoms for precipitation [10]. Therefore, with more nitrogen atoms coming in, the crystalline structure collapses and an amorphous structure is obtained. Since it is difficult for the system to reduce its energy by precipitation, disruption of crystalline structure is the only option available for the system to decrease its free energy which is continuously increased by addition of nitrogen.

The high nitrogen concentration in the amorphous layer exerts a very high stress on the substrate. Therefore, a 3-4 μm thick heavily stressed γ substrate with stress induced α and ε-martensite precipitation is formed under the amorphous layer. The poor mobility of nitrogen in both γ and α phases at such a low temperature is primarily responsible for the absence of nitride precipitates in this stressed area.

The expansion of the amorphous layer is mainly controlled by the speed of substrate - amorphous interface reaction, which in turn is controlled by the nitrogen concentration gradient and diffusion speed of nitrogen in the amorphous structure.

The clustered nature of the amorphous structure shows that the rearrangement of nitrogen and metal atoms, driven by the extra high nitrogen concentration, is only achieved over a very short distance.

It should be stressed that the presence of a 1 μm thick amorphous layer obtained by PI^3 treatment at 150°C has very little to do with radiation damage since the thickness of the amorphous layer is far beyond the range of implanted nitrogen.

5.3.1.2 Microstructural evolution for 250°C PI^3 treatment

Microstructural evolution at 250°C is similar to that at 150°C. First, the high nitrogen concentration is built up by implantation because of the poor mobility of the nitrogen in γ. The high nitrogen concentration then activates the γ-α transformation. Since metal atoms are still not mobile at 250°C, the atom rearrangement necessary for nitride precipitation again can not be realised. When the nitrogen concentration reaches a certain level, the amorphous structure is obtained. The fact that the γ-α transformation leads to amorphisation can be proven by the existence of α phase just in front of the interface between the amorphous sublayer and the substrate, as shown in Figure 32. Unlike the 150°C treated sample, only the N-W relation is observed between the γ and α. Though it is still not clear why no K-S relationship is observed between γ and α at 250°C, the reason may be attributed to the higher γ ---> α transformation temperature.

Compared to 150°C, the mobility of nitrogen atoms in α and amorphous phases is expected to be higher at 250°C. Therefore, the diffusion of the nitrogen in these phases almost totally annihilates the heavily stressed α, γ and ε-martensite region. Instead, a much thicker modified layer is obtained, with a thin slightly stressed zone located under the modified layer.

With implantation continuing, more nitrogen atoms are accumulated in the modified layer, resulting in a very high nitrogen concentration. The high nitrogen concentration will offer an extra driving force for short range rearrangement of the metal atoms. Therefore, very fine CrN and α will gradually precipitate from the amorphous structure through a process of nucleation and growth. Thus, the amorphous structure is gradually converted to a semi-amorphous structure, with very fine CrN and α crystals, and finally becomes a nanocrystalline structure composed of CrN and α. The longer implantation time may also contribute to the precipitation of nanocrystalline CrN and α. Bain and N-W relationships are found to exist between the f.c.c. CrN and α phases.

The thick amorphous sublayer underneath the nanocrystalline sublayer is a further proof that amorphisation in the PI^3 treated sample has nothing to do with radiation damage from the nitrogen ions.

The high nitrogen concentration in the nanocrystalline sublayer can be proven by the existence of traces of ε-$Fe_{2-3}N$. As mentioned previously, thermodynamic factors still prevail even in the non-equilibrium process of ion implantation [91]. Therefore, the more negative the heat of formation of a nitride is, the greater is the driving force for its nucleation and growth and, as a result, this nitride forms in the implantation treated layer. Turkdogan and Ignatowicz reported that in nitrided Fe-Cr alloy, iron nitrides were only formed after all the Cr bonded with nitrogen [93]. Based on the above discussion, it can be expected that, thermodynamically, the ε-$Fe_{2-3}N$ can only precipitate when all of the Cr atoms have been bonded with nitrogen, and there are still extra nitrogen atoms for the precipitation of ε-$Fe_{2-3}N$.

Since the diffusion of nitrogen atoms in γ-austenite is very low, the growth of the implanted layer is controlled by nitrogen diffusion in the modified layer, and the modified layer-substrate interface reaction, resulting in a sharp interface.

As nitrogen concentration is not very high at the interface, some tiny Cr_2N precipitates can be detected. The structural and concentration fluctuations also resulted in some tiny metastable (Cr,Fe)N crystals in an amorphous matrix at the interface area. With increasing nitrogen concentration, and rearrangement of the atoms to form stable CrN and α precipitates, this thin transition semi-amorphous region with metastable nitrides collapses into an amorphous structure in a short time. The HREM image of the interface shows the transition from crystalline substrate to amorphous sublayer (Figure 34).

5.3.1.3 Microstructural evolution for 350°C PI³treatment

The microstructural evolution of the PI³350°C sample is similar to the PI³250°C sample. However, the interface reaction of the γ - modified layer is faster than that at 250°C due to the higher mobility of nitrogen atoms and possible slight rearrangement of metal atoms. The faster moving interface produces a wider transition semi-amorphous region between the amorphous sublayer and substrate as shown for the 250°C treated sample. The relatively thick semi-amorphous sublayer III is composed of very fine metastable (Cr,Fe)N and α in an amorphous matrix. Some Fe_4N or $(Fe,Cr)_4N$, as a transition phase, may form at the interface area as well.

Since both (Cr,Fe)N and γ′ are actually nitrogen expanded γ, with nitrogen atoms being orderly located in the octahedral interstices, the (Cr,Fe)N and γ′ precipitates in the semi-amorphous sublayer III exhibit a structure inherited from the original γ substrate, as HREM revealed.

The 3% γ expansion at the interface shows that solubility of nitrogen in γ is also increased at 350°C compared to that at 250°C. However, the diffusion rate of nitrogen in

γ is still low since this expanded γ can only be found within a few tens of nanometres from the interface.

Another structural difference between the $PI^3$350°C and the $PI^3$250°C samples, is the thinner amorphous sublayer and the sharp transition from the amorphous sublayer to the nanocrystalline sublayer in the $PI^3$350°C sample, with the consequence that the semi-amorphous sublayer between the nanocrystalline and amorphous sublayers of the $PI^3$250°C sample is almost absent in the $PI^3$350°C sample. This difference is caused by the higher mobility of nitrogen atoms and slight rearrangement of metal atoms at 350°C.

It should be noted that the treatment time at 350°C is much shorter than that at 250°C. Therefore, the total thickness of the 350°C treated layer is thinner than the 250°C treated layer.

5.3.1.4 Microstructural evolution for 450°C PI^3 treatment

Since the mobility of metal atoms is still low at 450°C, the amorphous structure is obtained by PI^3 treatment in the same way as it is for the 150°C, 250°C and 350°C treated samples. However, both diffusibility of nitrogen in γ and the amorphous structure, and the speed of growth of the modified layer are obviously increased.

The fast growth of the modified layer and the fast diffusion of the nitrogen atoms in the amorphous layer prevent the accumulation of the super high nitrogen concentration in the amorphous layer, and therefore the nanocrystalline sublayer existing in 250°C and 350°C implanted samples is not present. Only a very thin semi-amorphous transition region is present between the amorphous layer and the high dislocation region of the γ substrate.

The diffusion of nitrogen atoms in the γ substrate resulted in an expanded high dislocation density region γ_{exp} under the amorphous layer. The expansion of the γ_{exp}

gradually decreases from about 3% at the amorphous - γ_{exp} interface to zero at the high dislocation γ - normal γ interface.

The 3 μm thick amorphous layer obtained by only 70 minutes implantation also supports the faster diffusion of the nitrogen atoms at 450°C.

5.3.1.5 Microstructural evolution for 520°C PI³ treatment

At 520°C, the metal atoms possess sufficient mobility to allow nucleation and growth of equilibrium cellular CrN+α precipitates. Both Bain and N-W relationships are observed between CrN and α phases. The growth of the pearlite-like CrN+α precipitates into the substrate controls the growth of the modified layer. Therefore, a sharp ragged interface is observed between the PI^3 modified layer and the substrate. No stress affected zone or expanded γ can be detected in the substrate in front of the interface.

However, the outermost layer (about 0.4-0.5 μm thick) does not exhibit the typical lamellar precipitation morphology. It is proposed that in this region, the collision cascades set up by continuous implantation block the equilibrium growth of γ and α precipitates, and enhance the disorder of the structure, making possible the precipitation of other nitrides such as hexagonal $(Cr,Mo)N_x$, Cr_2N and ε-nitride in this high nitrogen concentration region.

At the near surface layer of the lamellar CrN+α region, after all Cr atoms are consumed by the formation of CrN, the accumulation of the extra nitrogen provided by continuous implantation will cause formation of the ε-$Fe_{2-3}N$, according to thermodynamic criteria.

At the interface, the nitrogen potential is low, so that Cr_2N can be formed. But Cr_2N is very difficult to grow because of kinetic limitations. By implanting nitrogen into

pure Cr, Zhao et al [94] found that most of products of the implantation were CrN. Cr_2N could only be found at the node area. According to the Cr to Cr nitride transformation model proposed by Zhao et al [116], fcc CrN can grow in six directions which can easily transfer to each other, and can also grow very large. By contrast, Cr_2N (hexagonal) grows in exact crystal directions and is difficult to transfer from one direction to the other. Therefore, the growth of Cr_2N can easily be stopped. Thus only a few very small Cr_2N crystals can be found at the boundaries of the CrN and α colonies. The same kinetic limitation also applies to the hexagonal $CrMoN_x$. With the development of the CrN+α colonies, the tiny Cr_2N and $CrMoN_x$ crystals will gradually be consumed.

5.3.2 Plasma Nitrided Samples

5.3.2.1 Microstructural evolution for 350°C nitriding

It is reported that CrN is more stable than Cr_2N at temperatures below 575°C [10]. So CrN generally precipitates in most cases of nitriding and nitrogen ion implantation. However, it has been reported that Cr_2N is also able to precipitate under 575°C at low nitrogen concentration [10, 84].

It is known [12-21] that in plasma nitriding the sample is heated by the kinetic energy of the nitrogen ions released upon their impact on the sample surface. Therefore, low nitriding temperature corresponds to less nitrogen ions impacting the sample, resulting in low nitrogen concentration at the sample surface. Based on the above description, the low nitrogen concentration on the surface of the 350°C nitrided sample can be expected.

Since the metal atoms at 350°C have little mobility [10], when nitriding at this temperature, if there is no additional high nitrogen concentration to offer sufficient driving force for precipitation through nucleation and growth, the readiness of structural transformation may play a predominant part in case of the formation of nitrides. Only those nitrides which are formed through a fast structural transition, e.g., martensitic

transformation, could be achieved under the kinetic conditions of low temperature and low nitrogen concentration.

As it is discussed in 4.1.1.2, that austenitic stainless steel has a very low stacking fault energy, and ε-martensite (h.c.p.) actually consists of multi-layer overlapped stacking faults. Thus, the γ to ε-martensite transformation can be activated at very low rates of strain. The amount of the ε-martensite reaches a maximum at about 5% strain and decreases thereafter, while the γ to α transformation increases steadily with increasing amount of deformation [95]. At 350°C, the low nitrogen concentration produced by nitriding may activate both γ to ε-martensite and γ to α' transformation, which can be proved by Figures 74 and 75. The nitrogen atoms driven out of the α' phase may then be accommodated in the interstices of the ε-martensite, thereby causing ε-martensite to transform to hexagonal nitride, since it needs only very small lattice adjustment. However, as 316 stainless steel is very rich in chromium, which has a much stronger affinity for nitrogen than iron, instead of ε-nitride which forms in the low chromium condition, $(Cr,Fe)_2N$ is formed.

It is reported [92] that $(Cr,Fe)_2N$ is not a stable phase and only exists as a transition phase between γ and Cr_2N. However, due to the poor mobility of the metal atoms because of low nitriding temperature (the mobility of metal atoms is further hindered by the low nitrogen concentration which corresponds to reduced lattice distortion), some $(Cr,Fe)_2N$ may not be able to transform to stable Cr_2N in a short time. So $(Cr,Fe)_2N$ precipitates are observed together with Cr_2N. However, after nitriding for a longer time at 350°C, it is possible that all $(Cr,Fe)_2N$ will transform to Cr_2N.

The observed orientation relationship between the γ and Cr_2N (or $(Cr,Fe)_2N$) is as follows:

$$(011)\gamma \,//\, (\bar{3}211)Cr_2N,\ [100]\gamma \,//\, [12\bar{3}2]Cr_2N$$

No discernable orientation relationship was found between the α and Cr_2N. The fact that only γ and Cr_2N exhibit a structural relationship strongly supports the idea that Cr_2N is precipitated from γ.

A significant amount of retained γ co-existed with Cr_2N and α in the nitrided layer. This also shows the low nitrogen concentration of the 350°C nitrided layer.

The kinetic limitation for the growth of Cr_2N mentioned before can be proven again by the constant precipitate size throughout the 350°C nitrided layer.

By extending the nitriding time, the near surface area of the nitrided layer may achieve a higher nitrogen concentration, such that traces of CrN are detected at this area.

It is interesting that the thin transition zone between the nitrided layer and the substrate has the same components as the nitrided layer. However, the proportion of the individual components in this transition zone may be different from that in the nitrided layer, although there is no direct proof to support this hypothesis at the present time.

As the nanocrystalline structure of the nitrided layer is evolved from the crystalline structure of the substrate, there may be some sort of structural continuity between the nitrided layer and the substrate. Besides, the nitrogen concentration in the nitrided layer is not high enough to activate amorphisation to relieve the stress. Therefore, the heavy stress in the nitrided layer may pass through to the substrate to form a thick, stressed, high dislocation region in the substrate.

The stress distorted γ and the high dislocation density may help nitrogen atoms to diffuse more quickly in γ to cause the high dislocation γ region to become expanded. The expansion of γ is approximately 3%, then gradually decreases to zero at the end of this high dislocation region.

5.3.2.2 Microstructural evolution for 450°C nitriding

Nitriding at 450°C means more nitrogen ion bombardment on the sample surface, and therefore a higher nitrogen concentration than that obtained in 350°C nitrided layer will be expected.

At the beginning of nitriding, the nitrogen solution forms expanded γ, and the γ to α transformation is then activated. Since both nitrogen concentration and the

The different precipitation mechanisms in the 350°C and 450°C nitrided samples also explain why the precipitates in the 450°C nitrided layer are much finer than those in 350°C nitrided layer.

The significant amount of retained γ in the nanocrystalline nitrided layer further proves that the nitrogen concentration in the 450°C nitrided layer is lower than by PI^3 treatment at the same temperature. Comparing the 450°C plasma nitrided sample, which only has a thin amorphous transition sublayer, to the 450°C PI^3 treated sample, it is quite reasonable to suppose that nitrogen concentration plays an important role in amorphisation of the microstructure.

The lower nitrogen concentration in 450°C nitrided layer offers less driving force for diffusion of nitrogen in γ, so no expanded high dislocation γ region like that in the 450°C PI^3 treated sample is observed in this case.

5.3.2.3 Microstructural evolution for 520°C nitriding

Similar to the 520°C PI^3 treated sample, the evolution of the 520°C plasma nitrided layer is controlled by equilibrium nucleation and growth of cellular CrN+α precipitates. As a result of the much longer nitriding time, a very thick nitrided layer is obtained.

However, the nitrogen concentration in the 520°C nitrided layer is lower than that in the 520°C PI^3 treated layer. Therefore, instead of ε-nitride, some small retained γ islands are observed between the CrN and α colonies.

The ion energy of plasma nitriding is much lower than PI^3 treatment. Hence there is no collision cascade damage caused by ion bombardment on the surface to form a thin nanocrystalline outer most layer on top of the lamellar CrN and α precipitates, like that observed in the 520°C PI^3 treated sample.

5.4 Amorphisation in Nitrogen Implanted Surface

5.4.1 About Amorphous Structure

Fujita proposed that the amorphous structure in metals was actually composed of crystalline polyhedrons which had a close-packed crystalline structure and random orientation [96]. By HREM observation of the amorphous materials, Ichinose and Ishida found that the so-called "amorphous" material was not always without crystalline features [97]. Cohen et al reported that crystalline clusters existed in the amorphous structure which were independent of temperature, i.e., unless the structure became crystalline, the crystalline clusters in the amorphous structure remained the same at any temperature [98]. Using different methods (proton irradiation, melt spinning and mechanical alloying) to produce amorphous $Cu_{50}Zn_{50}$ alloy, Lee et al found the short range atomic distribution in an amorphous alloy was the same, regardless of how it was prepared [99]. Ke reported that short and medium range order existed in amorphous structures, and proposed that the size of the ordered cluster determines the degree of amorphisation [90], ie., smaller clusters correspond to a higher degree of amorphisation. Serebryakov proposed that an amorphous metallic alloy can be conceived as consisting of small crystal like clusters and liquid like inter-cluster layers [100]. In his HREM study of the rapid cooled Pb-Si amorphous alloy, Hirotsu reported that under suitable defocus conditions, medium range order can be observed in amorphous alloys as clear lattice images [101].

The HREM study of the amorphous structure in 250°C and 350°C PI^3 treated samples proved the amorphous structure was actually composed of clusters which showed short or medium range crystalline order. All amorphous structures shown in this study, no matter whether they were obtained from PI^3 treatment at 150°C to 350°C or from 450°C plasma nitriding, showed about the same cluster size. From the results mentioned above, the present work strongly supports the concept that the solid state amorphous structures are not really "amorphous" but consist of crystalline short range order or medium range order structures.

5.4.2 Solid State Amorphisation

The formation of the thick amorphous modified layer obtained in this study, especially the thick amorphous sublayer under the nanocrystalline sublayer, provides a strong argument against the idea of radiation induced amorphisation in ion implanted steel.

In fact, a number of papers in the past few years have reported that implantation induced amorphisation only occurs if there is a chemical reaction between the implanted ions and the target metal. No amorphous structure has ever been found in self-implanted or inert gas implanted metals or alloys [102,103,104]. Furthermore, it has been reported that Fe, Cr and Ni implanted into 304L steel did not activate the γ to α transformation at very high doses [105]. From some previous work on implanting nitrogen into pure gold, it was found that nitrogen implantation did not change the dislocation density even at doses up to $2x10^{18}$ ions/cm^2, but increased the density of nitrogen bubbles formed in the gold matrix [106]. By studying high energy electron (2 MeV) irradiation introduced crystalline to amorphous transition in metal borides, Mori and Sakata found that the amorphisation tendency by both electron irradiation and rapid cooling was the same [107], i.e., if the rapid cooling could not transform material into the amorphous state, the high energy electron radiation would not make the material amorphous either. All the results mentioned above strongly support the idea that radiation damage has almost nothing to do with the amorphisation of ion implanted metals.

In fact, the stable disordering due to simple displacement-cascade-damage overlap has so far been proven only in semiconductors, and has not been observed in metals even at very low temperatures [98]. Implantation induced amorphisation in metals has only been found in cases where the disorder was produced by significant quantities of chemically active solute atoms.

Several factors may influence the formation of the amorphous phase by solid state reaction. Firstly, it has been reported that the composition of most amorphous alloys is

close to the eutectic concentration [108]. The widely different compositions of the precipitating phases requires large rearrangement of the atoms, making nucleation and growth of new crystals more difficult. Furthermore, according to the definition of the eutectic reaction, the eutectic structure must precipitate from a liquid phase. Therefore, when eutectic precipitation occurs in the solid state at low temperature, a solid state liquid, i.e. amorphous structure, should be formed prior to eutectic precipitation, unless the temperature is high enough to offer sufficient driving force for direct eutectic precipitation. In Fe-Cr-Ni austenitic stainless steel, it has been found that implanted nitrogen always binds with Cr and the two diffuse together [51]. Cr-N bonding makes the mobility of Cr even lower. Since lamellar CrN and α precipitate are a eutectic structure [84], it is therefore conceivable that, by analogy, amorphisation will result in regions with potential for CrN and α precipitation if the temperature is not high enough to produce precipitation.

Secondly, amorphisation can be greatly enhanced when a restricted solubility range exists for the compound which can precipitate [109]. A slight deviation from the compound's stoichiometric concentration can result in a large rise in the free energy of the system. When the free energy of the crystalline state becomes greater than that of the amorphous state, a spontaneous amorphous transformation is favoured. CrN is one such "line compound", without a significant composition range.

Summing up all of the above discussion, it is reasonable to conclude that for the ion implantation treated alloy system, the potential for low temperature solid state eutectic reaction, combined with the poor mobility of the reacting atoms are the key factors for solid state amorphisation.

5.4.3 Amorphisation at Elevated Temperature

The amorphisation obtained in the 450°C treated sample shows that the amorphous phase can be stable up to quite high temperatures in austenitic stainless steel if conditions such as the nitrogen concentration are suitable. Recent reports on Ti-(30-40%)Cr alloy

show that not only can the amorphous phase be stable at high temperatures, but the transformation between the partially amorphous and crystalline phases can be reversed by application of alternating annealing steps at 600-800°C [110]. Based on these reports, one can imagine that at proper concentration and temperature, the amorphous structure may be a stable phase at much higher temperatures than is usually expected.

It is well known that an amorphous structure has both very good wear resistance and corrosion resistance. Therefore, the thick amorphous layer obtained by elevated temperature implantation observed in the present work has a very bright future in practical applications.

It has also been reported that when austenitic stainless steels are nitrogen implanted or plasma nitrided between 300-500°C, they show not only excellent tribological properties but better corrosion resistance than that of untreated materials [1-4]. Formation of an amorphous structure or semi-amorphous structure is obviously the reason for this remarkable improvement.

5.5 Nitrides in PI^3 Treated and Plasma Nitrided Austenitic Stainless Steel

5.5.1 CrN and Cr_2N

Since thermodynamic factors still prevail even in the non-equilibrium process of ion implantation [91], the more negative the heat of formation for a nitride, the greater is the driving force for its nucleation and growth and, as a result, such nitrides should be present in the modified layer.

Table 9 shows the heats of formation for some of the metal nitrides [111] which may exist in austenitic stainless steels. From the ΔH_f values shown in the table, it can be seen that Cr and Mo nitride are thermodynamically favoured to form in nitrogen implantation modified 316 stainless steel. Considering kinetic factors, only f.c.c. nitrides like CrN and Mo_2N are favoured, with ΔH_f of Mo_2N being a little higher than that of

CrN. However, the content of Mo in 316 steel is very low (about 2.34%) and therefore, even if Mo_2N forms, the amount of Mo_2N will be very small. More importantly, not only do both CrN and Mo_2N have the same f.c.c. lattice, the lattice parameters of Mo_2N (4.16Å) and CrN (4.14Å) are very close which makes them difficult to distinguish by diffraction. Since it is almost impossible to identify a small amount of Mo_2N from CrN by the techniques used in this study, CrN is obviously the most easily detectable nitride.

Table.9. Heat of formation (ΔH_f) of some metal nitride (after reference 111)

	CrN	Cr_2N	Fe_4N	Fe_2N	MoN	Mo_2N	Ni_3N
	(f.c.c.)	(hex. or h.c.p.)	(f.c.c.)	(orth.)	(hex.)	(f.c.c.)	(hex.)
kJ/mol	-40	-38	-17	-18	-46	-38	-7

From a wide study of nitriding, Jack also pointed out that below 575°C, CrN is more stable than Cr_2N [10]. During nitriding of Cr-alloy steel, CrN always precipitates, except for a low nitrogen potential, for which Cr_2N may precipitate. The Cr_2N precipitates observed in the 350°C plasma nitrided sample proved that Cr_2N can precipitate at low nitrogen potential below 575°C. However, the difficulty in the growth of Cr_2N has been further proved by constant precipitate size in the 350°C plasma nitrided layer in the present study.

It should be noted that both CrN and Cr_2N can dissolve some iron to become (Cr,Fe)N and $(Cr,Fe)_2N$, especially at low temperatures when poor mobility of metal atoms does not allow atom rearrangement, or at the early stage of the precipitation because it takes some time to realise rearrangement of the metal atoms.

Although CrN has the same f.c.c. structure as the γ phase, it is unlikely that it can precipitate simply from the expansion of the γ phase. From the results obtained in the present work, it is shown that cellular CrN and α nucleate together from γ through a large amount of rearrangement of metal atoms. At low temperature, the large amount of rearrangement of metal atoms can not be realised, so γ will first collapse to amorphous

phase, then CrN and α nucleate and grow from the amorphous structure. At a high enough temperature, cellular CrN and α can also grow directly from γ. As a result, the orientation relationship between γ and the cellular structure of CrN and α can not always be found. Conversely, Cr_2N is always found to have a clear orientation relationship with γ since it is precipitated through shearing of γ, which needs only a small amount of atom rearrangement.

5.5.2 Transition Phase γ'

According to Table 9, the formation of γ' is thermodynamically unfavourable in austenitic stainless steel. However, at low temperature, where metal atoms are not able to diffuse, if nitrogen atoms are dissolved in the γ phase, γ' may form as a transition phase between the nitrogen-dissolved γ and the stable nitrides such as CrN or Cr_2N, based on the fact that some of the dissolved nitrogen atoms may possibly occupy one quarter of the octahedral interstices of the γ lattice to minimise the strain energy and the mutual repulsion between nitrogen atoms.

5.6 Pseudo-Phase Diagram of Fe-Cr-Ni-N System

It is quite surprising that only very limited information of the Fe-Cr-N and Fe-Cr-Ni-N systems is available even today. So far, almost all of the discussions on the microstructure of nitrogen ion implanted and nitrided austenitic stainless steels have been confined to the Fe-N or Cr-N binary phase diagrams, which is obviously inadequate for multi-phase systems. To obtain a clearer picture of the microstructural evolution through nitrogen ion implantation and nitriding in the Fe-Cr-Ni system, a vertical section of the phase diagram of the Fe-Cr-Ni-N system would be very helpful.

Frisk and Hillert gave a calculated vertical section of the Fe-25Cr vs N phase diagram but only the part above 1200K (927°C) [83].

By studying high nitrogen 304 and 316 stainless steels, melted under high nitrogen pressure, Rawers et al [84] proposed a quite rough vertical section of the Fe-

18Cr-8Ni vs N phase diagram with nitrogen up to 4 wt.% (Figure 93). According to their phase diagram, there are five solid state phase fields from 0-4 wt.% nitrogen. For nitrogen concentrations less than 0.8 wt.% (~1.8 at.%), only γ phase can be detected. A two phase field, eutectoid Cr_2N and γ, may exist at about 1 wt.% nitrogen. For nitrogen concentrations higher than about 1 wt.% (~2.2 at.%), both eutectoid Cr_2N and eutectic CrN can be found together with γ. With a further increase of the nitrogen concentration, the quantity of the nitrides precipitates increases, while dissolved nitrogen in γ decreases. Since Cr_2N is much less stable than CrN, only eutectic CrN and γ can be detected for nitrogen concentrations higher than about 2 wt.% (~4.4 at.%) At 3.9 wt.% (8.7 wt.%) nitrogen, almost all of the nitrogen and chromium combine to form CrN. Above 3.9 wt.% nitrogen, b.c.c. α begins to appear to form a three phase field of CrN, γ and α. The percentage of the α phase increases with growing total nitrogen concentration. A similar microstructural evolution with nitrogen has also been reported recently by J.A. Hawk et.al. [112] in Fe-16Cr-7Mn-5Ni austenitic stainless steel.

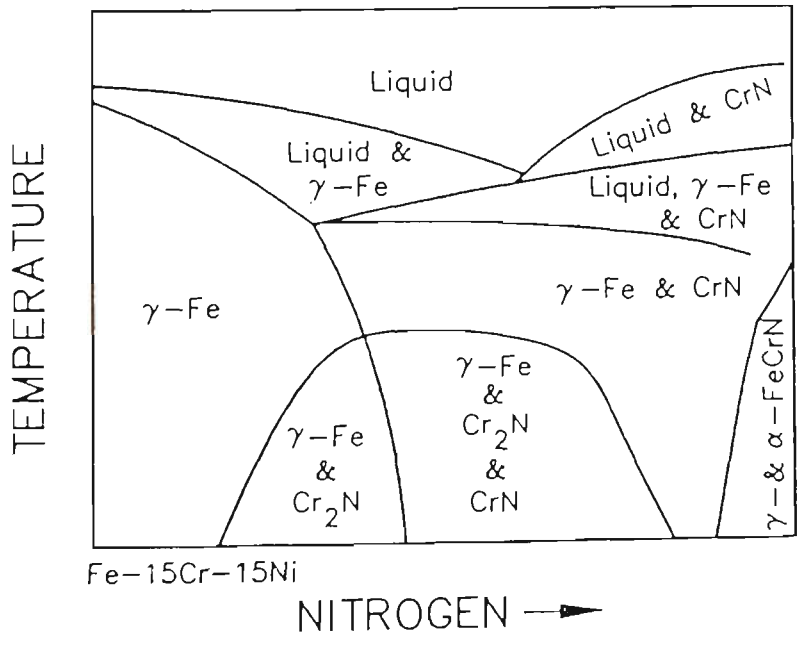

Figure 93 Proposed phase diagram for high nitrogen austenitc stainless steel by Rawers et al [84]

Based on the above information and the microstructural characterisation results of the present work, a vertical section of the part of the Fe-18Cr-8Ni-N pseudo-phase diagram below 550°C is proposed (Figure 94). It should be noted that the composition ranges of each phase field have not been specified since no quantitative nitrogen analysis of the PI^3 treated and plasma nitrided layer has been carried out.

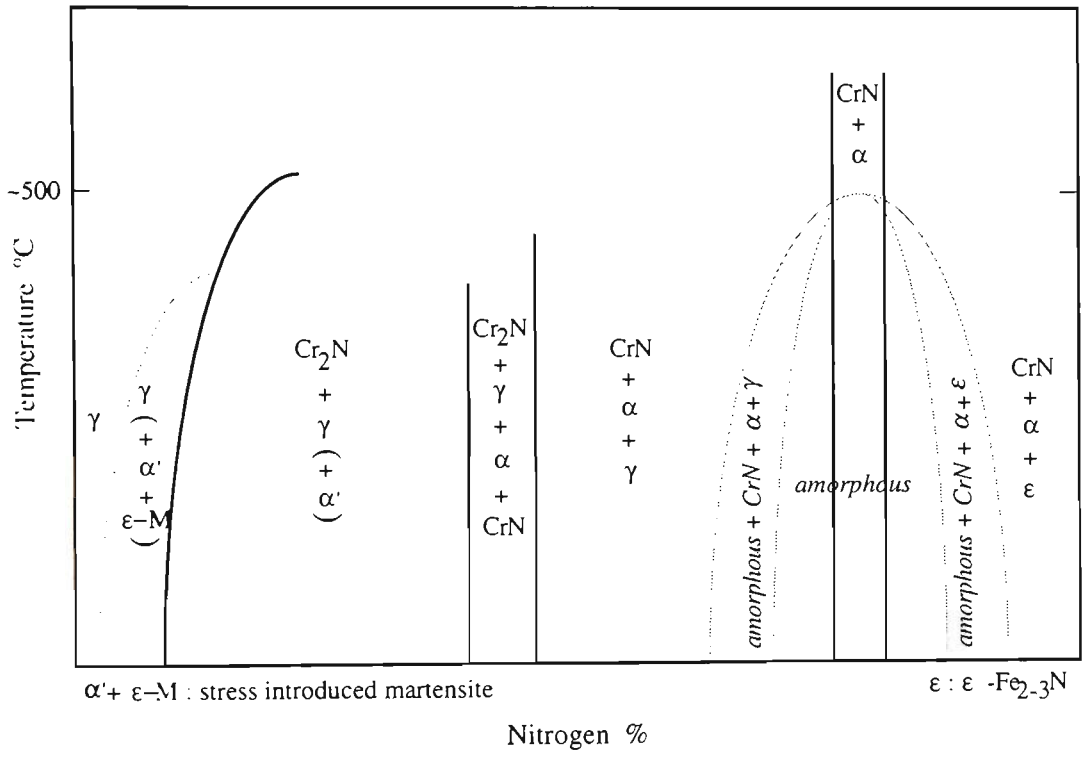

Figure 94 Proposed schematic lower part (below 550°C) of the vertical section of the Fe-18Cr-8Ni-N pseudo-phase diagram, applicable to phases detected in nitrogen treated 18/8 stainless steels.

Under the condition of nitrogen ion implantation and plasma nitriding, the accumulation of nitrogen at the sample surface will first activate γ to α' and ε-martensite transformation at low treatment temperature, since this temperature is lower than Md. However, this stress introduced α (labelled α' in the pseudo-phase diagram) and ε-martensite will not be the equilibrium phases. If the α' and ε-martensite phases are not considered, the left half of the current proposed phase diagram matches quite well with the one proposed by Rawers et. al. [84].

Although the phase diagram of Rawers et. al. [84] shows the CrN+α+γ three phase field following the CrN+γ two phase field directly with an increase in nitrogen, it is proposed that the CrN+γ two phase field may not exist (at least at the low temperature), while a four phase field, Cr_2N+γ+α+CrN, may exist between Cr_2N+γ (or Cr_2N+γ+α') and the CrN+α+γ three phase field. The reason for adding the Cr_2N+γ+α+CrN four phase field to the phase diagram lies in the fact that the stable α phase should precipitate together with CrN, due to their eutectic interaction.

The right half of the current proposed pseudo-phase diagram, corresponding to the high nitrogen concentration condition, may apply to most of the nitrogen implanted and nitrided austenitic stainless steel samples. Under equilibrium conditions, with increasing nitrogen concentration, the amount of γ will gradually decrease since nitrogen is not in solid solution but bonded with Cr, while the amount of α will gradually increase. So the CrN+α+γ three phase field will be replaced by the CrN+α two phase field. Further increase of the nitrogen concentration alters the system from CrN+α two phase field to CrN+α+ε three phase field, since ε-nitride starts to precipitate when all the chromium has combined with nitrogen.

However, at temperatures below 500°C, the equilibrium precipitation of eutectic CrN and α can not be realised. Based on the amorphous structure obtained below 500°C, an amorphous field is proposed in the current phase diagram. The proposed amorphous field can satisfactorily explain the amorphous structure in 250°C, 350°C and 450°C PI^3 treated samples. However, due to the lower implantation dose, and therefore a relatively low nitrogen concentration in the modified layer for the 150°C PI^3 treated sample in the present study, it is not clear whether the extra high-nitrogen concentration for the 150°C PI^3 treated sample could also drive the amorphous structure into the nanocrystalline state, like that for the 250°C and 350°C treated samples.

The phases found in the 450°C plasma nitrided sample show the composition of the nitrided layer is located in the CrN+α+γ three phase field. Therefore, as mentioned

before, the very thin amorphous sublayer observed in the 450°C plasma nitrided sample will not be a stable phase, but the early stage of precipitation. It is known that CrN and α eutectic precipitation is realised through nucleation and growth, which requires a large rearrangement of the metal atoms of the original γ structure, so the precipitation may take time. Thus, kinetically the unstable amorphous structure can form, but only as a very thin sublayer.

It is well known that nickel is a strong austenite former. With the formation of CrN in the nitrogen modified layer of austenitic stainless steel, almost all of the chromium atoms can be bonded with nitrogen, resulting in a matrix rich in nickel and iron. With possible dissolved nitrogen, which is a much stronger austenite former than nickel, it appears that the matrix should be austenite which coexists in a lamellar form with CrN. However, according to the present results, it is α phase which precipitates with CrN. With an increase in CrN, α increases while γ decreases. When the nitrogen concentration reaches a certain level, only CrN and α can be detected.

In fact, it is very hard to imagine that CrN and γ can cellularly precipitate together, since both have the same f.c.c. lattice and orientation, but one is obviously expanded with nitrogen atoms occupying octahedral interstices. In this case, the factor of structure compatibility should be taken into consideration. Phase transformation of the matrix, such as γ to α, or γ to ε-martensite, may be necessary to relieve the stress from the f.c.c. lattice expansion and to offset the rearrangement of the lattice structure. Therefore, structurally, α is a more favourable phase for cellular precipitation with CrN. Nevertheless, the details of why α is favoured for high Ni and N concentrations needs more study.

It should be pointed out that from author's other recent studies of XTEM+NBD characterisation of nitrogen implanted and plasma nitrided austenitic stainless steels, this proposed schematic diagram matches the characterisation results very well.

5.7 Comparison between PI^3 and Plasma Nitriding

From the previous discussion, it becomes clear that the microstructural evolution in the surface of the PI^3 treated and plasma nitrided austenitic stainless steel is essentially controlled by the nitrogen concentration introduced into the steel surface, and the temperature at which the sample is treated. This means that diffusion of the nitrogen atoms is the key to microstructural evolution.

It is well known that plasma nitriding, like other nitriding methods, requires the formation of nitrides to provide a concentration gradient for nitrogen diffusion. Under these conditions, the nitrogen gradient is limited by the speed of the chemical reaction.

The application of PI^3 for surface modification means that nitrogen atoms are directly implanted below the surface. By adjusting the implantation conditions, such as dose rate, a very high nitrogen concentration gradient can be obtained. At low temperature, due to the poor diffusibility of nitrogen in γ, a very high nitrogen concentration which can not be achieved by nitriding, can be built up in the modified layer, resulting in a high nitrogen concentration structures such as amorphous and even nanocrystalline CrN + α precipitation. At high temperature, a thicker modified layer can be obtained in a shorter time by faster nitrogen diffusion because of this high nitrogen gradient.

It has been reported that ion implantation itself does not introduce any structural change in metals [102,103,104,105,106]. In the present study, the nanocrystalline structure obtained at the surface of 250°C and 350°C PI^3 treated samples also shows that so called "radiation damage" may not really affect the surface microstructure of the PI^3 treated austenitic stainless steel, especially when the surface microstructure is nanocrystalline or amorphous. However, the thin nanocrystalline sublayer on the surface of the 520°C PI^3 treated sample shows that radiation damage does affect the equilibrium precipitation of the hard brittle phases, especially the growth of these precipitates. This

result is identical to the reported radiation damage on brittle materials such as implanted semiconductor materials [98].

Based on the above mentioned facts, it can be concluded that radiation damage only affects large hard brittle phases. However, this damage is limited to a very shallow layer, controlled by ion penetration depth.

Summing up the above discussion, it can be seen that the most important difference between PI^3 and plasma nitriding is that PI^3 offers a much higher nitrogen concentration and nitrogen gradient than plasma nitriding.

5.8 Factors Affecting Ion Implantation (PI^3)

From the previous discussion, it is obvious that PI^3 treatment, like nitriding, is basically a diffusion controlled process, e. g. the diffusibility of both nitrogen and metal atoms plays a key role in the microstructural evolution of the treated sample. Therefore, all factors affecting diffusibility of the nitrogen and metal atoms, such as nitrogen concentration obtained at the sample surface, temperature and time of the treatment, will control the microstructure obtained, and hence the properties, of PI^3 modified material.

5.8.1 Nitrogen Concentration on the Sample Surface

The high nitrogen gradient and lattice distortion caused by high nitrogen concentration helps to increase diffusion of the nitrogen atoms and metal atoms.

For PI^3 treatment, the surface concentration of the treated sample depends on how many nitrogen ions can be provided at the sample surface. Thus, it appears that the nitrogen dose will control the nitrogen concentration of the treated sample. In fact, the nitrogen dose has so far been considered as one of the most important factors for nitrogen ion implantation.

However, if the diffusion of the nitrogen atoms in the target material is taken into account, different treatment times will result in different nitrogen concentrations at the

same treatment temperature for a fixed ion dose. To balance the loss of the nitrogen atoms by diffusion and thereby maintain the nitrogen concentration on the sample surface at a certain level, the number of nitrogen ions implanted into the sample surface within a certain period of time, i.e. the dose rate, is actually a more important factor than the total implanted nitrogen dose.

5.8.2 Temperature

The temperature of treatment plays a very important role on affecting diffusibility of both interstitial and substitutional atoms and thus the microstructure and thickness of the modified layer. At low temperature, the very low dose rate may result in very high nitrogen concentration on the sample surface because of poor diffusibility of the nitrogen. At high temperature, very high dose rates may be required to maintain the nitrogen concentration level at the surface, since diffusion is fast.

5.8.3 Time

For a fixed dose rate and temperature of treatment, a longer treatment time by PI^3 will result in a thicker modified layer. The longer treatment time can also promote decomposition of the metastable phase, such as the amorphous phase, and so affect the final microstructures of the modified layer.

5.8.4 Radiation

Although the effect of radiation damage has been widely reported on ion implanted semiconductor materials, no radiation damage effects on metallic materials, such as radiation caused amorphisation or radiation enhanced diffusion, have so far been proved [98,183,32,103,222,51].

Based on the existence of a thin nanocrystalline sublayer (400-500 nm) obtained on the surface of the 520°C PI^3 treated sample, it is quite possible that nitrogen ion implantation does affect the hard brittle phases such as lamellar CrN and α by prohibiting

their coalescence and growth. However, apart from the smaller size of the precipitates, this radiation affected sublayer still has approximately the same components as in the non-radiation-affected area of the modified layer. Therefore, it is likely that the radiation effect of the implanted ions only has very limited affect on the growth of lamellar CrN and α at high temperature in a very shallow surface region.

5.9 Shortcomings of the Present Work and Proposed Research on PI^3 in Future

When all the samples for the present work were PI^3 treated a few years ago, the total implanted nitrogen dose was considered a dominant parameter. The prototype PI^3 chamber had no separate heating system and the sample was heated by the ion bombardment. Therefore, to obtain a fixed total ion dose for samples treated at different temperature, the treatment time for different samples had to be very different, e.g. from 45 minutes to 430 minutes. Similarly, the dose rate varied significantly for samples treated at different temperatures. The different times and dose rates resulted in some peculiar results, such as the lower temperature sample having a much thicker treated layer, making the comparison of samples PI^3 treated at different temperatures very difficult.

Table 10. Parameters of PI^3 treatment with fixed time of 5 hours

Sample ID	Voltage (keV)	Temperat. (°C)	Time (minute)	Nitrogen dose ($\times 10^{18}$ ions/cm^2)	Dose rate ($\times 10^{15}$ ions/cm^2·min)
PI350-5	40	350	300	2.0	6.7
PI450-5	40	450	300	3.2	10.7
PI520-5	40	520	300	4.5	15.0

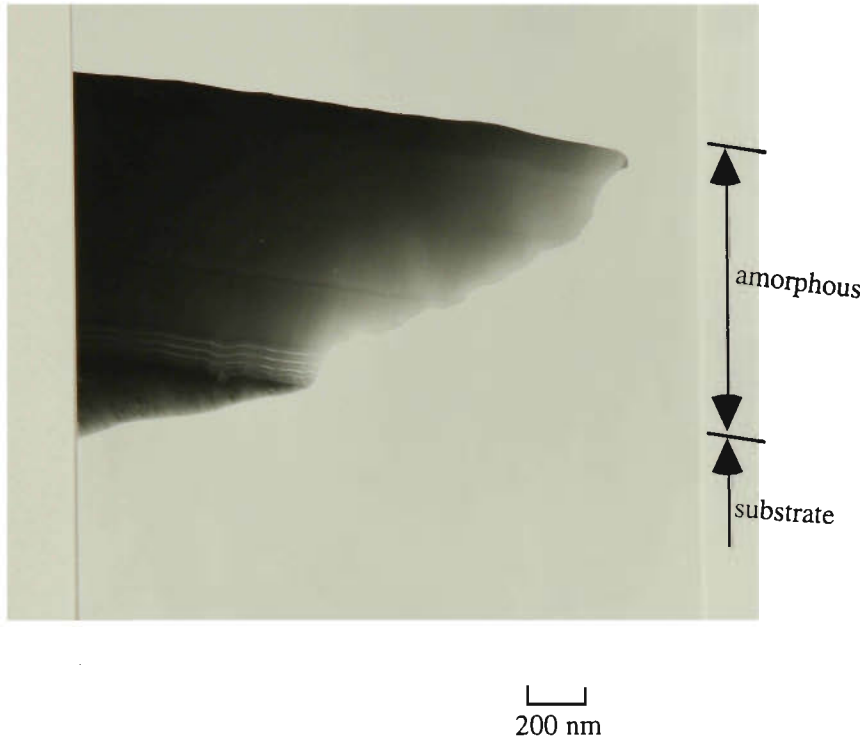

Figure 95 XTEM images of the implanted layer, PI[3] treated at 350°C, $2x10^{18}$ ions/cm^2, 5 hr. The implanted layer is amorphous, about 1.1 μm thick. The amorphous structure is characterised by 4-6 nm size clusters. An unusual transition band which is about 100 nm thick and also amorphous, is located at the bottom of the implanted amorphous layer. The first layer of the γ grains under the interface (3-5 μm thick) show obvious expansion, from about 3% at the interface to zero at the grain boundary. Some γ to α transformation has also occurred near the interface in this high dislocation γ region.

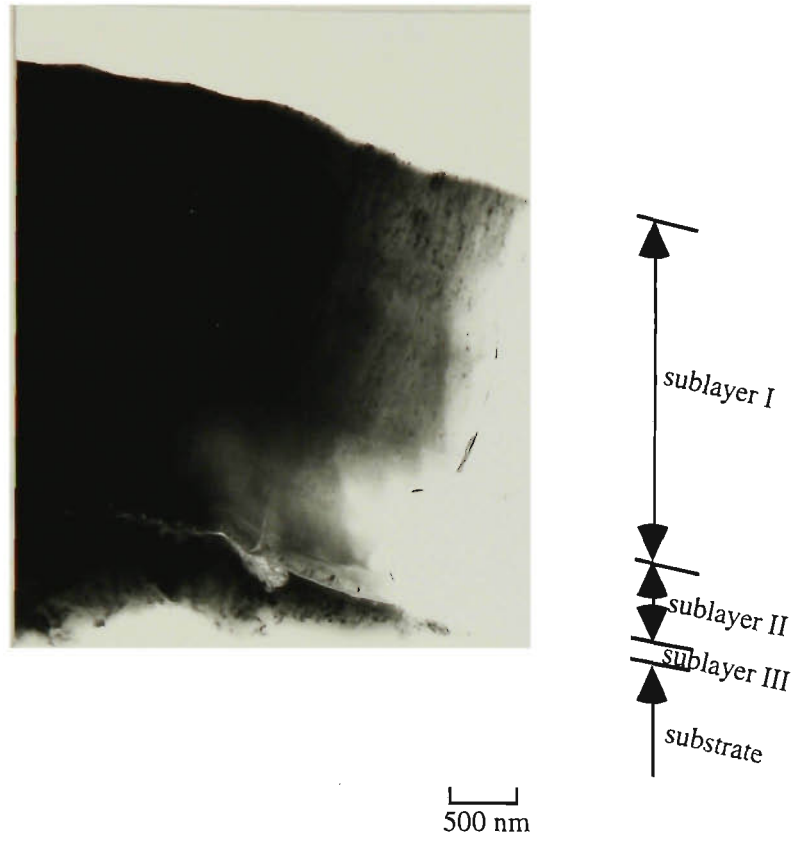

Figure 96 XTEM image of the implanted layer, PI^3 treated at 450°C, $3.2x10^{18}$ ions/cm^2, 5 hr. The thickness of the implanted layer is about 3.2 μm, divided into 3 sublayers. The first nano-crystalline sublayer is about 2.7 μm thick, composed of CrN, α and some γ precipitates at the size up to 50 nm at the surface and less than a few nm at the bottom. The second sublayer is semi-amorphous and about 0.4 μm thick, with CrN and α (may be small amount of γ as well) particles of less than 6-7 nm. The third sublayer is also nano-crystalline, about 0.1 μm thick, composed of (Cr,Fe)N and α precipitates, at sizes up to about 40 nm, plus some γ phase. There is an approximately 1.5 μm thick stress affected high dislocation γ region under the implanted layer which shows about 3% expansion near the interface with gradual decrease to zero at about 1.5 μm from the interface. According to the orientation of the γ grains in the substrate, some stress affected zones show a small amount α precipitates near the interface, while some other stress affected zones show a small amount of ε-martensite.

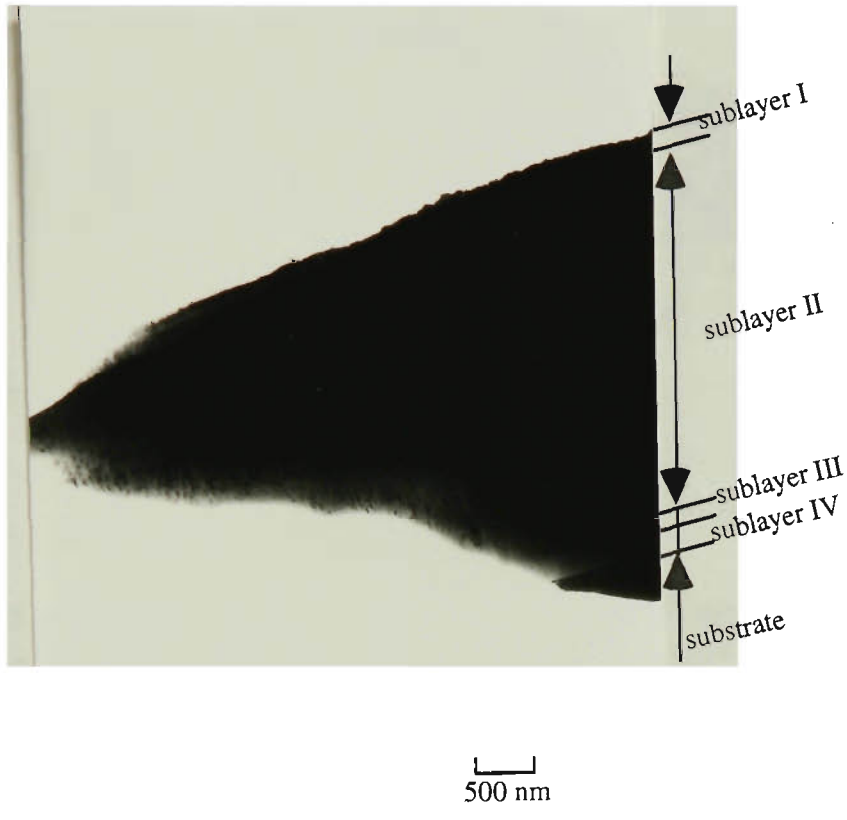

Figure 97 XTEM image of the implanted layer, PI^3 treated at 520°C, 4.5x10^{18} ions/cm^2, 5 hr. The whole implanted layer is about 3.5 μm and can be divided into 4 sublayers. The first sublayer is nano-crystalline with very fine CrN and α precipitates (less than 6-7 nm), about 0.1 μm thick. The second sublayer is also nano-crystalline and about 2.9 μm thick, composed of CrN and α precipitates up to 60-70 nm. Traces of γ phase is also detected in second sublayer. The third sublayer is amorphous and about 0.1 μm thick. The fourth sublayer is semi-amorphous with fine (Cr,Fe)N and α precipitates less than 20 nm, plus traces of γ-austenite. The thickness of the fourth sublayer is about 0.4 μm. There is no visible stress affected zone under the PI^3 treated layer, only a very thin area (about 6-7 nm thick) in front of the interface shows some stress effect as slightly expanded γ and traces of α detected by NBD.

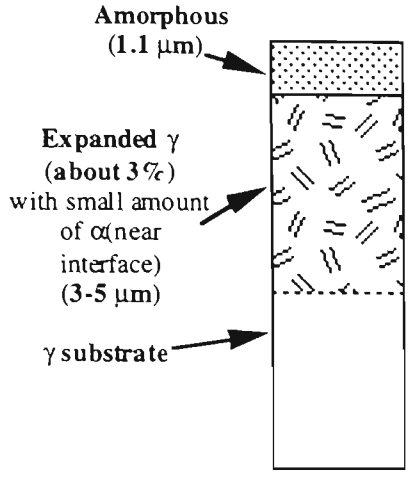

a. PI^3 treated at 350°C
2x10^{18} ions/cm^2, 5 hr.

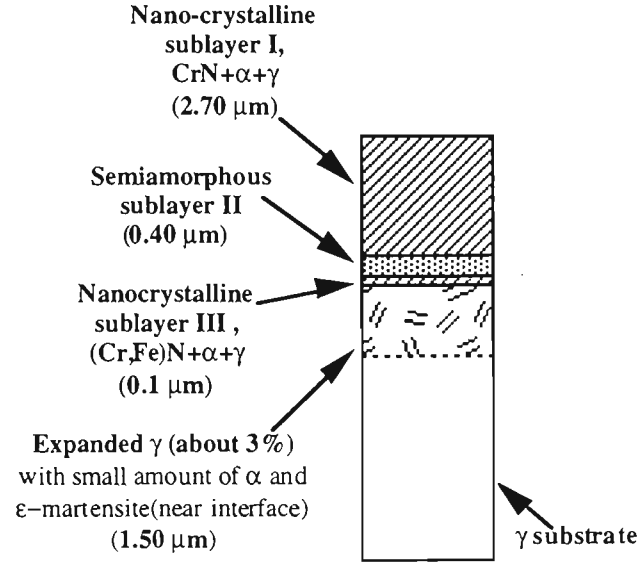

b. PI^3 treated at 450°C
3.2x10^{18} ions/cm^2, 5 hr.

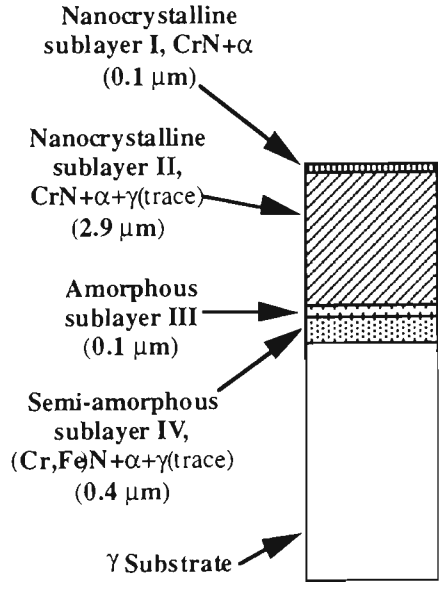

d. PI^3 treated at 520°C
4.5x10^{18} ions/cm^2, 5 hr.

Figure 98 Summarised description of the surface microstructure, 316 stainless steel, PI^3 treated with fixed time (5 hours).

As revealed by XTEM + NBD, PI^3 treatment is actually a diffusion controlled process. To clarify the effect of treatment time on surface microstructure, another

set of 316 stainless steel samples was subsequently PI^3 treated with a fixed treatment time of 5 hours in a new chamber at ANSTO. Table 10 gives the parameters of the treatment. Unfortunately this new chamber still had no separate heating system at the time of the treatment. Therefore, the dose rate had to change with different treatment temperatures, complicating the analysis of the PI^3 treatment results. However, by referring to XTEM images (Figure 95-97) and the summarised description of XTEM+NBD characterisation of samples PI^3 treated at fixed times (Figure 98), it is apparent that the higher treatment temperature corresponds to the thicker PI^3 treated layer. The stress exerted by the PI^3 treated layer onto the substrate also decreases with increase of the treatment temperature, from a 3-5 μm high dislocation zone in the 350°C treated sample to a 1.5 μm high dislocation zone in the 450°C treated sample, and finally no stress affected high dislocation zone for the 520°C treated sample.

By comparing the microstructure of the samples treated with fixed time to previous samples treated with fixed dose, it is very interesting to note that all samples with fixed time show lower nitrogen concentrations in the treated surface, even though the recorded dose rate for both group of samples are quite similar. For example, the sample treated at 350°C for 5 hours shows a single amorphous structure, while the sample treated with fixed dose at the same temperature shows a layered surface structure with a nanocrystalline CrN+α+ε(trace) outermost layer. Although the sample treated at 450°C with fixed dose shows a single amorphous layer, the sample treated for 5 hours shows no amorphous layer at all but a lower nitrogen structure, e. g. nanocrystalline CrN+α+γ with a very thin semi-amorphous transition sublayer at the interface. Instead of lamellar CrN and α precipitates, the lower nitrogen concentration in the 520°C treated sample surface resulted in an incompletely developed low nitrogen structure of very fine nanocrystalline CrN+α+γ precipitates with a thin transition amorphous sublayer between the CrN and α precipitates and the substrate.

The lower nitrogen concentration for samples PI^3 treated for 5 hours also resulted in a thinner treated layer than previous fixed dose samples though the treatment time is

much longer. The thinner treated layer with longer treatment time may also be explained by lower nitrogen concentration in the surface which provides less driving force for expansion of the treated layer.

The lower surface nitrogen concentration for the fixed 5 hours samples indicates the complexity and criticality of controlling the PI^3 process. As mentioned in Chapter 3, the PI^3 treatment is realised by applying the duty cycle of high voltage pulses to the plasma. When the high voltage pulse is on, nitrogen ions will be implanted into the sample surface. However, nitrogen will also reversely diffuse out when the pulse is off. Since the chamber is under high vacuum (a very low nitrogen potential around the sample), when the pulse is off, the loss of nitrogen at the sample surface by reverse diffusion may reach a very high level. Therefore, even for the same dose rate, different frequencies and durations of the high voltage pulse may result in different nitrogen concentrations and hence different surface microstructures. Unfortunately, the details of the high voltage pulses for the fixed 5 hours samples are not available, since the treatment was conducted during the set up of the new chamber.

Although it is clear that temperature, time, dose rate and high voltage pulses are all playing important roles in PI^3 treatment, it is very hard to control all those factors precisely in a PI^3 chamber without an independent heating system. It is obvious that when samples in a PI^3 chamber are heated by ion bombardment, changing of one control variable will result in changes of others as well. To understand and control the PI^3 process better, it is strongly recommended that an independent heating system be incorporated in the PI^3 chamber.

CHAPTER 6 CONCLUSIONS

In the present work, the cross-sectional transmission electron microscopy (XTEM) technique, traditional selected area diffraction (SAD), nanobeam electron diffraction (NBD), and high resolution electron microscopy (HREM) have been used to investigate the surface microstructure of PI^3 treated and plasma nitrided AISI 316 austenitic stainless steel. Glancing angle X-ray diffraction (GAXD) is also employed on all plasma nitrided and PI^3 treated samples for comparison. It has been found that the PI^3 treatment is a diffusion controlled process, so that the nitrogen concentration obtained on the sample surface plays a very important role in determining the microstructure in the surface layers, as it does for plasma nitrided 316 stainless steel. More specific conclusions are given below:

1. All the results obtained in the present study show that thermodynamic criteria are still valid for microstructural evolution during the non-equilibrium process of ion implantation. Generally, with increasing nitrogen concentration in austenitic stainless steel, the microstructure of the PI^3 treated or plasma nitrided 316 austenitic stainless steel surface evolves in the following way:

$$\gamma \rightarrow \begin{matrix}\gamma_{exp\ (>Md)} \\ \text{or} \\ \gamma_{exp}(+\alpha^* + \varepsilon\text{-M})\ (<Md)\end{matrix} \rightarrow \gamma + Cr_2N(+\alpha^*) \rightarrow \gamma + Cr_2N + \alpha + CrN$$

$$\rightarrow CrN + \alpha + \gamma \rightarrow \begin{matrix}CrN + \alpha\ (>500°C) \\ \text{or} \\ \text{amorphous}\ (<500°C)\end{matrix} \rightarrow CrN + \alpha + \varepsilon\text{-nitride}$$

2. The precipitation of CrN and α is strongly affected by the temperature. Above 500°C, CrN and α can directly nucleate from γ. Below about 500°C, precipitation of CrN and α needs excessive atomic rearrangement which results in collapse of the γ substrate into an "amorphous" phase from which very fine CrN and α precipitates nucleate. Both Bain and N-W relationships have been observed between CrN and α precipitates. The K-S relationship has also been observed between CrN and α at

low temperature and low nitrogen concentration (e.g. 350°C plasma nitrided sample).

3. It has been shown for the first time that if the nitrogen content in the austenite reaches eutectic concentration (CrN+α), e.g. PI^3 treatment at temperatures below 500°C, an amorphous layer up to 3 μm thick can be obtained. This thick amorphous layer, especially the one located under the nanocrystalline sublayer, strongly contradicts the prevailing theory that radiation damage causes the amorphisation of ion implanted steel. The present work indicates that the tendency for solid state eutectic reaction, provides the driving force for amorphisation.

4. For nitrogen implanted austenitic stainless steel, the radiation damage only has very trivial effects on the coalescence and growth of the hard brittle nanocrystalline phases such as eutectic CrN and α. The depth of this radiation damage is limited by the penetration depth of the implanted ions, which is less than a few hundred nanometres.

5. Cr_2N, an eutectoid phase, can precipitate directly from γ. The following orientation relationship has been observed between Cr_2N and γ:

$$(011)\gamma \,//\, (\bar{3}211)Cr_2N$$

$$[100]\gamma \,//\, [12\bar{3}2]Cr_2N$$

6. The expansion of γ by dissolving nitrogen is limited to about 3%. Further dissolved nitrogen will cause nitrides to precipitate. No γ expansion has been observed after nitrides are precipitated.

7. No γ′ is observed as a stable phase in PI^3 treated or plasma nitrided austenitic stainless steel. Traces of γ′ have only been detected as a transition phase at the interface.

8. GAXD is not suitable for thin nanocrystalline surface microstructural characterisation, especially for a complicated system such as nitrogen ion implanted and plasma nitrided austenitic stainless steel due to its poor lateral and depth resolution.

9. The most important difference between PI^3 and plasma nitriding is that the PI^3 treatment can provide much higher nitrogen concentrations on the sample surface, resulting in specific surface microstructures such as amorphous structure.

10. The amorphous structure can provide outstanding wear and corrosion resistance but more precise control of the PI^3 process is needed in order to optimise the development of the amorphous sublayer on austenitic stainless steels.

REFERENCES

[1] P.A. Dearnley, A. Namvar, G.G.A. Hibberd & T. Bell, *Plasma Surface Engineering: Proc. 1st Int. Conf. on Plasma Surface Engineering*, edited by E. Broszeit, W.D. Münz, H. Oechsner, K.-T. Rie & G.K. Wolf, Garmisch-Partenkirchen, Vol. 1, 1989 p.219-226.

[2] Z.L. Zhang, and T. Bell, *Surface Engineering*, 1 (1985) 131-136.

[3] E. Rolinski, *Surface Engineering*, 3 (1987) 35-40.

[4] M. Samandi, B.A. Sheddon, D.I. Smith, G.A. Collins, R. Hutchings & J. Tendys, *Surface Coatings and Technology*, 59 (1993) 261-266.

[5] J. Flis, J. Mankowski and E. Rolinski, *Surface Engineering*, 5 (1989) 151-157.

[6] S. Song, W. Song, and Z. Fang, *Passivation of Metals and Semiconductors Corrosion Science*, 31 (1990) 395-400.

[7] Y. Arnaud, M. Brunel, A.M. DeBecdelievre, M. Romand, P. Thevenard and M. Robelet, *Applied Surface Science*, 26 (1986) 12-26.

[8] F. Gaillard, A.M. DeBecdelievre, M. Romand, H. Hcoquaux and P. Thevenard, *Proceedings of 8th European Congress on Corrosion*, Volume 1, Paris, 19-21 November 1985, p.67-1 - 67-6.

[9] B.J. Lightfoot & D.H. Jack, *Heat Treatment 73'*, 1975, The Metals Society, London, 59-65.

[10] K.H. Jack, *Heat Treatment 73'*, 1975, The Metals Society, London, 39-50.

[11] T. Bell, B.J. Birch, V. Korotchenko & S.P. Evans, *Heat Treatment 73'*, 1975, The Metals Society, London, 51-57.

[12] B. Edenhofer, *Heat Treatment of Metals-part 1*, 1 (1974) 23-28.

[13] C.K. Jones, S.W. Martin, D.J. Sturges & M. Hudis, *Heat Treatment 73'*, 1975, The Metals Society, London, 72-77.

[14] M. Hudis, *Journal of Applied Physics*, 44 (1973) 1489-1496.

[15] B. Edenhofer, *Heat Treatment of Metals -part 2*, 2 (1974) 59-67.

[16] G.G. Tibbetts, *Journal of Applied Physics*, 45 (1974) 5072-5073.

[17] T. Spalvins, *Thin Solid Films*, 108 (1983) 157-163.

[18] S.-P. Hannula, P. Nenonen & J.P. Hirvonen, *Thin Solid Films*, 81 (1989) 343-350.

[19] A. Saker, Ch. Leroy, H. Michel & C. Frantz, *Materials Science & Engineering*, A140 (1991) 702-708.

[20] C. Leroy, H. Michel and M. Gantois, J. Materials Science, 21 (1986) 3467-3474.

[21] K. Ichii, K. Fujimura & T Takase, *Technology Reports of Kansa University*, 27 (1986) 135-144.

[22] N.E.W. Hartley, W.E. Swindlehurst, G. Dearnaley & J.F. Turner, *Journal of Materials Science Letters*, 8 (1973) 900-904.

[23] A.V. Byeli, S.K. Shikh & V.V. Khatko, *Wear*, 159 (1992) 185-190.

[24] S.Lo. Russo, P. Mazzoldi, I. Scotoni, C. Tosello & S. Tosto, *Applied Physics Letters*, 34 (1979) 627-629.

[25] H. Dimigen, K. Kobs, R. Leutenecker, H. Ryssel & P. Eichinger, *Materials Science & Engineering*, 69 (1985) 181-190.

[26] M. Baron, A.L. Chang, J. Schreur & R. Kossowsky, *Nuclear Instruments and Methods*, 182/183 (1981) 531-538.

[27] A. Cavalleri, L. Guzman, P.M. Ossi & I. Rossi, *Scripta Metallurgica*, 20 (1986) 37-42.

[28] F.G. Yost, S.T. Picraux, D.M. Follstaedt, L.E. Pope & J.A. Knapp, *Thin Solid Films*, 107 (1983) 287-295.

[29] M.J. Kenny, L.S. Wielunski, J. Tendys & G.A. Collins, *Nuclear Instruments and Methods in Physics Research*, B80 (1993) 262-266.

[30] G.A. Collins, R. Hutchings &J. Tendys, *Surface Coatings and Technology*, 59 (1993) 267-273.

[31] J.R. Conrad, J.L Radtke, R.A. Dodd, F.J. Worzala & N.C. Tran, *Journal of Applied Physics*, 62 (1987) 4591-4596.

[32] I.L. Singer and J.S. Murday, *J. Vac. Sci.Technol.*, 17 (1980) 327-329.

[33] R.G. Vardiman, R.N. Bolster and I.L. Singer, *Metastable Materials Formation by Ion Implantation*, Edited by S.T. Picraux and W.J. Choyke, published 1982 by Elsevier Science Publishing Company, Inc., 269-274.

[34] J.L. Whitton, M.M. Ferguson, G.T. Ewan, I.V. Mitchell and H.H. Plattner, *Appl. Phys. Lett.*, 41 (1982) 150-152.

[35] G.F. Vander Voort and H.M. James, *Metal Handbook, Nineth edition*, published by ASM, Metal Park, Ohio, USA, edited by K. Mills, J.R. Davis, J.D. Destefani, D.A. Dieterich, G.M. Crankvic, H.J. Frissell and D.M. Jenkins, Volume 9, 279-296.

[36] J. L. Whitton, G.T. Ewan, M.M. Ferguson, T. Laursen, I.V. Mitchell, H.H. Plattner, M.L. Swanson, A.V. Drigo, G. Celotti and W.A. Grant, *Mat. Sci. Engi.*, 69 (1985) 111-116.

[37] S. Fayeulle and D. Treheux, *Appl. Surface. Sci.*, 25 (1986) 288-304.

[38] S. Fayeulle and D. Treheux, *Nucl. Instr. Methods*, B19/20 (1987) 216-220.

[39] I.L. Singer, R.G. Vardiman and R.N. Bolster, *J. of Mater. Res.*, 3 (1988) 1134-1143.

[40] J. N. Feugeas, E.C. Llonch, C.O. de Gonzalez and G. Galambos, *J. Appl. Phys.*, 64 (1988) 2648-2651.

[41] R. Leutenecker, G. Wagner, T. Louis, U. Gonser, L. Guzman nd A. Molinari, *Mat. Sci. Eng.*, A115 (1989) 229-244.

[42] E. H. Lee and L. K. Mansur, *J. Mater. Res.*, 4 (1989) 1371-1378.

[43] B. Sheddon, B.E. Thesis, Department of Materials Engineering, University of Wollongong, December, 1992

[44] D. L. Williamson, O.Ozturk, S. Glick, R. Wei and P.J. Wilbur, *Nuc. Inst. Methods,* B59/60 (1991) 737-741.

[45] R. Wei, P.J. Wilbur, O.Ozturk and D.L. Williamson, *Nuc. Inst. Methods*, B59-60 (1991) 731-736.

[46] Sadhna Shrivastava, Ram D. Tarey, M.C. Bhatnagar, Amitabh Jain and K.L. Cohpra, *Surface and Coatings Technology*, 50 (1991) 41-44.

[47] M.E. Chanbica, D.L. Williamson, R. Wei and P.J. Wilbur, *Surface and Coatings Technology*, 51 (1992) 24-29.

[48] J. Rieu, A. Pichat, L-M. Rabbe, A. Rambert, C. Chabrol and M. Robelet, *Surface Modificatio Technologies V: Proc. Fifth international Conf.*, Birmingham, UK, 2-4 Sept., 1991, edited by T.S. Sudarshan and J.F. Braza, The Institute of Materials, 1992, p.155-165.

[49] G.R. Rao, E.H. Lee and B.A. Chin, *Surface and Coatings Technology*, 51 (1992) 112-117.

[50] S. Aggarwal, A.K. Goel, R.K. Mohindra, P.K. Ghosh and Ami Chand, *Thin Solid Films*, 223 (1993) 72-77.

[51] D.L. Williamson, O. Ozturk, R. Wei and P.J. Wilbur, *Surface and Coating Technology*, 5 (1994) 15-23.

[52] Okio Nishimura, Katsumasa Yabe, Kazuo Saito, Toshiro Yamashina and Masaya Iwaki, *Surface and Coatings Technology*, 66 (1994) 403-407.

[53] Ryoichi Urao, Kazue Yamagata and Hiroyuki Yoshida *Proc. 7th ICVM*, 1982, Tokyo, Japan, 585-591.

[54] B. Billon and A. Hendry, *EMAG 83: Proc. of the Institute of Physics Electron Microscopy and Analysis Group Conf.*, University of Guilford, 30 Aug. - 2 Sep., edited by P. Doig, Conference Series Number 68, The Insitute of Physics, Bristol and London, 1983, p.367-370.

[55] B. Billon and A. Hendry, *EMAG 83: Proc. of the Institute of Physics Electron Microscopy and Analysis Group Conf.*, University of Guilford, 30 Aug. - 2 Sep., edited by P. Doig, Conference Series Number 68, The Institute of Physics, Bristol and London, 1983, p.293-296.

[56] M.F. Chung, A.K. Yap and Y.K. Lim, *Scripta Metallurgica*, 19 (1985) 415-419.

[57] B. Billon and A. Hendry, *Surface Engineering*, 1 (1985) 114-124.

[58] M.F. Chung and Y.K. Lim, *Scripta Metallurgica*, 20 (1986) 807-812.

[59] M.F. Chung and Y.K.Lim, *Surface Engineering*, 3 (1987) 326-330.

[60] S-P Hannula, P Nenonen and J. Molarius, *High Nitrogen Steel 88, Conf. Proc. HNS-88*, Lille, France, May 18-20 1988, Institute of Metals, London, 266-271.

[61] F. El-Hossary, F. Mohammed, A. Hendry, D.J. Fabian and Z. Szaszne-Csih, *Surface Engineering*, 4 (1988) 150-154.

[62] P.A. Dearnley, G.G.A. Hibberd and T. Bell, *CHEMECA '90*, 27th - 30th Aug. 1990, Auckland, New Zealand, 262-271.

[63] J. D'haen, C. Quaeyhaegens, G. Knuyt, L. De, L.M. Stals and M. Van Stappen, *Surface and Coating Technol.*, 60 (1993) 468-473.

[64] T.L. Barr, *Practical Surface Analysis by Auger and X-ray Photoelectron Spectroscopy*, Edited by D. Briggs and M.P. Seah, © 1983, John Wiley & Sons, Ltd., p.283-358.

[65] A. Joshi, *Crystal Properties & Preparation*, 16 (1988) 95-110.

[66] U. Gonser, *An Introduction to Mössbauer Spectroscopy*, Edited by Leopold May, © 1971 Plenum Press, New York, 155-179.

[67] I.V. Mitchell, *Phys. Bull.*, 30 (1979) 23-25.

[68] G. Stein, J. Menzel and H. Dorr, *High Nitrogen Steel 88, Conf. Proc. HNS-88*, Lille, France, May 18-20 1988, Institute of Metals, London, p. 32.

[69] J.Menzel, G. Stein and P. Dahlman, *High Nitrogen Steel 88, Conf. Proc. HNS-88*, Lille, France, May 18-20 1988, Institute of Metals, London, p. 147

[70] A. Omsen and L. Eliasson, *J. Iron Steel Inst. (London)*, 209 (1971) 830.

[71] H.A. Wriedt, N.A. Gokcen and R.H. Nafziger, *ASM Handbook*, vol.3, Edited by Hugh Baker, Published by ASM International, Dec. 1992, U.S.A., p. 2-198.

[72] H.J. Grabke, *Ber. Bunsenges. Phys. Chem.*, 73 (1969) 596.

[73] H.A. Wriedt, *Trans. TMS-AIME*, 245 (1969) 43.

[74] K.H. Jack, *Acta Crystallog.*, 5 (1952) 404.

[75] K.H. Jack, *Proc. Roy. Soc.*, 208 (1951) 216-224.

[76] R. Blix, *Z. Physik. Chem.*, B3 (1929) 229-239.

[77] V.S. Mozgovoi and A.M. Samarin, *Doklady Akad. Nauk S.S.S.R.*, 74 (1950) 729-732.

[78] S. Eriksson, *Jernkontorets Ann.*, 118 (1934) 530-543.

[79] W. Hume-Rothery and W.B. Pearson, *J. Inst. Metals*, 76 (1949-1950) 722-725.

[80] F.C. Blake and J.O. Lord, *Phys. Rev.*, 35 (1935) 660.

[81] K.H. Jack, *Acta Crystallog.*, 13 (1950) 392.

[82] G. Hägg, *Z. Physik. Chem.*, B7 (1930) 339.

[83] K. Frisk and M. Hillert, *High Nitrogen Steel 88, Conf. Proc. HNS-88*, Lille, France, May 18-20 1988, Institute of Metals, London, p. 1.

[84] J.C. Rawers, J.S. Dunning, G. Asai and R.P. Reed, *Metall. Trans. A*, 23A (1992) 2061-2068.

[85] R.P.Goehner, *Metals Handbook*, Ninth Edition, Vol. 10, American Society for Metals, Metals Park, Ohio, 1986, 333-343.

[86] R.P.Goehner and M.O.Eatough, *Powder Diffraction*, 7 (1992) 2-5.

[87] Y.Arnaud, M.Brunel, A.M.DeBecdelievre, M.Romand, P.Thevenard and M.Robelet, *Applied Surface Science*, 26 (1986) 12-26.

[88] T.Takayama, and Y.Matsumoto, *The Sumitomo Search*, 44 (1990) 352-360.

[89] R.Alani, J.Jones and P.Swann, Specimen Preparation for Transmision Electron Microscopy of Materials II, *Mater. Res. Soc. Symp.Proc.*, 199 (1991) 85-101.

[90] Lu Ke, *Acta Metallurgica Sinica,* Series B, 5 (1992) 245-254.

[91] B.X. Liu, S. Zhou and H.D. Li, *Phys. Stat. Sol.* (a), 113 (1989) 11-22.

[92] H.J. Goldschmidt, *Interstitial Alloys*, chapter 3, Butterworths pub., London, Britain, 60

[93] E.T. Turkdogan and S. Ignatowicz, *JISI*, Mar. 1958, 242-247.

[94] Y.F. Zhao, S.Z. Sun, L.L. He, H.Q. Ye and S.J. Pang, *Vacuum*, 43 (1992) 1065-1067.

[95] T. Bell and W.S. Owen, *JISI*, 205 (1967) 428-434.

[96] Francisco Eiichi Fujita, *Structure and Properties of Aorphous Metals II, Pro. of the Symp.*, Seaside Irago, Aichi Prefecture, Dec. 13-15, 1979, Supplement to the Science Reports of the Research Institutes, Tohoku University, Series A, Vol. 28, 1980.

[97] Hideki Ichinose and Yoichi Ishida, *10th Int. Congress on Electron Microscopy: Electron Microscopy 1982*, Vol. 2, Hamboug, West Germany, Aug. 17-24 1982, 77-78.

[98] C. Cohen, A. Benyagoub, H. Bernas, J. Chaumont, L. Thomé, M. Berti and A.V. Drigo, *Physical Review B*, 31 (1985) 5-14.

[99] Dokyol Lee, J. Cheng, M. Yuan, C.N.J. Wagner and A.J. Ardell, *J. Appl. Phys.*, 64 (1988) 4772-4774.

[100] A. Serebryakov, *Scripta Metallurgica et Materialia*, 28 (1993) 1011-1016.

[101] Yoshihiko Hirotsu, *Materials Science and Engineering*, A179/A180 (1989) 97-101.

[102] W.A. Grant, A. Ali, L.T. Chadderton, P.J. Grundy and E. Johnson, *Rapidly Quenched Metals III: Proc. of the Third International Conf. on Rapidly Quenched Metals*, University of Sussex, Brighton, 3-7th July 1978, edited by B. Cantor, The Metals Society, Volume 1, 63-72.

[103] N.L. Lee, G.B. Fisher, Y.T. Cheng, *Environmental Degradation of Ion and Laser Beam treated Surfaces*, Edited by G.S. Was and K.S. Grabowski, TMS, 1989, 107-126.

[104] J.M. Hampikian and D.I. Potter, *Oxidation o Metals*, 38 (1992) 125-137.

[105] E.C. Cooney and D.I. Potter, *Surface and Coating Technology*, 51 (1992) 420-428.

[106] X. Li, *The effect of nitrogen implantation on gold*, Uni. of Adelaide, internal memo, Nov., 1991.

[107] H. Mori and T. Sakata, *J. of Alloys and Compounds*, 194 (1993) 381-387.

[108] S. Steeb and P. Lamparter, *J. Non-Crystalline Solids*, 150 (1993) 24-33.

[109] J.L. Brimhall and E.P. Simonen, *Nucl. Instr. and Methods*, B16 (1986) 187.

[110] D. L. Williamson, O. Ozturk, S. Glick, R. Wei and P.J. Wilbur, *Nuc. Inst. Methods*, B59/60 (1991) 737-741.

[111] E.T. Turkdogan and S. Ignatowicz, JISI, Mar. 1958, 242-247.

[112] J.A. Hawk, J.W. Simmons and J.C. Rawers, *Journal of Materials Engineering and Performance*, 3 (1994) 259-272.

[113] L.J. Swartzendruber and L.H. Bennett, *Metal Handbook, Nineth edition*, published by ASM, Metal Park, Ohio, USA, edited by K. Mills, J.R. Davis, J.D. Destefani, D.A. Dieterich, G.M. Crankvic, H.J. Frissell and D.M. Jenkins, Volume 10, 287-295

[114] U. Dahmen, P. Ferguson, *Acta Metall.*, 35 (1987) 1037-1046.

[115] P. Hirsch, A. Howie, R.B. Nicholson, D.W. Pashley, M.J. Whelan, *Electron Microscopy of Thin Crystals*, Published by Roberte. Krieger Publishing Com., Malabar, Florida, USA, 1965, 97-100.

[116] Y.F. Zhao, S.Z. Sun, L.L. He, H.Q. Ye and S.J. Pang, *Vacuum*, 43 (1992) 1065-1067.